Summer 6-8-2012

Laser-Based Spectroscopy and Spectrometry

Xiangnan He
University of Nebraska-Lincoln, hexiangnan@gmail.com

LASER-BASED SPECTROSCOPY AND SPECTROMETRY

by

Xiangnan He

A DISSERTATION

Presented to the Faculty of

The Graduate College at the University of Nebraska

In Partial Fulfillment of Requirements

For the Degree of Doctor of Philosophy

Major: Engineering

(Electrical Engineering)

Under the Supervision of Professor Yongfeng Lu

Lincoln, Nebraska

August, 2012

LASER-BASED SPECTROSCOPY AND SPECTROMETRY

Xiangnan He, Ph.D.

University of Nebraska, 2012

Adviser: Yongfeng Lu

Laser-based spectroscopy and spectrometry were extensively investigated in nanoscience, materials science, biomedical science, and etc. Different lasers with wavelengths from ultraviolet to infrared, and with duration from continuous-wave (CW) to femtoseconds have been employed in various spectroscopic techniques to investigate the properties of materials and nanostructures. However, the sensitivity, spectral resolution, and spatial resolution of these techniques still need to be improved to better serve the purposes of detecting and analyzing various materials. The objective of the research in this dissertation is to improve the sensitivity, spectral resolution, and spatial resolution of different laser-based spectroscopy and spectrometry techniques, such as tip- and surface-enhanced Raman spectroscopy (TERS and SERS), coherent anti-Stokes Raman spectroscopy (CARS), optical emission spectroscopy (OES), laser-induced breakdown spectroscopy (LIBS), and laser-assisted mass spectrometry (LAMS).

(1) To overcome the diffraction limit of light, a TERS system, using an apertureless metallic tip as a near-field probe, was built for measuring nanoscale materials and structures. (2) Gold-coated horizontally aligned carbon nanotubes (Au-HA-CNTs) were fabricated as a new type of SERS active substrate by using laser-assisted chemical vapor deposition (LCVD), followed by a sputtering coating process. (3) A broadband CARS system was built with a Ti:sapphire femtosecond (fs) laser as pump (ω_p)

and a photonic crystal fiber (PCF) as a white light source for Stokes beam generation (ω_s). (4) OES of combustion flames for diamond synthesis was carried out with laser resonant excitation (by a wavelength-tunable continuous wave (CW) CO_2 laser at a wavelength of 10.532 μm to resonantly excite the CH_2-wagging vibrational mode of the C_2H_4 molecules). (5) High-temperature and low-density plasmas were generated for improved spectral resolution in LIBS. (6) Laser-assisted mass spectrometry was realized using laser ionization combined with metastable ionization in open air for solid material measurement. In summary, the research on laser-based spectroscopy and mass spectrometry has rendered improved performance in sensitivity, spectral resolution, or spatial resolution, which are significantly important for the development of characterization techniques for various novel materials and structures.

ACKNOWLEDGEMENT

During the five years in his PhD program, the author has gained so much through the study here in the Department of Electrical Engineering at the University of Nebraska-Lincoln (UNL). The author would like to take this precious opportunity to thank all the people who have provided the author great help and valuable suggestions both in his academic study and personal life.

First of all, the author would like to thank his supervisor, Prof. Yongfeng Lu, who has provided the author this great opportunity to study in this fast growing research group. He is a great mentor giving the author invaluable advice to find the right way out of difficulties in both his academic pursuit and personal life. Without his supervision and financial support, the author cannot complete this PhD program smoothly without extra worries. From his help and advices, the author has made great progress not only in his research projects, but also in his writing and presentation skills. The most important thing the author has learned from Prof. Lu is the way to think, do, and learn in a fast-pacing environment.

Secondly, special thanks go to the author's degree committee members, Profs. Dennis R. Alexander and Ming Han from the Department of Electrical Engineering at UNL, and Prof. Stephen Ducharme from the Department of Physics and Astronomy at UNL, for their time and efforts on instructing him to complete the degree.

Thirdly, the author would like to thank his colleagues in the Laser-Assisted Nano Engineering (LANE) laboratory. Without them, he cannot imagine how hard life would be. Specifically, the author appreciate Dr. Kaijun Yi with whom he had worked on the

tip-enhanced Raman spectroscopy project, Dr. Hao Wang who taught him sample preparation techniques, Dr. Xiaokang Shen who instructed him on laser-induced breakdown spectroscopy and spectral analyzing techniques, Dr. Zhiqiang Xie who helped him significantly in research and gave him many valuable advices, Dr. Yunshen Zhou who gave him many good suggestions both in his research projects and in his life, and the author would also thank other members, including current and previous members in LANE laboratory: Drs. Yaoxuan Han, Wei Hu, Hao Ling, Jongbok Park, Changbao Ma, Jing Shi, Huifu Luo, Misters Wei Xiong, Yang Gao, Lianbo Guo, Masoud Mahjouri-Samanii, Xi Huang, Matt Mitchell, Xu Ji, Lijia Jiang, Mengmeng Wang, Weiqing Yang, Thomas Guillemet, Changmao Li, Jiaqi Guo, Tadiyos Gebre, Misses Lisha Fan, Lei Liu, and Min Qian, for their help. The author would also like to thank other people in UNL: Misters Fawen Guo, Cody Raml, John Bruce, and Craig Zuhlke, for their help.

The author is grateful to Drs. You Zhou and Han Chen from the Center for Biotechnology Core Research Facilities (CBCRF) at UNL for their help on scanning electron microscopy (SEM). The author would like to thank Dr. Paul Black from the Department of Biochemistry and his group member Dr. James Allen for their advices and sample preparation in the CARS project. The author would like to thank Dr. Tommaso Baldacchini, Mr. John Carter, and Dr. Ruben Zadoyan from Newport Corporation for their advices and help with our CARS system building and sample measurement.

Finally, the author would like to convey his great appreciation to his family members: Wanlin He (father), Qin Wang (mother), and Yanan He (sister). The author would like to thank his parents for all that they have done for him. It is his parents who taught him to be a kind, polite, and honest man with great integrity. Without them, his

accomplishment today would not be possible. The author's wife, Ms. Ting Chen who lately graduated as a Master of Art from the University of Nebraska-Lincoln, is a once-in-a-lifetime partner who had given the author so much love and help. Without her, the author would have never hoped to accomplish so much.

TABLE OF CONTENTS

LIST OF FIGURES

LIST OF TABLES

CHAPTER 1 INTRODUCTION

1.1 Background and motivation

As a monochromatic and coherent light source, lasers have been extensively used in different fields such as engineering, chemistry, physics, biology, and biomedicine. As material characterization tools, laser-based spectroscopy and spectrometry techniques are used to investigate the properties of materials. However, the sensitivity, spectral resolution, or spatial resolution of these techniques still need to be improved to better serve the purposes of detecting and analyzing various materials. The objective of the research in this dissertation is to improve the sensitivity, spectral resolution, and spatial resolution of different laser-based spectroscopy and spectrometry techniques, including conventional spontaneous Raman spectroscopy (micro-Raman), surface- and tip-enhanced enhanced Raman spectroscopy (SERS and TERS), coherent anti-Stokes Raman spectroscopy (CARS), optical emission spectroscopy (OES), laser-induced breakdown spectroscopy (LIBS), and laser-assisted mass spectrometry (LAMS).

As one of the laser-based spectroscopy techniques, Raman spectroscopy [1] is based on the Raman scattering effect, which is an inelastic scattering process [2-4]. A molecule is excited to a virtual state by an incident photon (from a laser in the visible, near infrared, or near ultraviolet range), and then it relaxes to a different vibration state, followed by a photon being emitted. The wavelength difference between the emitted photon and the incident photon is the Raman shift in Raman spectroscopy (x-axis in a Raman spectrum). Raman spectroscopy offers intrinsic chemical selectivity, because different molecules possess specific unique vibrational frequencies. However, Raman scattering is an extremely inefficient process (10^{-30} cm^2 cross-sections or 1 in 10^7 incident photon is Raman scattered) [5]. Therefore, research has been carried out to enhance

Raman signal. Another limitation of Raman spectroscopy is the diffraction limit of light [6], which is an intrinsic restriction for conventional optical characterization techniques. One of the solutions to overcome the diffraction limit of light is to use near-field optics [7]. TERS, based on near-field optics, has the capability to not only enhance the Raman scattering signal, but also break the diffraction limit. There are several types of TERS setup, and one of the most popular setups is to use a metallic tip (gold, silver, or copper) from a scanning probe microscope to enhance the optical field of a focused laser spot in Raman spectroscopy [8]. The enhanced optical field has the same size as the tip apex of the metallic tip (20-30 nm), and therefore, the resolution of Raman spectroscopy can be improved to nanoscale, breaking the diffraction limit of light. In the research in this dissertation, TERS system was built by the integration of a micro-Raman system and a scanning tunneling microscope (STM) system. TERS spectroscopic and mapping functions were realized using this system for measuring nanomaterials with a resolution of tens of nanometers, such as carbon nanotubes (CNTs) and nanosphere lithography (NSL) structures.

Another signal enhancement technique is SERS [9-11]. Adsorbed on noble metal nanostructures, materials can be detected with exceptionally high Raman intensity. Through this kind of surface-enhancement technique, SERS has been extensively applied to various fields, such as physics, chemistry, surface science, materials science, nanoscience, and life sciences [10, 12-16]. SERS exploits surface plasmons induced by the incident optical field in metallic nanostructures to significantly increase the Raman signal intensity [17]. Considerable efforts have been made toward designing highly SERS-active substrates using noble metal nanoparticles [18-20]. To reliably control the

surface characteristics (such as the size, shape, and materials), SERS substrates have been vastly developed to satisfy requirements from different materials, since the surface characteristics can greatly affect the excitation of the localized surface plasmon resonance. In this study, we present a simple, easy-to-prepare, and large active area SERS substrate. Au-coated horizontally aligned carbon nanotubes (Au-HA-CNTs) were used to act as an SERS substrate.

As another Raman (anti-Stokes) signal enhancement technique based on nonlinear optical effect (four wave mixing), CARS [21, 22] is much more efficient than spontaneous Raman spectroscopy [23-25], enabling faster, more sensitive analyses with less photoexposure. In the CARS process, a pump beam at frequency ω_p and a Stokes beam at frequency ω_s interact with a sample via a wave-mixing process. When the beat frequency $\omega_p-\omega_s$ matches the frequency of a Raman active molecular vibration, the excitation fields will coherently drive the resonant oscillators, thereby generating a strong anti-Stokes signal at $\omega_{as}=2\omega_p-\omega_s$. CARS has now been used for many areas in which it becomes an excellent tool for a variety of research [26-39]. A broadband CARS (B-CARS) system was built for both spectroscopic and microscopic study of materials, including biological and nonbiological samples, such as algae cells and diamond thin films. The system utilized a femtosecond (fs) laser and a photonics crystal fiber to generate pump and Stokes beams for the CARS measurement.

OES measures the emitted photons during the transitions of atoms or molecules from higher energy states to lower energy states. In a combustion flame, the energy of a molecule can change via rotational, vibrational, and vibronic (combined vibrational and electronic) transitions. More specifically, molecules are heated and excited by a high

temperature which is resulted from a highly exothermic combustion reaction. When the molecule falls back down from the excited state, energy is re-emitted in the form of a photon. The wavelength of the photon is determined by the energy difference between the two states. These energy transitions of molecules often lead to closely-spaced groups of many different spectral lines, known as spectral bands. During the combustion flame deposition of diamond, a number of excited chemical species are present in flames above substrate surfaces. Some examples are CH, C_2, and OH free radicals [40-43]. The presence and interactions of these species above the substrate surface are important factors in the combustion flame deposition of diamond films. Since radicals, or equivalently excited chemical species, can be detected and characterized using OES, it is widely employed to identify the excited atomic and molecular species in diamond deposition flames and to study parameters such as relative emission intensities and temperatures.

LIBS is a popular, useful, and effective spectroscopic tool for elemental analysis [44]. Laser-induced plasmas (LIPs) will be generated after powerful laser pulses are focused and illuminated on different targets, such as solid, liquid, or gas. Elemental compositions can be deduced by spectrally analyzing the line emissions from the LIPs. LIBS has been applied in different applications, such as soil and aerosol detection, aerospace exploration, artwork diagnostics and discrimination, remote elemental analysis, waste water diagnostics, and real-time monitoring of radioactive materials [45-48]. With the aim to improve the spectral resolution of LIBS through the generation of high-temperature and low-density plasmas, we studied the reablation of laser-induced particles by introducing a second pulse. Plasma temperatures and densities, estimated using the

emission intensities and line widths of atomic spectral line, are demonstrated to show the high-temperature and low-density properties of the plasmas generated.

LAMS utilizes laser ionization combined with ambient metastable ionization for higher sensitivity was investigated in this research. Lasers can ablate/ionize solid materials, as long as the laser energy can be absorbed. Laser ablation/ionization provides immediate acquisition of chemical information about solids without special pretreatment, especially when samples are difficult, hazardous or tedious to prepare. Little or no pretreatment, little sample consumption and fast analysis are some of the motivations for developing such techniques. Laser ablation/ionization, has been used extensively in solid sampling for chemical analyses, including laser-induced breakdown spectroscopy [49], laser ablation inductively coupled plasma mass spectrometry (LA-ICP-MS) [50], and laser ionization mass spectrometry (LIMS) [51]. Interferences can be minimized with laser-induced ionization compared with ionization by particle beams such as glow discharge mass spectrometry [52]. The LAMS system, using a time-of-flight mass spectrometry, was developed by employing laser ionization combined with metastable ionization in open air, to measure different samples (metal and nonmetal). Enhanced mass spectrometry signal was achieved for specific samples. Relative sensitivity coefficients (RSCs) and limit of detections (LODs) were numerically calculated for in-depth understanding of LAMS system.

In summary, to address the issues in the laser-based spectroscopy and spectrometry, the motivation of this research work was to improve the sensitivity, spectral resolution, and spatial resolution of laser-based spectroscopy and spectrometry techniques. Specifically, TERS systems have been developed to both enhance Raman

signal and increase spatial resolution of Raman spectroscopy; Au-coated horizontally aligned carbon nanotube (Au-HA-CNT) substrate was fabricated for SERS effect to measure different materials with significantly enhanced Raman signal; a broadband CARS system was built using an fs laser (ω_p) and a photonic crystal fiber (PCF) (ω_s) for CARS spectroscopic and microscopic study of biological and nonbiological samples; OES of radicals in diamond synthesis combustion flames with the excitation of a wavelength tunable CO_2 laser was carried out; high-temperature and low-density plasmas were generated in LIBS to improve the spectral resolution of LIBS; laser-assisted mass spectrometry was realized combined laser-ionization and ambient metastable ionization for enhanced mass spectrometry signal. These studies have both scientific and engineering significance. From perspectives of science, laser-based spectroscopy and mass spectrometry can be used to characterize materials and structures with exceptionally detailed information. From perspectives on engineering, the understanding of different spectroscopy techniques will pave the way to design and improve more powerful laser-based spectroscopy and spectrometry systems which will be ultimately served in various areas.

1.2 Dissertation outline

The most significant contributions of this dissertation are: 1) developed a TERS system which has a spatial resolution of 30 nm, 2) fabricated a gold-coated horizontally aligned carbon nanotube substrate for SERS, 3) developed a CARS system for measurement of biological and nonbiological samples, 4) studied diamond synthesis combustion flame with the excitation of a wavelength tunable CO_2 laser by OES, 5)

generated high-temperature and low-density plasmas for improved spectral resolution in LIBS, and 6) developed an LAMS technique using laser ionization combined with metastable ionization in open air. This dissertation includes nine chapters. In chapter 1, the motivation and background of this study is explained, and the dissertation outline is given. In chapter 2, fundamentals and recent development related to this study are reviewed. In chapter 3, details of designing micro- and tip-enhanced Raman spectrometers are discussed. In chapter 4, details of SERS substrate fabrication and SERS measurements of different materials are discussed. In chapter 5, details of a broadband CARS spectroscopy and imaging system are described. In chapter 6, optical emission spectroscopy study of diamond synthesis combustion flame is introduced. In chapter 7, details of the generation of high-temperature and low-density plasmas for improved spectral resolutions in LIBS are provided. In chapter 8, details of the laser-assisted mass spectrometry system are presented. In chapter 9, the summary is given and future research directions are discussed.

1.3 References

[1] D. J. Gardiner, *Practical Raman spectroscopy*, Springer-Verlag (1989).

[2] R. Singh, "C. V. Raman and the Discovery of the Raman Effect," Physics in Perspective (PIP) **4** (4), 399 (2002).

[3] G. Landsberg and L. Mandelstam, "Eine neue Erscheinung bei der Lichtzerstreuung in Krystallen," Naturwissenschaften **16** (28), 557 (1928).

[4] A. Smekal, "Zur Quantentheorie der Dispersion," Naturwissenschaften **11** (43), 873 (1923).

[5] D. C. Harris and M. D. Bertolucci, *Symmetry and Spectroscopy*, Dover Publications (1989).

[6] M. Born and E. Wolf, *Principles of Optics*, Cambridge University Press (1997).

[7] C. Girard and A. Dereux, "Near-field optics theories," Rep. Prog. Phys. **59**, 657 (1996).

[8] S. Kawata and V. M. Shalaev, *Tip Enhancement*, (Advances in Nano-Optics and Nano-Photonics), Elsevier (2007).

[9] M. Moskovits, "Surface-enhanced spectroscopy," Rev. Mod. Phys. **57**, 783 (1985).

[10] K. Kneipp, M. Moskovits, and H. Kneipp, Eds. *Surface-Enhanced Raman Scattering: Physics and Applications* (Springer-Verlag: Berlin, Heidelberg, 2006).

[11] S. Nie and S. R. Emory, "Probing single molecules and single nanoparticles by surface-enhanced Raman scattering," Science **275**, 1102 (1997).

[12] A. Campion and P. Kambhampati "Surface-enhanced Raman scattering," Chem. Soc. Rev. **27**, 241 (1998).

[13] K. Kneipp, H. Kneipp, I. Itzkan, R. R. Dasari, and M. S. Feld, "Surface-enhanced Raman scattering: a new tool for biomedical spectroscopy," Curr. Sci. **77**, 915 (1999).

[14] D. A. Stuart, C. R. Yonzon, X.Y. Zhang, O. Lyandres, N.C. Shah, M. R. Glucksberg, J. T. Walsh, and R. P. Van Duyne, "Glucose sensing using near-infrared surface-enhanced Raman spectroscopy: gold surfaces, 10-day stability, and improved accuracy," Anal. Chem. **77**, 4013 (2005).

[15] G. Braun, S. J. Lee, M. Dante, T. Q. Nguyen, M. Moskovits, and N. Reich, "Surface-enhanced Raman spectroscopy for DNA detection by nanoparticle assembly onto smooth metal films," J. Am. Chem. Soc. **129**, 6378 (2007).

[16] K. A. Willets and R. P. Van Duyne, "Localized surface plasmon resonance spectroscopy and sensing," Annu. Rev. Phys. Chem. **58**, 267 (2007).

[17] S. J. Lee, Z. Q. Guan, H. X. Xu, and M. Moskovits, "Surface-enhanced Raman spectroscopy and nanogeometry: the plasmonic origin of SERS," J. Phys. Chem. C **111**, 17985 (2007).

[18] M. Moskovits and D. H. Jeong, "Engineering nanostructures for giant optical fields," Chem. Phys. Lett. **397**, 91 (2004).

[19] N. Felidj, J. Aubard, G. Levi, J. R. Krenn, A. Hohenau, G. Schider, A. Leitner, and F. R. Aussenegg, "Optimized surface-enhanced Raman scattering on gold nanoparticle arrays," Appl. Phys. Lett. **82**, 3095 (2003).

[20] A. M. Schwartzberg, C. D. Grant, A. Woltcott, C. E. Talley, T. R. Huser, R. Bogomolni, and J. Z. Zhang, "Unique gold nanoparticle aggregates as a highly

active surface-enhanced Raman scattering substrate," J. Phys. Chem. B **108**, 19191 (2004).

[21] P. D. Maker and R. W. Terhune, "Study of optical effects due to an induced polarization third order in the electric field strength," Phys. Rev. **137**, A801 (1966).

[22] R. F. Begley, A. B. Harvey, and R. L. Byer, "Coherent anti-Stokes Raman scattering," Appl. Phys. Lett. **25**, 387 (1974).

[23] C. L. Evans, E. O. Potma, and X. S. Xie, "Coherent anti-Stokes Raman scattering spectral interferometry: determination of the real and imaginary components of nonlinear susceptibility $\chi(3)$ for vibrational microscopy," Opt. Lett. **29**, 2923 (2004).

[24] E. O. Potma, C. L. Evans, and X. S. Xie, "Heterodyne coherent anti-Stokes Raman scattering (CARS) imaging," Opt. Lett. **31**, 241 (2006).

[25] F. Ganikhanov, C. L. Evans, B. G. Saar, and X. S. Xie, "High sensitivity vibrational imaging with frequency modulation coherent anti-Stokes Raman scattering (FMCARS) microscopy," Opt. Lett. **31**, 1872 (2006).

[26] A. Zumbusch, G. R. Holtom, and X. S. Xie, "Three-dimensional vibrational imaging by coherent anti-Stokes Raman scattering," Phys. Rev. Lett. **82**, 4142 (1999).

[27] M. Hashimoto, T. Araki, and S. Kawata, "Molecular vibration imaging in the fingerprint region by use of coherent anti-Stokes Raman scattering microscopy with a collinear configuration," Opt. Lett. **25**, 1768 (2000).

[28] C. L. Evans, E. O. Potma, M. Puoris'haag, D. Cote, C. P. Lin, and X. S. Xie, "Chemical imaging of tissue in vivo with video-rate coherent anti-Stokes Raman scattering microscopy," Proc. Natl. Acad. Sci. USA **102**, 16807 (2005).

[29] C. L. Evans and X. S. Xie, "Coherent anti-Stokes Raman scattering microscopy: chemical imaging for biology and medicine," Annu. Rev. Anal. Chem. **1**, 833 (2008).

[30] J. X. Cheng, Y. K. Jia, G. Zheng, and X. S. Xie, "Laser-scanning coherent anti-Stokes Raman scattering microscopy and applications to cell biology," Biophys. J. **83**, 502 (2002).

[31] E. R. Dufresne, E. I. Corwin, N. S. Greenblatt, J. Ashmore, D. Y. Wang, A. D. Dinsmore, J. X. Cheng, X. S. Xie, J. W. Hutchinson, and D. A. Weitz, "Flow and fracture in drying nanoparticle suspensions", Phys. Rev. Lett. **91**, 224501 (2003).

[32] G. W. H. Wurpel, J. M. Schins, and M. Mueller, "Chemical specificity in three-dimensional imaging with multiplex coherent anti-Stokes Raman scattering microscopy," Opt. Lett. **27**, 1093 (2002).

[33] X. Nan, W. Y. Yang, and X. S. Xie, "CARS microscopy: lights up lipids in living cells," Biophotonics Int. **11**, 44 (2004).

[34] E. O. Potma and X. S. Xie, "Detection of single lipid bilayers in coherent anti-Stokes Raman scattering (CARS) microscopy," J. Raman Spectrosc. **34**, 642 (2003).

[35] X. Nan, E. O. Potma, and X. S. Xie, "Nonperturbative chemical imaging of organelle transport in living cells with coherent anti-Stokes Raman scattering microscopy," Biophys. J. **91**, 728 (2006).

[36] J. H. Strickler and W. W. Webb, "Two-photon excitation in laser scanning fluorescence microscopy," Proc. SPIE **1398**, 107 (1990).

[37] E. S. Wu, J. H. Strickler, W. R. Harrell, and W. W. Webb, "Two-photon lithography for microelectronic application," Proc. SPIE **1674**, 776 (1992).

[38] T. Baldacchini, M. Zimmerley, C. H. Kuo, E. O. Potma, and R. Zadoyan, "Characterization of microstructures fabricated by two-photon polymerization using coherent anti-Stokes Raman scattering microscopy," J. Phys, Chem. B, **113**, 12663 (2009).

[39] K. Ikeda and K. Uosaki, "Coherent phonon dynamics in single-walled carbon nanotubes studied by time-frequency two-dimensional coherent anti-Stokes Raman scattering spectroscopy," Nano Lett. **9**(4), 1378 (2009).

[40] J. S. Kim and M. A. Cappelli, "Temperature measurements in low-pressure, diamond-forming, premixed flames," J. Appl. Phys. **84**(8), 4595 (1998).

[41] M. D. Welter and K. L. Menningen, "Radical density measurements in an oxyacetylene torch diamond growth flame," J. Appl. Phys. **82**, 1900 (1997).

[42] S. J. Firchow and K. L. Menningen, "Radical density measurements in an atmospheric pressure oxyacetylene torch," J. Phys. D: Appl. Phys., **32**, 937 (1999).

[43] S. Roy, J. DuBois, R. P. Lucht, and N. G. Glumac, "Hydroxyl radical concentration measurements near the deposition substrate in low-pressure diamond-forming flames," Combustion and Flame, **138**(3), 285 (2004).

[44] W. M. Andrzej, P. Vincenzo, and S. Israel, *Laser-induced Breakdown Spectroscopy: Fundamentals and Applications* (Cambridge University Press, 2006).

[45] D. W. Hahn and M. M. Lunden, "Detection and analysis of aerosol particles by laser-induced breakdown spectroscopy," Aerosol Sci. Technol. **33**, 30 (2000).

[46] D. Anglos, S. Couris, and C. Fotakis, "Laser diagnostics of painted artworks: laser induced breakdown spectroscopy of pigments," Appl. Spectrosc. **51**, 1025 (1997).

[47] D. A. Cremers, J. E. Barefield, and A. C. Koskelo, "Remote elemental analysis by laser-induced breakdown spectroscopy using a fiber-optic cable," Appl. Spectrosc. **49**, 857 (1995).

[48] J. P. Singh, F. Y. Yueh, H. Zhang, and K. P. Karney, "A preliminary study of the determination of uranium, plutonium and neptunium by laser-induced breakdown spectroscopy," Rec. Res. Dev. Appl. Spectrosc. **2**, 59 (1999).

[49] L. J. Radziemski, "From LASER to LIBS, the path of technology development," Spectrochim. Acta Part B: Atomic Spectroscopy **57**, 1109 (2002).

[50] R. E. Russo, X. L. Mao, H. C. Liu, J. Gonzalez, and S. S. Mao, "Laser ablation in analytical chemistry-a review," Talanta **57**, 425 (2002).

[51] A. Vertes, R. Gijbels, and F. Adams, *Laser Ionization Mass Analys*is, Wiley Interscience: New York (1993).

[52] N. Omenetto, "Role of lasers in analytical atomic spectroscopy: where, when and why – Plenary lecture," J. Anal. At. Spectrom. **13**, 385 (1998).

CHAPTER 2 BACKGROUND AND REVIEWS

2.1 Raman spectroscopy

Raman scattering, an inelastic scattering effect, is used in Raman spectroscopy for the detection of vibrational modes of molecules, lattice vibration in solids, and etc. [1]. In a Raman spectroscopy system, lasers (visible, near-infrared (NIR), or near ultraviolet) are extensively used to interact with different vibrational states, and then the energy of the incident photons will be shifted up or down (also known as Raman shift). The vibrational mode information will then be obtained through this Raman shift in a Raman spectrum. Complementary information can be achieved through infrared spectroscopy. Spontaneous Raman scattering is extremely weak (10^{-30} cm^2 cross-sections, or 1 in 10^7 incident photon is Raman scattered) [2]. In conventional spontaneous Raman spectrometer (see Fig. 2.1), laser light (usually continuous-wave) is focused by an objective lens and then illuminated onto a sample (usually on a microscope frame). The scattered light from the illuminated spot is collected with the same lens and then sent through a monochromator and finally detected with a charge-coupled device (CCD) camera. The light with wavelengths close to the laser light wavelength (from elastic Rayleigh scattering) is filtered out using a notch filter (or long-pass filters). For Raman imaging, the detector can also be replaced by an avalanche photodiode (APD) or a photomultiplier tube (PMT).

In spontaneous Raman spectroscopy, molecules (or lattice in solids) from the ground state are excited to a virtual energy state by an incident photon. After relaxing from the virtual energy state, it will emit a photon with different energy (inelastic scattering or Raman scattering) or with the same energy (elastic scattering or Rayleigh scattering) [3]. The Raman shift originates from the difference in energy between the original state and this new state (see Fig 2.2). If the final vibrational state of the molecule

is higher (in energy) than the initial state, the emitted photon will be shifted to a longer wavelength (lower frequency), known as Stokes Raman scattering. On the other hand, when the final vibrational state is lower than the initial state, then the emitted photon will be shifted to a shorter wavelength (higher frequency), known as anti-Stokes Raman scattering.

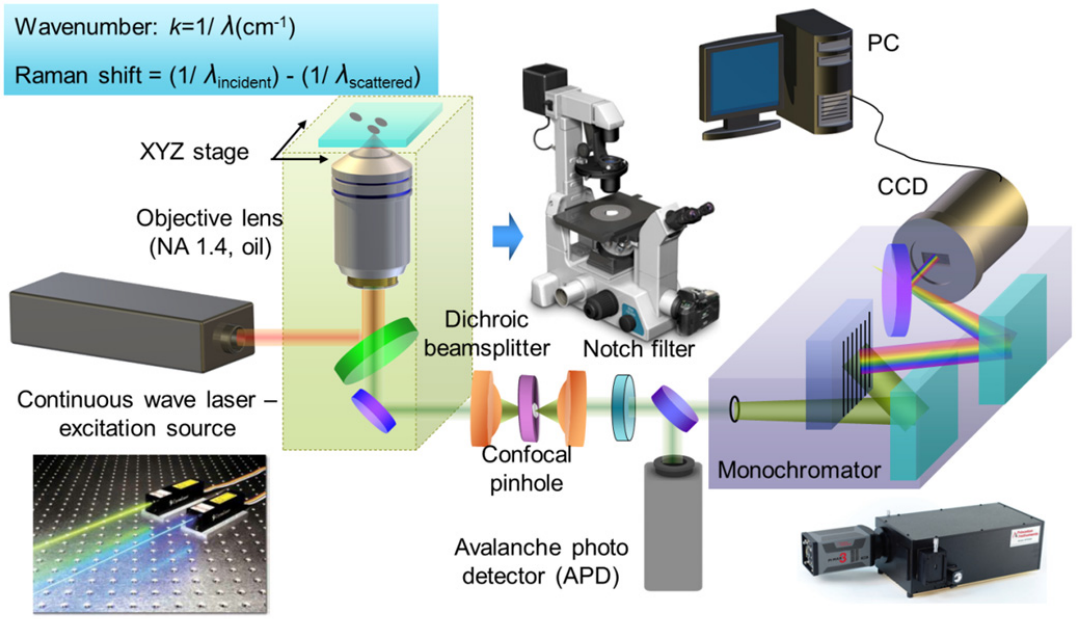

Figure 2.1 Schematic setup of a conventional spontaneous Raman spectroscopy system. Inset blue box is the Raman shift calculation equations.

Raman shifts are typically expressed in wavenumbers (cm^{-1}). Raman spectrum typically uses inverse centimeters (cm^{-1}) as its unit of Raman shift. Therefore, the following formula is used to convert between wavelength (nm) and wavenumbers of shift in the Raman spectrum:

$$\Delta\omega(cm^{-1}) = \left(\frac{1}{\lambda_{incident}(nm)} - \frac{1}{\lambda_{scattered}(nm)}\right) \times 10^7, \quad (2.1)$$

where $\Delta\omega$ is the Raman shift (cm^{-1}), $\lambda_{incident}$ is the wavelength of the incident photons, and $\lambda_{scattered}$ is the wavelength of the Raman scattered photons.

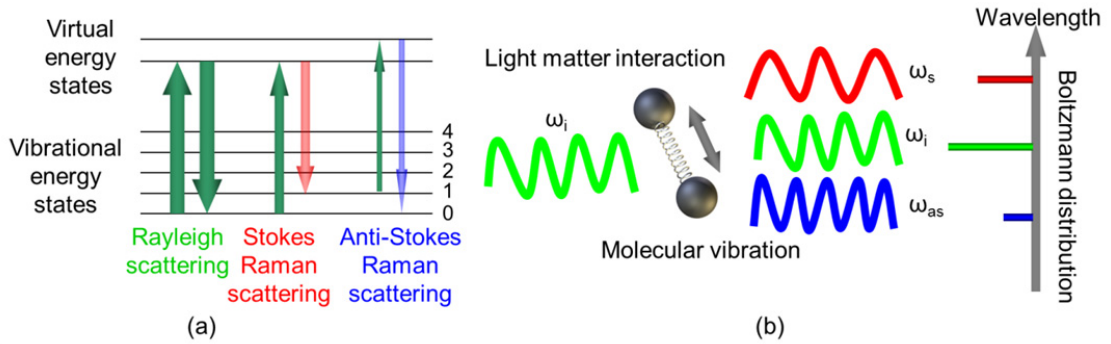

Figure 2.2 (a) Energy level diagram showing the states involved in Raman signal. The line thickness is roughly proportional to the signal strength. (b) Diagram showing light-matter interaction process in Raman spectroscopy with Boltzmann distribution of different scattering effects.

Raman spectroscopy has many advantages, including minimal invasive, non-photobleaching signal for live cell studies, adaptable to different conditions (temperatures and pressures), chemical imaging without exogenous tagging, different excitation wavelengths. However, spontaneous Raman spectroscopy also has several disadvantages, including fluorescence interference, limited spatial resolution and extremely weak signal (Raman scattering is extremely inefficient: 10^{-30} cm^2 cross-sections). In order to improve the performance, such as sensitivity and spatial resolution, of Raman spectroscopy, a number of advanced types of Raman spectroscopy, including surface-enhanced Raman spectroscopy, resonance Raman spectroscopy, tip-enhanced Raman spectroscopy, polarized Raman spectroscopy, stimulated Raman spectroscopy (analogous to stimulated emission), hyper Raman spectroscopy [4-6], are developed by researchers to achieve improved capability of Raman spectroscopy.

2.2 Tip-enhanced Raman spectroscopy (TERS)

The typical spatial resolution of the micro-Raman spectrometer is about 1 μm. In searching of high-resolution approaches, near-field scanning optical microscopy (NSOM) was therefore invented. NSOM is capable of providing higher detecting accuracy [10-12].

The integration of a micro-Raman spectrometer with an NSOM was developed in a nanoscale Raman spectrometer, known as the near-field scanning Raman microscopy (NSRM). However, NSRM employs an aperture NSOM, which has been limited by its poor signal to noise ratio. In NSRM, an optical fiber tip with a small aperture (with a diameter of 50-200 nm) is used to deliver laser beam, and the fiber tip is kept at a close distance (~tens of nanometers) above the sample surface. Raman signal is collected in far-field through either a microscope objective or a lens [13-15]. The scattering signal is then delivered into a Raman spectrometer, and the Raman spectrum at each point on the target will be acquired by scanning the fiber tip across the sample surface. However, this kind of tip is extremely inefficient due to the weak incident light (100 nW) [16-18].

An approach, by using a well-prepared metal tip, is to enhance Raman signal from the sample close to the tip by several orders of magnitude, usually called tip-enhanced Raman spectroscopy (TERS). TERS results from a combination of two phenomena, including the electrostatic lightning-rod effect and localized surface plasmon resonances (LSPR). The lightning rod effect is based on the singularity of a sharp tip, while the LSPR effect depends on the excitation wavelength. The free electrons in the metal tips are driven by the incident light electric field (E-field) along the direction of light polarization. Since the charges accumulate on the surface of the tip leaving the inside of the tip charge free, the charges will have opposed points on the tip surface with opposite

charge when the incident polarization is parallel to the tip axis. The induced surface charge density on the tip is almost rotationally symmetric and has the highest amplitude at the apex of the tip [7-9]. TERS can be used to record Raman images either in transmission mode [19] or in reflection mode [20] (see Fig. 2.3). The impact of the tip on the Raman enhancement is similar to the impact of the metal-island film on surface-enhanced Raman spectroscopy (SERS) [21]. However, a single metallic tip can achieve nanoscale resolutions [22-24]. TERS typically uses a metallic (usually silver-/gold-coated AFM or STM) tip to enhance the Raman signals of molecules situated in its vicinity (see Fig. 2.3). The spatial resolution is approximately the size of the tip apex (20-30 nm) [6].

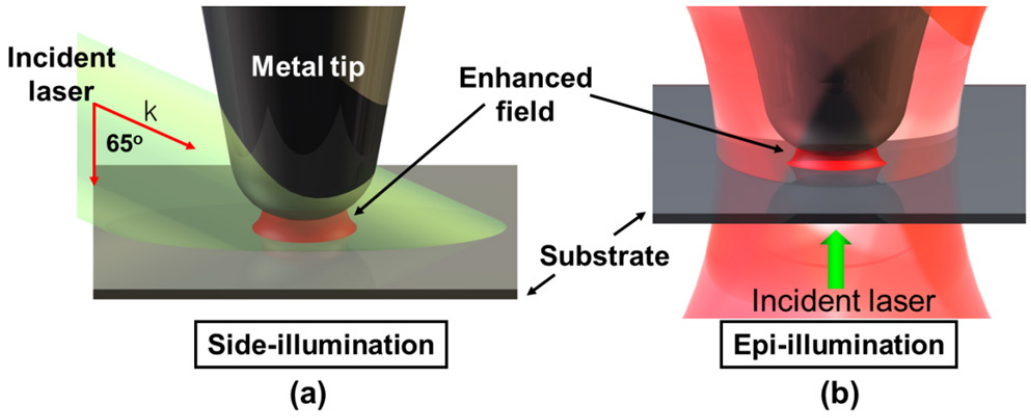

Figure 2.3 (a) Close look schematic setup of a side-illuminated TERS system. (b) Close look schematic setup of a back-illuminated (transmission) TERS system.

In this study, mapping of individual single-walled carbon nanotubes (SWCNTs) is demonstrated using the TERS system with a sharp Au STM tip. We show that individual SWCNTs can be detected optically with a spatial resolution around 30 nm. This high-resolution capability is applied to resolve local variations in the Raman spectrum along an individual SWCNT which would be hidden in the measurements using the micro-

Raman system. We also demonstrate the detection of silver (Ag) nanostructures on Si substrate using the TERS system, and the resolution of the system is around 100 nm [25].

2.3 Surface-enhanced Raman spectroscopy (SERS)

SERS is one kind of advanced Raman spectroscopy techniques that utilizes surface enhancement from particular surface structures (nanostructures). SERS occurs when molecules are adsorbed on metal surfaces. The reported enhancement factor can be as high as 10^{10} to 10^{11} [26,27], which suggests capability of SERS for single molecule detection. SERS from pyridine adsorbed on roughened silver surface was firstly observed by M. Fleischman *et al.* in 1974 [28]. They attributed the large signal to the number of molecules, instead of an enhancement effect. In 1977, two groups (Jeanmaire and van Duyne [29] and Albrecht and Creighton [30]) independently noted and reported that the concentration of molecules could not account for the enhanced Raman signal. The first group proposed an electromagnetic effect, while the latter group proposed a charge-transfer effect. Kneipp and coworkers [31-33] and Nie and coworkers [34-36] reported that intense enough SERS emissions could be achieved to detect single molecules, which returned SERS as an active research area again.

SERS [4,36,37] has been rapidly developed into an effective characterization and analyzing tool in different applications, such as physics, chemistry, surface science, materials science, nanoscience, and life sciences [4,38-42]. SERS employs localized surface plasmons (LSPs) induced by the incident optical field in metallic nanostructures to drastically increase the Raman signal intensity [43]. Substrates used for SERS have been extensively researched, developed, and analyzed with emphasis on the

electromagnetic field enhancement due to LSP resonances related to the highly profiled metallic nanostructure on SERS-active substrates. To reliably control the surface characteristics (such as the size, shape, and materials), SERS substrates have been developed to satisfy requirements from different materials, since the surface characteristics can greatly affect the excitation of the localized surface plasmon resonance. Considerable efforts have been made toward designing and fabricating highly SERS-active substrates using noble metal nanoparticles [44-46]. There are also many other kinds of SERS-active substrates, such as highly roughened metal films or electrodes [47], metallic structures fabricated using techniques based on self-assembly and nanosphere lithography [48], and metallic structures fabricated using standard photolithographic and electron beam lithographic methods [49-51].

2.4 Coherent anti-Stokes Raman scattering (CARS)

Since Raman scattering signal is very weak, (typical photon conversion efficiencies for Raman are lower than 1 in 10^7), and therefore, Raman microscopy requires high laser powers and long integration times of 100 ms to 1 s per pixel [52]. This long integration drawback severely blocks the application of Raman microscopy to the study of living systems. CARS, based on nonlinear (four-wave mixing) optical effect, has much stronger Raman signals (anti-Stokes) [53], first reported in 1965 by Maker and Terhune [54] as a method of spectroscopy for chemical analysis. The energy diagram of the process is depicted in Fig. 2.4(a). CARS involves the interaction of four waves designated as pump (p), Stokes (s), probe (p') and anti-Stokes (CARS), where pump and probe are usually fixed to the same frequency ($\omega_p = \omega_{p'}$). When we match the beat

frequency between the pump and Stokes beams with the vibrational frequency Ω_R of the molecules in the sample, a resonant enhancement of the third-order nonlinear optical process will occur to greatly promote the sensitivity with chemical selectivity. The information acquired from CARS (anti-Stokes Raman shift information) is the same as that from Raman spectroscopy (Stokes Raman shift information) due to the intrinsic same Raman scattering effect. The major difference between CARS and spontaneous Raman is that CARS is a four-wave mixing process, which will need two coherent laser beams with different wavelengths. The sensitivity of CARS is also much higher than spontaneous Raman spectroscopy by several orders of magnitude.

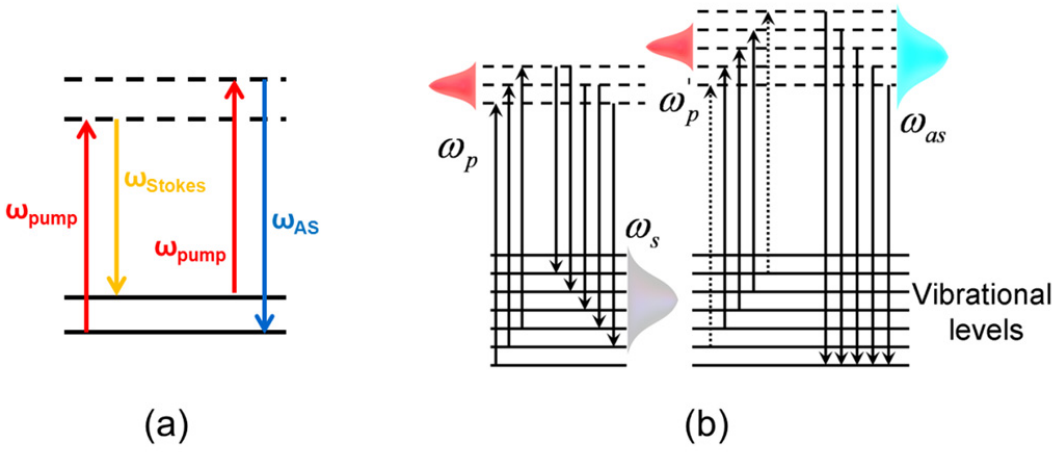

Figure 2.4 (a) Energy diagram of the CARS process. The CARS signal is resonantly enhanced when the difference between the pump ω_p and Stokes ω_s frequencies matches a vibrational transition Ω_R of a molecule. (b) Energy diagram of the broadband CARS process. The pump is from an fs laser, while the Stokes is from a supercontinuum generator.

CARS [55,56] is much more efficient than spontaneous Raman spectroscopy [57-59], enabling faster, more sensitive analyses with less photo exposure. CARS circumvents the need for extrinsic labels, allowing observation of dynamic phenomena for which tags are not available. CARS also enables detection in the presence of one-photon fluorescence, 3-D sectioning, penetrating to a depth of ~0.4 mm while minimizing

photodamages [60-62]. CARS microscopy has been utilized to image living cells with the Raman signals from different vibrational modes, such as the amide I vibration from protein, OH stretching from water, the phosphate stretch from DNA, and the CH group of stretching from lipids [53,63-66]. There are also many other examples, such as single phospholipid bilayers visualization [67], the trafficking and growth of lipid droplets [68], intracellular water diffusion, and biomedical imaging of tissues *in vivo* [62]. CARS has also been used for two-photon polymerization characterization [69-71] and carbon nanotube [72] characterization. As a nonlinear optical effect and similar to two-photon excited fluorescence microscopy (TPEF), CARS allows image sectioning without the requirement of labeling [73-76]. In the research in this dissertation, we focused on the broadband CARS approach, as illustrated in Fig. 2.4(b), was first proposed by Akhmanov et al [77].

The intensity of the CARS signal can be deduced as the following equation:

$$I_{CARS}(\Omega) \propto \left|x_{CARS}^{(3)}(\Omega)\right|^2 I_p^2 I_s, \tag{2.2}$$

where the pump and probe signals are the same, I_p and I_s are the intensities of the pump (or probe) and Stokes beams, and $\chi^{(3)}$ is the third-order nonlinear susceptibility. CARS spectroscopy can be realized when the scattering signals are recorded on a spectrometer. For narrow bandwidth pump and Stokes sources, the wavelength of the Stokes beam can be scanned to get a CARS spectrum (intensity versus Raman shift). However, single-short CARS spectrum can be achieved with broadband Stokes beam. The broadband Stokes beam in collinear alignment with narrower pump beam will excite a wide range of Raman transitions [73]. Since the Stokes shifts in the range of 500-4000 cm^{-1} are known as the finger print region, it is desirable to have a Stokes beam with a broadband

spectrum to cover these vibrational states for a fast spectrum generation. A potential method is to employ a supercontinuum (SC) source for the generation of laser pulses with 4000-cm^{-1} bandwidth [78], which is not possible (too wide) for femtosecond pulses. Significant advances in the development and fabrication of photonic crystal fibers (PCF) facilitated the use of PCF as a stable and reliable solution for supercontinuum generation, since an input of a few tens of mW from an fs oscillator is sufficient.

2.5 Optical emission spectroscopy (OES)

OES is a spectroscopic technique which records the wavelengths and intensity of transitions (usually electronic transitions) from higher level states to lower level states. In a combustion flame, the energy of a molecule can change via rotational, vibrational, and vibronic (combined vibrational and electronic) transitions. More specifically, molecules are heated and excited to a high temperature which is resulted from a highly exothermic combustion reaction. When the molecule falls back down from the excited state, energy is re-emitted in the form of a photon. The wavelength of the photon is determined by the energy difference between the two states. These energy transitions of molecules often lead to closely-spaced groups of many different spectral lines, known as spectral bands.

Chemical vapor deposition of diamond films has been extensively studied since the discovery of simple low-pressure methods to deposit polycrystalline films on a variety of substrates [79,80]. The underlying reason is that diamond coatings on different materials and equipment are very useful due to the superior properties of diamond, including outstanding optical, electrical, and mechanical properties that make it attractive for various applications [81]. As a result of these properties, diamond film research has

continued to attract more and more interest over the past decade. The combustion flame deposition method has received considerable attention since its discovery by Hirose [82,83] because of its simplicity and high growth rate. In the combustion flame method, C_2H_2 and O_2 have been commonly used as precursors to produce proper combustion flames for deposition of diamond films. Other carbon-based precursors, such as C_2H_4 and C_3H_6, can also be used to deposit diamond [84].

During the combustion-flame deposition of diamond, a number of excited chemical species are present in flames above substrate surfaces. Some examples are CH, C_2, OH, and CN radicals [85-88]. The presence and interactions of these species above the substrate surface are important factors in the combustion-flame deposition of diamond films. Since radicals, or equivalently excited chemical species, can be detected and characterized using OES. OES is widely employed to identify the excited atomic and molecular species in diamond deposition flames and to study parameters such as relative emission intensities and temperatures.

OES spectra [89] can provide information in a temperature range of 2000-8000 K where atomic spectra are not strong enough to ensure a good sensitivity [90]. Emission spectra from various molecules have been used for temperature determinations in combustion flame diagnostics. Ultraviolet OH spectrum was employed by Chales [91] as a molecular pyrometer to determine flame temperatures. C_2 Swan band is also used for temperature determination in flames. Emission spectra of C_2 Swan band (band head: 516.611 nm) were employed for evaluation of the rotational temperature in different plasma sources [92]. The rotational temperature, T_r, of molecular species in a plasma is generally very close to the gas kinetic temperature. This is due to strong coupling

between translational and rotational energy states [87,92]. To determine the rotational temperature of a premixed $C_2H_4/C_2H_2/O_2$ flame, one method is the well-known Boltzmann plot when a high-resolution optical spectrometer is available to resolve the rotational lines. In our studies, laser-assisted combustion flame deposition of diamond films was performed to improve the deposition rate of diamond thin films. A wavelength-tunable CO_2 laser was used to irradiate the $C_2H_4/C_2H_2/O_2$ combustion flames during the deposition of diamond films. Although C_2H_2/O_2 flame is efficient in diamond growth, there is no suitable wavelength in the tuning range of the CO_2 laser that can excite the molecules in the C_2H_2/O_2 flame. C_2H_4, which is one of the suitable precursors for diamond deposition [85,93], was added in the flame to resonantly match the laser wavelength by its CH_2-wagging vibrational mode to enable CO_2 laser excitation. C_2H_4 molecule has an infrared absorption band corresponding to the CH_2-wagging vibration mode at a frequency of 949 cm^{-1}. Since this frequency is very close to the common CO_2 laser line – 10.591 μm, the CO_2 laser can be used to excite the C_2H_4 molecules at this wavelength because of the broadening of the absorption band and to promote the production of species beneficial to diamond deposition. Furthermore, the wavelength of 10.532 μm produced by the wavelength tunable CO_2 laser was also used to resonantly excite the CH_2-wagging mode. The previous results have shown that the resonant excitation by the CO_2 laser can improve both the growth rate and the film quality. However, the mechanism of the enhancement in the diamond deposition was still not clear. Therefore, OES was performed in this study to identify the excited species and determine the rotational temperatures in the deposition flames with and without CO_2 laser excitation. OES spectra were also used to calculate relative emission intensities. The

electronic transitions of CH [$A^2\Delta$ - $X^2\Pi$ (0, 0), center near 430 nm] were used to determine the rotational temperatures using the Boltzmann plot method. The CH radicals were chosen because they have relatively high emission intensity. Previous studies by Welter [86] and Firchow [87] have shown that they are one of the species that correlate best with diamond growth.

2.6 Laser-induced breakdown spectroscopy (LIBS)

LIBS is also called laser-induced plasma spectroscopy (LIPS). The principle of LIBS is quite simple. By focusing a powerful pulsed laser beam onto a sample, which could be solid, liquid, or gas, the laser electric field would be sufficiently strong to cause breakdown, and a hot luminous spark would be generated. The spark is called laser-induced plasma. By spectrally analyzing the optical emission from the plasma, the element composition of the sample could be deduced. Qualitative and quantitative analyses can be carried out by monitoring emission line positions and intensities. The analysis can range from a simple identification of the atomic constituents of the sample to a more detailed determination of relative concentrations or absolute masses. Examination of the emitted light provides the analysis because each element has a unique emission spectrum useful to “fingerprint” the species. Extensive compilations of emission lines exist [94-96]. The position of the emission lines identifies the elements and, when properly calibrated, the intensity of the lines permits quantification.

LIBS has been applied in different applications, such as soil and aerosol detection, aerospace exploration, artwork diagnostics and discrimination, remote elemental analysis,

waste water diagnostics, and real-time monitoring of radioactive materials [97-100]. There have been a number of commercial LIBS systems in the markets.

However, as compared with other elemental analysis techniques, LIBS has some disadvantages, such as low detection sensitivity, poor selectivity, and low reliability. Due to the quick expansion and fast motion of the laser-induced plasmas, the lifetime of laser induced plasmas is very short (typically microseconds). The detection sensitivity is low since the plasmas move out from the effective field of the detection optics in a short period of time. LIBS has poor selectivity and low reliability because of interference effects. The interference effects are present because LIBS spectra are very complex and many emission lines from different elements overlap with each other in wavelength.

A number of techniques, such as introduction of purge gas [101] and dual-pulse excitation [102-108], have been used to improve the sensitivity of LIBS. A higher temperature of plasmas is beneficial to the sensitivity of LIBS. However, plasmas in typical LIBS also have high densities correlated to their high temperatures. High plasma density causes the widened line widths and increased self-absorption of atomic lines, therefore, results in lower spectral resolutions. Spectral resolution of LIBS is very important for element analysis. Higher spectral resolution will improve the accuracy of element determination. To improve the LIBS resolution, low density and high temperature in plasmas need to be achieved simultaneously. The profile of a line is the result of many effects, but under typical LIBS conditions the main contribution to the line width comes from the Stark effect (see Gornoshkin *et al.* [109], for a discussion of the different broadening effects influencing the spectral line shape in LIBS). In fact, the electric field generated by electrons in plasma perturbs the energy levels of ions, thereby

broadening the emission lines from these upper (or excited) levels. Thus the Stark broadening has a well-established relation with plasma density (or plasma electron density). On the other hand, the self-absorption effect [110], in which some of the radiation emitted by a material is absorbed by the material itself, also takes place in the radiation from laser-induced plasmas.

Dual-pulse LIBS (DP-LIBS) originated in research performed more than 20 years ago, in which spatially overlapping laser-induced plasmas formed in bulk aqueous solution could improve the detection limits by orders of magnitude over those seen in nanosecond single-pulse LIBS [102]. Collinear and orthogonal reheating multipulse LIBS of solids were examined in air [103,104]. Orthogonal pre-ablative spark dual-pulse configuration was also characterized [105,106]. The fundamental physics of laser ablation and the recent explosion of applications of single- and dual-pulse LIBS have been discussed in the literature [107,108].

In conventional reheating DP-LIBS, optical emission drops drastically with interpulse delays (the delay between the two pulses in DP-LIBS) of more than 100 μs due to the limited plasma lifetime [111]. However, when the laser fluence is sufficiently large, there is an appreciable amount of laser-induced particles. With delays up to milliseconds, a second pulse can reablate the laser-induced particles to generate plasmas with high temperature but low density for improved spectral resolutions in LIBS.

With the aim to improve the spectral resolution of LIBS through the generation of high-temperature and low-density plasmas, we studied the reablation of laser-induced particles by introducing the second pulses with delays up to milliseconds. Fast imaging of optical scattering from particles generated by the first pulse was investigated to study the

evolution of the first-pulse plasmas and the formation of the laser-induced particles. Time-integrated LIBS spectra of plasmas produced by reablation were studied. Plasma temperatures and densities, estimated using the emission intensities and line widths of atomic spectral line, were plotted to show the high-temperature and low-density properties of the plasmas generated.

2.7 Laser-assisted mass spectrometry (LAMS)

Mass spectrometry (MS) is an analytical tool for the measurement of mass-to-charge ratio of different charged particles (or ions) [112]. It is an efficient and reliable technique to characterize the masses of particles, analyze the elemental composition of a target, and elucidate the chemical composition of molecules. There are several steps in a MS characterization process. Firstly, a sample is mounted onto the MS followed by ionization process, which has many variants. Secondly, the ions generated from previous step are separated out based on the different mass-to-charge ratios using electromagnetic fields followed by a quantitative detection approach. Finally, mass spectra are generated based on the signal from the detector according to different mass-to-charge ratio.

Immediate acquisition of chemical information about solids without special pretreatment provides many advantages, especially when samples are difficult, hazardous, or tedious to prepare. Little or no pretreatment, little sample consumption and fast analysis are some of the motivations for developing such techniques. One of these techniques, laser ablation/ionization, has been used extensively in solid sampling for chemical analyses, including laser-induced breakdown spectroscopy [113], laser ablation inductively coupled plasma mass spectrometry (LA-ICP-MS) [114], and laser ionization

mass spectrometry (LIMS) [115]. Lasers can ablate/ionize solid materials, as long as the laser energy can be absorbed. Interferences can be minimized with laser-induced ionization compared with ionization by particle beams such as glow discharge mass spectrometry [116]. Lasers have already been used in fields of solid analyses, including analysis of long-lived radio nuclides in solid samples [117], depth profiling of multilayer samples [118], elemental imaging of biological tissues [119], as well as geological and environmental analysis [120].

Direct Analysis in Real Time (DART) is an ambient ionization method, which has the capability to rapidly ionize different materials in open air under ambient conditions, which was developed by Laramee and Cody in 2005 [121]. As a new ion source, DART was developed for rapid, noncontact analysis of materials at ambient pressure and at ground potential, such as currency bills, tablets, bodily fluids (blood, saliva and urine), glass, plant leaves, fruits & vegetables and even clothing. This technique is unique because of its ability to directly detect chemicals on sample surfaces. This method is mainly based on the chemical reactions of electronic or vibronic excited-state species with the analyte atoms or molecules. Thanks to its sampling versatility, DART is now an extremely powerful atmospheric pressure ion source that could be combined with mass spectrometry [122].

In this study, a series of NIST copper rod samples and a pure carbon target were measured in the experiment for laser ionization only and for laser ionization combined with DART. The objective of this research was to investigate the combined laser and metastable ionizations in TOF-MS for element analysis of metallic or nonmetallic solids in open air. The results were compared to those from LIBS spectra simultaneously

acquired from the laser-induced plasmas. Trace elements were detected with this system in open air with or without DART, whereas singly ionized carbon atoms were detected from a pure carbon target only when DART was combined with laser ionization. The relative sensitivity coefficient (RSC) was calculated and plotted as a function of concentration and laser pulse energy for a multielemental analysis. Limit of detections (LODs) were also calculated for different elements in both LI-TOFMS and LIBS.

2.8 References

[1] D. J. Gardiner, *Practical Raman spectroscopy*, Springer-Verlag (1989).

[2] D. C. Harris and M. D. Bertolucci, *Symmetry and Spectroscopy*, Dover Publications (1989).

[3] M. Born and E. Wolf, *Principles of Optics*, Cambridge University Press (1997).

[4] K. Kneipp, M. Moskovits, H. Kneipp, Eds. *Surface-Enhanced Raman Scattering: Physics and Applications* (Springer-Verlag: Berlin, Heidelberg, 2006).

[5] J. R. Ferraro, K. Nakamoto, C. W. Brown, *Introductory Raman Spectroscopy*, Academic Press, Amsterdam, Second Edition (2003).

[6] S. Kawata and V. M. Shalaev, *Tip Enhancement*, (Advances in Nano-Optics and Nano-Photonics), Elsevier (2007).

[7] R. E. Larsen and H. Metiu, "Resolution and polarization in apertureless near-field microscopy," J. Chem. Phys. **114**, 6851 (2001).

[8] Y. C. Martin, H. F. Hamann, H. K. Wickramasinghe, "Strength of the electric field in apertureless near-field optical microscopy," J. Appl. Phys. **89**, 5774 (2001).

[9] L. Novotny, E. J. Sánchez, X. S. Xie, "Near-field optical imaging using metal tips illuminated by higher-order Hermite–Gaussian beams," Ultramicroscopy **71**, 21 (1998).

[10] D. W. Pohl, W. Denk, M. Lanz, "Optical stethoscopy: Image recording with resolution λ/20," Appl. Phys. Lett. **44**, 651 (1984).

[11] A. Harootunian, E. Betzig, M. Isaacson, A. Lewis, "Super-resolution fluorescence near-field scanning optical microscopy," Appl. Phys. Lett. **49**, 674 (1986).

[12] S. Kawata (Ed.), *Near-Field Optics and Surface Plasmon Polaritons*, Springer, Berlin (2001).

[13] S. Webster, D. A. Smith, D. N. Batchelder, "Raman microscopy using a scanning near-field optical probe," Vib. Spectrosc. **18**, 51 (1998).

[14] E. J. Ayars and H. D. Hallen, "Surface enhancement in near-field Raman spectroscopy," Appl. Phys. Lett. **76**, 3911 (2000).

[15] C. L. Jahncke, M. A. Paesler, H. D. Hallen, "Raman imaging with near-field scanning optical microscopy," Appl. Phys. Lett. **67**, 2483 (1995).

[16] M. N. Islam, X. K. Zhao, A. A. Said, S. S. Mickel, C. F. Vail, "High-efficiency and high-resolution fiber-optic probes for near field imaging and spectroscopy," Appl. Phys. Lett. **71**, 2886 (1997).

[17] T. Yatsui, M. Kourogi, M. Ohtsu, "Increasing throughput of a near-field optical fiber probe over 1000 times by the use of a triple-tapered structure," Appl. Phys. Lett. **73**, 2090 (1998).

[18] Y. H. Chuang, K. G. Sun, C. J. Wang, J. Y. Huang, C. L. Pan, "A simple chemical etching technique for reproducible fabrication of robust scanning near-field fiber probes," Rev. Sci. Instrum. **69**, 437 (1998).

[19] R. M. Stöckle, Y. D. Suh, V. Deckert, R. Zenobi, "Nanoscale chemical analysis by Tip-enhanced Raman Scattering," Chem. Phys. Lett. **318**, 131 (2000).

[20] D. Mehtani, N. Lee, R. D. Hartschuh, A. Kisliuk, M. D. Foster, A. P. Sokolov, J. F. Maguire, "Nano-Raman spectroscopy with side-illumination optics," J. Raman Spectrosc. **36**, 1068 (2005).

[21] R. K. Chang and T. E. Furtak (Eds.), *Surface Enhanced Raman Scattering*, Plenum Press, New York (1981).

[22] Y. Inouye, N. Hayazawa, K. Hayashi, Z. Sekkat, S. Kawata, "Near-field scanning optical microscope using a metallized cantilever tip," Proc. SPIE **3791**, 40 (1999).

[23] R. M. Stockle, Y. D. Sur, V. Dekkert, R. Zenobi, "Nanoscale chemical analysis by tip-enhanced Raman spectroscopy," Chem. Phys. Lett. **318**, 131 (2000).

[24] M. S. Anderson, "Locally enhanced Raman spectroscopy with an atomic force microscope," Appl. Phys. Lett. **76**, 3130 (2000).

[25] K. J. Yi, X. N. He, Y. S. Zhou, W. Xiong, Y. F. Lu, "Tip-enhanced near-field Raman spectroscopy with a scanning tunneling microscope and side-illumination optics," Rev. Sci. Instrum. **79**, 051807 (2008).

[26] E. J. Blackie, E. C. Le Ru, P. G. Etchegoin, "Single-molecule surface-enhanced Raman spectroscopy of nonresonant molecules," J. Am. Chem. Soc. **131**, 14466 (2009).

[27] E. C. Le Ru, E. Blackie, M. Meyer, P. G. Etchegoin, "Surface enhanced Raman scattering enhancement factors: A comprehensive study," J. Phys. Chem. C **111**, 13794 (2007).

[28] M. Fleischmann, P. J. Hendra, A. J. McQuillan, "Raman spectra of pyridine adsorbed at a silver electrode," Chem. Phys. Lett. **26**, 163 (1974).

[29] D. L. Jeanmaire and R. P. Van Duyne, "Surface raman spectroelectrochemistry: Part I. Heterocyclic, aromatic, and aliphatic amines adsorbed on the anodized silver electrode," J. Electroanal. Chem. **84**, 1 (1977).

[30] M. G. Albrecht and J. A. Creighton, "Anomalously intense Raman spectra of pyridine at a silver electrode," *J. Am. Chem. Soc.* **99** (15), 5215 (1977).

[31] K. Kneipp, H. Kneipp, I. Itzkan, R. R. Dasari, M. S. Feld, "Surface-enhanced non-linear Raman scattering at the single-molecule level," Chem. Phys. **247**, 155 (1999).

[32] K. Kneipp, H. Kneipp, R. Manoharan, E. B. Hanlon, I. Itzkan, R. R. Dasari, M. S. Feld, "Extremely large enhancement factors in surface-enhanced Raman scattering for molecules on colloidal gold clusters," Appl. Spectrosc. **52**, 1493 (1998).

[33] K. Kneipp, H. Kneipp, V. B. Kartha, R. Manoharan, G. Deinum, I. Itzkan, R. R. Dasari, M. S. Feld, "Detection and identification of a single DNA base molecule using Surface- Enhanced Raman Scattering (SERS)," Phys. Rev. E **57**, R6281 (1998).

[34] J. T. Krug, G. D. Wang, S. R. Emory, S. Nie, "Efficient Raman enhancement and intermittent light emission observed in single gold nanocrystals," J. Am. Chem. Soc. **121**, 9208 (1999).

[35] S. R. Emory, W. E. Haskins, S. Nie, "Direct observation of size-dependent optical enhancement in single metal nanoparticles," J. Am. Chem. Soc. **120**, 8009 (1998).

[36] S. Nie and S. R. Emory, "Probing single molecules and single nanoparticles by surface-enhanced Raman scattering," Science **275**, 1102 (1997).

[37] M. Moskovits, "Surface-enhanced spectroscopy," Rev. Mod. Phys. **57**, 783 (1985).

[38] A. Campion and P. Kambhampati, "Surface-enhanced Raman scattering," Chem. Soc. Rev. **27**, 241 (1998).

[39] K. Kneipp, H. Kneipp, I. Itzkan, R. R. Dasari, M. S. Feld, "Surface-enhanced Raman scattering: A new tool for biomedical spectroscopy," Curr. Sci. **77**, 915 (1999).

[40] D. A. Stuart, C. R. Yonzon, X.Y. Zhang, O. Lyandres, N.C. Shah, M. R. Glucksberg, J. T. Walsh, R. P. Van Duyne, "Glucose sensing using near-infrared surface-enhanced Raman spectroscopy: Gold surfaces, 10-day stability, and improved accuracy," Anal. Chem. **77**, 4013 (2005).

[41] G. Braun, S. J. Lee, M. Dante, T. Q. Nguyen, M. Moskovits, N. Reich, "Surface-enhanced Raman spectroscopy for DNA detection by nanoparticle assembly onto smooth metal films," J. Am. Chem. Soc. **129**, 6378 (2007).

[42] K. A. Willets and R. P. Van Duyne, "Localized surface plasmon resonance spectroscopy and sensing," Annu. Rev. Phys. Chem. **58**, 267 (2007).

[43] S. J. Lee, Z. Q. Guan, H. X. Xu, M. Moskovits, "Surface-enhanced Raman spectroscopy and nanogeometry: The plasmonic origin of SERS," J. Phys. Chem. C **111**, 17985 (2007).

[44] M. Moskovits and D. H. Jeong, "Engineering nanostructures for giant optical fields," Chem. Phys. Lett. **397**, 91 (2004).

[45] N. Felidj, J. Aubard, G. Levi, J. R. Krenn, A. Hohenau, G. Schider, A. Leitner, F. R. Aussenegg, "Optimized surface-enhanced Raman scattering on gold nanoparticle arrays," Appl. Phys. Lett. **82**, 3095 (2003).

[46] A. M. Schwartzberg, C. D. Grant, A. Woltcott, C. E. Talley, T. R. Huser, R. Bogomolni, J. Z. Zhang, "Unique gold nanoparticle aggregates as a highly active

surface-enhanced Raman scattering substrate," J. Phys. Chem. B **108**, 19191 (2004).

[47] P. Dawson, K. B. Alexander, J. R. Thompson, J. W. Haas, T. L. Ferrell, "Influence of metal grain size on surface-enhanced Raman scattering," Phys. Rev. B **44**, 6372 (1991).

[48] Y. Fang, N. H. Seong, D. D. Dlott, "Measurement of the distribution of site enhancements in surface-enhanced Raman scattering," Science **321**, 388 (2008).

[49] G. Laurent, N. Félidj, J. Aubard, G. Lévi, J. R. Krenn, A. Hohenau, G. Schider, A. Leitner, F. R. Aussenegg, "Evidence of multipolar excitations in surface enhanced Raman scattering," Phys. Rev. B **71**, 045430 (2005).

[50] C. J. Orendorff, L. Gearheart, N. R. Jana, C. J. Murphy, "Aspect ratio dependence on surface enhanced Raman scattering using silver and gold nanorod substrates," Phys. Chem. Chem. Phys. **8**, 165 (2006).

[51] G. H. Gu, J. Kim, L. Kim, J. S. Suh, "Optimum length of silver nanorods for fabrication of hot spots," J. Phys. Chem. C **111**, 7906 (2007).

[52] H. J. Van Manen, Y. M. Kraan, D. Roos, C. Otto, "Single-cell Raman and fluorescence microscopy reveal the association of lipid bodies with phagosomes in leukocytes," Proc. Natl. Acad. Sci. **102**, 10159 (2005).

[53] C. L. Evans and X. S. Xie, "Coherent anti-Stokes Raman scattering microscopy: chemical imaging for biology and medicine," Annu. Rev. Anal. Chem. **1**, 833 (2008).

[54] P. D. Maker and R. W. Terhune, "Study of optical effects due to an induced polarization third order in the electric field strength," Phys. Rev. **137**, A801 (1965).

[55] J. X. Cheng, Y. K. Jia, G. F. Zheng, X. S. Xie, "Laser-scanning coherent anti-Stokes Raman scattering microscopy and applications to cell biology," Biophys J. **83**, 502 (2002).

[56] R. F. Begley, A. B. Harvey, R. L. Byer, "Coherent anti-Stokes Raman spectroscopy," Appl. Phys. Lett. **25**, 387 (1974).

[57] C. L. Evans, E. O. Potma, X. S. Xie, "Coherent anti-Stokes Raman scattering spectral interferometry: determination of the real and imaginary components of nonlinear susceptibility $\chi(3)$ for vibrational microscopy," Opt. Lett. **29**, 2923 (2004).

[58] E. O. Potma, C. L. Evans, X. S. Xie, "Heterodyne coherent anti-Stokes Raman scattering (CARS) imaging," Opt. Lett. **31**, 241 (2006).

[59] F. Ganikhanov, C. L. Evans, B. G. Saar, X. S. Xie, "High-sensitivity vibrational imaging with frequency modulation coherent anti-Stokes Raman scattering (FM CARS) microscopy," Opt. Lett. **31**, 1872 (2006).

[60] A. Zumbusch, G. R. Holtom, X. S. Xie, "Three-dimensional vibrational imaging by coherent anti-Stokes Raman scattering," Phys. Rev. Lett. **82**, 4142 (1999).

[61] M. Hashimoto, T. Araki, S. Kawata, "Molecular vibration imaging in the fingerprint region by use of coherent anti-Stokes Raman scattering microscopy with a collinear configuration," Opt. Lett. **25**, 1768 (2000).

[62] C. L. Evans, E. O. Potma, M. Puoris'haag, D. Cote, C. P. Lin, X. S. Xie, "Chemical imaging of tissue in vivo with video-rate coherent anti-Stokes Raman scattering microscopy," Proc. Natl. Acad. Sci. USA **102**, 16807 (2005).

[63] J. X. Cheng, Y. K. Jia, G. Zheng, X. S. Xie, "Laser-scanning coherent anti-Stokes Raman scattering microscopy and applications to cell biology," Biophys. J. **83**, 502 (2002).

[64] E. R. Dufresne, E. I. Corwin, N. S. Greenblatt, J. Ashmore, D. Y. Wang, A. D. Dinsmore, J. X. Cheng, X. S. Xie, J. W. Hutchinson, D. A. Weitz, "Flow and fracture in drying nanoparticle suspensions," Phys. Rev. Lett. **91**, 224501 (2003).

[65] G. W. H. Wurpel, J. M. Schins, M. Mueller, "Chemical specificity in three-dimensional imaging with multiplex coherent anti-Stokes Raman scattering microscopy," Opt. Lett. **27**, 1093 (2002).

[66] X. Nan, W. Y. Yang, X. S. Xie, "CARS microscopy lights up lipids in living cells," Biophotonics Int. **11**, 44 (2004).

[67] E. O. Potma and X. S. Xie, "Detection of single lipid bilayers with coherent anti-Stokes Raman scattering (CARS) microscopy," J. Raman Spectrosc. **34**, 642 (2003).

[68] X. Nan, E. O. Potma, X. S. Xie, "Nonperturbative chemical imaging of organelle transport in living cells with coherent anti-Stokes Raman scattering microscopy," Biophys. J. **91**, 728 (2006).

[69] J. H. Strickler and W. W. Webb, "Two-photon excitation in laser scanning fluorescence microscopy," Proc. SPIE, **1398**, 107 (1990).

[70] E. S. Wu, J. H. Strickler, W. R. Harrell, W. W. Webb, "Two-photon lithography for microelectronic application," Proc. SPIE, **1674**, 776 (1992).

[71] T. Baldacchini, M. Zimmerley, C. H. Kuo, E. O. Potma, R. Zadoyan, "Characterization of microstructures fabricated by two-photon polymerization using coherent anti-Stokes Raman scattering microscopy," J. Phys, Chem. B, **113**, 12663 (2009).

[72] K. Ikeda and K. Uosaki, "Coherent phonon dynamics in single-walled carbon nanotubes studied by time-frequency two-dimensional coherent anti-stokes Raman scattering spectroscopy," Nano Lett. **9**(4), 1378 (2009).

[73] J. X. Cheng and X. S. Xie, "Coherent anti-Stokes Raman scattering microscopy: Instrumentation, theory, and applications," J. Phys. Chem. **108**, 827 (2004).

[74] A. Volkmer, "Vibrational imaging and microspectroscopies based on coherent anti-Stokes Raman scattering microscopy," J. Phys. D. Appl. Phys. **38**, R59 (2005).

[75] J. X. Cheng, "Coherent anti-Stokes Raman scattering microscopy," J. Appl. Spectrosc. **61**, 197A (2007).

[76] M. Mueller and A. Zumbusch, "Coherent anti-Stokes Raman Scattering Microscopy," Chem. Phys. Chem. **8**, 2156 (2007).

[77] S. A. Akhmanov, N. I. Koroteev, A. I. Kholodnykh, "Excitation of the coherent optical phonons of Eg-type in calcite by means of the active spectroscopy method," J. Raman Spectrosc. **2**, 239 (1974).

[78] H. Kano and H. Hamaguchi, "Ultrabroadband (>2500 cm^{-1}) multiplex coherent anti-Stokes Raman scattering microspectroscopy using a supercontinuum generated from a photonic crystal fiber," Appl. Phys. Lett. **86**, 121113 (2005).

[79] W. A. Yarbrough and R. Messier, "Current issues and problems in the chemical vapor deposition of diamond," Science **247**, 688 (1990).

[80] J. C. Angus and C. C. Hayman, "Low-pressure, metastable growth of diamond and "diamondlike" Phases," Science **241**, 913 (1988).

[81] D. Das and R. N. Singh, "A review of nucleation, growth and low temperature synthesis of diamond thin films," Int. Mater. Rev. **52**(1), 29 (2007).

[82] Y. Hirose, 1st Int. Conf. on the New Diamond Science and Technology ed R. Roy, R. Messier, J. E. Butler and J. T. Glass (Pittsburgh, PA: Materials Research Society) p 38 (1988).

[83] Y. Hirose, S. Amanuma, K. Komaki, "The synthesis of high-quality diamond in combustion flames," J. Appl. Phys. **68**, 6401 (1990).

[84] K. Tanabe, Y. Nishibayashi, T. Imai., A. Ikegaya, N. Fujimori, "Deposition of Diamond Film from the O_2-CH_4 System", Science and Technology of New Diamond, edited by Saito S., Fukunaga O., Yoshikawa M., 71-77, KTK Scientific Publishers/ Terra Scientific Publishing Company (1990).

[85] J. S. Kim and M. A. Cappelli, "Temperature measurements in low-pressure, diamond-forming, premixed flames," J. Appl. Phys. **84**(8), 4595 (1998).

[86] M. D. Welter and K. L. Menningen, "Radical density measurements in an oxyacetylene torch diamond growth flame," J. Appl. Phys. **82**, 1900 (1997).

[87] S. J. Firchow and K. L. Menningen, "Radical density measurements in an atmospheric pressure oxyacetylene torch," J. Phys. D: Appl. Phys., **32**, 937 (1999).

[88] S. Roy, J. DuBois, R. P. Lucht, N. G. Glumac, "Hydroxyl radical concentration measurements near the deposition substrate in low-pressure diamond-forming flames," Combustion and Flame, **138**(3), 285 (2004).

[89] A. G. Gaydon, *The Spectroscopy of Flames* (London: Chapman and Hall) (1957).

[90] S. Pellerin, J. Koulidiati, O. Motret, K. Musiol, M. de Graaf, B. Pokrzwka, J. Chapelle, "Temperature determination using molecular spectra simulation," High Temp. Mat. Proc. **1**, 493 (1997).

[91] C. de Izarra, "UV OH spectrum used as a molecular pyrometer," J. Phys. D: Appl. Phys. **33**, 1697 (2000).

[92] S. Pelleriny, K. Musiolz, O. Motrety, B. Pokrzywkax, J. Chapelley, "Application of (0, 0) Swan band spectrum of C_2 for temperature measurement" J. Phys. D: Appl. Phys. **29**, 2850 (1996).

[93] J. S. Kim and M. A. Cappelli, "Diamond film growth in low pressure premixed ethylene-oxygen flames," Appl. Phys. Lett. **65**, 2786 (1994).

[94] J. Reader and C. H. Corliss, *Wavelengths and Transition Probabilities for Atoms and Atomic Ions Part II. Transition Probabilities, NSRDS-NSB 68* (Washington, DC: US Government Printing Office, 1980).

[95] A. R. Striganov and N. S. Sventitskii, *Tables of Spectral Lines of Neutral and Ionized Atoms* (New York: IFI/Plenum, 1968).

[96] R. Payling and P. Larkins, *Optical Emission Lines of the Elements* (Chichester: John Wiley, 2000).

[97] D. W. Hahn and M. M. Lunden, "Detection and analysis of aerosol particles by laser-induced breakdown spectroscopy," Aerosol Sci. Technol. **33**, 30 (2000).

[98] D. Anglos, S. Couris, C. Fotakis, "Laser diagnostics of painted artworks: laser induced breakdown spectroscopy of pigments," Appl. Spectrosc. **51**, 1025 (1997).

[99] D. A. Cremers, J. E. Barefield, A. C. Koskelo, "Remote elemental analysis by laser-induced breakdown spectroscopy using a fiber-optic cable," Appl. Spectrosc. **49**, 857 (1995).

[100] J. P. Singh, F. Y. Yueh, H. Zhang, K. P. Karney, "A preliminary study of the determination of uranium, plutonium and neptunium by laser-induced breakdown spectroscopy," Rec. Res. Dev. Appl. Spectrosc. **2**, 59 (1999).

[101] S. Nakamura, Y. Ito, K. Sone, "Determination of an iron suspension in water by laser-induced breakdown spectroscopy with two sequential laser pulses," Anal. Chem. **68**, 2981 (1996).

[102] D. A. Cremers, L. J. Radziemski, R. R. Loree, "Spectrochemical analysis of liquids using the laser spark," Appl. Spectrosc. **38**, 721 (1984).

[103] R. Sattmann, V. Sturm, R. Noll, "Laser-induced breakdown spectroscopy of steel samples using multiple Q-switch Nd:YAG laser pulses," J. Phys., D. Appl. Phys. **28**, 2181 (1995).

[104] J. Uebbing, J. Brust, W. Sdorra, F. Leis, K. Niemax, "Reheating of a laser-produced plasma by a second pulse laser," Appl. Spectrosc. **45**, 1419 (1991).

[105] F. Colao, S. Pershin, V. Lazic, R. Fantoni, "Investigation of the mechanisms involved in formation and decay of laser-produced plasmas," Appl. Surf. Sci. **197**, 207 (2002).

[106] L. St-Onge, V. Detalle, M. Sabsabi, "Enhanced laser-induced breakdown spectroscopy using the combination of fourth-harmonic and fundamental Nd:YAG laser pulses," Spectrochim. Acta, Part B **57**, 121 (2002).

[107] L. J. Radziemski and D. A. Cremers, Eds. *Laser-Induced Plasmas and Applications* (Marcel Dekker: New York 1989).

[108] R. E. Russo, X. Mao, S. S. Mao, "The physics of laser ablation in microchemical analysis," Anal. Chem. **74**, 70A (2002).

[109] I. B. Gornushkin, L. A. King, B. W. Smith, N. Omenetto, J. D. Winefordner, "Line broadening mechanisms in the low pressure laser-induced plasma," Spectrochim. Acta, Part B **54**, 1207 (1999).

[110] A. Essoltani, P. Proulx, M. I. Boulos, A. Gleizes, "Radiation and self-absorption in argon-iron plasmas at atmospheric pressure," J. Anal. At. Spectrom. **5**, 543 (1990).

[111] J. Scaffidi, S. M. Angel, D.A. Cremers, "Emission enhancement mechanisms in dual-pulse laser-induced breakdown spectroscopy," Anal. Chem. **78**, 24 (2006).

[112] O. D. Sparkman, *Mass spectrometry desk reference*. Pittsburgh: Global View Publication (2000).

[113] L. J. Radziemski, "From LASER to LIBS, the path of technology development," Spectrochim. Acta Part B **57**, 1109 (2002).

[114] R. E. Russo, X. L. Mao, H. C. Liu, J. Gonzalez, S. S. Mao, "Laser ablation in analytical chemistry-a review, " Talanta **57**, 425 (2002).

[115] A. Vertes, R. Gijbels, F. Adams, *Laser Ionization Mass Analys*is, Wiley Interscience: New York (1993).

[116] N. Omenetto, "Role of lasers in analytical atomic spectroscopy: where, when and why – Plenary lecture," J. Anal. At. Spectrom. **13**, 385 (1998).

[117] J. S. Becker, C. Pickhardt, H. J. Dietze, "Laser ablation inductively coupled plasma mass spectrometry for the trace, ultratrace and isotope analysis of long-lived radionuclides in solid samples," Int. J. Mass Spectrom. **202**, 283 (2000).

[118] V. Margetic, M. Bolshov, A. Stockhaus, K. Niemax, R. Hergenroder, "Depth profiling of multi-layer samples using femtosecond laser ablation," J. Anal. At. Spectrom. **16**, 616 (2001).

[119] J. S. Becker, M. Zoriy, J. S. Becker, J. Dobrowolska, A. Matusch, "Laser ablation inductively coupled plasma mass spectrometry (LA-ICPMS) in elemental imaging of biological tissues and in proteomics," J. Anal. At. Spectrom. **22**, 736 (2007).

[120] L. Matus, H. M. Seufert, K. P. Jochum, "Microanalysis of geological samples by laser plasma ionization mass spectrometry (LIMS)," Fres. J. Anal. Chem. **350**, 330 (1994).

[121] R. B. Cody, J. A. Laramée, H. D. Durst, "Versatile new ion source for the analysis of materials in open air under ambient conditions," Anal. Chem. **77** (8), 2297 (2005).

[122] R. G. Cooks, Z. Ouyang, Z. Takats, J. M. Wiseman, "Ambient mass spectrometry," Science 311 (2006) 1566.

CHAPTER 3 TIP-ENHANCED RAMAN SPECTROSCOPY

3.1 Introduction

Raman spectroscopy has been applied extensively in a variety of fields, such as chemistry, physics, material science, biology, space exploration, and semiconductor industry [1], attributing to its uniqueness in providing chemical and structural specific information. Raman technique is non-contact, non-destructive and does not require special sample preparation. However, the spatial resolution of conventional micro-Raman is governed by optical diffraction limit [2]. The typical spatial resolution of popular micro-Raman spectrometers is about 1 μm. In searching of high resolution approaches to improve Raman system, near-field scanning optical microscopy (NSOM) was therefore developed to combine with Raman spectroscopy. Near-field scanning optical microscopy (NSOM) provides better detecting resolution [3-5]. The integration of a micro-Raman spectrometer with an NSOM was developed in a nanoscale Raman spectrometer, known as the near-field scanning Raman microscopy (NSRM). However, NSRM employs an aperture NSOM, which has been limited by its poor signal to noise ratio. In NSRM, an optical fiber tip with a small aperture (with a diameter of 50-200 nm) is used to deliver laser beam and the fiber tip is kept at a close distance (tens of nanometers) above the sample surface. Raman signal is collected in far-field through either a microscope objective or a lens [6-8]. The scattering signal is then delivered into a Raman spectrometer, and Raman spectrum at each point on the target will be acquired by scanning the fiber tip across the sample surface. However, this kind of tip is extremely inefficient due to the weak incident light (100 nW) [9-11].

An approach, by using an apertureless metal tip, is usually called tip-enhanced Raman spectroscopy (TERS). TERS results from a combination of two phenomena, the

electrostatic lightning-rod effect and localized surface plasmon resonances (LSPR) [5]. The lightning rod effect is based on the singularity of a sharp tip, while the LSPR effect depends on the excitation wavelength. The free electrons in the metal tip are driven by the incident light electric field (E-field) along direction of light polarization. Since the charges are accumulate on the surface of the tip leaving the inside of the tip charge free, the charges have opposed points on the tip surface with opposite charge when the incident polarization is parallel to the tip axis, the induced surface charge density on the tip is almost rotationally symmetric and has the highest amplitude at the apex of the tip. TERS can be used to record Raman images either in transmission mode [12] or in side illumination optics [13]. Schematic diagrams of a side-illumination and a transmission mode setup are shown in Fig. 3.1. The effect of TERS is similar to the one seen in the detection of molecules on the metal-island films, known as surface-enhanced Raman spectroscopy (SERS) [14], while in this case a single metallic tip works for the field enhancement in a nanometer scale [15-17].

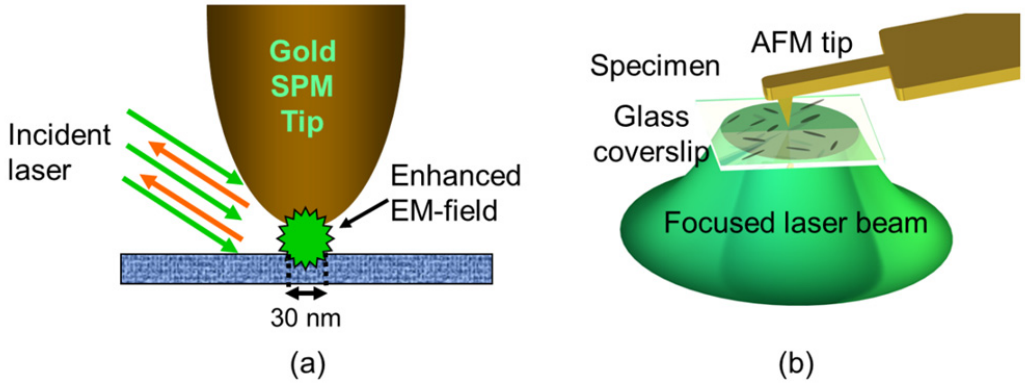

Figure 3.1 Schematic diagrams of (a) an STM-based TERS setup (side-illumination) and (b) an AFM-based TERS setup (transmission or back-illumination).

Although SERS employs metallic surfaces (Ag, Au, and Cu) formed by grains, fractals, clusters, and nanoparticles to achieve presently the strongest Raman enhancement with an enhancement factor of 10^{14} [18-19], the controllability of the SERS substrate is poor for quantitative analysis. TERS, on the other hand, makes use of a metallic tip to induce LSPs [20-22]. One can take advantages of the localized field to improve both the lateral resolution and detection sensitivity because the enhancement only occurs in a nanometer range dictated by the geometry of the tip apex. Due to the rapid degradation along the propagation of evanescent field from tip apex, the tip-surface distance must be precisely controlled at nanometer or even angstrom scale for a high field intensity. The distance control is usually realized by a scanning probe microscope (SPM), including atomic force microscope (AFM) and scanning tunneling microscope (STM). Both AFM and STM can provide atomic-resolution images by scanning a tip across sample surfaces and monitoring either the atomic force or tunneling current. TERS, by a combination of a Raman spectrometer and an SPM, has the ability to obtain accurate in-depth understanding of the morphology, electronic, thermal, chemical, mechanical, and optical properties of nanoscale materials and devices in a correlated manner, eliminating sample contamination during transportation

Single-walled carbon nanotubes (SWCNTs) have been the focus of intense interest due to a large variety of potential nanotechnological applications, for example, CNTs are assembled to fabricate electrical and mechanical nanodevices. The unique properties of SWCNTs arise from their particular one dimensional structure which is directly linked to the characteristic Raman bands. Raman spectroscopy is one of the most used tools in the characterization of CNTs. Due to the high Raman cross-section for the

active vibrational modes and to the possibility to work at resonant excitation frequencies, Raman scattering on SWCNTs has been studied intensively in the literature (see, e.g., Refs. [23-26]) and Raman enhancements of up to 10^{12} have been reported for tubes in contact with fractal silver colloidal clusters [27]. There are limitless opportunities to take advantage of CNTs in engineered materials. For instance, composites will take advantage of the tensile strength of the tubes, and metallic tubes have already been used in integrated circuits [28].

Near-field Raman mapping of SWCNTs was demonstrated using a sharp gold STM tip as a probe. We show that single isolated SWCNTs can be detected with a spatial resolution around 30 nm. This high-resolution capability was applied to resolve local variations in the Raman spectrum along a single SWCNT which would be hidden in far-field measurements. We also demonstrate detection of 30-nm-scale near-field Raman scattering and Raman spectral imaging of nanosphere lithography samples [29] using a metalized (silver coated tungsten) apertureless tip. Ag nanostructures fabricated on Si substrates by the nanosphere lithography (NSL) technique were used for system evaluation because the SERS induced by nanoscale dipoles are promising to further enhance the local optical field in addition to TERS.

3.2 Development of micro-Raman spectrometers

3.2.1 A micro-Raman spectrometer on a microscope frame

In order to build a TERS system, a micro-Raman (spontaneous Raman) system has to be built and tested first, and then integrated the micro-Raman system to a scanning probe microscope (SPM) system for building of a TERS system. The schematic diagram

of a micro-Raman spectrometer with 180º back scattering configuration is shown in Fig. 3.2. The laser beam with 514.5 nm wavelength from an Ar^+ laser passes through a line filter. The intensity of the laser plasma lines is much suppressed by line filter while most of the laser line can pass.

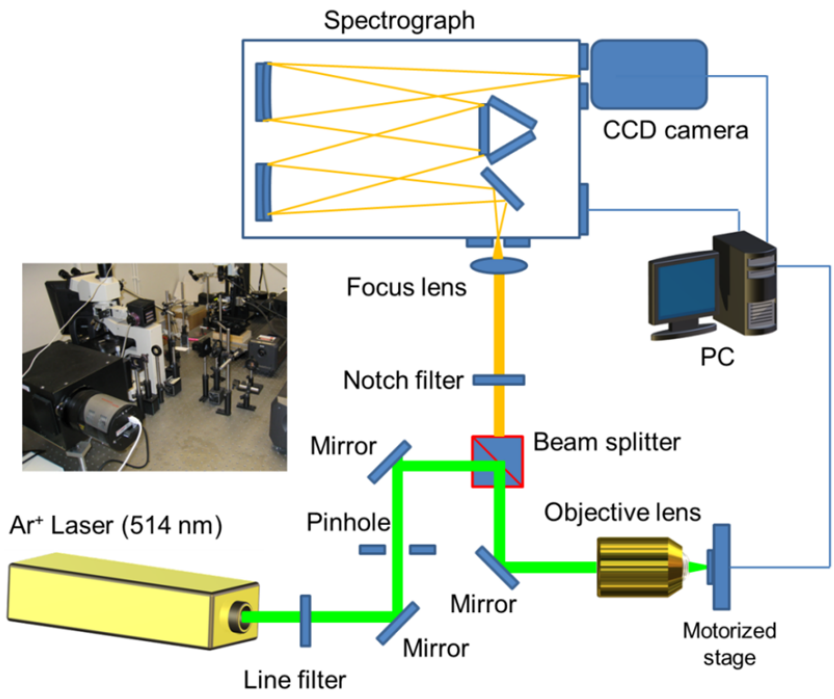

Figure 3.2 Schematic diagram of the micro-Raman spectrometer. Inset: experimental setup of the micro-Raman spectrometer.

The dielectric beam splitter (25 mm in diameter, Newport), which has a reflection/transmission ratio of 30/70 for the incident unpolarized light with the wavelength of 514.5 nm, plays two roles: direct the laser light to the objective lens for excitation; deliver the scattered signal back to the spectrometer for detection. The microscope frame is an Olympus BH-2 system. A standard 50× objective lens (NA=0.8) from Olympus is used to focus laser light reflected by the beam splitter to the sample surface. The scattered light is collected by the same objective lens. A holographic notch

filter (Kaiser Optics, SuperNotch®) placed between the beam splitter and the focus lens attenuates the Raleigh scattering light which is much higher than the Raman signal.

The collected scattered light is focused into the entrance slit of the spectrograph by the focus lens (triplet astigmatic lens), dispersed by gratings of the spectrograph and collected by the CCD camera. A triple-grating dispersive imaging spectrograph (Princeton Instrument, SP-2300i), which has a focal length of 300 mm and is equipped with a CCD camera (Princeton Instrument, PIXIS 400B with a software WinSpec32), is a highly efficient spectrometer optimized for the wide spectral field Raman or fluorescence measurement in the range from 0 to 1400 nm. A 600 g/mm grating is frequently used in the experiments due to its high optical throughput (~80%) at the wavelength of 514.5 nm.

Raman images are obtained by translating the sample across the microscopic objective focus with a motorized stage and using the Raman peaks extracted from each spectrum as the fingerprints. The focusing can be roughly-adjusted manually or fine-tuned automatically. The coordination among the spectrometer, the CCD camera and the *XYZ* stage is managed by a homebuilt mapping program using LabVIEW. The sample is scanned under the microscope objective lens in the *XYZ* plane using a commercial *XYZ* motorized stepper stage (ALIO Industries) equipped with position sensors and closed-loop position feedback (Delta Tau). The sample can be moved in the range of 18 mm along each axis with adjustable steps. The travel resolution is 3.175 μm per step.

The mapping software was developed using LabVIEW as the programming platform. The main operations and functions include the adjustment of focusing conditions, the data representation, and the control of the scanning speeds, the control of the *XY* scanning area and the control of the spectra readout. The driver interfaces for

controlling the *XYZ* motorized stage and the spectrometer were provided by the vendor. Both individual spectra and spectral images can be analyzed either by the program or the available data analysis software. Represented by the 2D projection or the pseudo-3D visualization, a spectral image is a multidimensional data set with two spatial dimensions and one wavenumber dimension. The fingerprints to perform imaging include the integral intensity in an interested range, the average value of several points near the interested peak, and the Raman peak.

3.2.2 A single crystal sapphire fiber probe in micro-Raman spectrometer

A single crystal sapphire fiber was used as a probe for a micro-Raman spectrometer for improved Raman signal sensitivity. The system was built by Cody Raml and the author [30]. The experimental setup, shown in Fig. 3.3, employed an Ar^+ laser (Coherent, Innova 300) set to a wavelength of 514.5 nm. The beam firstly passed through a band-pass filter centered at 515 nm (Omega Optical, 515ASP, min. optical density (OD) of 5.0). The beam was then coupled into the fiber using a microscope objective lens (Newport M-10×, NA=0.25) focused onto one fiber end. A beam splitter was placed between the laser and the fiber coupler to direct the scattered beam from the sample into a dark box, which contained two identical edge filters (Omega Optical, 525ALP, min. OD of 4.5) in series, leading to a lens (Newport, KBX046, focal length 25.4 mm) focusing the signal into the spectrometer fiber. The spectrometer used was a Princeton Instruments SP2300i utilizing a thermal electric cooled CCD camera (Princeton Instruments, PIXIS). The fiber bundle used to couple the signal into the spectrometer was a bundle of 19 fibers (400-2200 nm, 1 m long, each 200 μm in diameter, Princeton Instruments, LG-456-020). The probe/signal collection fiber used was an unclad, single-crystal sapphire fiber with a

diameter of 200 μm (MicroMaterials, Inc., FS200-50). The silica fiber used for comparison was a 100-μm core diameter Newport multimode fiber (F-MLD). Both ends of the sapphire fiber were polished for high optical quality. Each fiber was 50 cm in length. The effective NA (NA_{eff}) of each fiber was measured by recording the optical transmission of the fibers when the laser was launched into the fiber at different incident angles, and the NA_{eff} is defined by the sine of the angle at which the transmission is half of the maximum [31]. The measured NA_{eff} for both fibers was 0.21 at the excitation laser wavelength of 514.5 nm.

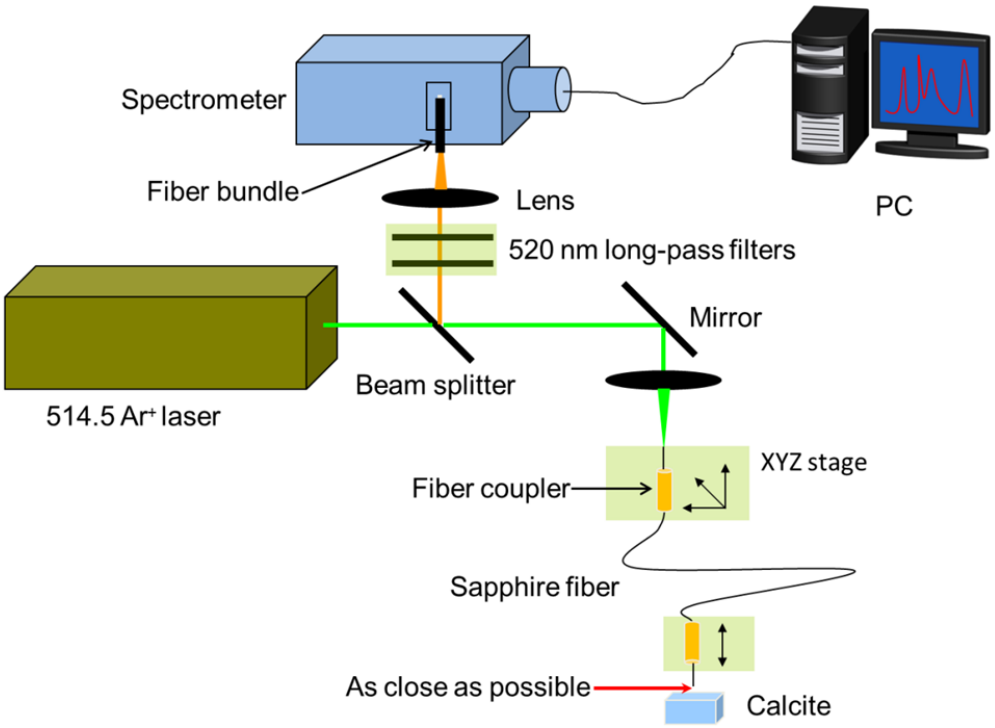

Figure 3.3 Schematic of the experimental setup for Raman spectroscopy.

A natural calcite crystal was tested using either a sapphire fiber or a glass fiber. Calcite, due to its crystalline nature, has a strong, documented peak at 1086 cm^{-1} [32]. Figure 3.4 plots the measured Raman spectra of the sample using the glass and sapphire

fibers, respectively. Almost no calcite peak (1088 cm^{-1}) can be found in the Raman spectra taken using glass fiber as a probe, as shown in Figs. 3.4(a) and (b). In Figs. 3.4(c) and (d), a Raman peak can be clearly seen at approximately 1088 cm^{-1} in the spectrum, measured using the sapphire fiber probe. Though the Raman signal may also be present in the measurement utilizing the silica fiber, the amorphous nature of this material produces a background noise that leads to a poor SNR, leaving the calcite Raman peak indistinguishable.

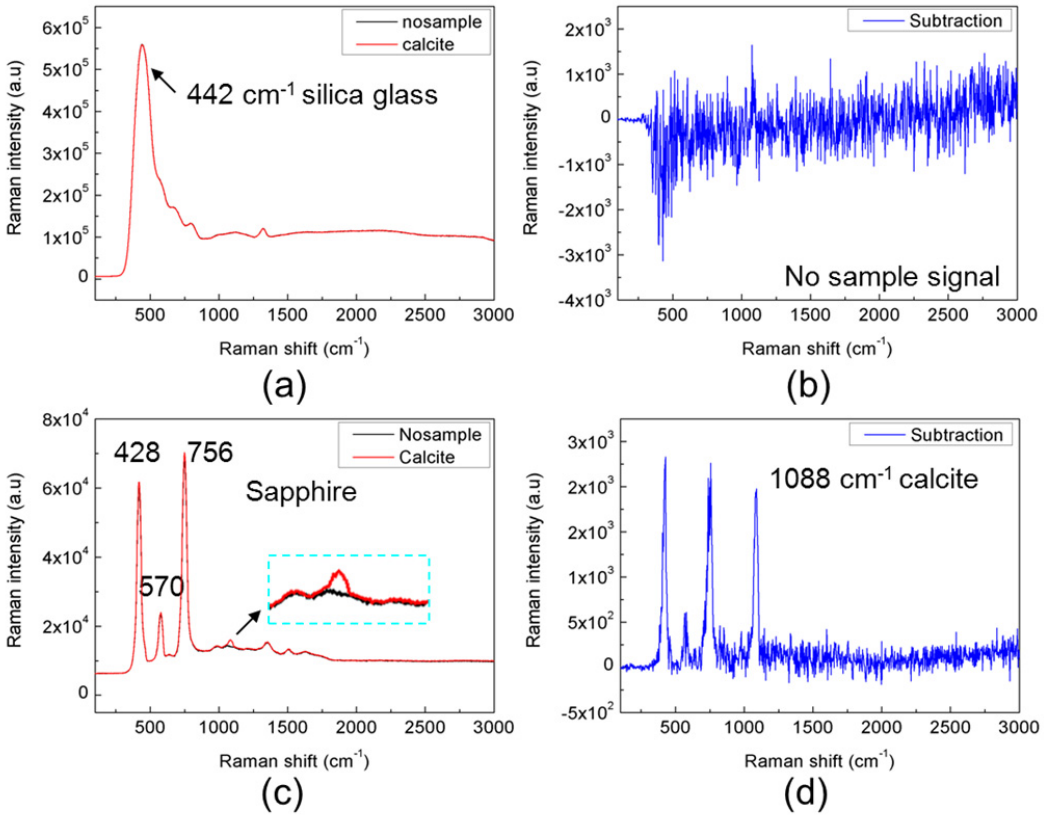

Figure 3.4 (a) Raman spectra of a calcite crystal (red curve) at the detecting end of the glass fiber and a glass fiber only (with air at the detecting end) (black curve: covered by the red curve in the diagram). (b) Subtraction of the two spectra in (a). (c) Raman spectra of with a calcite crystal (red curve) at the detecting end of the sapphire fiber and a sapphire fiber only (with air at the detecting end) (black curve). (d) Subtraction of the two spectra in (c).

In summary, two fibers, one made from a single sapphire crystal and one made from silica, were placed into an identical experimental setup and used to acquire Raman spectra from three different materials, calcite, SWCNTs, and Na_2CO_3 solution [30]. Each of these spectra demonstrates a clear advantage of using the sapphire fiber for Raman signal detection because of the significantly reduced Raman background noise of the single crystal sapphire fiber. This Raman configuration could be useful in a number of industries where the size of a traditional fiber-based Raman system would be a limiting factor, such as in *in vitro* studies of tissues in biomedical applications.

3.3 Development of a tip-enhanced Raman spectrometer

3.3.1 System description

The schematic diagram of the TERS system is shown in Fig. 3.5. The system includes an optical path, a Raman spectrometer module (spectrograph and CCD camera), an STM module, a motorized stage module (nanopositioner), an optical microscope, and a computer [29]. The optical path is used to deliver the excitation laser beam for sample surfaces illumination and collect the scattered Raman signals from the sample surfaces. The Raman spectrometer module is used to collect the scattered signals and convert the optical signals into electronic signals. The STM is used to control tip-to-sample distance. The nanopositioner is used to position the samples in x and y directions. The optical microscope above the sample holder equipped with a CCD camera is used to locate the regions of interest and monitor the laser spot and the tip for optical alignment. STM control, acquisition, processing and visualization of Raman signals are controlled by a computer.

As shown in Fig. 3.5, a laser beam from an Ar^+ laser (Coherent, Innova 300) passes through a line filter (Newport) that only allows the wavelength of 514.5 nm to pass through. Before reaching a beam splitter (Newport Inc.), the beam is reflected by a mirror, and its polarization is varied by a half-wave plate (CVI) which is constantly aligned vertical to the surface of the optical table. The transmitted beam is then reflected by three mirrors before being focused on a sample surface by an objective lens (Olympus, LWD 50×, NA=0.45, WD=15 mm).

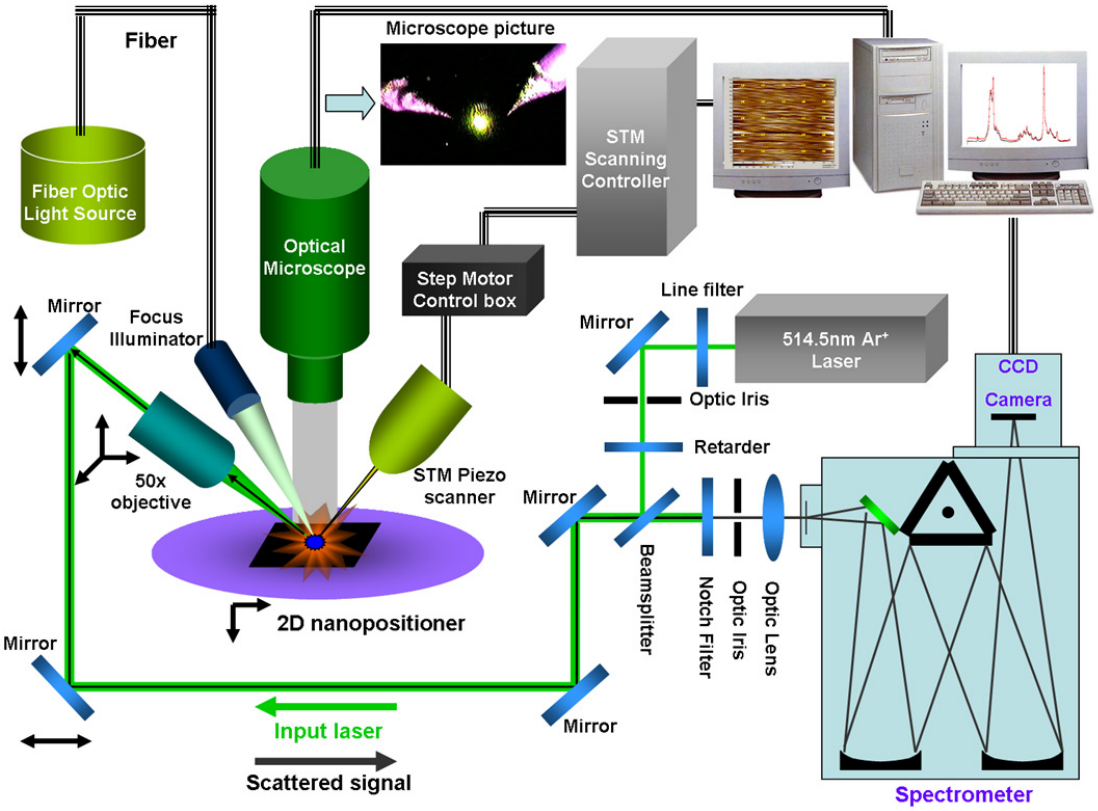

Figure 3.5 Schematic diagram of the STM based tip-enhanced Raman spectroscopy system with side-illumination optics.

Next, the tip mounted on the STM (Agilent, SPM 5500) approaches the sample surface with the tip-to-surface distance in the tunneling range of ~1 nm. The position of the objective lens is controlled by a motorized *XYZ* stage with a resolution of 3 μm,

indicated by the arrows beside the objective lens. With a successful optical alignment, near-field Raman scattering signals are collected by the objective lens and reflected by the mirrors. After passing through a notch filter (Kaiser, SuperNotch®, OD=4.0) and an iris (Newport), the light with Raman signals is focused by a lens (CVI) into the slit of the spectrograph (Princeton Instruments, Acton SP2300i). A back-illuminated CCD camera (Princeton Instruments, PIXIS-400B) with high quantum efficiency (90% at 514.5 nm) is used to acquire the Raman spectra. The spectra are then analyzed, processed, and visualized by the computer. The nanopositioner (Mad City Laboratories, nano-H100) is placed below the sample holder for Raman mapping.

3.3.2 Optical alignment

To obtain the TERS spectra, precise alignment of the focused laser beam with respect to the tip was essential. The beam center was aligned in between the tip-surface gap, with the challenge that the micron-sized laser beam was required to be aligned with the nanoscale tip apex. Three steps, including coarse, intermediate, and precise alignments, were used to address this challenge. More specifically, the laser beam was aligned to the tip with millimeter-range accuracy in the coarse alignment, micrometer-range accuracy in the intermediate alignment, and nanometer-range accuracy in the precise alignment. As shown in Fig. 3.5, two mirrors (bidirectional arrows), one objective lens (three arrows), and one tip, all movable, are the key components to perform the optical alignment. Both mirrors, mounted on two orthogonally arranged translation stages, are used to perform the coarse alignment. The objective lens, mounted on the motorized *XYZ* stage, is used for the intermediate alignment. The precise alignment is implemented by the piezoelectric transducer mounted on the STM scanner. The tip position and sample

surface are both monitored by the optical microscope. Before the coarse alignment, the objective lens is moved away from the optical path. The laser beam is positioned in a targeted region completely covering the tip apex. The objective lens is then moved back and gradually approached to the sample surface. At this stage, the position of the focused beam is near the tip position. Subsequently, by moving the objective lens in the intermediate alignment, the focused beam is brought to the tip position with an accuracy of 50 μm. Finally, the tip is brought back and moved in a range of 100 μm with a resolution of 0.4 nm. Since the beam is within a range of 50 μm from the tip position, the laser beam eventually meet with the tip at a certain position. Figure 3.6 shows the nano-Raman system (a) and the micro-Raman system (b). In Fig. 3.6(a), the STM tip is approached onto the sample surface, and therefore, strong scattering light is seen. In Fig. 3.6(b), the STM tip is withdrawn and only micro-Raman signal is detected.

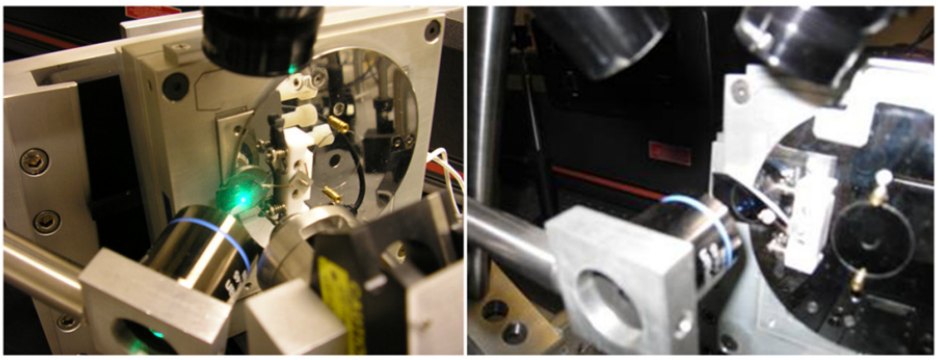

Figure 3.6 Photos of the nano-Raman (a) and micro-Raman setups with tip withdrawn (b).

In Fig. 3.7(a), a microscopic view of the STM tips approached close to the sample surface is shown. The structures on the substrates are electrodes made from photolithography. The tip on the left side is the mirror of the real tip on the right side. In Fig. 3.7(b), the STM tip (Ag-coated W tip) is approached on the sample surface and

aligned right into the laser focal point. Strong scattering from the tip apex is seen in this photo. Figure 3.7(c) is a view of an STM tip (Au tip) close to the surface of a Si substrate. As shown in Fig 3.7(d), the TERS system experimental setup is demonstrated.

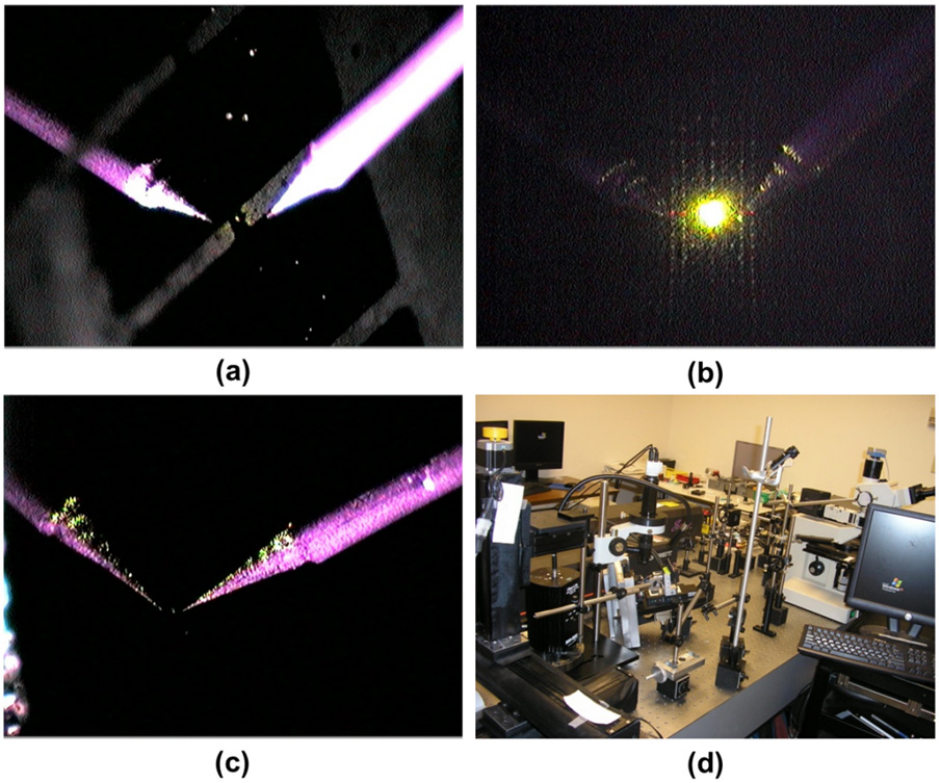

Figure 3.7 (a) A microscopic view of the STM tip approached close to the sample surface, which are electrodes made from photolithography. The tip on the left side is the mirror of the real tip on the right side. (b) A microscopic view of the STM tip when the tip is approached on the sample surface and aligned right into the laser focal point. (c) Tip close to the surface of a Si substrate. (d) The TERS system experimental setup.

3.3.3 Tip preparation

Au STM tips were fabricated by an electrochemical etching apparatus. Etching voltage, etching time, shape of cathode and solution were controlled for optimization. To fabricate a gold tip, a gold wire (Aldrich) of 0.25 mm diameter was immersed in a solution prepared using analytical grade fuming hydrochloric acid and ethanol (Merck). To achieve optimum round shape, the cathode was made in a ring shape. A bias voltage

of 2.4 V was then applied between the ring and the Au tip for a time period of ~ 6-8 min [33].

The setup for etching Au tips is based on a commonly used configuration, as shown in Fig. 3.8(a). The ring of about 8 mm diameter on the surface of the solution is immersed in the solution to ~ 3/4 height. A gold wire after a quick flame-annealing is immersed in the center of the ring. The immersed length is controlled to be about ~3 mm. In order to control the shape of the tip apex, a light indicator is used to monitor the etching process. The DC voltage is supplied by a home-made DC power supply (see Fig. 3.8(b)), which allows an easy control of the voltage and a quick switch to open circuit when the lower part of the wire falls down. A multimeter is used for recording the etching current. The etching solution is prepared using analytical grade fuming hydrochloric acid and ethanol from Merck. Ethanol is used to reduce bubbling, and produces a smooth surface during the etching process [34].

The current falls as the Au wire is etched. Once the current reaches a specific value (I_{stop}) [35] to obtain the Au tip with the expected curvature radius, the generator is switched off to stop the process. The tip is then washed with the distilled water and acetone, and then blew with the compress air with the direction right against the tip apex. The reaction time is in the 6-10 minutes range. The Au tips are characterized with a scanning electron microscope (SEM, HITACHI 4700) operated at a low accelerate voltage.

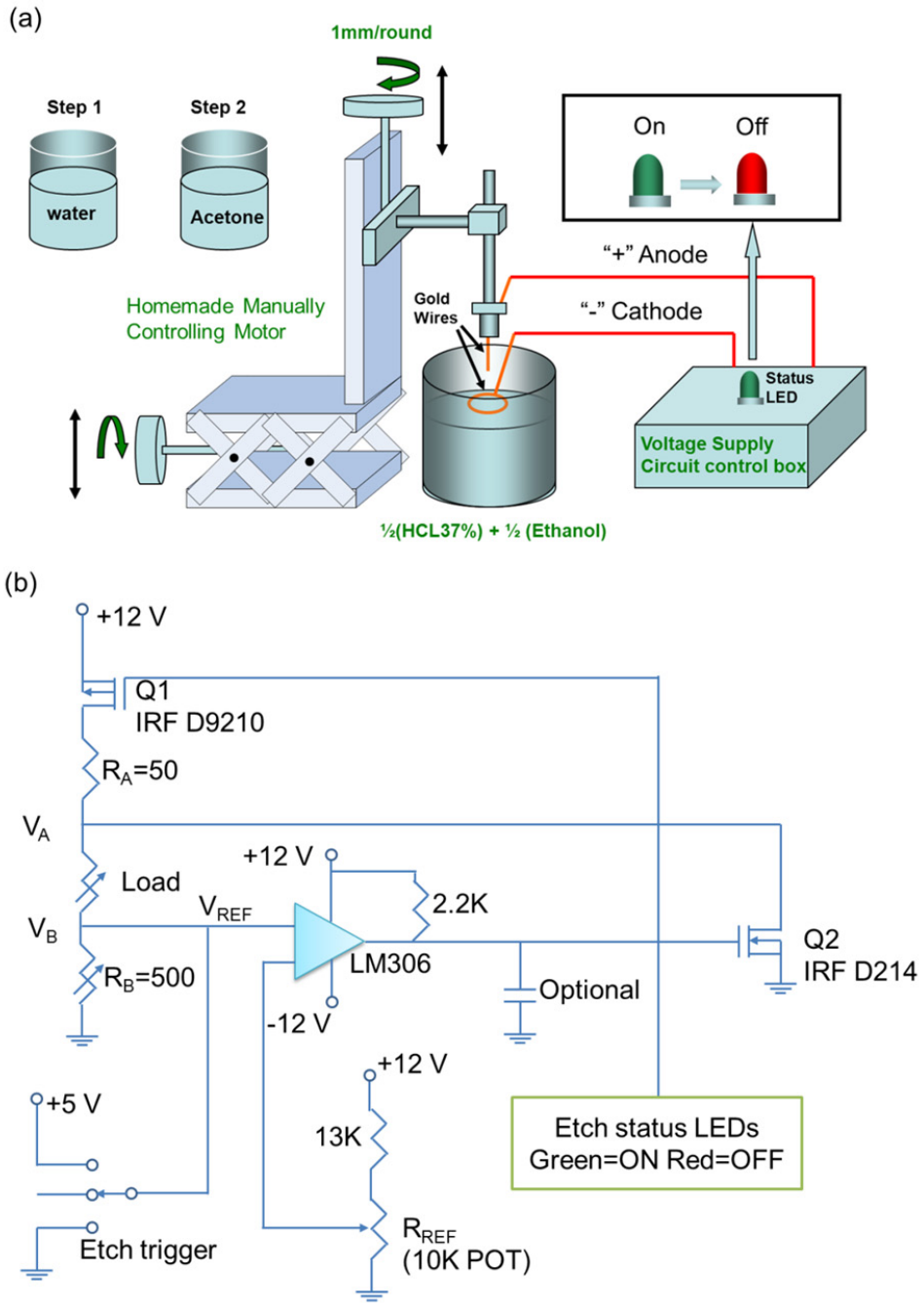

Figure 3.8 Schematic diagram of the Au tip fabrication setup (a) and the circuit in the voltage supply circuit control box (b).

Generally, under optimal conditions, an efficient Au tip can be reproducibly produced within 6 to 7 min. The actual etching time depends on the temperature and

freshness of the etching solution and the relative proportion of HCl to ethanol. It should be noted that at the ending point of the etching process, the most etched portion of the Au wire becomes very thin. If the Au wire is not very well vertically aligned, it can result in an Au tip with bent apex. The fabricated tips are shown in Fig. 3.9. These two tips are different because the stop current is different. The current of anode to cathode for Fig. 3.9(a) is stopped at the optimized stop current point, while Fig. 3.9(c) is not. The tip shown in Fig. 3.9(a) is easier to achieve enhanced Raman spectra because the tip apex curvature-to-diameter ratio is higher.

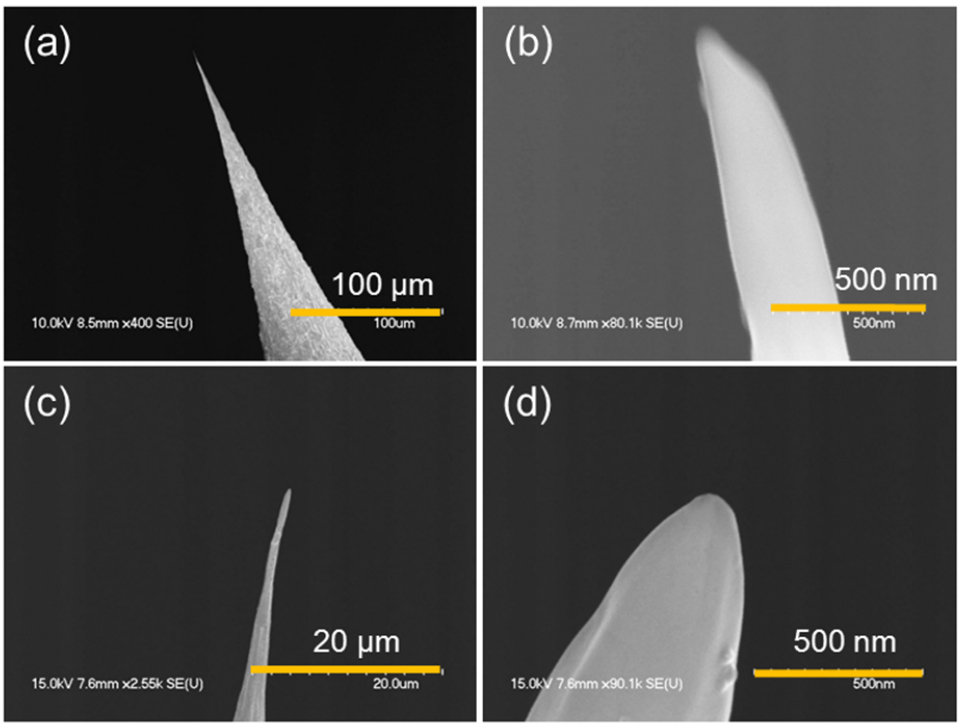

Figure 3.9 F-SEM images of gold STM tips taken out from the fabricating process at different current with the same DC voltage applied. (a) and (c) are two different tips, (b) and (d) are their higher magnification SEM images.

3.3.4 Sample preparation

P-type Si (110) substrates (Virginia Semiconductor) with a resistivity of 0.02-0.09 Ω·cm were cleaned in an ultrasonic cleaner with acetone and alcohol solutions for 10 min, respectively, followed by a passivation process in 5% HF solution for 5 min. Commercialized CNT powder from Aldrich was utilized to be dispersed onto the surface of the prepared silicon surface. CNT powder purity is 50-70 vol%, and contains residual catalyst impurities (Ni, and etc.). Nanotubes occur in bundles of length ~20 μm. Individual tube diameter is within the range of 1.2-1.5 nm.

The metals (Ni-Y) were removed by a reflux in acid solution using a weakly oxidizing HCl solution for 24 hr. pH 10 NaOH solution was then poured over the filtrate to reduce its acidity. After NaOH passed through the filter, and litmus paper was used to check the pH in the funnel. The NaOH wash and pH check were repeated until the pH was ~7. Next we used ultrasonic to agitate the impurity and remove them. We then used Nd:YAG laser (Continuum, Powerlite Precision II 8010) at 532 nm to irradiate the CNTs in the water which was placed in a petridish to separate the CNT bundles more complete. The power of the laser used was 100 mW, and the process persisted for 10 minutes. The single-walled CNT (SWCNT) sample was then diluted in 2,2,3,3-tetrafluoro-1-propanol to make a suspension for ultrasonic agitation. The suspension was then spin coated (3000 RPM, 1 min) on a gold-coated glass coverslip (100-nm coating) (or a Si substrate), and let dried in an oven at a temperature of 110 °C for 4 hr. After these processing steps, isolated SWCNTs appeared in certain areas on the substrate.

Using of tetrafluoropropanol and spin coating is very important for the sample preparation process. Figure 3.10(a) shows an SEM image of the CNT sample made from

directly dropping of CNTs in deionized water onto the substrate. Figure 3.10(b) is an AFM topography image of the sample as shown in Figure 3.10(a). Figure 3.10(c) is some typical area on the sample, especially in the outer area of the substrate, with tetrafluoropropanol and spin coating. Most of the CNTs were well separated in this process. As shown in Fig. 3.10(d) and (e), typical structures on the sample, especially in the central area of the substrate, show very well dispersed CNTs. Short CNTs were totally separated and well distributed over the area. Structures like this made very good testing structure for TERS performance test.

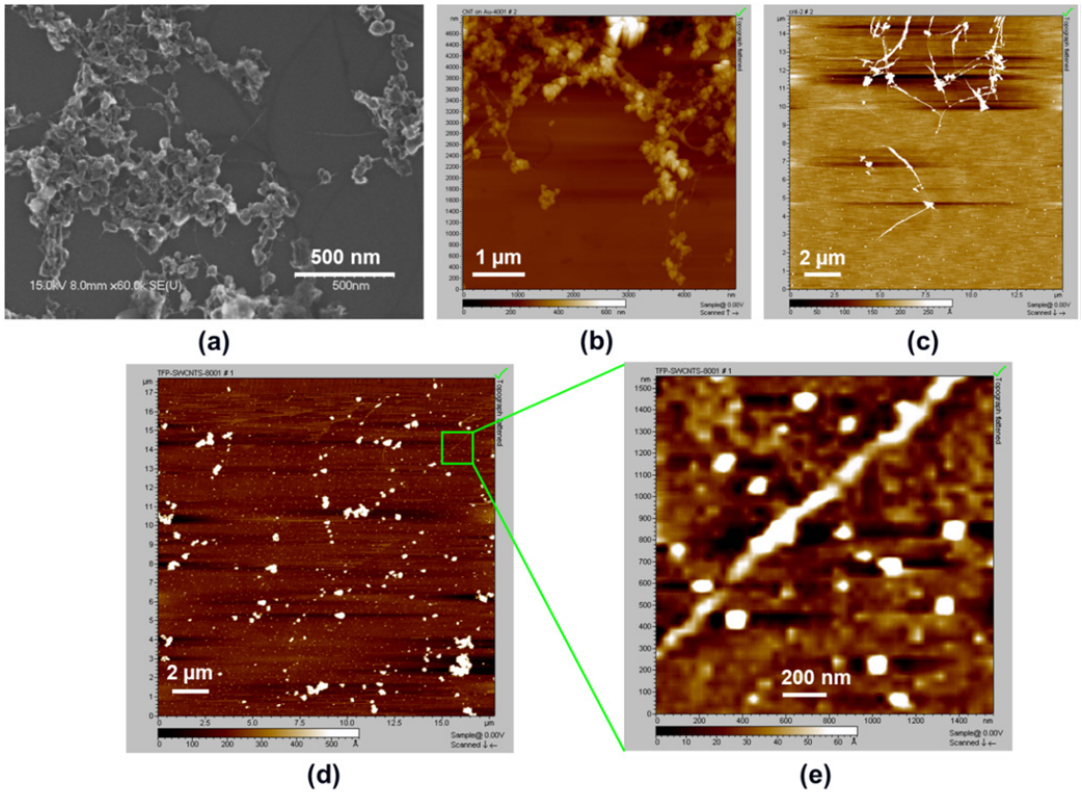

Figure 3.10 (a) SEM image of the prepared CNT sample without dilution in tetrafluoropropanol and spin coating. (b) AFM topography image of the same sample in (a). (c) AFM image of specific area of the CNT sample with tetrafluoropropanol and spin coating. (d) AFM image of typical area of the same CNT sample as in (c). (e) Magnified green circle area in (d).

3.4 Performance of the TERS system

3.4.1 Micro-Raman mapping of CNTs

From the micro-Raman spectra in Fig. 3.11 (black, dashed curve), there are four peaks from left to right: Radial Breathing Mode (RBM) at 170 cm^{-1}, D band at 1338 cm^{-1}, G band at 1591 cm^{-1}, and G' band at 2660 cm^{-1}.

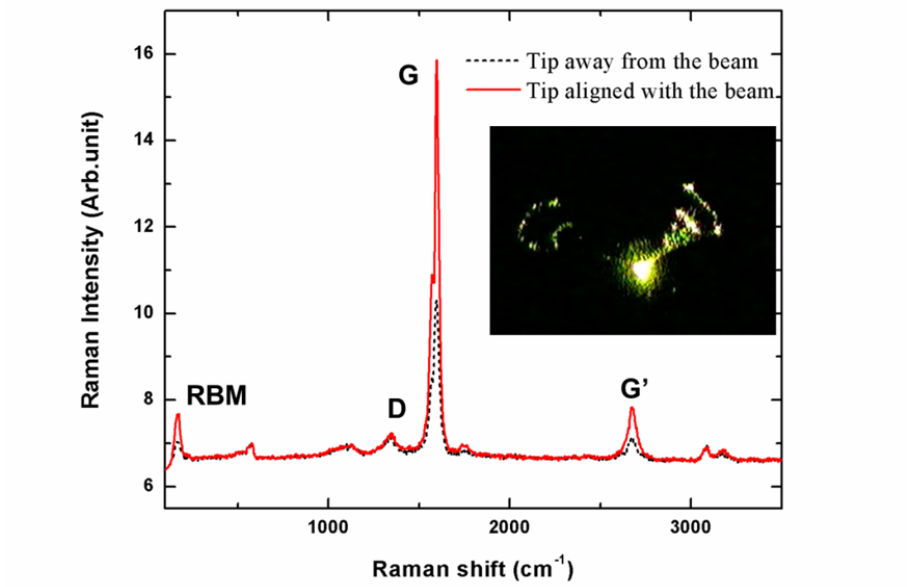

Figure 3.11 Raman spectra of the SWCNT with the tip away from (dotted curve) and aligned with (solid curve) the laser beam.

The most obvious feature in the Raman spectrum of SWCNTs is the RBM signals, which is often observed between 100 and 250 cm^{-1}. Although the D, G, and G' modes are found in graphite, the RBM is specific to SWCNTs and is representative of the isotropic radial expansion of the tube. The RBM frequency is inversely proportional to the diameter of the tube, making it an important feature for determining the diameter distribution in a sample. The RBM bands are a useful diagnostic tool for confirming the presence of SWCNTs [36]. Non-isolated SWCNTs are subject to inter-tube interactions

which increase the frequency of the RBM. The D mode (the disorder band) is expected to be observed in multi-walled carbon nanotubes (MWCNTs). In SWCNTs, it is ascribed to the defects in the tubes. The G mode (Tangential Mode), located near 1580 cm^{-1}, corresponds to the stretching mode of the carbon-carbon bond in the graphite plane.

For micro-Raman mapping, the nanopositioner was used to move the sample in *x* and *y* directions for raster scanning. The sample holder mounted on the nanopositioner was placed perpendicular to the microscope objective which was used for laser beam focusing. Because the scattered Raman signal is higher in the direction vertical to the substrate surface than any other directions, the highest sensitivity could be achieved in this direction. In addition, the nanopositioner was perpendicular to the objective to guarantee the image mapping without distortion. Considering the focused spot of the laser was ~5μm, the step was set to 2 μm, and the area was 40×40 μm^2. Figure 3.12(c) shows the mapping results of the CNT samples. The highest resolution achieved was 5 μm, close to the diameter of the laser spot.

3.4.2 Nano-Raman mapping of CNTs

By applying the tip-enhancement, the Raman spectra of the individual CNTs dispersed on the substrates were obtained by measuring the Raman spectra with (near-field and far-field) and without (far-field only) the tip. With a good alignment, the Raman enhancement for all vibration modes (RBM, D, G and G') can be found, as shown in Fig. 3.11. The Raman peak of the silicon substrate (when an Si substrate was used) was observed, but not enhanced, because the tip was exactly placed above the SWCNTs, and thus the enhanced optical fields only enhanced the Raman signal of the SWCNTs but not of the substrate.

By identifying different Raman intensities from different region using a specific vibration mode as the fingerprint, Raman mapping can be performed to visualize the individual carbon nanotubes. Figure 3.12(b) shows the Raman image of the SWCNTs dispersed on the Si substrate. As evidenced by the images, this instrument has a spatial resolution of 30 nm. The mapping image is acquired with a line scanning step of 20 nm and a total scanning area of ~500 nm^2.

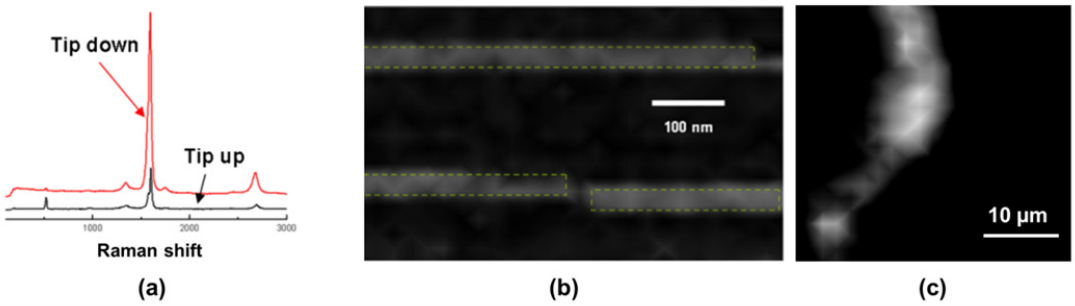

Figure 3.12 (a) TERS spectra of CNTs on a Si substrate. (b) Raman mapping of the individual SWCNTs dispersed on the Si substrate. (c) Micro-Raman mapping of the same sample as in (b).

3.4.3 Raman mapping of nanostructures on Si surfaces

TERS is also able to resolve individual nanostructures. In this study, nanostructures were fabricated on Si substrate using nanosphere lithography (NSL), the whole process of which can be found in Appendix. When the tip was right on top of the nanostructures on the silicon substrate, the Raman signal of Si cannot be excited because the Si surface around the tip apex region was blocked by the nanostructures. When the tip was placed in between the terminal ends of two adjacent nanostructures (dipole), a significant Raman enhancement can be observed. When the tip was located in the lift-off area, only the normal tip enhancement was present.

By identifying different Raman intensities, Raman mapping images can be obtained. These images can be used to differentiate different regions. Fig. 3.13(a) is a

schematic diagram of the TERS illumination setup. Fig. 3.13(c) shows the Raman image using Si peak (520 cm^{-1}) at the rectangular area enclosed with dashed lines in Fig. 3.13(b) (SEM image of the NSL structures). It is clearly seen that the individual nanostructures have been spatially resolved, leading to a conclusion that the system has a spatial resolution below 100 nm. We attribute this significant Raman enhancement to the strong coupling between the LSPs from the tip and the nanostructure dipole (NSL structures). The metallic nanostructures have nanopyramid geometries, as shown in Fig. 3.13(b). Therefore it is easy to understand the significant enhancement occurs between the dipole tips, since the Raman signal in this gap is the highest. The enhancement of the localized optical fields in the proximity of the dipole tips is determined by several factors such as the material, geometry, angle and radius of curvature of the tip, and the wavelength of the excitation light [29].

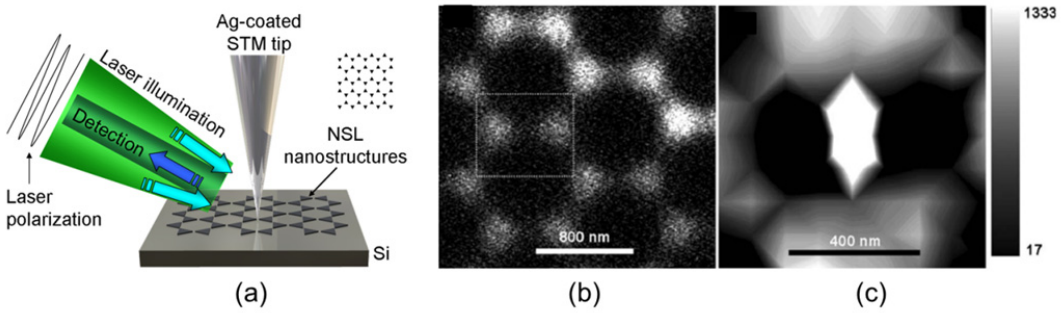

Figure 3.13 Raman mapping of the NSL nanostructures. (a) Schematic diagram of the TERS illumination setup. (b) SEM image of the NSL structure. The Raman scanning region (c) corresponds to the area enclosed by the dashed lines in (b).

3.5 Conclusions

Micro-Raman and TERS systems were developed for measurement of different micro-/nanostructures and micro-/nanomaterials. Two micro-Raman systems were developed. One was based on a microscope (later on combined with an STM system for

TERS), while the other one was based on a single crystal fiber probe. Better sensitivity of sapphire fiber probe compared to normal glass fiber probe was demonstrated. Near-field optical effect was realized by using apertureless metallic gold tips mounted on an STM system. TERS spectra of NSL nanostructures and SWCNTs were demonstrated. Using side-illumination optics, the TERS instrument can accommodate both opaque and transparent samples. Au STM tips were fabricated and used in SWCNT imaging, while Ag-coated W tips were used for NSL structure mapping. The SWCNT samples on the Si substrates were prepared. The Raman peaks of different bands, including the RBM, D, G, and G´ bands, were obtained and analyzed. The Raman mapping of the SWCNTs at microscales and nanoscales was performed. The successful mapping of the individual SWCNTs using the TERS system demonstrated that this apparatus had a spatial resolution of 30 nm. The correlated characterization capability of the system provided a new approach to understanding the relationship among the morphology, electronic, thermal, chemical, mechanical, and optical properties of nanoscale materials and devices, while eliminating sample contaminations during transportation among different instruments.

Table 3.1 Summary of TERS techniques.

Tip-enhanced Raman spectroscopy (TERS)		
Realization approaches	Combine Raman system with an atomic force microscopy (AFM), conductive or nonconductive substrate	Combine Raman system with an scanning tunneling microscope (STM), conductive (or semiconducting) substrate
Principle	Detection of molecular or crystal lattice vibrational states using excited localized surface plasmons due to the geometric singularity	
Combination possibility	Tip-enhancement can be combined with SERS or CARS. However, SERS is usually acquired in the epi-direction, while CARS can be acquire in the forward direction (epi-direction signal is weak).	
Resolution	<30 nm (mainly depend on the radius of tip apex)	
Application	Spectroscopy and imaging of nanostructures, such as graphene, single-walled carbon nanotubes, and single molecules	
Enhancement factor	Peak intensity enhancement ~200% (vary with different samples)	

3.6 References

[1] M. Moskovits, "Surface-enhanced Raman spectroscopy: A brief retrospective," J. Raman Spectrosc. **36**, 485 (2005).

[2] M. Born and E. Wolf, *Principles of Optics*, seventh ed., Cambridge University Press, Cambridge, MA, 1999.

[3] D.W. Pohl, W. Denk, M. Lanz, "Optical stethoscopy: Image recording with resolution λ/20," Appl. Phys. Lett. **44**, 651 (1984).

[4] A. Harootunian, E. Betzig, M. Isaacson, A. Lewis, "Super-resolution fluorescence near-field scanning optical microscopy," Appl. Phys. Lett. **49**, 674 (1986).

[5] S. Kawata (Ed.), *Near-Field Optics and Surface Plasmon Polaritons*, Springer, Berlin, (2001).

[6] S. Webster, D.A. Smith, D.N. Batchelder, "Raman microscopy using a scanning near-field optical probe," Vib. Spectrosc. **18**, 51 (1998).

[7] E. J. Ayars and H. D. Hallen, "Surface enhancement in near-field Raman spectroscopy," Appl. Phys. Lett. **76**, 3911 (2000).

[8] C. L. Jahncke, M. A. Paesler, H. D. Hallen, "Raman imaging with near-field scanning optical microscopy," Appl. Phys. Lett. **67**, 2483 (1995).

[9] M. N. Islam, X. K. Zhao, A. A. Said, S. S. Mickel, C. F. Vail, "High-efficiency and high-resolution fiber-optic probes for near field imaging and spectroscopy," Appl. Phys. Lett. **71**, 2886 (1997).

[10] T. Yatsui, M. Kourogi, M. Ohtsu, "Increasing throughput of a near-field optical fiber probe over 1000 times by the use of a triple-tapered structure," Appl. Phys. Lett. **73**, 2090 (1998).

[11] Y. H. Chuang, K. G. Sun, C. J. Wang, J. Y. Huang, C. L. Pan, "A simple chemical etching technique for reproducible fabrication of robust scanning near-field fiber probes," Rev. Sci. Instrum. **69**, 437 (1998).

[12] R. M. Stöckle, Y. D. Suh, V. Deckert, R. Zenobi, "Nanoscale chemical analysis by tip-enhanced Raman spectroscopy," Chem. Phys. Lett. **318**, 131 (2000).

[13] D. Mehtani, N. Lee, R. D. Hartschuh, A. Kisliuk, M. D. Foster, A. P. Sokolov, J. F. Maguire, "Nano-Raman spectroscopy with side-illumination optics," J. Raman Spectrosc. **36**, 1068 (2005).

[14] R. K. Chang and T. E. Furtak (Eds.), *Surface Enhanced Raman Scattering*, Plenum Press, New York (1981).

[15] Y. Inouye, N. Hayazawa, K. Hayashi, Z. Sekkat, S. Kawata, "Near-field scanning optical microscope using a metallized cantilever tip for nanospectroscopy," Proc. SPIE **3791**, 40 (1999).

[16] R. M. Stockle, Y. D. Sur, V. Dekkert, R. Zenobi, "Nanoscale chemical analysis by tip-enhanced Raman spectroscopy," Chem. Phys. Lett. **318**, 131 (2000).

[17] M.S. Anderson, "Locally enhanced Raman spectroscopy with an atomic force microscope," Appl. Phys. Lett. **76**, 3130 (2000).

[18] S. M. Nie and S. R. Emory, "Single-molecule detection and spectroscopy by surface-enhanced Raman scattering," Abstr. Pap. - Am. Chem. Soc. **213**, 177 (1997).

[19] A. J. Haes, W. P. Hall, R. P. Van Duyne, "Nanoscale plasmonics begins to unravel Alzheimer's disease," Laser Focus World **41**, 105-109 (2005).

[20] A. Barbara, T. Lopez-Rios, P. Quemerais, "Near-field optical microscopy with a scanning tunneling microscope," Rev. Sci. Instrum. **76**, 023704 (2005).

[21] N. Hayazawa, Y. Inouye, Z. Sekkat, S. Kawata, "Near-field Raman scattering enhanced by a metallized tip," Chem. Phys. Lett. **335**, 369 (2001).

[22] A. Hartschuh, M. R. Beversluis, A. Bouhelier, L. Novotny, "Tip-enhanced optical spectroscopy," Philos. Trans. R. Soc. London, Ser. A **362**, 807 (2004).

[23] A. Jorio, R. Saito, J. H. Hafner, C. M. Lieber, M. Hunter, T. McClure, G. Dresselhaus, M. S. Dresselhaus, "Structural (*n*,*m*) determination of isolated single-wall carbon nanotubes by resonant Raman scattering," Phys. Rev. Lett. **86**, 1118 (2001).

[24] Z. Yu and L. Brus, "Rayleigh and Raman scattering from individual carbon nanotube bundles," J. Phys. Chem. B **105**, 1123 (2001).

[25] G. S. Duesberg, I. Loa, M. Burghard, K. Syassen, S. Roth, "Polarized Raman Spectroscopy on Isolated Single-Wall Carbon Nanotubes," Phys. Rev. Lett. **85**, 5436 (2000).

[26] J. Maultzsch, S. Reich, C. Thomsen, "Raman scattering in carbon nanotubes revisited," Phys. Rev. B **65**, 233402 (2002).

[27] K. Kneipp, H. Kneipp, P. Corio, S. D. M. Brown, K. Shafer, J. Motz, L. T. Perelman, E. B. Hanlon, A. Marucci, G. Dresselhaus, M. S. Dresselhaus, "Surface-enhanced and normal Stokes and anti-Stokes Raman spectroscopy of single-walled carbon nanotubes," Phys. Rev. Lett. **84**, 3470 (2000).

[28] R. V. Seidel, A.P. Graham, J. Kretz, B. Rajasezkharan, G. S. Duesberg, M. Liebau, E. Unger, F. Kreupl, W. Hoenlein, "Sub-20 nm short channel carbon nanotube transistors," Nano Lett. **5,** 147 (2005).

[29] K. J. Yi, X. N. He, Y. S. Zhou, W. Xiong , Y. F. Lu , "Tip-Enhanced Near-Field Raman Spectroscopy with a Scanning Tunneling Microscope and Side-Illumination Optics," Rev. Sci. Instrum. **79**, 051807 (2008).

[30] C. Raml, X. N. He, M. Han, D. R. Alexander, Y. F. Lu, "Raman spectroscopy based on a single-crystal sapphire fiber," Opt. Lett. **36**, 1287 (2011).

[31] R. K. Nubling and J. A. Harrington, "Optical properties of single-crystal sapphire fibers," Appl. Opt. **36**, 5934 (1997).

[32] T. T. Basiev, A. A. Sobol, P. G. Zverev, V. V. Osiko, R. C. Powell, "Comparative spontaneous Raman spectroscopy of crystals for Raman lasers," Appl. Opt. **38**, 594 (1999).

[33] B. Ren, G. Picardi, B. Pettinger, "Preparation of gold tips suitable for tip-enhanced Raman spectroscopy and light emission by electrochemical etching," Rev. Sci. Instrum. **75**, 837 (2004).

[34] V. Lehmann, *Electrochemistry of Silicon*, Wiley VCH, Weinheim (2002).

[35] L. Billot, L. Berguiga, M. L. de la Chapellea, Y. Gilbert, R. Bachelot, "Production of gold tips for tip-enhanced near-field optical microscopy and spectroscopy: analysis of the etching parameters," Eur. Phys. J. Appl. Phys. **31**, 139 (2005).

[36] M. S. Dresselhaus and P. C. Eklund, "Phonons in Carbon Nanotubes," Adv. Phys. **49**, 705 (2000).

CHAPTER 4 SURFACE-ENHANCED RAMAN SPECTROSCOPY

4.1 Introduction

SERS [1-3] has rapidly been developed as an effective characterization and analyzing tool in different applications, such as physics, chemistry, surface science, materials science, nanoscience, and life sciences [2, 4-9]. SERS employs localized surface plasmons (LSPs) induced by the incident optical field in metallic nanostructures to drastically increase the Raman signal intensity [10]. Substrates used for SERS have been extensively researched, developed, and analyzed with emphasis on the electromagnetic field enhancement due to LSP resonances related to the highly profiled metallic nanostructure on SERS-active substrates. To reliably control the surface characteristics (such as the size, shape, and materials), SERS substrates have been vastly developed to satisfy requirements from different materials, since the surface characteristics can greatly affect the excitation of the localized surface plasmon resonance. Considerable efforts have been made toward designing and fabricating highly SERS-active substrates using noble metal nanoparticles [11-13]. There are also many other kinds of SERS-active substrates, such as highly roughened metal films or electrodes [14], metallic structures fabricated using techniques based on self-assembly and nanosphere lithography [15], and metallic structures fabricated using standard photolithographic and electron beam lithographic methods [16-18].

In the context of carbon nanotube (CNT) applications, significant effort has been directed toward nanotube functionalization [19]. This can involve a wide range of treatments, typically with a view to the attachment of a species of interest [20] or to the modification of the band structure for electronic device applications [21]. CNTs of different alignments yield applications in different fields [22-28]. Growth of CNTs with

controlled alignments is a key prerequisite for developing CNT-based devices. Extensive investigations have been made on controllable growth of CNTs with different alignments, including template-assisted [27], gas-flow induced [29], fast heating induced [30], and E-field alignments [25].

In this study, we fabricated simple, easy-to-prepare, and large active area SERS substrates. Arrays of vertically aligned multi-walled carbon nanotubes (MWNTs) were used as a framework for a thin Au layer to act as SERS substrates. Although there are a great number of substrates prepared by different fabrication approaches [3,5-8,11-13], there has been no report on Au-coated horizontally aligned CNT (Au-HA-CNT) substrates. Here, we employed laser-assisted chemical vapor deposition (LCVD) to synthesize vertically aligned CNTs (VA-CNTs) and subsequently mechanically press the CNT arrays to form horizontally aligned CNTs (HA-CNTs). It is shown that Au-HA-CNTs are powerful substrates for SERS. This Au-coating treatment may be regarded as an easy-to-prepare, simple, large active area, and cost-effective means of functionalizing MWNTs for SERS applications. R6G molecule was measured using this SERS substrate, and strong enhancement was observed. Biological samples including ^{13}C- and D-labeled long chain fatty acids [31] and Coccomyxa sp. c-169 microalgae cells were also measured to demonstrate the capability of the Au-HA-CNT SERS substrate with limit of detection on nanomolar level. Stable isotope labeled fatty acid sample is one of the most important research topics for monitoring the fatty acid trafficking across the membrane and into downstream metabolic pathways [31]. Rapid composition analysis using Raman scattering can greatly facilitate the selection of suitable algal strains and their associated

growing conditions for different applications, ranging from biofuels to nutritional supplements [32-35].

4.2 Substrate preparation

As shown in Figure 4.1(a), heavily doped Si wafers covered with a 2-μm-thick SiO_2 layer were used as substrates, which were cut into 8×8 mm^2 squares for CNT growth. The substrates were prepared by DC sputtering of iron (Fe) films of 2 nm thickness (Fig. 4.1(b)). The Fe thin film was used as the catalyst for MWNT growth. Growth of MWNTs was carried out in a home-built LCVD chamber [22-24]. A continuous-wave (CW) CO_2 laser (Synrad, firestar v40, wavelength 10.6 μm) was used to irradiate the substrates in Fig. 4.1(c). A gas mixture of acetylene (C_2H_2) and anhydrous ammonia (NH_3) with a volume ratio of 1:10 was introduced into the chamber. NH_3 was used as a buffer gas in the LCVD process to dilute C_2H_2, creating an etching environment to suppress the growth of amorphous carbon, and protecting catalyst particles from being poisoned by amorphous carbon. The reaction pressure was maintained at 10 Torr. The reaction temperature for MWNT growth was controlled at around 550 °C, which is almost 150 °C lower than the reaction temperature required in conventional CVD processes. Then VA-CNT array was prepared on the substrate, as shown in Fig. 4.1(d). For all the VA-CNT substrates, the reaction process lasts for 3 min. As shown in Fig. 4.1(e), the prepared VA-CNT substrates were then mechanically pressed by an aluminum roller with a smooth surface. In Fig. 4.1(f), after pressing, the substrates were sputtered with Au of ~20 nm thick (ATC 2000-F, AJA International, 300 W RF gun at 20% power with Au target deposition rate of ~5 nm/min = 0.85 Å/s). A field-emission scanning

electron microscope (Hitachi S4700 FE-SEM system, maximum resolution of 1.2 nm at 25 kV) was used to observe the prepared substrates.

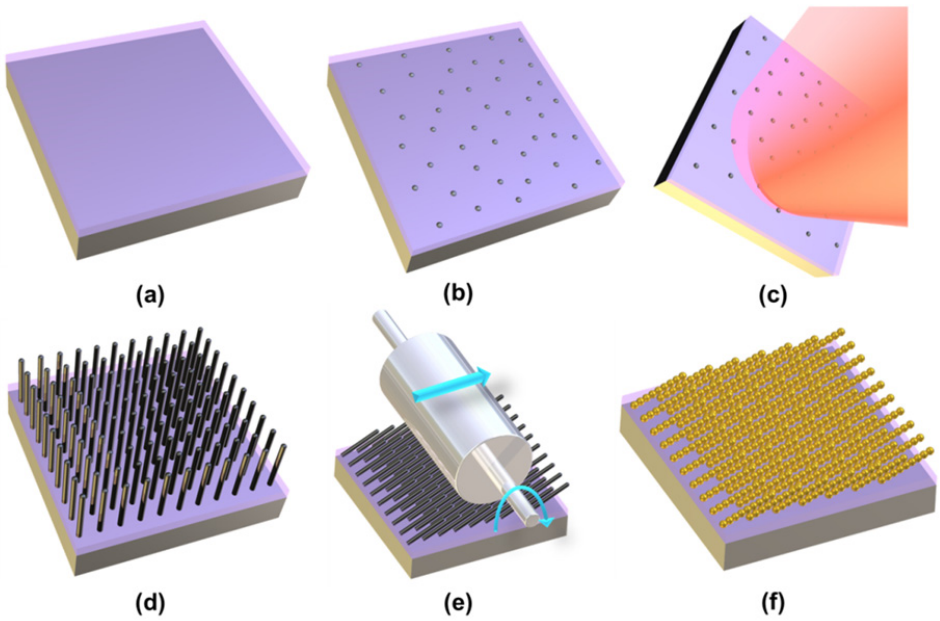

Figure 4.1 Preparation steps for the Au-coated HA-CNTs: (a) Si substrate with a SiO_2 layer on top (SiO_2/Si); (b) 2 nm of iron layer sputtered on the SiO_2/Si substrate; (c) LCVD growth of VA-CNTs on the substrate; (d) VA-CNTs grown on SiO_2/Si; (e) Mechanical press VA-CNTs to form HA-CNTs; (f) Au-coated HA-CNTs.

Rhodamine 6G (R6G, Sigma-Aldrich, R4127, ~95%) was used as the test molecule in the SERS study. The R6G has a formula of $C_{28}H_{31}N_2O_3Cl$ with a molecular weight of 479.01. The Au-HA-CNT substrate was incubated in 5 ml of R6G 10^{-6} M solution for 24 hours to realize an even deposition of R6G molecules. Raman spectra were recorded with a Renishaw Raman microscope (Renishaw inVia, excitation wavelength of 514.5 nm) using a 50× objective with a numerical aperture of 0.75 (Leica N PLAN EPI 50×/0.75). The laser power incident on the sample surface was typically in a range of 0.5-1 mW. OptiFDTD simulation software from Optiwave Systems Inc. was used for the simulation study.

Biological samples were also measured using the Au-HA-CNT substrate for SERS. Firstly, we carried out SERS on stable isotope labeled fatty acids, including ^{13}C- and D-labeled. ^{13}C-labeled [U-13C] C18:1 fatty acid (C-801, Medical Isotope, Inc.) and D-labeled [D_{47}] C24:0 fatty acid (D-3901, C/D/N isotopes, Inc). The fatty acids were diluted in ethanol solution with different concentrations from 1 μM to 10 nM. Droplets of the solutions were dropped onto the SERS substrate and then dried for 30 minutes. The algal strain used is Coccomyxa sp (strain C169), grown under nitrogen different depletion conditions to promote triglyceride (TAG) (oil) accumulation.

In this study, HA-CNTs were used as a framework for a thin Au overlayer to act as an SERS substrate. This Au coating serves as a simple, convenient, and cost-effective way to functionalize MWNTs for SERS enhancement. Granular-shaped nanowires formed after DC sputtering of Au layer on prepared MWNTs. Figure 4.2(a) is a typical SEM image of a well aligned Au-VA-CNT array prepared using the LCVD method. After mechanical pressing, the VA-CNTs become HA-CNTs. After sputtering, the Au-HA-CNT substrate is prepared, as shown in Fig. 4.2(b). The further magnified Au-VA-CNTs and Au-HA-CNTs are shown in the insets of Figs. 4.2(a) and (b), respectively. After Au sputtering deposition, both VA-CNTs and HA-CNTs become granular nanowires. For the substrate investigated in detail here, the average length and diameter of the Au-coated MWNTs (or gold nanowires) are 30 μm and 50 nm, respectively, as observed from the SEM images (Figure 4.2). The uncoated MWNTs have an average diameter of 10 nm (not shown). A feature of critical importance is that the Au coating of the nanowires is highly granular in nature. Given this structure, this study was to explore,

by a combination of experiment and modeling, how SERS enhancement are related to the angle between the laser polarization and the CNT orientation.

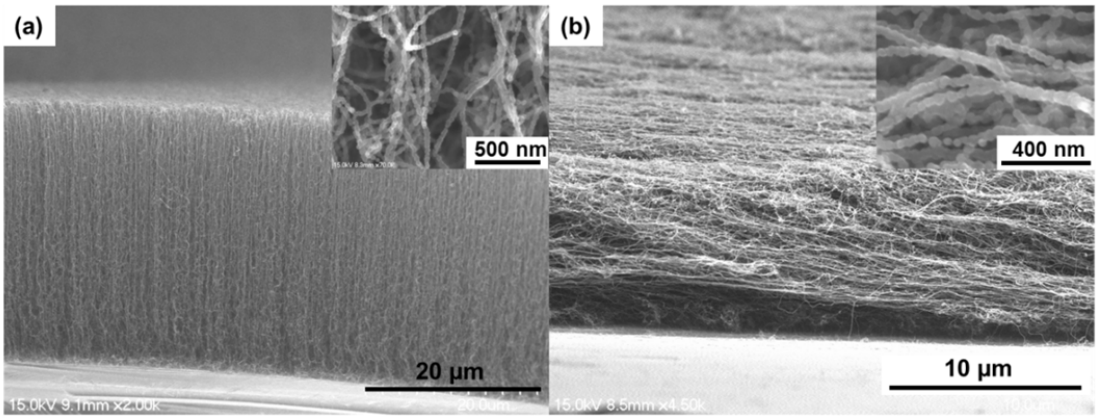

Figure 4.2 SEM images of (a) an Au-VA-CNT sample with low magnification (Inset: the same Au-VA-CNT sample with high magnification) and (b) an Au-HA-CNT sample with low magnification (Inset: the Au-HA-CNT substrate with high magnification).

4.3 SERS performance of the Au-HA-CNT substrate

Raman spectra of R6G molecules acquired from the Au-HA-CNT substrate exhibit strong lines at 611, 773, 1127, 1183, 1310, 1360, 1507, 1573, and 1648 cm^{-1}, as shown in Table 4.1. 611 cm^{-1} is C-C-C ring in-plane bending vibration. 773 cm^{-1} is C-H out-of-plane bending vibration. 1127 cm^{-1} is C-H in-plane bending vibration. Peaks at 1310, 1360, 1507, 1573, and 1648 cm^{-1} are assigned to the aromatic stretching vibrations [36].

Table 4.1 Assignment of Raman bands in SERS spectra of R6G.

Raman shift (cm^{-1})	Assignment	Raman shift (cm^{-1})	Assignment
611	C-C-C ring in-plane bending	1310	Aromatic C-C stretching
659		1360	Aromatic C-C stretching
773	C-H out-of-plane bending	1420	
1088		1507	Aromatic C-C stretching
1127	C-H in-plane bending	1573	Aromatic C-C stretching
1183		1595	
1276	C-O-C stretching	1648	Aromatic C-C stretching

Each of the Raman spectra was corrected by subtracting a six-order polynomial fitting curve of fluorescence backgrounds, which was done using a software named WiRE 3.2 from Renishaw. From Fig. 4.3 (pink short dash dot line), we cannot see any signal from R6G (almost a flat line) when using HA-CNT substrate without gold coating. There are two weak and broad bands centered at 1340 and 1570 cm^{-1}, which are D- and G-bands of CNTs, respectively. As another comparison, we also placed R6G on a flat SiO_2/Si substrate surface, and no apparent peaks are found except the Si peak at 520 cm^{-1}. When the R6G molecules are placed onto an Au-coated SiO_2/Si surface, the Raman signal of R6G is improved and we can see some of the Raman peaks of R6G from the spectrum. The Au-HV-CNT substrate enhances the Raman signal of R6G significantly to the extent that all the reported peaks of R6G are observed through the spectra with high intensity. There is no Si peak at 520 cm^{-1} because the HA-CNT layers are sufficiently thick to block the beam from reaching the SiO_2/Si substrate surface.

The diameter of the focal spot was estimated to be 0.837 μm using the equation below [37]

$$D = \frac{1.22\lambda}{NA}, \tag{4.1}$$

where D is the diameter of the objective focal spot, λ is the excitation wavelength used for Raman measurements, and NA is the numerical aperture of the objective lens.

The absolute EFs have been further evaluated. When the intensities are normalized for the laser power, acquisition time, and detector sensitivity under the same collection conditions, the EF is given by [38]

$$EF = \frac{I_{surf}}{I_{vol}} \frac{N_{vol}}{N_{surf}}, \tag{4.2}$$

where I_{vol} and I_{surf} are the conventional Raman (not enhanced) and SERS intensities and N_{vol} and N_{surf} represent the number of molecules detected in the bulk sample (SiO_2/Si flat surface) and on the SERS-active substrate, respectively.

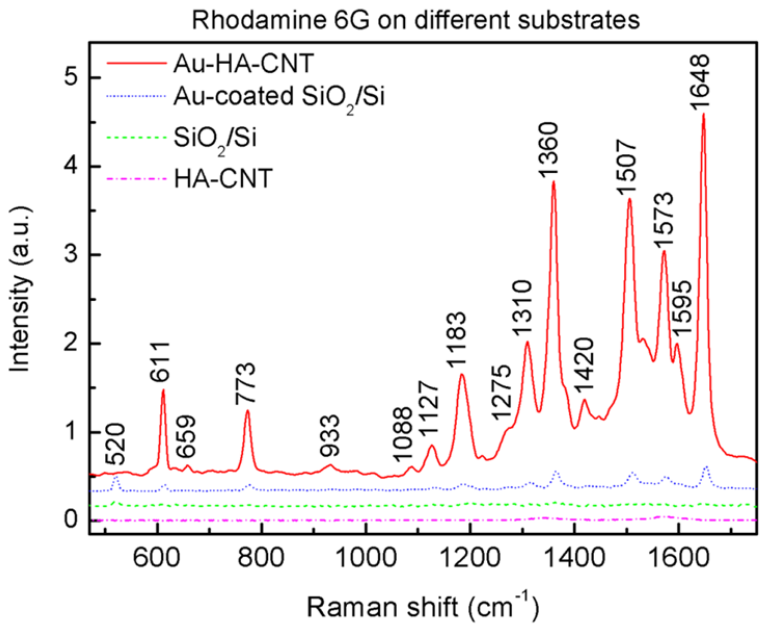

Figure 4.3 Raman spectra of rhodamine 6G molecules on different substrates: Au-HA-CNTs (red solid); Au-coated SiO_2/Si (blue shot dot); SiO_2/Si with no coating (green short dash); HA-CNTs with no coating (pink short dash dot).

The focus spot size of the objective and the density of the Au granular nanowire determine the number of gold nanoparticles in the measured area. Supposing that a single molecule should not take more than 4 nm^2 in area in the densely packed R6G monolayer, the number of molecules adsorbed per nanoparticle can be calculated. This number and the total number of Au nanoparticles in the focal spot area determine the total number of adsorbed molecules that can contribute to the SERS signal (N_{surf}) (averaged gold nanoparticle number in the illuminated area). In the conventional Raman spectroscopy,

the excitation volume is considered a focal tube with a waist diameter of 0.837 μm and a depth of ~15 μm. From the density of the bulk sample (ρ = 1.26 g/cm^3), the number of molecules contributing to the Raman intensity (N_{vol}) can be determined. When the SERS spectrum of the R6G molecules are adsorbed on a 20 nm flat Au film, very small SERS signal is obtained. This proves that the obtained enhancement is not due to the nanocluster (gold thin film on flat SiO_2/Si surface) surface roughness. Moreover, it becomes obvious that the SERS enhancement is mostly due to the granular nanowires.

Theoretical simulations have shown that exceptionally large EM field enhancements occur at specific locations (corners among Au particles). According to these findings, we estimated that huge EM fields are located on approximately 10% from the corner area. Extrapolating this percentage to the entire nanoparticle exposed area, we evaluated the effective SERS active areas of the Au nanoclusters and further calculated the absolute EF values. The N_{vol} and N_{surf} obtained values along with the intensities of the 1648 cm^{-1} band were substituted in Eq. (4.2). It was found that the substrates exhibit an EF in the order of 10^7. The nanoparticles with 50 nm diameter provided an enhancement of 5×10^7, while the EF value of the Ag nanoclusters with 20 nm height was calculated to be 1×10^3. The EF lay in the range of 10^3 with reference to the case of a droplet of 10^{-6} M solution of R6G on a flat Au substrate. This value took into account an areal enhancement of 10^4 of the structured substrate relative to the planar Au substrate. However, the source of the SERS signal was not evenly distributed.

From Fig. 4.4, the highest EF reaches ~5×10^7 when the polarization direction of the incident laser beam is parallel to the HA-CNT orientation. The EF reaches its minimum of ~1×10^7, when the laser polarization and the HA-CNTs are perpendicular to

each other. This can be explained that the E-field of the incident beam is further enhanced at the localized area in the corner between two Au nanoparticles on a granular Au nanowire. The error bar on the plot is large due to the randomness of Raman scattering on this kind of SERS substrates. However, after many data acquisition at different spots on the samples with spectra averaging, the polarization dependence can be seen clearly. The polarization dependence of the SERS enhancement was investigated using a precise rotating stage for rotating the sample with varying angles for polarization measurements.

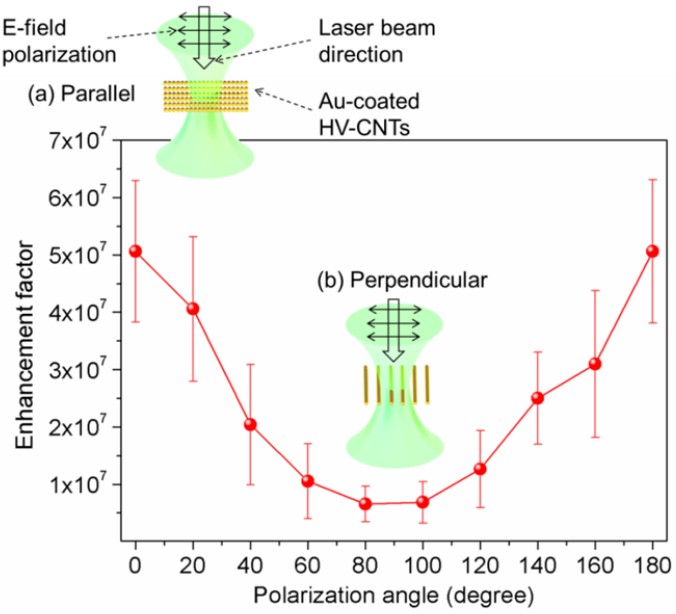

Figure 4.4 EF of the Raman intensity of R6G molecules on Au-HA-CNT sample as a function of the angle between the laser polarization and the CNT orientation.

The EF changed according to different angle of the sample relative to the polarization of the incident beam. The EF reached its maximum when the polarization direction of the laser beam was parallel to the alignment direction of Au-HA-CNTs, which can be explained using following simulation results. Within each point, 30 SERS spectra were averaged for each angle for better accuracy. R6G on the Au-VA-CNT

substrate was also measured, and SERS can also be found (not shown), but not as high as HA-CNT substrate when the polarization of the incident beam was parallel to CNT direction. There was no polarization effect when using Au-VA-CNTs in this study.

Different approaches have been used to perform the simulation in SERS studies by researchers [39,40]. In this study, the FDTD algorithm in conjunction with the Lorentz–Drude model under the perfectly matched layer boundary conditions was used to simulate the optical fields. The nanoparticles were simulated as pure Au particles. As shown in Fig. 4.5, rectangular-shaped continuous wave laser with a wavelength of 514.5 nm propagating along the *k* direction was input into the structure from bottom with its polarization direction perpendicular to *k*, and parallel to the granular nanowire. The magnitude of the E-field of the beam was assumed to be 1 V/m. The uniform mesh step for each axis was 0.2 nm. Figures 4.5(a) and (b) show the E-field distribution in a two-dimensional view. It can be observed that the E-field is locally enhanced 1000 times around the single nanoparticle with a diameter of 50 nm. While an enhancement of 2500 is found when the nanoparticles are aligned in a continuous line, the highest enhancement is located at the corner between two nanoparticles. Such modeling of the electromagnetic response should take into account the granular nature of the Au nanowire surface. The granular nanowires can enhance the E-field within the corner when the polarization is parallel to the CNTs.

The single Au nanoparticle model is used to simulate the condition when the laser polarization is perpendicular to the CNT orientation, serving as a comparison with the enhancement in the corner of the granular nanowires. The E-field in the corner is 2.5 times larger than the enhanced field with single particle only. Raman scattering

approximately scales as E^4 [1]. Therefore, Raman intensity enhancement should be ~40 times larger than single particle only, however, the experiment results only show 5 times higher enhancement. This is due to the random growth and pressing processes of CNTs on the HA-CNT substrate, which affect the distribution of the CNTs. Not all of the CNTs align in the same direction, which leads the lower enhancement. Another factor that reduces the EF is the unevenness of the Au coating. Not all of the coating is distributed evenly with the same diameter. Simulation of locally enhanced E-fields within the corner between Au coating particles provides insight into the mechanisms behind the enhancement as well as information on how to optimize the enhancement by coordinating relevant factors, such as deposition thickness, pressing force, excitation wavelength, incident angle, and polarization direction.

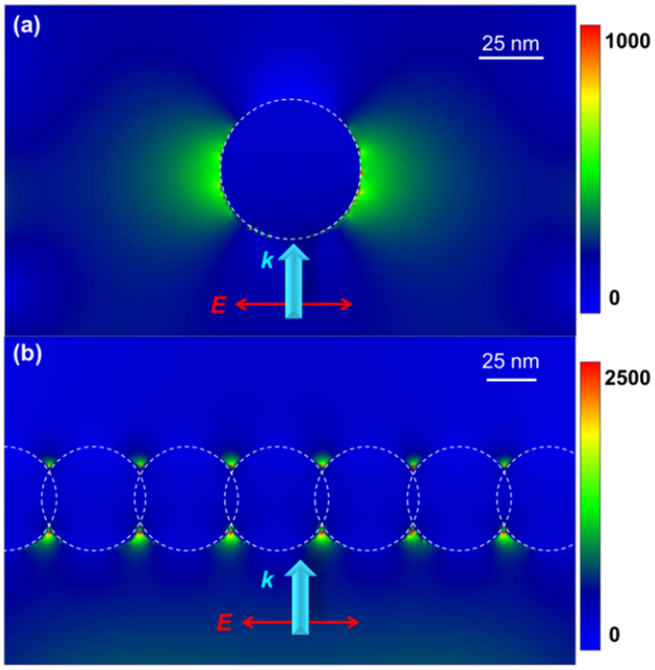

Figure 4.5 Simulation results of (a) a single 50-nm diameter Au particle and (b) a row of 50-nm diameter Au particles. The E-field polarizations of the incident beams are shown with double sided arrows. The propagation directions of the incident beam are showing by wide arrows labeled *k* (*k* vector).

As shown in Fig. 4.6(a) and (c), the Raman spectra of D-labeled [D_{47}] C24:0 and ^{13}C-labeled [U-^{13}C] C18:1 fatty acids are shown on different substrates. Strong enhancement is shown on Au-HA-CNT substrate compared to gold-coated silicon substrate. The fatty acids diluted in ethanol solution with a concentration of 1 μM were dropped onto the SERS substrate and then dried out. In Figs. 4.6(b) and (d), the Raman signal changes for [D_{47}] C24:0 and [U-^{13}C] C18:1 fatty acids as a function of concentration (ranging from 10-1000 and 20-1000 nM, respectively) are plotted. The insets of Figs. 4.6(a) and (c) are the molecule structures. Deuterium has been a label in the structure of C24:0, but the ^{13}C is not labeled in the structure due to limited space in the diagram (all of the C atoms in the structure are ^{13}C). Through the plots, we can estimate the limit of detections (LODs) of [D_{47}] C24:0 and [U-^{13}C] C18:1 are ~10 and ~20 nM, respectively.

LODs have also been evaluated using the 3σ-International Union of Pure and Applied Chemistry (IUPAC) criteria [41,42]. According to the 3σ-IUPAC definition, the LOD for a given element is the concentration that produces a net line intensity proportional to three times the standard deviation of the background, σ_B:

$$LOD = 3\frac{\sigma_B}{S}, \tag{4.3}$$

where S is the slope of the linear fit. Linear fit was calculated with ORIGIN 7.5.

The Raman peak shifted when the fatty acids were isotope labeled, in which the most obvious peak shift appears in D-labeled fatty acid. In Fig. 4.6(a), the peak at 2100 cm^{-1} (-CD_2) is shifted from the peak at ~ 2850 cm^{-1} (-CH_2) [45]. The peaks at 988 and 1144 cm^{-1} are shifted peaks from the lipid peaks shown in Table 4.2. The peak shift due

to ^{13}C labeling is much less than that of D-labeling. In Fig. 4.6(c), the peak at 1597 cm^{-1} is shifted from 1650 cm^{-1} (Table 4.2). The Raman peak of CH_2 bending at 1440 cm^{-1} has not shifted much in our measurement.

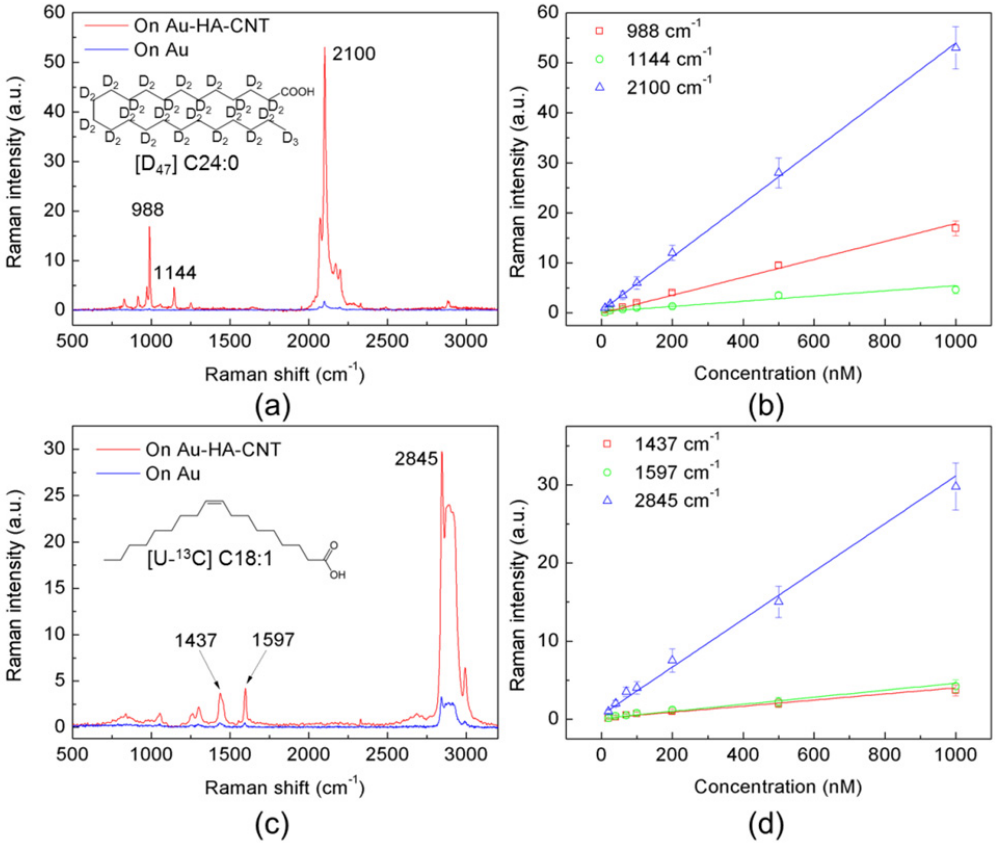

Figure 4.6 (a) Surface-enhanced Raman spectrum of [D_{47}] C24:0 fatty acid using Au-HA-CNT substrate (red curve), and Raman spectrum of [D_{47}] C24:0 fatty acid taken on Au-coated silicon substrate; (b) Raman signal changes for [D_{47}] C24:0 fatty acid concentrations of 10-1000 nM at three different Raman peaks (988, 1144, and 2100 cm^{-1}), and the linear fits of each Raman intensity change; (c) Surface-enhanced Raman spectrum of [U-^{13}C] C18:1 fatty acid using Au-HA-CNT substrate (red curve), and Raman spectrum of [U-^{13}C] C18:1 fatty acid taken on Au-coated silicon substrate; (b) Raman signal changes for [U-^{13}C] C18:1 fatty acid concentrations of 20-1000 nM at three different Raman peaks (1437, 1597, and 2197 cm^{-1}), and the linear fits of each Raman intensity change.

Surface-enhanced Raman spectrum (red curve) of Coccomyxa sp. c-169 microalgae cells is demonstrated in Fig. 4.7(a). The cells were grown in a nitrogen-depleted environment for triglyceride (TAG), one kind of lipid, generation for biofuel

research. As shown in Fig. 4.7(b), a transmission bright field microscopy image shows the microalgae cells with an average size of ~5 μm. The black dots in some of the cells are TAG droplets. The cell measured is in the early stage of N-depletion environment, and therefore, there are very strong carotenoid Raman peaks at 1004, 1160, and 1520 cm^{-1}. However, with the Au-HA-CNT substrate, we can observe enhanced Raman peaks at 1260 and 1440 cm^{-1} (as indicated using red arrows), which are assigned to lipid signals, that is, very small amount of TAG has formed but can only be detected after signal enhancement using the SERS substrate. Therefore, this substrate is ideal for measurement of cell components with high enhancement factor and large active area.

Table 4.2 Assignment of Raman bands in Raman spectra of fatty acids and microalgae cells [43,44].

Raman peaks (cm^{-1})	Components	Peak assignment
1004	Carotenoid	Carotene C-H bend
1056,1116	Lipid	Alkyl C-C trans and gauche stretches
1075	Lipid	Alkyl C-C gauche stretches
1160	Carotenoid	Carotene C-H stretches
1260	Lipid	Alkyl =C-H cis stretches
1300	Lipid	Alkyl C-H_2 twist
1440	Lipid	Alkyl C-H_2 bend
1520-1538	Carotenoid	Carotene C=C stretches
1650	Lipid	Alkyl C=C stretches
~2800-3000	Lipid, carbonhydrate	CH_2 symmetric and asymmetric stretches
3023	Lipid	Alkyl =C-H stretches

Figures 4.8 and 4.9 are the Raman spectra of unlabeled and D-labeled C24:0, and the unlabeled and ^{13}C-labeled C18:1 dried out on 100-nm gold-coated Si substrates. The spectra are demonstrated to give a comparison between the labeled and unlabeled fatty acids. The laser power used for acquiring these spectra is much higher than the SERS experiment (>20 mW).

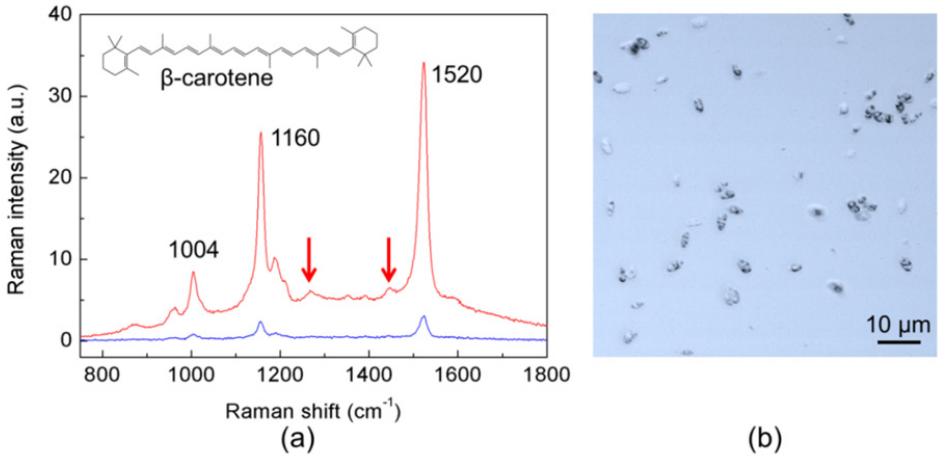

Figure 4.7 (a) Raman spectrum of Coccomyxa sp. c-169 microalgae cells (red curve) on an Au-HA-CNT substrate, and on gold-coated silicon substrate (blue curve); (b) Transmission bright field microscopy image the Coccomyxa sp. c-169 microalgae cells.

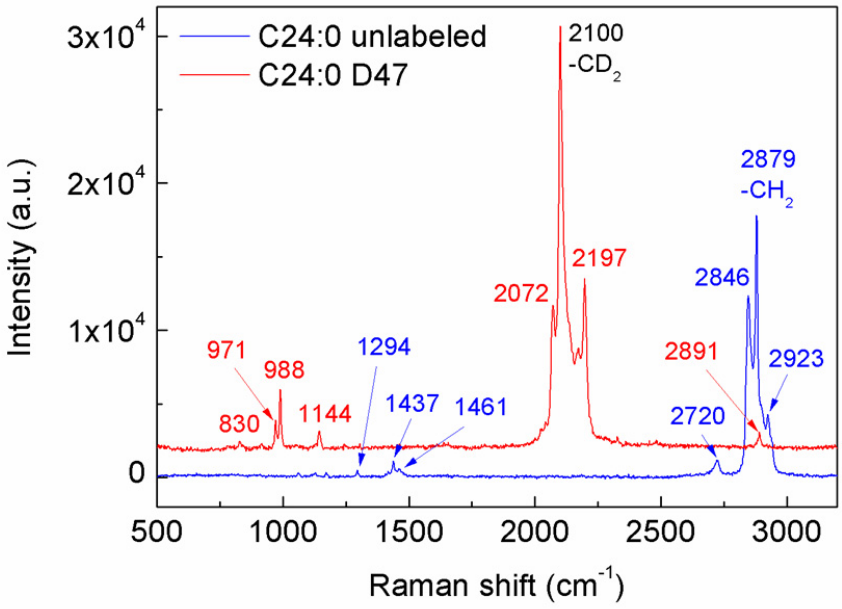

Figure 4.8 Raman spectra of 1 mM solution of the unlabeled and D-labeled C24:0 D47 dried out on 100-nm gold-coated Si substrates.

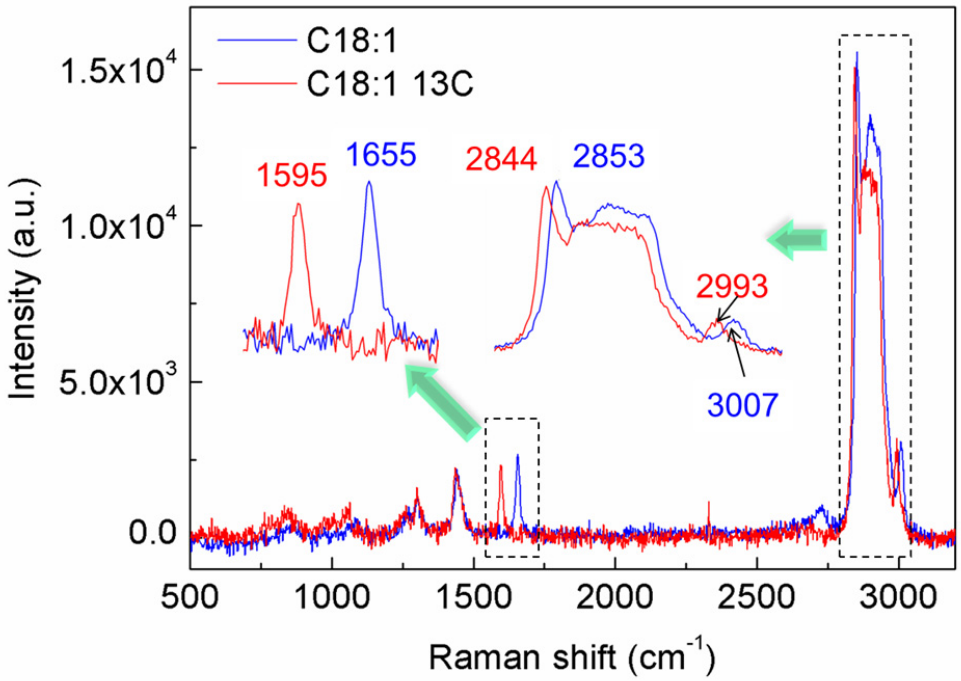

Figure 4.9 Raman spectra of 1 mM solution of the unlabeled and ^{13}C-labeled C18:1 dried out on 100-nm gold-coated Si substrates.

4.4 Conclusions

In conclusion, SERS substrates with high EFs and simple preparation steps were fabricated for SERS measurements. SERS EFs as high as 5×10^7 were achieved for R6G molecules on Au- HA-CNT substrates. EF varies with the relative direction of the CNTs to the polarization direction of the incident laser beam. When the direction of the CNTs is parallel to the polarization of the incident beam, the EF reaches its maximum. The EF decreases to its minimum when the alignment direction of the CNTs is perpendicular to the E-field of the incident beam. Simulations using the 2D FDTD method were carried out to explain the experimental results. The simulation results closely agree with the experimental results. Biological samples, including [D_{47}] C24:0 and [U-^{13}C] C18:1 fatty

acids and Coccomyxa sp. c-169 microalgae cells, were also measured using the SERS substrate. The limit of detection (LODs) of D- and ^{13}C-labeled fatty acids on the SERS substrate were measured to be around 10 and 20 nM, respectively. Significantly enhanced Raman signal of carotene and TAG in the microalgae cells was acquired using the SERS substrate.

Table 4.3 Summary of SERS techniques.

Surface-enhanced Raman spectroscopy (SERS)	
Realization approaches	Nanostructured metallic surfaces, such as gold, silver, and copper
Principle	Detection of molecular or crystal lattice vibrational states using excited localized surface plasmons among metallic nano-surfaces
Combination possibility	SERS can be combined with TERS or CARS. Surface- and tip-enhancement can be combined for higher signal. Surface-enhanced CARS has also been reported very recently.
Resolution	Depending on the uniformity and size of the metallic nanosurfaces
Application	Spectroscopy and imaging of nanostructures or very thin films, such as graphene, thin polymer film, and single molecules, and small biomolecules
Enhancement factor (EF)	Peak intensity enhancement >10 times. Calculated EF of substrates in this study is 10^7 (highest reported EF is ~ 10^{14}).

4.5 References

[1] M. Moskovits, "Surface-enhanced spectroscopy," Rev. Mod. Phys. **57**, 783 (1985).

[2] K. Kneipp, M. Moskovits, H. Kneipp, Eds. *Surface-Enhanced Raman Scattering: Physics and Applications* (Springer-Verlag: Berlin, Heidelberg, 2006).

[3] S. Nie and S. R. Emory, "Probing single molecules and single nanoparticles by surface-enhanced Raman scattering," Science **275**, 1102 (1997).

[4] A. Campion and P. Kambhampati, "Surface-enhanced Raman scattering," Chem. Soc. Rev. **27**, 241 (1998).

[5] K. Kneipp, H. Kneipp, I. Itzkan, R. R. Dasari, M. S. Feld, "Surface-enhanced Raman scattering: a new tool for biomedical spectroscopy," Curr. Sci. **77**, 915 (1999).

[6] D. A. Stuart, C. R. Yonzon, X.Y. Zhang, O. Lyandres, N.C. Shah, M. R. Glucksberg, J. T. Walsh, R. P. Van Duyne, "Glucose sensing using near-infrared surface-enhanced Raman spectroscopy: gold surfaces, 10-day stability, and improved accuracy," Anal. Chem. **77**, 4013 (2005).

[7] G. Braun, S. J. Lee, M. Dante, T. Q. Nguyen, M. Moskovits, N. Reich, "Surface-enhanced Raman spectroscopy for DNA detection by nanoparticle assembly onto smooth metal films," J. Am. Chem. Soc. **129**, 6378 (2007).

[8] R. Aroca, *Surface-Enhanced Vibrational Spectroscopy*, John Wiley & Sons, Ltd (2007).

[9] K. A. Willets and R. P. Van Duyne, "Localized surface plasmon resonance spectroscopy and sensing," Annu. Rev. Phys. Chem. **58**, 267 (2007).

[10] S. J. Lee, Z. Q. Guan, H. X. Xu, M. Moskovits, "Surface-enhanced Raman spectroscopy and nanogeometry: the plasmonic origin of SERS," J. Phys. Chem. C **111**, 17985 (2007).

[11] M. Moskovits and D. H. Jeong, "Engineering nanostructures for giant optical fields," Chem. Phys. Lett. **397**, 91 (2004).

[12] N. Felidj, J. Aubard, G. Levi, J. R. Krenn, A. Hohenau, G. Schider, A. Leitner, F. R. Aussenegg, "Optimized surface-enhanced Raman scattering on gold nanoparticle arrays," Appl. Phys. Lett. **82**, 3095 (2003).

[13] A. M. Schwartzberg, C. D. Grant, A. Wolcott, C. E. Talley, T. R. Huser, R. Bogomolni, J. Z. Zhang, "Unique gold nanoparticle aggregates as a highly active surface-enhanced Raman scattering substrate," J. Phys. Chem. B **108**, 19191 (2004).

[14] P. Dawson, K. B. Alexander, J. R. Thompson, J. W. Haas, T. L. Ferrell, "Influence of metal grain size on surface-enhanced Raman scattering," Phys. Rev. B **44**, 6372 (1991).

[15] Y. Fang, N. H. Seong, D. D. Dlott, "Measurement of the distribution of site enhancements in surface-enhanced Raman scattering," Science **321**, 388 (2008).

[16] G. Laurent, N. Félidj, J. Aubard, G. Lévi, J. R. Krenn, A. Hohenau, G. Schider, A. Leitner, F. R. Aussenegg, "Evidence of multipolar excitations in surface enhanced Raman scattering," Phys. Rev. B **71**, 045430 (2005).

[17] C. J. Orendorff, L. Gearheart, N. R. Jana, C. J. Murphy, "Aspect ratio dependence on surface enhanced Raman scattering using silver and gold nanorod substrates," Phys. Chem. Chem. Phys. **8**, 165 (2006).

[18] G. H. Gu, J. Kim, L. Kim, J. S. Suh, "Optimum length of silver nanorods for fabrication of hot spots," J. Phys. Chem. C **111**, 7906 (2007).

[19] K. Balasubramanian and M. Burghard, "Chemically functionalized carbon nanotubes," Small **1**, 180 (2005).

[20] T. Ramanathan, F. T. Fisher, R. S. Ruoff, L. C. Brinson, "Amino-functionalized carbon nanotubes for binding to polymers and biological systems," Chem. Mater. **17**, 1290 (2005).

[21] J. J. Zhao, H. K. Park, J. Han, J. P. Lu, "Electronic properties of carbon nanotubes with covalent sidewall functionalization," J. Phys. Chem. B **108**, 4227 (2004).

[22] J. Shi, Y. F. Lu, K. J. Yi, Y. S. Lin, S. H. Liou, J. B. Hou, and X. W. Wang, "Direct synthesis of single-walled carbon nanotubes bridging metal electrodes by laser-assisted chemical vapor deposition," Appl. Phys. Lett. **89**, 083105 (2006).

[23] W. Xiong, Y. S. Zhou, M. Mahjouri-Samani, W. Q. Yang, K. J. Yi, X. N. He, S. H. Liou, Y. F. Lu, "Self-aligned growth of single-walled carbon nanotubes using optical near-field effects," Nanotechnology **20**, 025601 (2009).

[24] Y. Gao, Y. S. Zhou, W. Xiong, M. Mahjouri-Samani, M. Mitchell, Y. F. Lu, "Controlled growth of carbon nanotubes on electrodes under different bias polarity," Appl. Phys. Lett. **95**, 143117 (2009).

[25] Y. G. Zhang, A. Chang, J. Cao, Q. Wang, W. Kim, Y. M. Li, N. Morris, E. Yenilmez, J. Kong, H. J. Dai, "Electric-field-directed growth of aligned single-walled carbon nanotubes," Appl. Phys. Lett. **79**, 3155 (2001).

[26] C. J. Lee, D. W. Kim, T. J. Lee, Y. C. Choi, Y. S. Park, Y. H. Lee, W. B. Choi, N. S. Lee, G. S. Park, J. M. Kim, "Synthesis of aligned carbon nanotubes using thermal chemical vapor deposition," Chem. Phys. Lett. **312**, 461 (1999).

[27] S. Fan, M. G. Chapline, N. R. Franklin, T. W. Tombler, A. M. Cassell, H. Dai, "Self-oriented regular arrays of carbon nanotubes and their field emission properties," Science **283**, 512 (1999).

[28] G. L. Che, B. B. Lakshmi, E. R. Fisher, C. R. Martin, "Carbon nanotubule membranes for electrochemical energy storage and production," Nature **393**, 346 (1998).

[29] Y. T. Liu, X. M. Xie, Y. F. Gao, Q. P. Feng, L. R. Guo, X. H. Wang, X. Y. Ye, "Gas flow directed assembly of carbon nanotubes into horizontal arrays," Mater. Lett. **61**, 334 (2007).

[30] S. M. Huang, M. Woodson, R. Smalley, J. Liu, "Growth mechanism of oriented long single walled carbon nanotubes using "fast-heating" chemical vapor deposition process," Nano Lett. **4**, 1025 (2004).

[31] E. M. Melton, R. L. Cerny, P. A. Watkins, C. C. DiRusso, P. N. Black, "Human fatty acid transport protein 2a/very long chain acyl-CoA synthetase 1 (FATP2a/Acsvl1) has a preference in mediating the channeling of exogenous n-3 fatty acids into phosphatidylinositol," J. Biol. Chem. **286**, 30670 (2011).

[32] A. Demirbas, "Importance of biodiesel as transportation fuel," Energy Policy **35**, 4661 (2007).

[33] R. J. Radmer and B. C. Parker, "Commercial applications of algae: Opportunities and constraints," J. Appl. Phycol. **6**, 93 (1994).

[34] J. Sheehan, T. Dunahay, R. Benemann, G. Roessler, C. Weissman, "A look back at the U.S. department of energy's aquatic species program biodiesel from algae," NREL **580**, 24190 (1998).

[35] G. A. Thompson, Jr., "Lipids and membrane function in green algae," Biochim. Biophys. Acta **1302**, 17 (1996).

[36] P. Hildebrandt and M. Stockburger, "Surface-enhanced resonance Raman spectroscopy of rhodamine 6G adsorbed on colloidal silver," J. Phys. Chem. **88**, 5935 (1984).

[37] J. M. Cowley, *Diffraction physics* (North-Holland, Amsterdam, 1975).

[38] M. Baia, L. Baia, S. Astilean, J. Popp, Surface-enhanced Raman scattering efficiency of truncated tetrahedral Ag nanoparticle arrays mediated by electromagnetic couplings, Appl. Phys. Lett. **88**, 143121 (2006).

[39] P. Kambhampati, C. M. Child, M. C. Foster, A. Campion, "On the chemical mechanism of surface enhanced Raman scattering: Experiment and theory," J. Chem. Phys. **108**, 5013 (1998).

[40] M. Micic, N. Klymyshyn, Y. D. Suh, H. P. Lu, "Finite element method simulation of the field distribution for AFM tip-enhanced surface-enhanced Raman scanning microscopy," J. Phys. Chem. B **107**, 1574 (2003).

[41] D. -K. Lim, K. -S. Jeon, J. -H. Hwang, H. Kim, S. Kwon, Y. D. Suh, J. -M. Nam, "Highly uniform and reproducible surface-enhanced Raman scattering from DNA-tailorable nanoparticles with 1-nm interior gap," Nat. Nanotechnol. **6**, 452 (2011).

[42] X. N. He, Z. Q. Xie, Y. Gao, W. Hu, L. B. Guo, L. Jiang, Y. F. Lu, "Mass spectrometry of solid samples in open air using combined laser ionization and

ambient metastable ionization," Spectrochimica. Acta Part B: Atomic Spectroscopy **67**, 64 (2012).

[43] H. Wu, J. V. Volponi, A. E. Oliver, A. N. Parikh, B. A. Simmons, S. Singh, "In vivo lipidomics using single-cell Raman spectroscopy," Proc. Natl. Acad. Sci. **108**, 3809 (2011).

[44] Z. Movasaghi, S. Rehman, I. Rehman, "Raman spectroscopy of biological tissues," Appl. Spectrosc. Rev. **42**(5), 493 (2007)

[45] X. S. Xie, J. Yu, W. Y. Yang, "Living cells as test tubes," Science 312, 228 (2006).

CHAPTER 5 COHERENT ANTI-STOKES RAMAN SPECTROSCOPY AND MICROSCOPY

5.1 Introduction

Since Raman scattering signal is very weak (typical photon conversion efficiencies for Raman are lower than 1 in 10^7), Raman microscopy imaging requires high laser powers and long integration times of 100 ms to 1 s per pixel [1]. This drawback severely blocked the application of Raman microscopy to the study of living systems. CARS, based on nonlinear (four-wave mixing) optical effect, has much stronger Raman signals (anti-Stokes) [2], first reported in 1965 by Maker and Terhune [3] as a method of spectroscopy for chemical analysis. The energy diagram of the process is depicted in Fig. 2.4(a). CARS involves the interaction of four waves designated as pump (p), Stokes (s), probe (p') and anti-Stokes (CARS) where pump and probe are usually fixed to the same frequency ($\omega_p = \omega_{p'}$). When we match the beat frequency between the pump and Stokes beams with the vibrational frequency Ω_R of the molecules in the sample, a resonant enhancement of the third-order nonlinear optical process occurs to greatly promote the sensitivity with chemical selectivity. The information acquired from CARS (anti-Stokes Raman) is the same as that from Raman spectroscopy (Stokes Raman) due to the intrinsic same Raman scattering effect. The major difference between CARS and spontaneous Raman is that CARS is a four-wave mixing process, which needs two coherent laser beam with different wavelength. The sensitivity of CARS is also much higher than Raman by several orders of magnitude.

CARS [4,5] is much more efficient than spontaneous Raman spectroscopy [6-8], enabling faster, more sensitive analyses with less photoexposure. CARS circumvents the need for extrinsic labels, allowing observation of dynamic phenomena for which tags are not available. CARS also enables detection in the presence of one-photon fluorescence,

3-D sectioning, penetrating to a depth of ~0.4 mm while minimizing photodamages [9-11]. CARS microscopy has been utilized to image living cells with the Raman signals from different vibrational modes, such as the amide I vibration from protein, OH stretching from water, the phosphate stretch from DNA, and the CH group of stretching from lipids [2,12-15]. There are also many other examples, such as single phospholipid bilayers visualization [16], the trafficking and growth of lipid droplets [17], intracellular water diffusion, and biomedical imaging of tissues *in vivo* [11]. CARS also has been used for two-photon polymerization [18-20] and carbon nanotubes [21] characterization. In this study, we focused on the broadband CARS approach, as illustrated in Fig. 2.4(b), was first proposed by Akhmanov *et al* [22].

CARS spectroscopy can be realized when the scattering signals are recorded on a spectrometer. For narrow bandwidth pump and Stokes sources [25-26], the wavelength of the Stokes beam can be scanned to get a CARS spectrum (intensity versus Raman shift), which is time consuming and makes it difficult to follow dynamics in a biological structure. However, single-shot CARS spectrum can be achieved with very broad Stokes beam. The broad Stokes beam in collinear alignment with narrower pump beam will excite a wide range of Raman transitions [23]. Since the Stokes shifts in the range of 500-4000 cm^{-1} are known as the finger print region, it is desirable to have a Stokes beam with a broad spectrum to cover this broad spectrum for a fast spectrum generation. A potential method is to employ a supercontinuum (SC) source for the generation of laser pulses with 4000-cm^{-1} bandwidth [24], which is not possible (too wide) for femtosecond pulses. Significant advances in the development and fabrication of photonic crystal fibers (PCF) facilitated the use of PCF as a stable and reliable solution for supercontinuum generation,

since an input of a few tens of mW from an fs oscillator is sufficient. Therefore, broadband CARS (B-CARS) [25,27,28] that uses an fs pump beam (ω_p) and a super-continuum Stokes beam (ω_s) for fast acquisition of CARS spectra was employed for building the B-CARS system in this study. Both the pump and Stokes beams have broad spectral bands that allow simultaneous stimulation and detection of Raman shifts over a wide range.

5.2 System description

Broadband CARS microscopy based on a photonic crystal fiber light source has been considered as a simpler solution for CARS microscopy than the complex picosecond laser and OPO systems [25,26]. The pump pulses have a narrow bandwidth and define the spectral resolution. The Stokes pulses are spectrally broad, in ps regime. The pump and Stokes pulses excite multiple Raman transitions within the bandwidth of the Stokes pulses. Vibrationally excited states are probed with a third spectrally narrow probe pulse, usually the same as the pump pulse. In a single shot, the entire CARS spectrum of the excited states is generated. In Chapter 2, Fig. 2.4(a) and (b) show the energy-level diagram of CARS and B-CARS scheme. Both the pump and Stokes beams are provided by a single fs laser (Mira 900, Coherent) in conjunction with a super-continuum generator (SCG). The SCG ensures that broadband anti-Stokes spectra can be obtained without tuning the laser wavelength. As shown in Fig. 5.1, the collinear pump and Stokes beams are recombined after a razor-edge long-pass filter, and then projected onto a sample through a 40× objective lens to generate CARS signals. A spectrometer (SP2300i, Princeton Instruments) was used to acquire the CARS spectra. After

acquisition of B-CARS spectra, an *XY* galvo scanner (6210HM40B, Cambridge Tech) and a PMT (H7422A-40, Hamamatsu) were used to realize B-CARS microscopy. The galvo scanner was used to scan the collinear pumping and Stokes beams on the sample. The PMT was used to detect the CARS signal from the laser spot with their positions registered in the PC. Both the galvo scanner and the PMT were controlled by MPscope (free software by Kleinfeld Lab at UCSD) through DAQ cards (PCI 6110 E and PCI 6711, National Instruments). After scanning a region on the sample, the B-CARS imaging of the region was generated by the software.

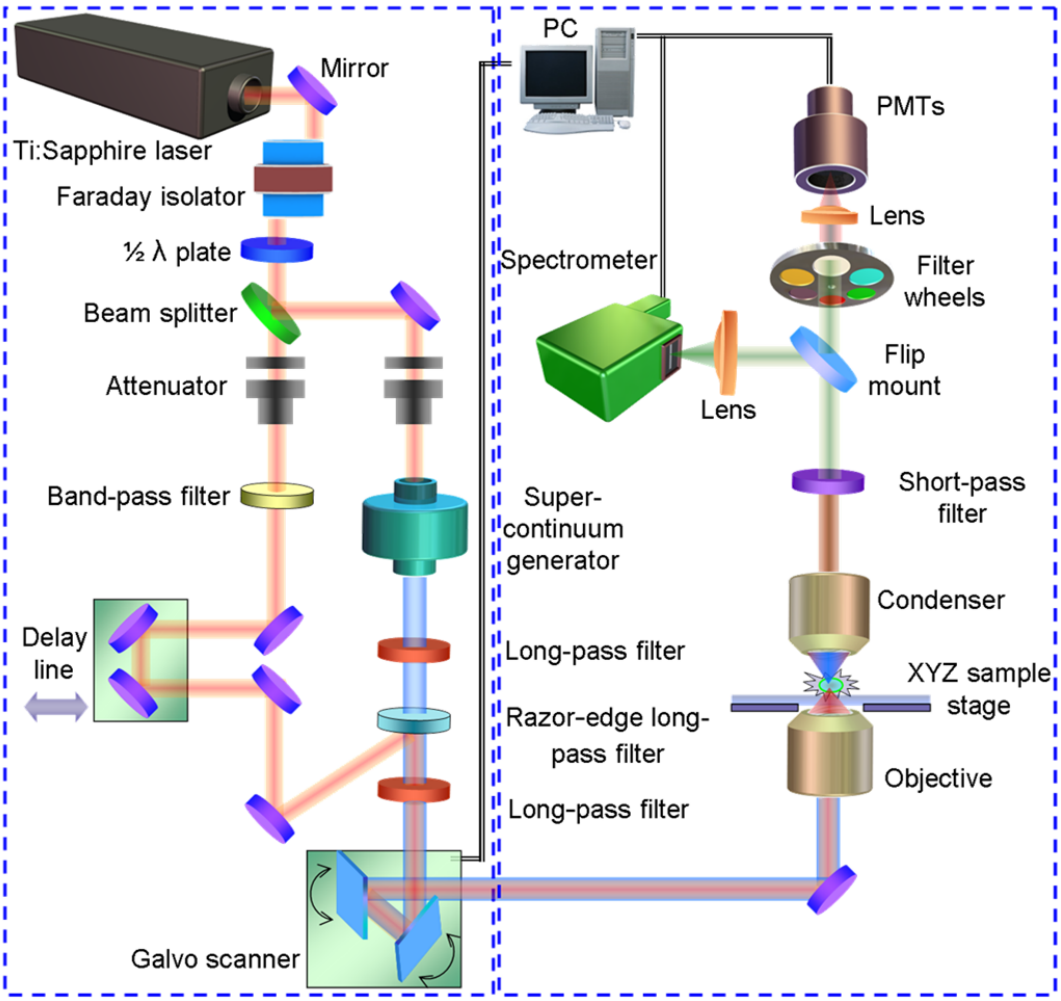

Figure 5.1 Broadband CARS spectroscopy and microscopy system.

3D CARS imaging can be attained using an *XYZ*-PZT stage on the sample holder, or integrate the CARS system with a laser scanning microscope. The pump pulses (800 nm) can be used to generate SHG (400 nm) and TPF (450 ~ 550 nm) signals simultaneously from the sample by utilizing 400 and 500 nm band-pass filters before the PMT. Multimodal nonlinear optical (NLO) imaging can be performed to characterize fresh biological tissues that contain various cellular constituents. Since CARS signals are mainly in the range of 600 ~ 800 nm (0 ~ 4000 cm^{-1}), all the three nonlinear optical signals can be easily separated. The two experimental setups used in this study can be seen in Fig. 5.2.

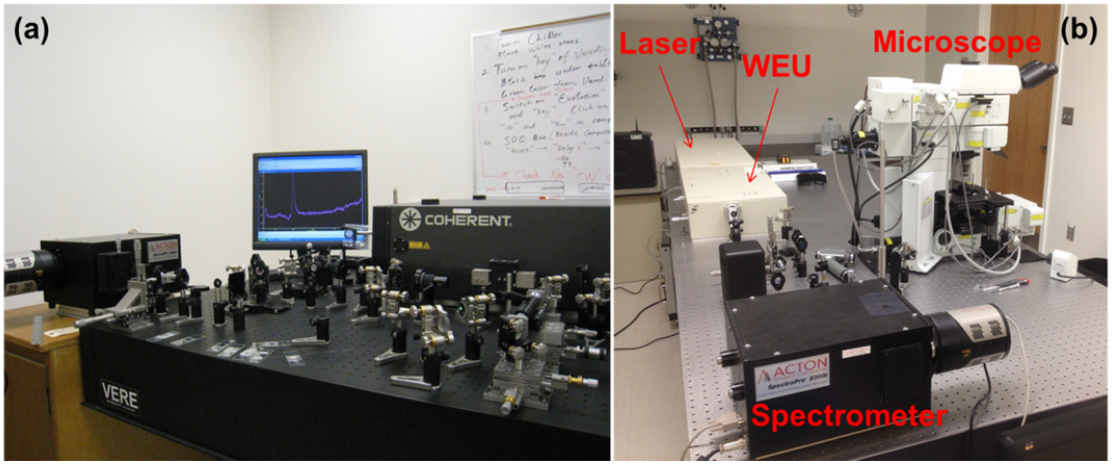

Figure 5.2 Experimental setups of the B-CARS systems based a lens pair (a) and based on a laser scanning microscope (b).

As shown in Fig. 5.1, the laser is isolated from the rest of the setup by means of a Faraday isolator (FI). The laser output is divided into beams to form the pump and Stokes beams. A 50/50 ultrafast beam splitter designed for S-polarization is used. Rotation of the input polarization with a 1/2 wave-plate continuously varies the splitting ratio between 20% and 50%. Each arm of the setup has a variable attenuator, allowing independent control of intensity and polarization. The Stokes beam is formed by filtering through a long pass

filter LP (RG750) after the collimating objective, and then passes a 808 nm razor edge long pass filter (RELP) (LP02-808RU-25 Semrock). A second long pass filter LP (RG 750) provides additional filtering of the visible light. The Stokes beam is then routed into the back aperture of the focusing objective and is focused into the sample. The other 800-nm beam passes through an attenuator and is guided to a delay line. The band-pass filter (LL01-808-25, Semrock) narrows the spectrum of the 800 nm beam down to 3 nm to form the pump beam. The filter is mounted on a rotation stage, and the angle of incidence is adjusted to shift the center of the band to 800 nm. The pump beam recombines with the Stokes beam after reflecting from an 808-nm RELP long pass filter (LP02-808RU-25, Semrock).

At this point it is important to verify that the beams propagate on top of each other. First, both beams are overlapped on the RELP filter by adjusting the 800 nm pump beam with the routing mirror just before the filter. Let the beams propagate certain distance and overlap them in the far field by adjusting the RELP filter. After careful alignment, the pump and Stokes beams are routed to the back aperture of the focusing objective. The sample is attached to an *XYZ* manual stage for accurate positioning. An *XY* galvo scanner mirror is placed before the focusing objective. The microscope objective behind the sample collimates the beams. The combination of a razor edge short pass filter SP1 (Semrock SP01-785RU) and SP2 (Edmund Optics® NT 47-588) positioned after the sample, transmits wavelengths shorter than 780 nm. The flip mirror mount is used to direct the collimated anti-Stokes beam into a spectrometer or photomultiplier (PMT).

Figure 5.3 is a photo of the galvo scanner part of the CARS system. After the galvo mirror scanner, CARS beam will be directed into two lenses for imaging function

in the B-CARS system. The beam will then be guided into the back aperture of the focusing objective and illuminated on a glass slide substrate. The scattered light is collected by another objective (condenser, 10×), followed by a lens and a low-pass filter. The light goes to either a spectrometer or a PMT unit.

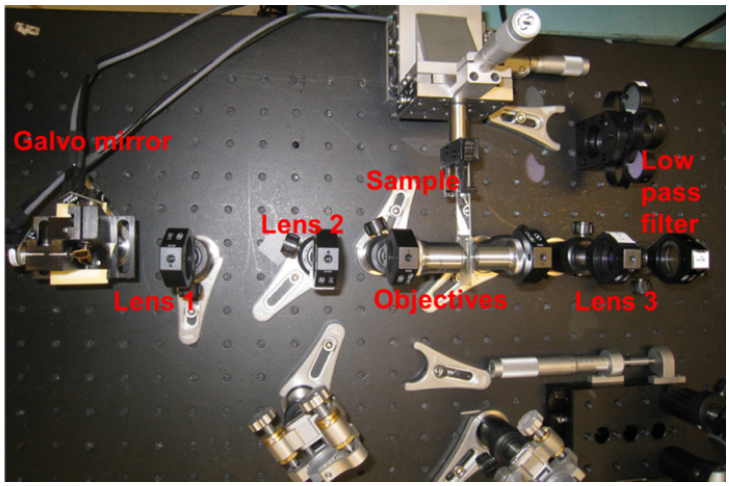

Figure 5.3 Scanning and focusing units in the CARS system.

Raman measurement was also conducted for a comparison with the B-CARS system built. Raman system used here is Renishaw inVia dispersive micro-Raman spectrometer with 514-nm Ar^+ laser. The laser power used was 5 mW with an exposure time of 10 sec for Raman spectroscopy and ~3 hr for Raman imaging. Substrate used was 100-nm gold-coated silicon wafer (Platypus Technologies, LLC). Raman image generation was realized using the software from Renishaw, named WiRE 3.2, and Origin 7.5 was used for spectra graph generation, too.

CARS spectroscopy results are from the home built B-CARS system, while the high quality CARS image of microalgae cells was based on a B-CARS system with a laser scanning microscope from Olympus (Olympus BX61WI) (See Fig. 5.2 (b)). The objective employed was PLAN 25× objective with water immersed, an NA of 1.05, and a

working distance (WD) of 2 mm. The pump beam provided for CARS imaging was from a Mai Tai DeepSee HP DS femtosecond laser (800 nm, 30 mW) (From SpectraPhysics, Newport Corporation). On the other hand, a Stokes beam was from the wavelength extension unit (WEU) (1040 nm, 70 mW) (Newport Corporation). The Substrate used for measuring of algae cells was transparent glass sildes with coverslips on top. The exposure time for each CARS image of algae was ~1 min and ~40 min for Z-stacks (3D). The band-pass filter used for CARS imaging was 650 nm with an FWHM of 40 nm, while the band-pass filter used for autofluorescence was at 450 nm with an FWHM of 10 nm. The software used was Olympus FV1000 for imaging generation and ImageJ for 3D image generation.

5.3 CARS spectroscopy

The CARS spectroscopy function was tested using ethanol (C_2H_5OH) and methanol (CH_3OH) solutions. CARS spectra of ethanol and methanol are shown in Figs. 5.4(b) and (c), respectively. Fittings of the ethanol spectra were carried out using Origin 7.5. The *x*-axis is negative value, since we used the subtraction of the incident light to the anti-Stokes scattering light. Three Raman peaks were fitted from the acquired CARS spectra of ethanol: 2888, 2926, and 2961 cm^{-1} for asymmetric CH_3, symmetric CH_3, and symmetric CH_2 vibrations, respectively. Two Raman peaks are distinguished from the acquired CARS spectra of ethanol: 2822 and 2932 cm^{-1} for asymmetric and symmetric CH_3 vibrations, respectively [29].

Diamond thin films grown using laser-excited combustion flame [30] deposition were also measured, as can be seen in Fig. 5.4(a). The sp^3 structure of diamond has a

Raman peak at 1345 cm^{-1}. Although the spectral resolution was not very high (FWHM ≈ 100 cm^{-1}), which was due to the pump beam (femtosecond laser), the sensitivity was much higher compared to normal spontaneous Raman spectroscopy. This high sensitivity enables fast microscopy function, which is ideal for biological samples, especially for those that sensitive to photodamage.

The algal cell used was Coccomyxa sp (strain C169), grown under nitrogen depletion conditions to promote triglyceride (TAG) (lipid) accumulation. Lipid has many Raman peaks, which can be seen in Table 4.2. When the cell was grown in normal healthy environment, there were very strong carotenoid Raman peaks at 1004, 1160, and 1520 cm^{-1}. However, when the algal cells were prepared in an N-depleted environment, we can observe significant Raman peaks at 1440, 1650, and 2840-2950 cm^{-1} (as indicated in Fig. 5.5), which were assigned to lipid signals. Figure 5.5 shows the Raman spectra of normal (blue) and N-depleted (red) algal cells. The most prominent difference is the strong lipid peaks for the cells grown under N-depletion environment. Growth conditions can have a significant effect on the composition of algal cultures. It is known that algal cells increase triglyceride production during nitrogen starvation [31]. With additional data processing algorithms and the development of standardized calibrations for the spectral analysis, Raman spectroscopy has the potential to provide a rapid composition analysis tool for the quantification of triglyceride content or other components, such as carotenoids, for the growing industry striving to produce fuels and chemicals from algae.

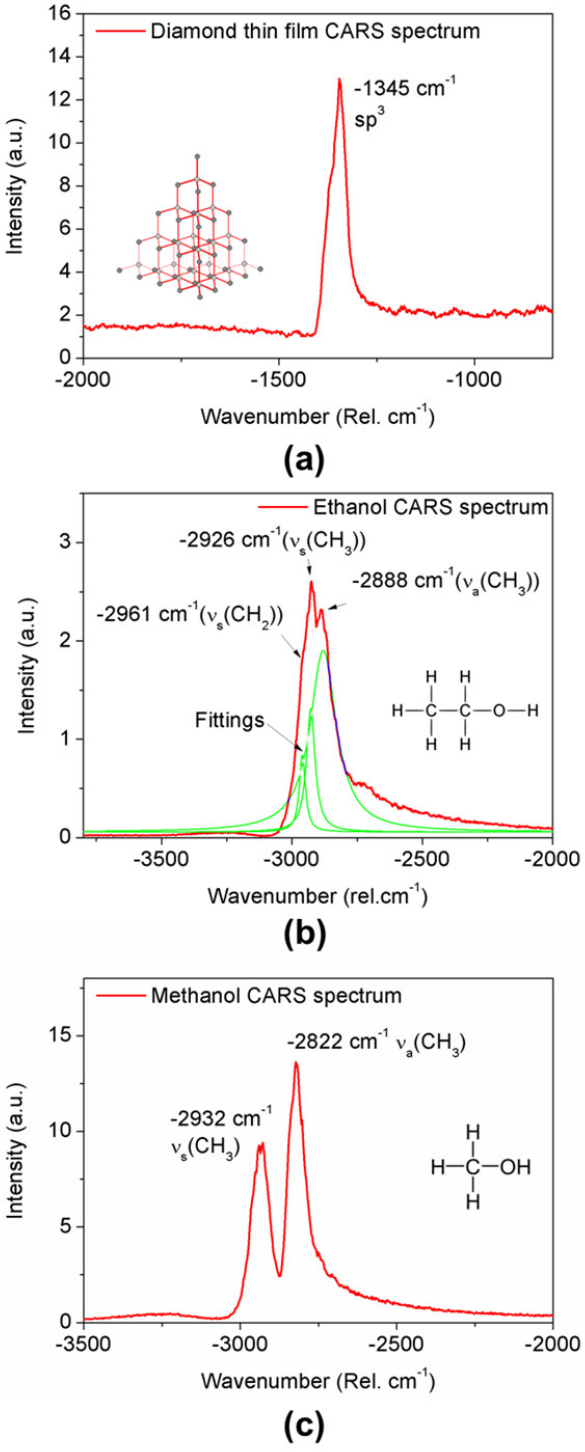

Figure 5.4 CARS spectra. (a) CARS spectrum of diamond thin film grown in laser-excited combustion flame deposition process. (b) CARS spectrum (red) and fitting (green) of ethanol. (c) CARS spectrum of methanol.

CARS spectra of the algal cells were also acquired using the B-CARS spectroscopy system. In Fig. 5.6, CARS spectra of healthy (blue) and N-depleted algal cells are presented. Beside the lipid peak at 2871 cm^{-1}, there is another broad peak at 2097 cm^{-1} (corresponding to a wavelength of 685 nm), which is due to the autofluorescence of chlorophyll, which has a wavelength of 680 nm [32], in the algal cells. When the cell was prepared in a normal healthy environment, the chlorophyll part was much more than those in N-depleted cells, which can directly be seen from the solutions with algae cells (more greenish in normal cell solution).

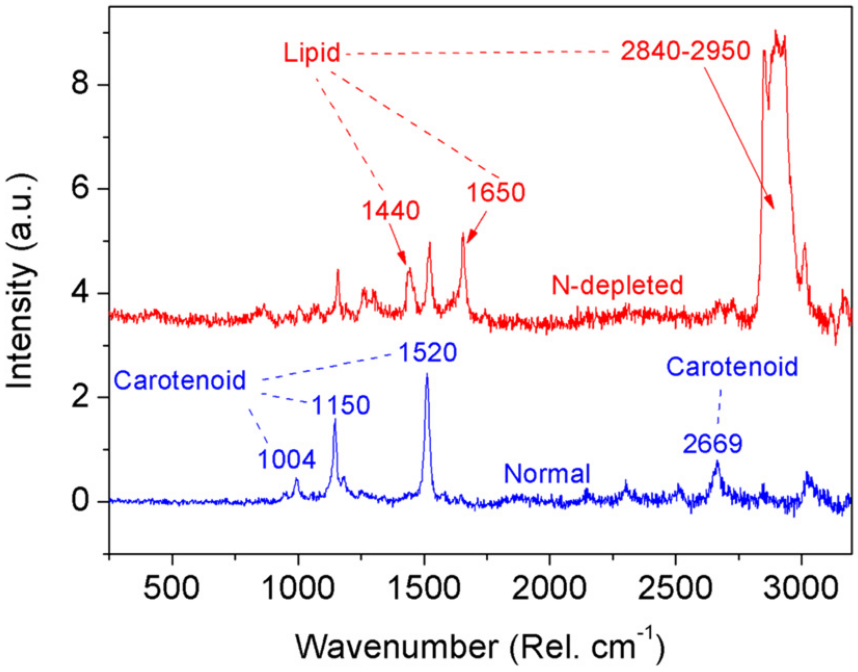

Figure 5.5 Raman spectra of the Coccomyxa sp (strain C169) grown normally (blue) and under nitrogen depletion condition (red) to promote triglyceride (TAG) (oil) accumulation, which is detected as the lipid peaks.

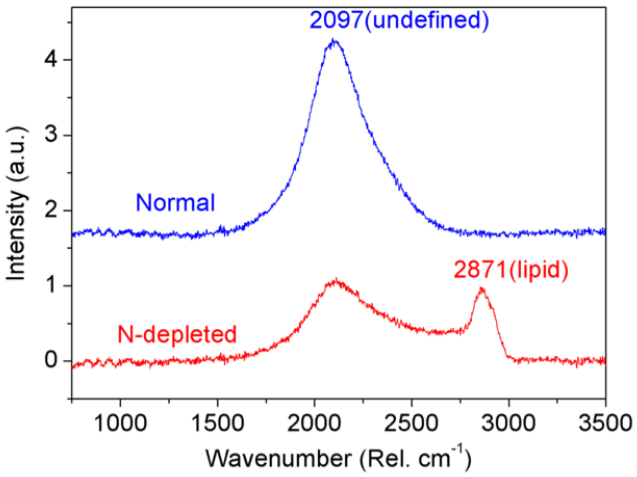

Figure 5.6 CARS spectra of Coccomyxa sp (strain C169), grown normally (blue) and under nitrogen depletion condition (red) to promote triglyceride (TAG) (oil) accumulation, which is detected as the 2871 cm^{-1} peak. The undefined peak at 2097 cm^{-1} (corresponding to ~685 nm) comes from chlorophyll (due to two-photon fluorescence)

5.4 CARS microscopy

CARS microscopy was conducted using the home-built B-CARS system with a galvo mirror and PMT detector (Fig. 5.1). We have successfully obtained CARS images from C-C bond of diamond thin films (sp^3) and CH_2 stretching bond of lipid (around 2800-2900 cm^{-1}) of neuroblastoma cells (SHSY5Y), as shown in Fig. 5.7. The band-pass filter used for diamond thin film imaging is centered at 711 nm with an FWHM of 25 nm. With the high sensitivity of CARS, large area of the diamond thin films can be quickly imaged for monitoring the film quality in 2D. On the other hand, the CARS intensity of lipid was also mapped for neuroblastoma cells. Due to the high transparency of the neuroblastoma cells, Raman signal of the cells is extremely week. However, with the high intensity of CARS imaging, we can acquire information of the neuroblastoma cell with very high speed and reduced photodamage.

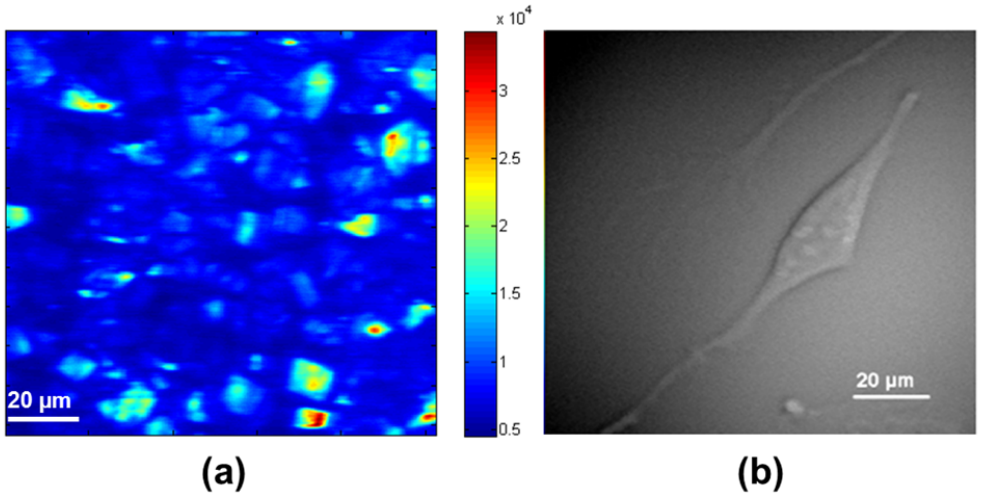

Figure 5.7 CARS microscopy of the diamond thin film sample imaging using diamond peak (band-pass filter: 711 nm, 25 nm spectral width) averaged over 30 images.

Rapid composition analysis using Raman spectroscopy can greatly facilitate the selection of suitable algal strains and their associated growing conditions for different applications, ranging from biofuels to nutritional supplements [33-36].

The Raman maps shown in Figs. 5.8-10 provide a qualitative assessment of the relative composition of algae via Stokes Raman scattering. The Raman mapping shown in Figs. 5.8 and 5.9 confirms that a significant portion of the cell is composed of lipids when the cells are grown in an environment lack of nitrogen (N-depletion). The spectral imaging is based on the signal intensity between 2840 and 2950 cm^{-1}, with background intensity subtracted (the intensity near the edge of the peak). Applying nitrogen-starvation for a longer duration has been shown to yield even greater lipid content in algae [37,38].

An optical micrograph (50×) of Coccomyxa sp (strain C169) N-depleted algae cells is shown in Fig. 5.8(a). Figures 5.8(b) and (c) are spectral composition maps that were constructed from acquired spectra at each pixel point. The signal intensity within

the desired wavenumber regions (1505-1535 cm^{-1} for carotenoid and 2840-2950 cm^{-1} for triglyceride) were measured for every spectra and the map was created such that locations with high intensity were denoted in bright red and low intensity were denoted in black. Figures 5.9 and 5.10 demonstrate the Raman imaging of single algae cells with and without N-depletion, respectively. Figure 5.9 is similar to Fig. 5.8, which contains much more lipid than carotenoid, while Fig. 5.10 contains much more carotenoid and little signal from lipid.

The actual resolving power of Raman spectroscopy is limited to be about 1 μm. An additional limitation is that fluorescence can overwhelm the component specific peaks in some cases. Therefore, near infrared excitation wavelengths (e.g., 785 nm) or coherent anti-Stokes Raman spectroscopy are much more suitable for algae imaging. There are also limitations to the spatial resolution which may cause the detection of components with low abundance not possible. For instance, some amount of triglyceride may present in healthy and starved cultures of Coccomyxa. Therefore, CARS imaging was used for measurement of algae cells for improved sensitivity and scanning speed.

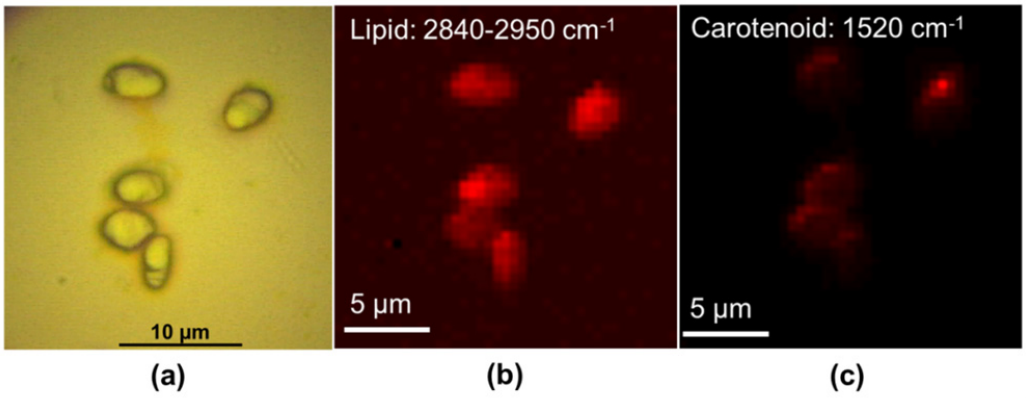

Figure 5.8 Raman imaging of the Coccomyxa sp (strain C169) grown under nitrogen depletion condition. (a) Optical microscope image. (b) Raman spectral imaging of TAG using the Raman band from 2840 to 2950 cm^{-1}. (c) Raman spectral imaging of carotenoid at 1520 cm^{-1}.

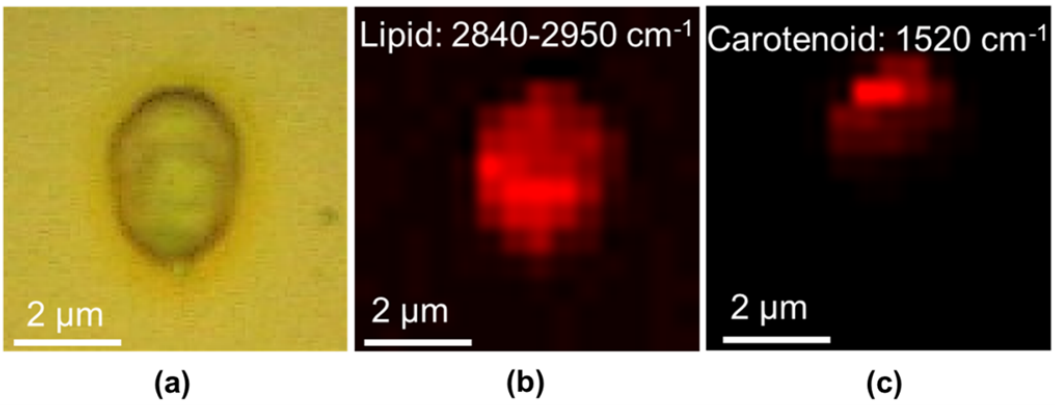

Figure 5.9 Another group of Raman imaging for a single algae cell. Raman imaging of the Coccomyxa sp (strain C169) grown under nitrogen depletion condition. (a) Optical microscope image. (b) Raman spectral imaging of TAG using the Raman band from 2840 to 2950 cm^{-1}. (c) Raman spectral imaging of carotenoid at 1520 cm^{-1}.

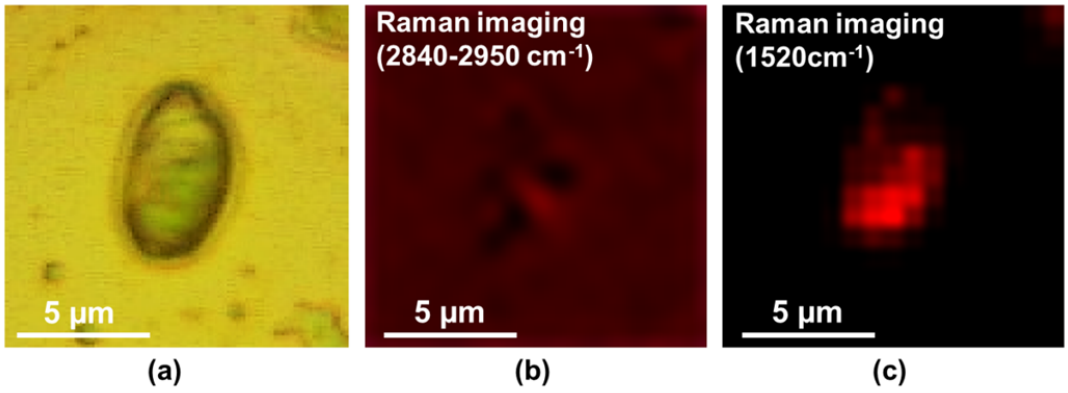

Figure 5.10 Raman imaging of normal algae cell. (a) Optical microscope image. (b) Raman spectral imaging of TAG using the Raman band from 2840 to 2950 cm^{-1}. (c) Raman spectral imaging of carotenoid at 1520 cm^{-1}.

CARS imaging of algae cells using a laser scanning microscope system (Fig. 5.2(b)) was carried out to study the Coccomyxa algae cells. Higher spatial resolution can be achieved using this system (<500 nm). Figure 5.11(a) is a bright field transmission optical microscopic image of N-depleted cells. The small black dots in each cell are TAG lipid droplets. Significant difference between the normal (Fig. 5.11(b)) and N-depleted

cells (Fig. 5.11(c)) is the existence of much more lipid droplets in the N-depleted cells. The brighter points in the images represent higher lipid signal (2800-3000 cm^{-1}).

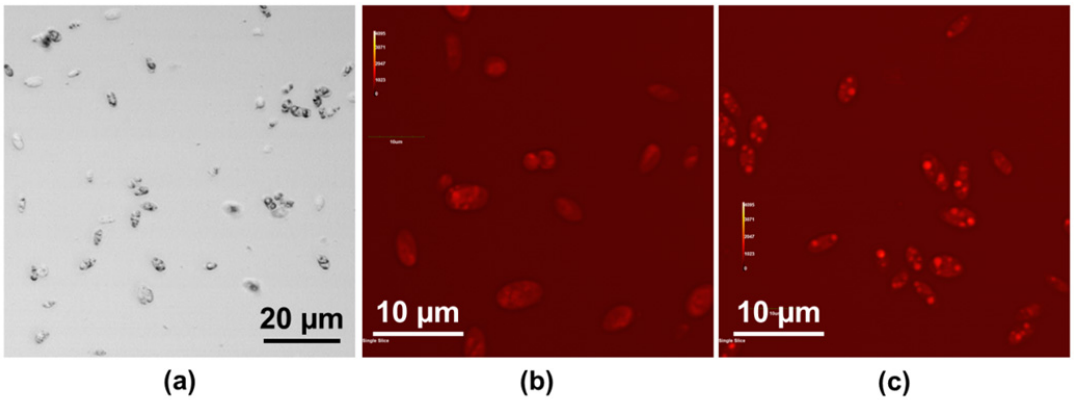

Figure 5.11 (a) Bright field optical image of N-depleted algae cells (strain C169). CARS microscopy image of normal algae cells (b) and N-depleted algae cells (c).

In Fig. 5.12, algae cells were dried out before CARS imaging. The two images of Fig 5.12(a) and (b) were taken at exactly the same imaging parameters, such as laser power. The cells with N-depletion have much higher intensity of lipid (brighter) (Fig. 5.12(b)), however, the image of the normal cells (Fig. 5.12(a)) is very dark, indicating much less lipid containment.

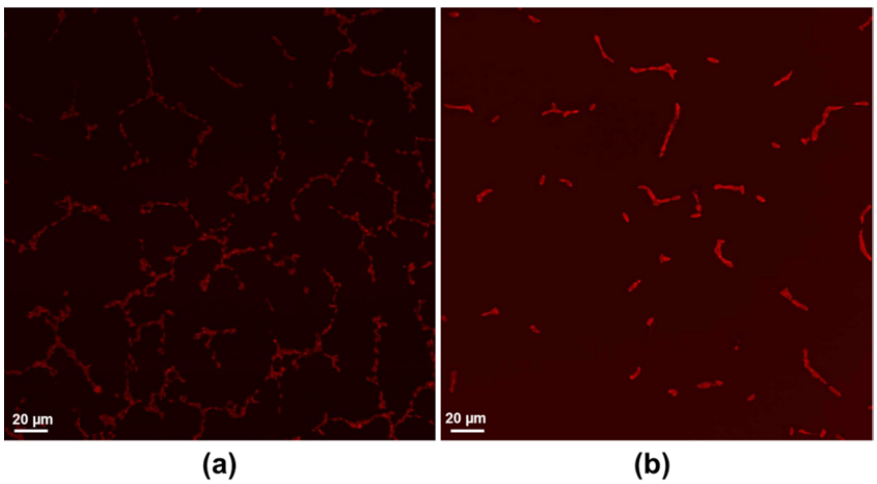

Figure 5.12 CARS microcopy of dried algae cells. (a) Normal algae cell. (b) N-depleted algae cell.

Figure 5.13(a) is a CARS image of lipids in cells grown in N-depletion environment. Each of the cells has many TAG droplets with very high lipid signal (very bright points), indicating positive relationship between lipid increase and N-depletion treatment. From Fig. 5.13(b) we used a band-pass filter centered at 450 nm with an FWHM of 10 nm for autofluorescence acquisition. The autofluorescence signal is very weak compared to the CARS signal. Therefore the contrast of Fig 5.13(b) was increased to give a better view of this image. The autofluorescence parts mostly exist in the outer area of the cells, which may be due to the carotenoid or chlorophyll components of the cells. Further study need to be carried out to finally determine the cause of the autofluorescence. Figure 5.13(c) is an overlap of CARS image on top of autofluorescence image.

Figure 5.14 is a 3D view of the TAG droplets processed using ImageJ, based on a Z-stack CARS imaging of N-depleted algae cells. Plugins of ImageJ need to be installed for 3D image generation, including “3D Viewer” and “Volume Viewer”. Figure 5.14(b) is a 2D top view of the sample.

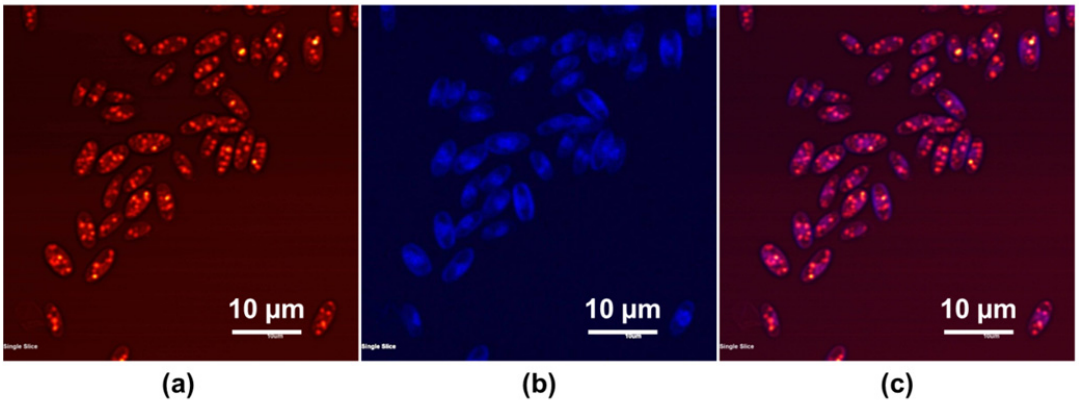

Figure 5.13 (a) CARS microscopy image of N-depleted algae cells. (b) Autofluorescence of the sample at the same time. (c) Overlap of (a) and (b).

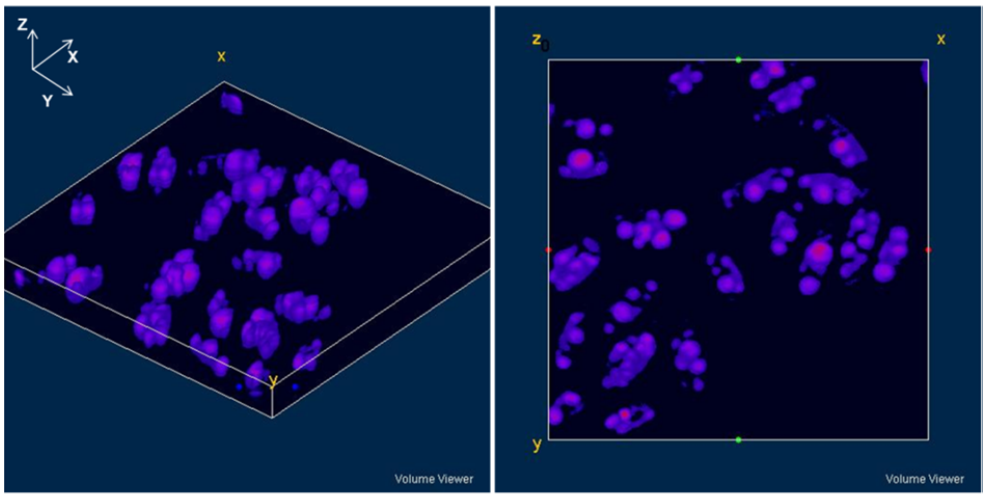

Figure 5.14 (a) 3D view of the TAG droplets process using ImageJ from a Z-stack CARS imaging of N-depleted algae cell. (b) 2D view from the top of the sample.

5.5 Conclusions

A broadband CARS system was built for CARS spectroscopy and imaging based on a lens pair setup. A laser scanning microscope based B-CARS was built and used for CARS imaging of algae cells. The CARS spectroscopy and imaging was compared to Raman spectroscopy and imaging. CARS spectra were taken from microalgae cells with or without nitrogen depletion, diamond thin film, ethanol, and methanol. CARS images of diamond thin film and neuroblastoma cells were successfully taken using the home-built lens pair based CARS system. The Raman spectra, from a commercial Raman, were taken from microalgae cells with or without N-depletion for comparison with the CARS spectra. The spectral resolution of Raman spectroscopy is much better than the B-CARS system. However, the imaging ability is not as good as CARS system from speed and spatial resolution for the microscope based CARS system.

Table 5.1 Summary of CARS techniques.

Coherent Anti-Stokes Raman spectroscopy (CARS)	
Realization approaches	Nonlinear optical approach-four wave mixing. Two beams [pump-800 nm and Stokes-1050 nm (for lipid imaging)] are employed. Ti:sapphire oscillator, 80 MHz, 100 fs. A broad spectrum for the Stokes from 800 nm to 1050 nm was from a pump beam illuminated photonic crystal fiber (PCF).
Principle	Detection of molecular or crystal lattice vibrational states using four wave mixing process when the pump and Stokes beam beat frequency matches the vibrational band.
Combination possibility	CARS can be combined with TERS or SERS. Surface- or tip-enhanced CARS are studied very recently. Although not much results are reported, they are very promising research directions.
Resolution	Higher than normal linear optical microscopy due to its nonlinear nature. Only the highest intensity part of a Gaussian shaped focused laser spot can contribute to CARS imaging. (<500 nm)
Application	Spectroscopy and imaging of biological samples (mainly on lipids), such as animal tissue, cells, and protein.
Spectral resolution	Mainly depend on the pump beam bandwidth (here we used a 3 nm bandpass filter: ~50 cm^{-1})

5.6 References

[1] H. J. Van Manen, Y. M. Kraan, D. Roos, C. Otto, "Single-cell Raman and fluorescence microscopy reveal the association of lipid bodies with phagosomes in leukocytes," Proc. Natl. Acad. Sci. **102**, 10159 (2005).

[2] C. L. Evans and X. S. Xie, "Coherent anti-stokes Raman scattering microscopy: chemical imaging for biology and medicine," Annu. Rev. Anal. Chem. **1**, 833 (2008).

[3] P. D. Maker and R. W. Terhune, "Study of optical effects due to an induced polarization third order in the electric field strength," Phys. Rev. **137**, A801 (1965).

[4] J. X. Cheng, Y. K. Jia, G. F. Zheng, "Laser-scanning coherent anti-Stokes Raman scattering microscopy and applications to cell biology," X. S. Xie, Biophys J. **83**, 502 (2002).

[5] R. F. Begley, A. B. Harvey, R. L. Byer, "Coherent anti-Stokes Raman spectroscopy," Appl. Phys. Lett. **25**, 387 (1974).

[6] C. L. Evans, E. O. Potma, X. S. Xie, "Coherent anti-Stokes Raman scattering spectral interferometry: determination of the real and imaginary components of nonlinear susceptibility $\chi(3)$ for vibrational microscopy," Opt. Lett. **29**, 2923 (2004).

[7] E. O. Potma, C. L. Evans, X. S. Xie, "Heterodyne coherent anti-Stokes Raman scattering (CARS) imaging," Opt. Lett. **31**, 241 (2006).

[8] F. Ganikhanov, C. L. Evans, B. G. Saar, X. S. Xie, "High-sensitivity vibrational imaging with frequency modulation coherent anti-Stokes Raman scattering (FM CARS) microscopy," Opt. Lett. **31**, 1872 (2006).

[9] A. Zumbusch, G. R. Holtom, X. S. Xie, Phys. "Three-dimensional vibrational imaging by coherent anti-Stokes Raman scattering," Rev. Lett. **82**, 4142 (1999).

[10] M. Hashimoto, T. Araki, S. Kawata, "Molecular vibration imaging in the fingerprint region by use of coherent anti-Stokes Raman scattering microscopy with a collinear configuration," Opt. Lett. **25**, 1768 (2000).

[11] C. L. Evans, E. O. Potma, M. Puoris'haag, D. Cote, C. P. Lin, X. S. Xie, "Chemical imaging of tissue in vivo with video-rate coherent anti-Stokes Raman scattering microscopy," Proc. Natl. Acad. Sci. USA **102**, 16807 (2005).

[12] J. X. Cheng, Y. K. Jia, G. Zheng, X. S. Xie, "Laser-scanning coherent anti-Stokes Raman scattering microscopy and applications to cell biology," Biophys. J. **83**, 502 (2002).

[13] E. R. Dufresne, E. I. Corwin, N. A. Greenblatt, J. Ashmore, D. Y. Wang, A. D. Dinsmore, J. X. Cheng, X. S. Xie, J. W. Hutchinson, D. A. Weitz, "Flow and fracture in drying nanoparticle suspensions," Phys. Rev. Lett. **91**, 224501 (2003).

[14] G. W. H. Wurpel, J. M. Schins, M. Mueller, "Chemical specificity in three-dimensional imaging with multiplex coherent anti-Stokes Raman scattering microscopy," Opt. Lett. **27**, 1093 (2002).

[15] X. Nan, W. Y. Yang, X. S. Xie, "CARS microscopy lights up lipids in living cells," Biophotonics Int. **11**, 44 (2004).

[16] E. O. Potma and X. S. Xie, "Detection of single lipid bilayers with coherent anti-Stokes Raman scattering (CARS) microscopy," J. Raman Spectrosc. **34**, 642 (2003).

[17] X. Nan, E. O. Potma, X. S. Xie, "Nonperturbative chemical imaging of organelle transport in living cells with coherent anti-Stokes Raman scattering microscopy," Biophys. J. **91**, 728 (2006).

[18] J. H. Strickler and W. W. Webb, "Two-photon excitation in laser scanning fluorescence microscopy," Proc. SPIE **1398**, 107 (1990).

[19] E. S. Wu, J. H. Strickler, W. R. Harrell, W. W. Webb, "Two-photon lithography for microelectronic application," Proc. SPIE, **1674**, 776 (1992).

[20] T. Baldacchini, M. Zimmerley, C. H. Kuo, E. O. Potma, R. Zadoyan, "Characterization of microstructures fabricated by two-photon polymerization using coherent anti-Stokes Raman scattering microscopy," J. Phys, Chem. B, **113**, 12663 (2009).

[21] K. Ikeda and K. Uosaki, "Coherent phonon dynamics in single-walled carbon nanotubes studied by time-frequency two-dimensional coherent anti-stokes Raman scattering spectroscopy," Nano Lett. **9**(4), 1378 (2009).

[22] S. A. Akhmanov, N. I. Koroteev, A. I. Kholodnykh, "Excitation of the coherent optical phonons of E_g-type in calcite by means of the active spectroscopy method," J. Raman Spectrosc. **2**, 239 (1974).

[23] J. X. Cheng and X. S. Xie, "Coherent anti-Stokes Raman scattering microscopy: Instrumentation, theory, and applications," J. Phys. Chem. **108**, 827 (2004).

[24] H. Kano and H. Hamaguchi, "Ultrabroadband (>2500 cm^{-1}) multiplex coherent anti-Stokes Raman scattering microspectroscopy using a supercontinuum generated from a photonic crystal fiber,"Appl. Phys. Lett. **86**, 121113 (2005).

[25] J. X. Cheng, A. Volkmer, L. D. Book, X. S. Xie, "Multiplex coherent anti-Stokes Raman scattering microscopy and study of lipid vesicles," J. Phys. Chem. B **106**, 8493 (2002).

[26] J. X. Cheng, L. D. Book, X. S. Xie, "Polarization coherent anti-Stokes Raman scattering microscopy," Opt. Lett. **26**, 1341 (2001).

[27] G. W. H. Wurpel, J. M. Schins, M. Mueller, "Chemical specificity in three-dimensional imaging with multiplex coherent anti-Stokes Raman scattering microscopy," Opt. Lett. **27**, 1093 (2002).

[28] S. H. Parekh, Y. J. Lee, K. A. Aamer, M. T. Cicerone, "Label-free cellular imaging by broadband coherent anti-Stokes Raman scattering microscopy," Biophys. J. **99**, 2695 (2010).

[29] J. R. Ferraro, K. Nakamoto, C. W. Brown, *Introductory Raman Spectroscopy*, Academic Press, Amsterdam, Second Edition (2003).

[30] Z. Q. Xie, X. N. He, W. Hu, T. Guillemet, J. B. Park, Y. S. Zhou, J. Bai, Y. Gao, X. C. Zeng, L. Jiang, Y. F. Lu, "Excitations of Precursor Molecules by Different Laser Powers in Laser-Assisted Growth of Diamond Films," Cryst. Growth Des., **10**(11), 4928 (2010).

[31] Y. Y. Huang, C. M. Beal, W. W. Cai, R. S. Ruoff, E. M. Terentjev, "Micro-Raman spectroscopy of algae: Composition analysis and fluorescence background behavior," Biotechnol Bioeng. **105**(5), 889 (2010).

[32] G. H. Krause and E. Weis, "Chlorophyll fluorescence and photosynthesis: The basics," Annu. Rev. Plant Physiol. Plant Mol. Biol. **42**, 313 (1991).

[33] A. Demirbas, “Importance of biodiesel as transportation fuel,” Energy Policy **35**, 4661 (2007).

[34] R. J. Radmer and B. C. Parker, “Commercial applications of algae: Opportunities and constraints,” J. Appl. Phycol. **6**, 93 (1994).

[35] J. Sheehan, T. Dunahay, R. Benemann, G. Roessler, C. Weissman, “A look back at the U.S. department of energy’s aquatic species program biodiesel from algae,” NREL **580**, 24190 (1998).

[36] G. A. Thompson, Jr., “Lipids and membrane function in green algae,” Biochim. Biophys. Acta **1302**, 17 (1996).

[37] Q. Hu, M. Sommerfeld, E. Jarvis, M. Ghirardi, M. Posewitz, M. Seibert, A. Darzins. “Microalgal triacylglycerols as feedstocks for biofuel production: Perspectives and advances,” Plant J. **54**, 621 (2008).

[38] T. G. Tornabene, G. Holzer, S. Lien, N. Burris. “Lipid composition of the nitrogen starved green alga Neochloris oleoabundans,” Enzyme Microb Technol **5**, 435 (1983).

CHAPTER 6 OPTICAL EMISSION SPECTROSCOPY

6.1 Introduction

Optical emission spectroscopy (OES) and spectroscopic temperature determination were carried out to study $C_2H_4/C_2H_2/O_2$ flames used for diamond deposition with and without an excitation by a wavelength-tunable CO_2 laser. Strong emissions from C_2 and CH radicals were observed in the visible range in all the acquired OES spectra. By irradiating a the flames using a continuous-wave CO_2 laser at a wavelength of 10.591 μm, the emission intensities of the C_2 and CH radicals in the flames increased due to the laser excitation. The CO_2 laser was also tuned to a wavelength of 10.532 μm to precisely match the resonant frequency of the CH_2–wagging vibrational mode of the C_2H_4 molecules. OES spectroscopy of the C_2 and CH radicals were performed at different laser powers. The rotational temperatures of CH radicals in the flames were determined by analyzing the spectra of the R-branch of the $A^2\Delta \rightarrow X^2\Pi$ (0, 0) electronic transition near 430 nm. The deposited diamond thin-films were characterized by scanning electron microscopy, stylus profilometry, and Raman spectroscopy. The deposition mechanism with and without the CO_2 laser excitation was discussed based on the OES spectral results.

Chemical vapor deposition of diamond films has been extensively studied since the discovery of simple low-pressure methods to deposit polycrystalline films on a variety of substrates [1, 2]. The underlying reason is that diamond coatings on different materials and equipment are very useful due to the superior properties of diamond, including outstanding optical, electrical, and mechanical properties that make it attractive for various applications [3]. As a result of these properties, diamond film research has continued to attract more and more interest over the past decade. The combustion-flame

deposition method has received considerable attention since its discovery by Hirose [4, 5] because of its simplicity and high growth rate. The combustion-flame method shows advantages over the other methods in that it is the only proven method to deposit diamond films in open atmosphere. In the combustion-flame method, C_2H_2 and O_2 have been commonly used as precursors to produce proper combustion flames for deposition of diamond films. However, other carbon-based precursors, such as C_2H_4 and C_3H_6, can also be used to deposit diamond [6].

During the combustion-flame deposition of diamond, a number of excited chemical species are present in flames above substrate surfaces. Some examples are CH, C_2, OH and CN free radicals [7-10]. The presence and interactions of these species above the substrate surface is an important factor in the combustion-flame deposition of diamond films. Since radicals, or equivalently excited chemical species, can be detected and characterized using OES. OES is widely employed to identify the excited atomic and molecular species in diamond deposition flames and to study parameters such as relative emission intensities and temperatures.

OES is a spectroscopic technique which examines the wavelengths of photons emitted from atoms or molecules during their transitions from an excited state to a lower energy state. In a combustion-flame, the energy of a molecule can change via rotational, vibrational, and vibronic (combined vibrational and electronic) transitions. More specifically, molecules are heated and excited by a high temperature which is resulted from a highly exothermic combustion reaction. When the molecule falls back down from the excited state, energy is re-emitted in the form of a photon. The wavelength of the photon is determined by the energy difference between the two states. These energy

transitions of molecules often lead to closely-spaced groups of many different spectral lines, known as spectral bands.

OES spectra [11] can provide information in a temperature range of 2000–8000 K where atomic spectra are not strong enough to ensure a good sensitivity [12]. Emission spectra from various molecules have been used for temperature determinations in combustion flame diagnostics. Ultra violet OH spectrum was employed by Chales [13] as a molecular pyrometer to determine flame temperatures. C_2 Swan band is also used for temperature determination in flames. Emission spectra of C_2 Swan band (band head: 516.611 nm) were employed for evaluation of the rotational temperature in different plasma sources [14]. The rotational temperature, T_r, of molecular species in a plasma is generally very close to the gas kinetic temperature. This is due to strong coupling between translational and rotational energy states [9,14]. To determine the rotational temperature of a premixed $C_2H_4/C_2H_2/O_2$ flame, one method is the well-known Boltzmann plot when a high-resolution optical spectrometer is available to resolve the rotational lines.

In our previous studies, laser-assisted combustion-flame deposition of diamond films has been performed to improve the deposition rate of diamond thin films. A wavelength-tunable CO_2 laser was used to irradiate the $C_2H_4/C_2H_2/O_2$ combustion flames during the deposition of diamond films. Although C_2H_2/O_2 flame is efficient in diamond growth, there is no suitable wavelength in the tuning range of the CO_2 laser that can excite the molecules in the C_2H_2/O_2 flame. C_2H_4, which is one of the suitable precursors for diamond deposition [7, 15], was added in the flame to resonantly match the laser wavelength by its CH_2-wagging vibrational mode to enable CO_2 laser excitation. Two

different wavelengths of the tunable CO_2 laser were used for comparison with the cases without laser excitation: 10.591 μm (equivalent to a wave number of 944 cm^{-1}, the common CO_2 laser wavelength) and 10.532 μm (equivalent to a wavenumber of 949 cm^{-1}). C_2H_4 molecule has an infrared absorption band corresponding to the CH_2-wagging vibration mode at a frequency of 949 cm^{-1}. Since this frequency is very close to the common CO_2 laser line-10.591 μm, the CO_2 laser can be used to excite the C_2H_4 molecules at this wavelength because of the broadening of the absorption band and to promote the production of species beneficial to diamond deposition. Furthermore, the wavelength of 10.532 μm produced by the CO_2 laser was also used to resonantly excite the CH_2-wagging mode. It is believed that the resonant excitation by the CO_2 laser can improve both the growth rate and the film quality. However, the mechanism of the enhancement in the diamond deposition was still not clear. Therefore, OES was performed in this study to identify the excited species and determine the rotational temperatures in the deposition flames with and without CO_2 laser excitations. OES spectra were also used to calculate relative emission intensities. The electronic transition of CH [$A^2\Delta$ - $X^2\Pi$ (0, 0), center near 430 nm] was used to determine the rotational temperatures using the Boltzmann plot method. The CH radicals were chosen because they have relatively high emission intensity. Previous studies by Welter [8] and Firchow [9] have shown that they are one of the species that correlate best with diamond growth. The diamond films deposited on WC-Co (tungsten carbide with cobalt binder) substrates (BS-6S, Basic Carbide Corp., containing 6% cobalt) were characterized using scanning electron microscopy (SEM), stylus profilometry, and Raman spectroscopy.

6.2 Experimental setup

Figure 6.1 (also see Fig. 6.2 for experimental setup) shows a schematic diagram of the CO_2 laser-assisted $C_2H_4/C_2H_2/O_2$ combustion-flame deposition system used in this study. A CW tunable CO_2 laser (STS 1000T, PRC Company) was used to irradiate the flames. The initial diameter of the laser beam was 14 mm. A ZnSe convex lens (f = 25.4 cm) was placed 29.2 cm in front of the flame to focus the laser beam to a diameter of approximately 1 mm. A welding torch with a nozzle diameter of 1.5 mm was used to produce a $C_2H_4/C_2H_2/O_2$ flame (with a gas ratio 0.23/0.49/1.21 slpm). These precursor gases were mixed in the torch through three mass flow controllers (Smart-Trak series 100, SIERRA Instruments, Inc). The CO_2 laser beam was directed perpendicular to the flame feather and parallel to the substrate. In this study, we only used unseeded substrates for diamond film deposition. There was no diamond powder dispersed onto the WC-Co substrate surfaces, which has a surface roughness of 0.4 μm. The substrates were cleaned in a supersonic bath of acetone for 15 min before deposition. During the deposition, the substrates were placed on a hollow brass block with water cooling. The distance between the substrate surface and the inner cone of the flame was around 1 mm in all experiments. The surface temperature of the substrates during deposition was monitored by a pyrometer (OS3752, Omega Engineering, Inc.) to ensure a steady substrate temperature at approximately 780 to 800 °C. The diamond depositions were carried out for 15 min under several different laser powers. The inset image in Fig. 6.1 shows the structure of a flame in its unperturbed state and in the configuration used for diamond deposition. There are three distinct regions in a flame: (1) the inner flame, (2) the feather, and (3) the outer diffusion flame [16]. The substrate is placed in the feather region for diamond growth.

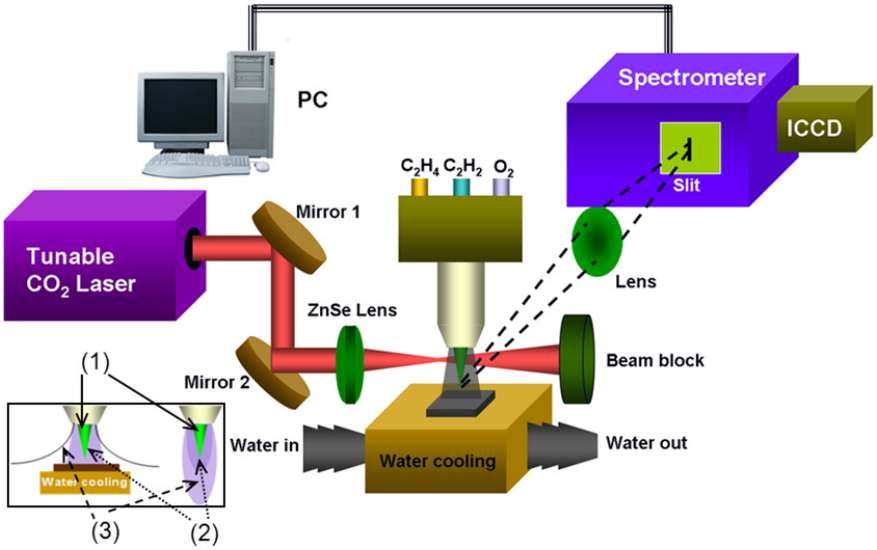

Figure 6.1 Schematic diagram of the experimental setup for OES measurements.

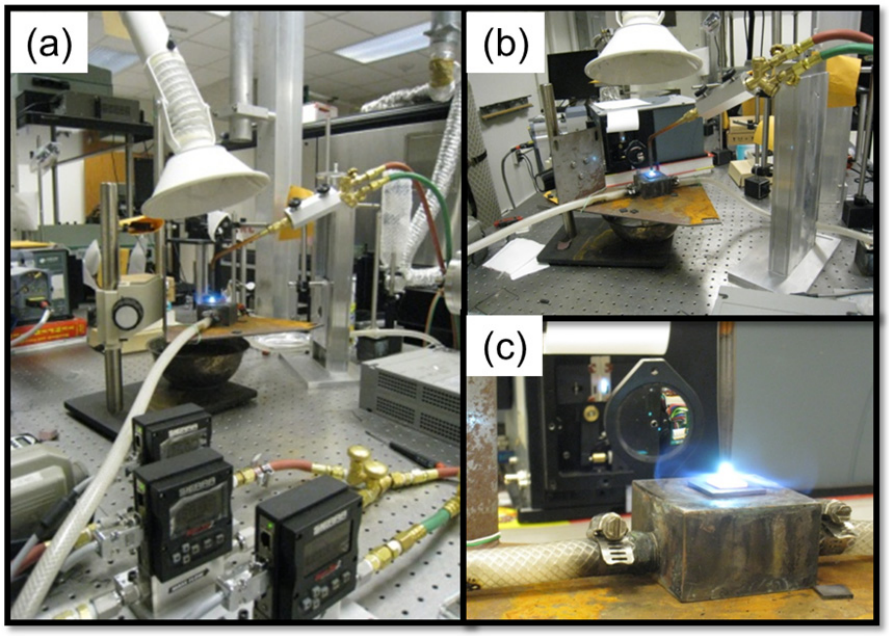

Figure 6.2 Experimental setup of the diamond synthesis system and the OES setup.

Optical emission spectra of flames were collected during diamond deposition in a direction perpendicular to the flame feather. The flame was imaged through one ultraviolet (UV) grade quartz lens (f = 10 cm) and introduced into a spectrometer (Andor

Shamrock SR-303i-A) via a slit of 0.5 mm × 10 μm in size. The spectral information was collected by an intensified charge-coupled-device (ICCD, Andor iStar DH-712) and analyzed by a PC. The wide-range OES spectra for studying the overall emission intensities were obtained using a grating of 150 lines/mm (spectral resolution: 0.52 nm), whereas the high-resolution spectra for rotational temperature calculations were obtained using a grating of 2400 lines/mm (spectral resolution: 0.02 nm). Micrographs of the deposited diamond films were obtained using an SEM (S-4700, Hitachi High-Technologies Corporation).

6.3 Determining rotational temperature

The CH rotational temperatures were obtained using the Boltzmann plot method from the R-branch $A^2\Delta$ - $X^2\Pi$ (0, 0) band of the CH molecules. Figure 6.3(a) shows the rotational spectrum used for the case without CO_2 laser irradiating the flame and Fig. 6.3(b) shows the Boltzmann plot for the spectra.

Figure 6.3(a) shows a typical OES spectrum of the R-branch of the $A^2\Delta$ - $X^2\Pi$ (0, 0) band of the CH radicals. Population density distribution of radicals in flame can be described by the Boltzmann equation [14, 17]. The emission intensity *I* of a spectral emission line within a rotational band due to a transition from an upper state *J'* to a lower state *J''* can be described using Eq. (6.1). The method used for calculations are described in detail by Kim [7], Pellerin [14], and Moon [17].

$$I = CS_{J'J''}\lambda^{-4}\exp(-\frac{E_{J'}}{k_B T_r}). \tag{6.1}$$

In the above equation, *I* is the relative emission intensity of a rotational line obtained from the experimental spectra, *C* is a proportionality constant which is the same

for all rotational transitions within a band, $S_{J'J''}$ is the rotational intensity factor or Höln-London factor, λ is the wavelength of the emitted spectral line, $E_{J'}$ is the rotational energy of the initial level, k_B is the Boltzmann constant, and T_r is the rotational temperature [7, 14, 17].

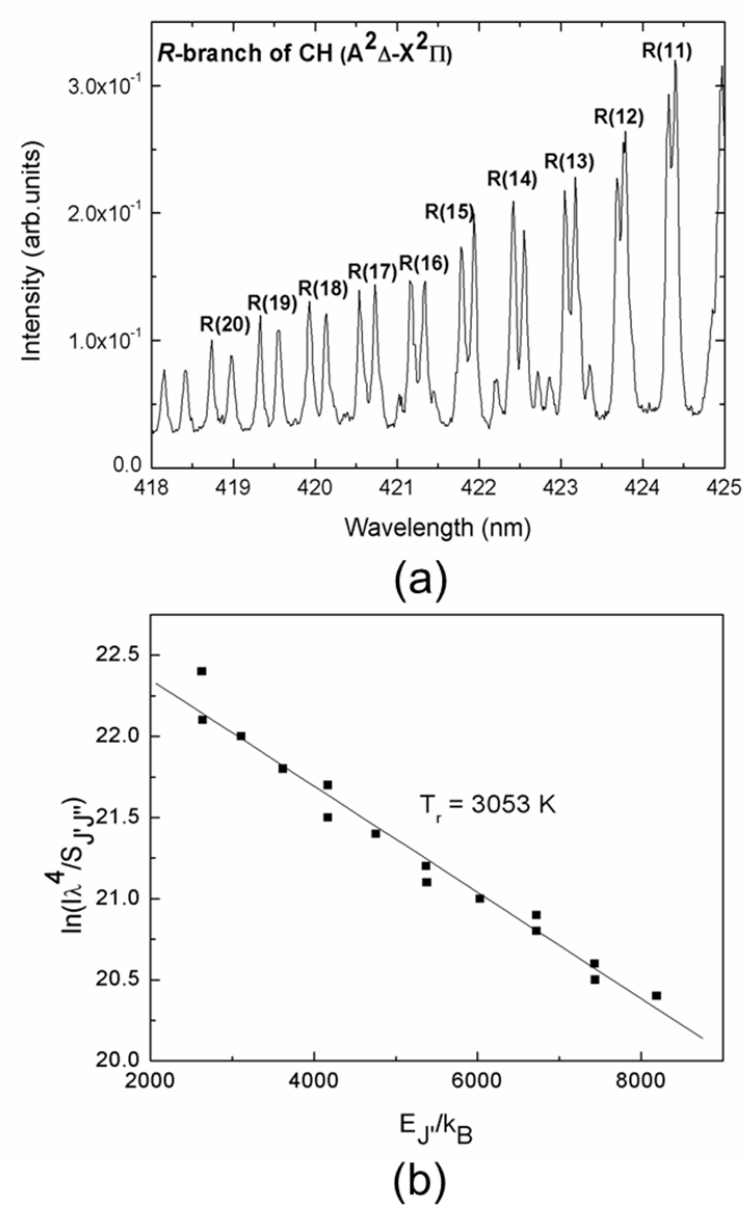

Figure 6.3 The R-branch of the CH band used in calculations and Boltzmann plot to obtain the rotational temperatures.

By taking the natural logarithm of the above expression, the expression for the Boltzmann plot was obtained as shown in Fig. 6.3(b). Notice that the value -1/T_r is the slope of the Boltzmann plot of ln($I\lambda^4/S_{J'J''}$) versus $E_{J'}/k_B$, which should be a straight line [7,14,17]. Since the values of $S_{J'J''}$ and $E_{J'}$ for the transitions in the CH molecular spectra are constants that can be calculated for each rotational transition, the value of the rotational temperature can be found by calculating the slope of the Boltzmann Plot.

$$\ln(I\lambda^4 / S_{J'J''}) = -\frac{1}{T_r} * \frac{E_{J'}}{k_B} + \ln C \,. \tag{6.2}$$

For the R-branch of the $A^2\Delta$ - $X^2\Pi$ (0, 0) band of CH, which is shown in Fig. 6.3(a), centered near 430 nm used for the CH rotational temperature calculation, Kim [7] has given both the $S_{J'J''}$ and $E_{J'}$ values. The $S_{J'J''}$ and $E_{J'}$ values can also be calculated from formulas and rotational transition data given by Pellerin [14], Herzberg [18], and Kovacs [19].

It is important to define the quantities involved in the use of OES as a diagnostic tool. A portion of the flame volume emission was focused onto the slit of a spectrometer via a lens or mirror optical system. The calibration of the detected signals are normally carried out by substituting a surface emitting continuum source of known spectral radiance, like a calibrated tungsten strip lamp, in place of the volume emitting source. This calibrated lamp was positioned at the focus of the emission optical system and the amount of its radiation per unit time per unit solid angle per unit wavelength-band per unit area element is accurately known. Thus, the signal from the spectrometer and detection system is calibrated [20].

6.4 Results and discussion

The shapes of the combustions under different laser power excitations are shown in Fig. 6.4. In Fig. 6.4(a), the optical emission of the flame went through the slit and then was reflected by a totally reflective grating onto the ICCD. The flame was irradiated by the 10.591-μm CO_2 laser at different powers (from left to right) of 0 (no laser), 200, 400, 600, 800, and 1000 W. From the images of the flames, the inner flame became shorter as the laser power increased. The original (no laser) inner flame was around 5 mm. However, it changed to ~3.5 mm when irradiated by a CO_2 laser power of 1000 W. The flame changed gradually as the laser power increased. However, as shown in Fig. 6.4(b), the flame became much shorter when a 10.532-μm laser beam was used to irradiate the flame. The inner flame changed from ~5 to ~2 mm as the laser power changed from 0 to 1000 W. The differences between the 10.591 and 10.532 μm laser excitations were due to the different levels of wavelength matching with the 949 cm^{-1} CH_2 wagging vibrational mode. 10.532 μm is more precisely in resonance with the CH_2 wagging mode than 10.591 μm. When gas precursors left from the nozzle outlet and traveled into the inner flame, the laser beam was aligned orthogonally to the flame inner feather and the diameter laser beam of 1 mm size was positioned immediately under the flame nozzle. The flame shape variation proves that C_2H_4 molecules were resonantly excited by the 10.532 μm laser beam when C_2H_4 was mixed in the flame. Furthermore, more molecules were excited to higher excited states under the 10.532-μm CO_2 laser irradiation. Higher energy-state molecules then relax to lower states, thus produce much stronger optical emission. Since more molecules from lower states were excited to higher states,

combustion reactions became faster, the inner feather became shorter than those without laser excitation.

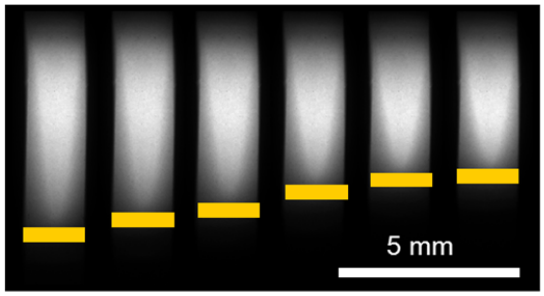

With 10.591 μm CO_2 laser excitation
(a)

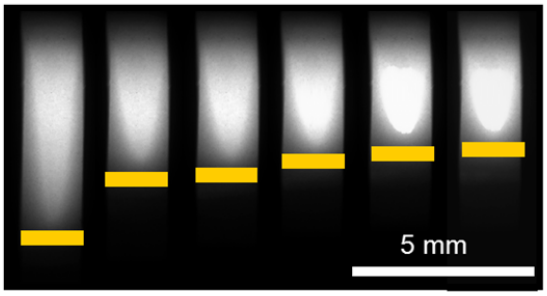

With 10.532 μm CO_2 laser excitation
(b)

Figure 6.4 Optical emission images of the $C_2H_4/C_2H_2/O_2$ combustion-flame with laser irradiations at (a) 10.591 μm and (b) 10.532 μm at 0 (no laser), 200, 400, 600, 800, and 1000 W.

SEM microscopy was used to characterize the morphologies of the deposited diamond films. From Fig. 6.5, it can be seen that there is an increase in the average size of the diamond grains deposited when the CO_2 laser was introduced into the flame. Figure 6.5(a)-(c) show the diamond films deposited without laser excitation, with an 800-W 10.591-μm CO_2 laser excitation, and with an 800-W 10.532-μm CO_2 laser excitation, respectively. In all cases, the temperature of the WC-Co substrate was maintained at 780-800 °C. The deposition time was fixed at 15 min. The 10.532-μm CO_2 laser excitation

provided more significant improvement in deposition rate than the 10.591-μm CO_2 laser excitation, which can be seen from the stylus profiles in Fig. 6.6.

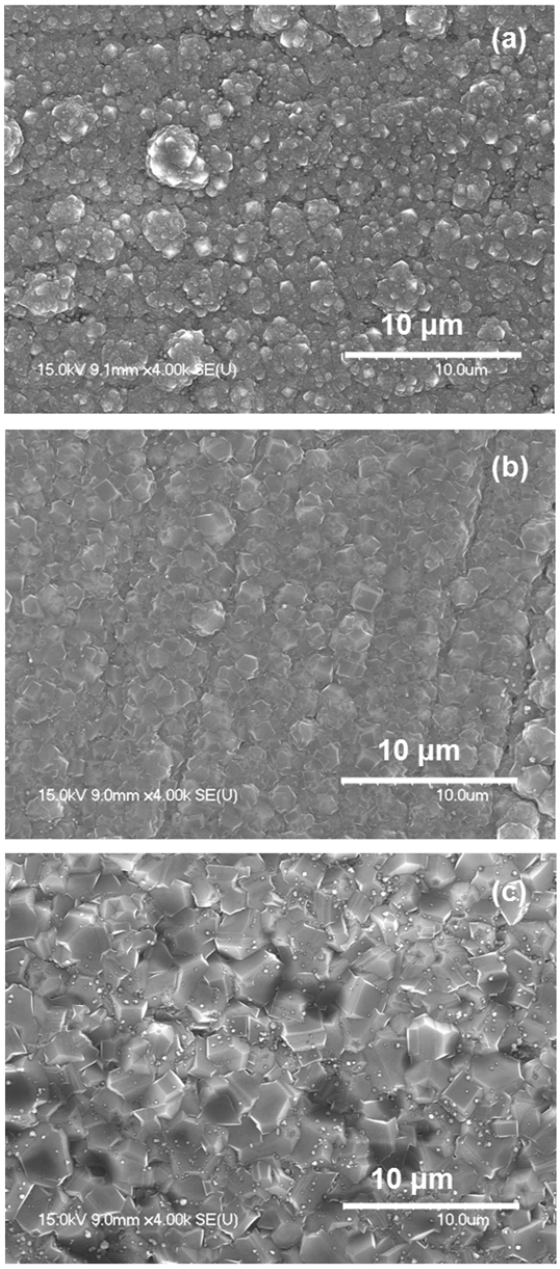

Figure 6.5 SEM micro-images of diamond films with: (a) no laser excitation, (b) an 800-W 10.591-μm CO_2 laser excitation, and (c) an 800-W 10.532-μm CO_2 laser excitation.

In Fig. 6.6, the thickness of the deposited films was characterized by a stylus profiler (XP-2, AMbios Technology). From the profiles, we can see that the diamond films deposited without laser excitation, with the 800-W 10.591-μm CO_2 laser excitation, and with the 800-W 10.532-μm CO_2 laser excitation are 4, 8, and 11.5 μm, respectively. Therefore, the increase in the deposition rate was not purely due to thermal effects on the substrate, but more likely due to the enhancement in the population of exited species which are beneficial to the diamond formation.

Raman spectroscopy (inVia Raman microscope, Renishaw Inc.) was used to characterize the deposited diamond films. The characteristic fingerprint of diamond is a single sharp Raman line at 1332 cm^{-1}. As can be seen in Fig. 6.7, Raman peaks slight shifted due to the stress in the films. The Raman peak intensity increased significantly when 800 W 10.591 and 10.532-μm CO_2 laser excitations were applied into the flame. The diamond line and the G and D peaks are all present. In addition, there is also a small broad band at ~1150 cm^{-1} which is an evidence for the existence of nano-sized diamond crystals [21, 22]. This broad band became weaker when the CO_2 laser excitation was added into the flame, and disappeared when the 10.532-μm CO_2 laser excitation was applied. Therefore, there were less nano-sized diamond crystals in the diamond films deposited with the 10.532-μm CO_2 laser excitation. From the three Raman spectra, it can be seen that the 10.532 μm CO_2 laser excitation can greatly improve the diamond film quality, which is also evidenced by the decreasing G band around 1550 cm^{-1}. 10.591 μm CO_2 laser excitation can also improve the diamond film quality, but not as significant as the 10.532 μm excitation.

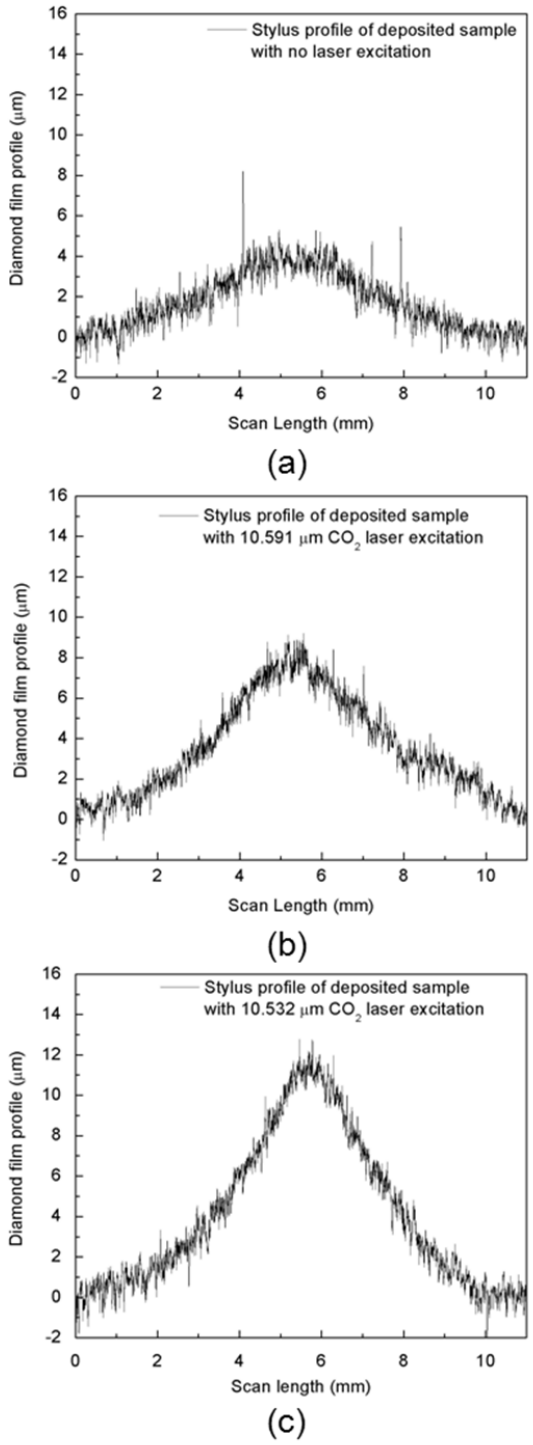

Figure 6.6 Stylus profiler graphs of deposited diamond films: (a) without CO_2 laser excitation, (b) with an 800-W 10.591-μm CO_2 laser excitation, and (c) with an 800-W 10.532-μm CO_2 laser excitation.

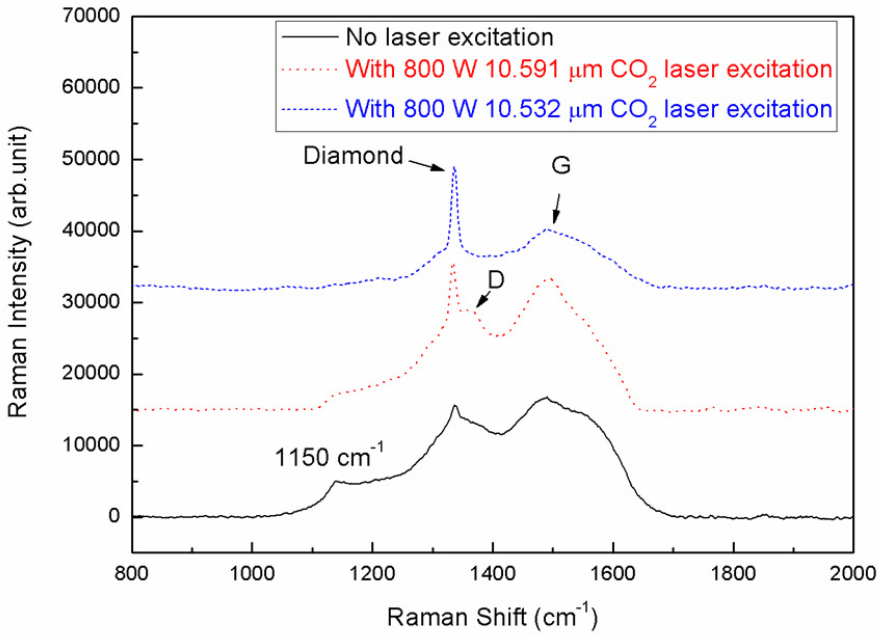

Figure 6.7 Raman spectra of diamond films with no laser excitation, a 10.591-μm CO_2 laser excitation, and a 10.532-μm CO_2 laser excitation.

The $C_2H_4/C_2H_2/O_2$ combustion flame had much stronger optical emissions when the CO_2 laser was introduced into the flame. The spectra in Fig. 6.8(a) show the increases in the intensities of CH and C_2 species as the laser power increased. All the spectra were taken at the point 0.5 mm above a WC substrate. The inset spectrum is a highly resolved spectrum of the CH band, including the R- (pure rotation), P-, and Q-branches. The OES spectra were taken under the condition that the $C_2H_4/C_2H_2/O_2$ combustion-flame was excited by the 10.591-μm CO_2 tunable laser excitation remotely matching the CH_2 wagging mode. The emission intensity of C_2 (centered at 516 nm) was enhanced by 176% and 272% at laser powers of 400 and 1000 W, respectively. This increase in the population of excited species in the flame is due to the excitation of the flame through resonant absorption of laser energy by the C_2H_4 molecules. Figure 6.8(b) shows the

optical emission intensities at different powers from 0 to 1000 W of the 10.532-μm CO_2 laser. The 10.532-μm CO_2 laser can excite the intensity of C_2 by a factor of 292% at the laser power of 400 W, and to 658% at the power of 1000 W, which was much stronger than those with 10.591-μm excitation.

Figure 6.9(a) shows the calculated CH rotational temperature distribution along the vertical axis of the feather flame. The three curves show the cases with no laser excitation, an 800-W 10.591-μm CO_2 laser excitation, and an 800-W 10.532-μm CO_2 laser excitation, respectively. This figure shows the CH rotational temperature distribution as a function of distance from the nozzle. The nozzle was placed at a point of x = 0 mm. The substrate was positioned at different places due to different inner flame lengths under various excitation conditions. The last point of each curve was taken at 0.5 mm above the substrate surface under that condition. From the trend of the temperature distribution, it can be seen that the CH rotational temperature gradually increased from the nozzle to the substrate surface as the distance increased. The CH rotational temperature at 1.5 mm below nozzle was as low as 2200 K because combustion reactions have not fully completed, resulting in less heat generation. The temperature at 0.5 mm above the substrate increased with the laser excitation. With the 10.532-μm CO_2 laser excitation, the temperature increased to the highest point. Apparently, molecules were excited to higher rotational energy states, and thus higher rotational temperature was obtained.

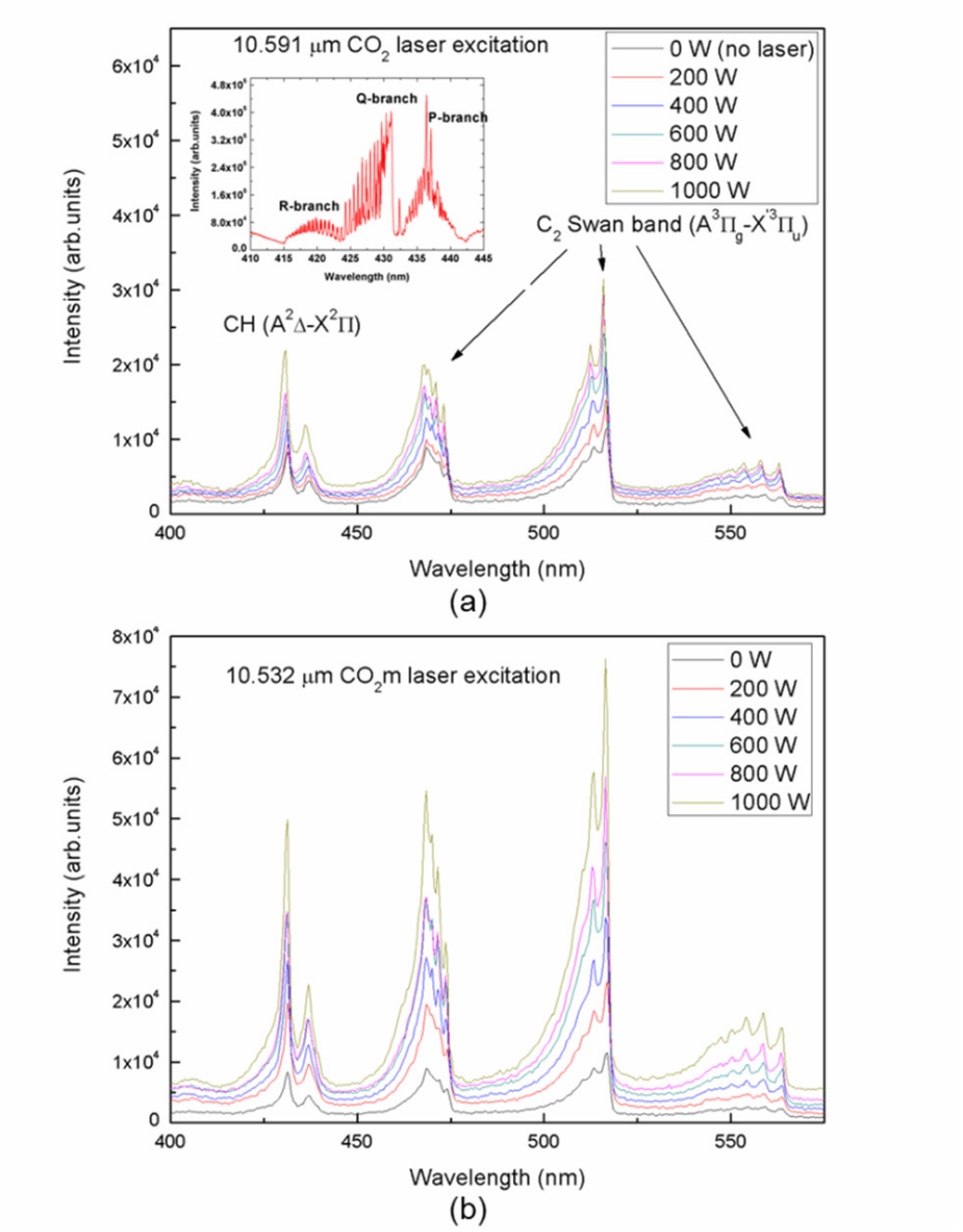

Figure 6.8 Series of optical emission spectra of $C_2H_4/C_2H_2/O_2$ combustion-flame exited by 0, 200, 400, 600, 800, and 1000 W CO_2 laser at a wavelength of (a) 10.591 μm and (b) 10.532 μm, respectively.

Figure 6.9(b) shows optical emission intensities at 431 nm (CH band head) as a function of distances from the torch without and with the 10.532-μm, 10.591-μm laser excitations. The flame with the 10.532-μm CO_2 laser excitation is the shortest but has the

highest intensity. Therefore, the intensity was highly increased by the 10.532-μm CO_2 laser excitation. The C_2 emission intensities have almost the same trend as the CH emission.

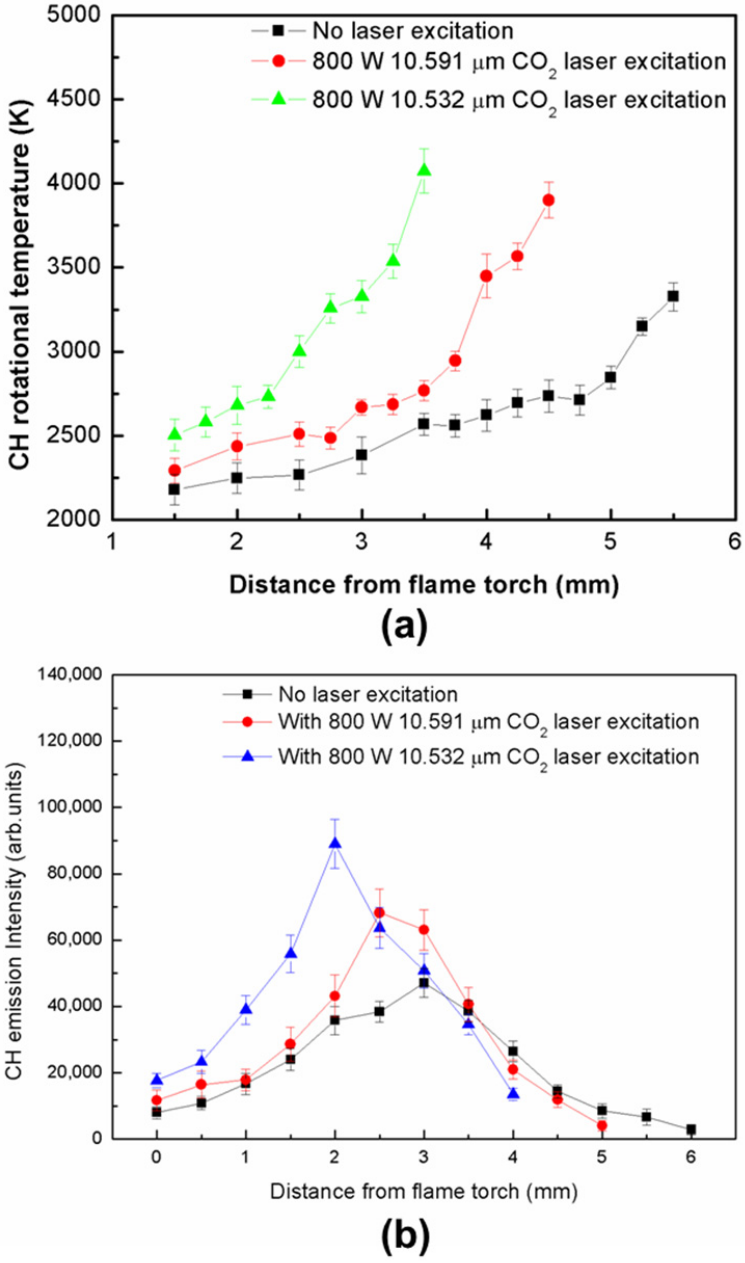

Figure 6.9 (a) CH rotational temperature distributions along the flame feather vertical direction with and without CO_2 laser excitation; (b) optical emission intensity distributions of CH radical (centered at 431 nm) along the flame feather vertical direction.

Figure 6.10 shows the calculated CH rotational temperatures as a function of excitation laser power ranging from 0 to 1000 W with two wavelengths of 10.591 and 10.532 μm. All spectra used for temperature calculation were taken at 0.5 mm above the sample surface with the presence of a substrate. Figure 6.10(a) shows the rotational temperature in the flame excited by the 10.591 μm CO_2 laser. The increase in the rotational temperature is not significant as the laser power increases. In Fig. 6.10(b), however, the CH rotational temperature increased obviously when the 10.532-μm CO_2 laser power increased from 0 to 1000 W, due to the much higher energy coupling efficiency between the 10.532-μm CO_2 laser and the flames.

Excited intermediate species in the flame and higher collision frequency could affect diamond nucleation. In this study, the film quality and growth rate were greatly improved by the CO_2 laser excitation. More significant effects can be seen from the 10.532-μm excitation which has a perfect match with the CH_2-wagging mode. Both higher growth rate and higher flame temperature were observed.

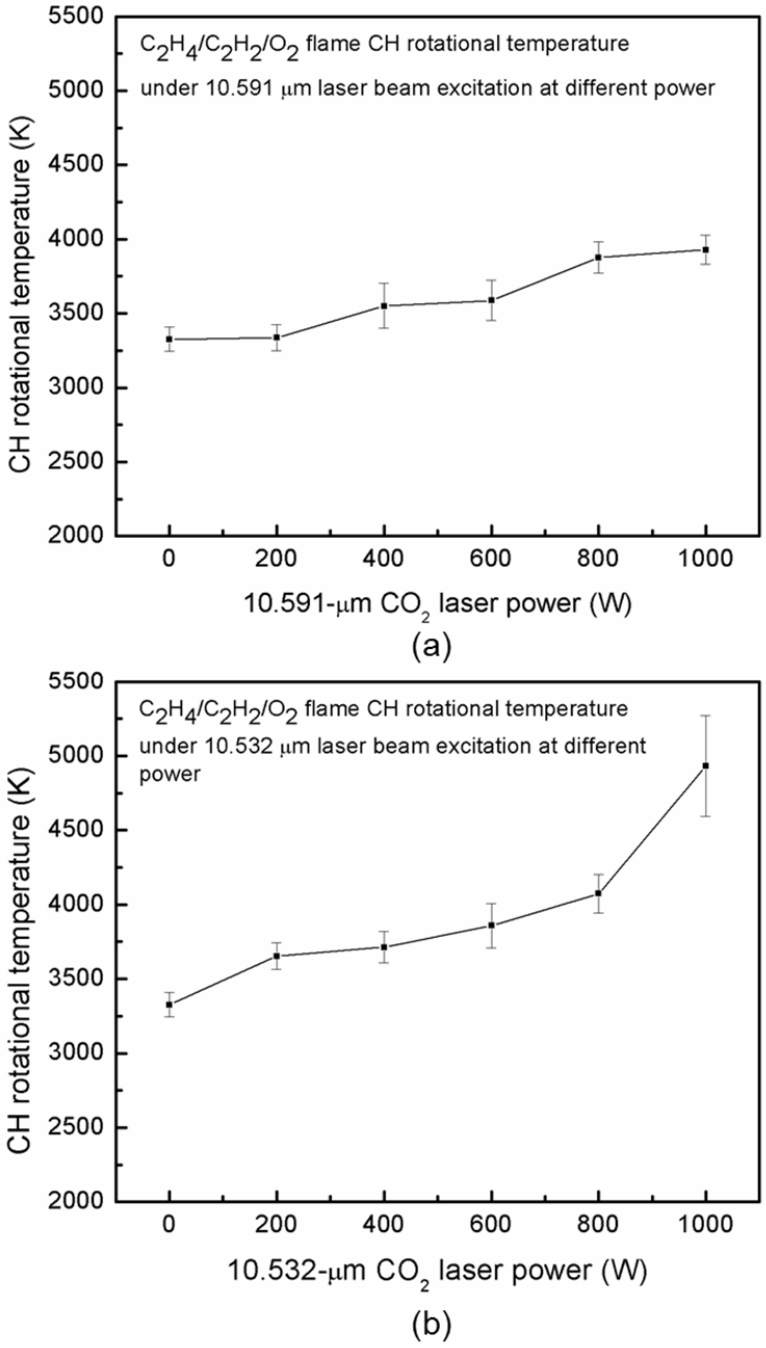

Figure 6.10 CH rotational temperatures at different CO_2 laser powers for $C_2H_4/C_2H_2/O_2$ combustion-flames with: (a) 10.591-μm and (b) 10.532-μm CO_2 laser excitations.

6.5 Conclusions

The optical emission from the excited species in a $C_2H_4/C_2H_2/O_2$ combustion-flame was enhanced by introducing a CO_2 laser excitation and the CH rotational temperatures increased with increasing laser powers. The increase in the emission intensity from the flames was found to be proportional to the laser power used. The emission intensities of the C_2 and CH radicals in the flames increased due to the laser excitation. The laser excitation of the flame resulted in the deposition of diamond films with larger grains on the substrate. The CH rotational temperatures calculations showed that the 10.591-μm laser excitation had relatively smaller effects on the CH rotational temperature. Great temperature change appeared when the flame was excited by the 10.532-μm laser beam. From the increasing OES intensities and temperatures, it is concluded that the CO_2 laser can excite the C_2H_4 molecules by infrared absorption corresponding to the CH_2-wagging vibrational mode of the C_2H_4 molecules centered at 949 cm^{-1}, and this excitation is beneficial to diamond film depositions.

Table 6.1 Summary of OES techniques.

Optical Emission Spectroscopy (OES)	
Realization approaches	UV or visible light emitted from a diamond synthesis combustion flame detected by an ICCD spectrometer with a slit input port to determine the vertical location of interest.
Principle	Electronic, vibrational, and rotational transitions in the species in the flame system. Very broad bands are formed on the spectra due to different vibration and rotation states.
Combination possibility	The principle is similar to LIBS, which is electronic transition of atoms in a laser-induced plasma.
Spectral resolution	The spectral resolution of the OES spectra is mainly determined by the grating used and the slit width, provided that the flame conditions are similar. The best can be achieved using a 2400 l/mm grating is <0.1 nm.
Application	Determining species and temperature (numerical calculation using OES spectra) in the diamond synthesis combustion flame for monitoring the process

6.6 References

[1] W. A. Yarbrough and R. Messier, "Current issues and problems in the chemical vapor deposition of diamond", Science **247**, 688 (1990).

[2] J. C. Angus and C. C. Hayman, "Low-pressure, metastable growth of diamond and 'diamondlike' phases", Science **241**, 913 (1988).

[3] D. Das and R. N. Singh, "A review of nucleation, growth and low temperature synthesis of diamond thin films", International Materials Reviews **52**(1), 29 (2007).

[4] Y. Hirose, 1st Int. Conf. on the New Diamond Science and Technology ed R. Roy, R. Messier, J. E. Butler and J. T. Glass (Pittsburgh, PA: Materials Research Society) p 38 (1988).

[5] Y. Hirose, S. Amanuma and K. Komaki, "The synthesis of high-quality diamond in combustion flames", J. Appl. Phys. **68**, 6401 (1990).

[6] K. Tanabe, Y. Nishibayashi, T. Imai., A. Ikegaya, and N. Fujimori, "Deposition of Diamond Film from the O_2-CH_4 System", Science and Technology of New Diamond, edited by Saito S., Fukunaga O., Yoshikawa M., 71-77, KTK Scientific Publishers/ Terra Scientific Publishing Company (1990).

[7] J. S. Kim and M. A. Cappelli, "Temperature measurements in low-pressure, diamond-forming, premixed flames", J. Appl. Phys. **84**(8), 4595 (1998)

[8] M. D. Welter and K. L. Menningen, "Radical density measurements in an oxyacetylene torch diamond growth flame", J. Appl. Phys. **82**, 1900 (1997)

[9] S. J. Firchow and K. L. Menningen, "Radical density measurements in an atmospheric pressure oxyacetylene torch", J. Phys. D: Appl. Phys. **32**, 937 (1999).

[10] S. Roy, J. DuBois, R. P. Lucht, and N. G. Glumac, “Hydroxyl radical concentration measurements near the deposition substrate in low-pressure diamond-forming flames”, Combustion and Flame **138**(3), 285 (2004).

[11] A. G. Gaydon, *The Spectroscopy of Flames* (London: Chapman and Hall) (1957).

[12] S. Pellerin, J. Koulidiati, O. Motret, K. Musiol, M. de Graaf, B. Pokrzwka, and J. Chapelle, "Temperature determination using molecular spectra simulation", High Temp. Mat. Proc. **1**, 493 (1997).

[13] C. de Izarra, “UV OH spectrum used as a molecular pyrometer” J. Phys. D: Appl. Phys. **33**, 1697 (2000).

[14] S. Pelleriny, K. Musiolz, O. Motrety, B. Pokrzywkax and J. Chapelley, "Application of (0, 0) Swan Band Spectrum of C_2 for Temperature Measurement", J. Phys. D: Appl. Phys. **29**, 2850 (1996).

[15] J. S. Kim and M. A. Cappelli, “Diamond film growth in low pressure premixed ethylene-oxygen flames”, Appl. Phys. Lett. **65**, 2786 (1994).

[16] J. Asmussen and D. Reinhard, *Diamond Film Handbook*, 303-304, Marcel Dekker, Inc., New York (2002)

[17] S. Y. Moon and W. Choe, “A comparative study of rotational temperatures using diatomic OH, O_2 and N_2^+ molecular spectra emitted from atmospheric plasmas”, Spectrochimica Acta Part B **58**, 249 (2003).

[18] G. Herzberg, *Molecular Spectra and Molecular Structure*, 465-472, Litton Educational Publishing, Inc., New York (1950).

[19] I. Kovacs, *Rotational Structure in the Spectra of Diatomic Molecules*, 115-135, American Elsevier Publishing Company Inc., New York (1969).

[20] J. H. Walker, R. D. Saunders, and A. T. Hattenburg, *Spectral Radiance Calibrations*, NBS Spec. Publ. 250 (1987).

[21] R. J. Nemanich, J. T. Glass, G. Lucovsky, and R. E. Shroder, "Raman scattering characterization of carbon bonding in diamond and diamondlike thin films", J. Vac. Sci. Technol. A **6**, 1783 (1988).

[22] R. E. Shroder, R. J. Nemanich, and J. T. Glass, "Analysis of the composite structures in diamond thin films by Raman spectroscopy", Phys. Rev. B **41**, 3738 (1990).

[23] P. R. Buerki, and S. Leutwayler, "Homogeneous nucleation of diamond powder by CO2 -laser-driven gas-phase reactions", J. Appl. Phys. **69**, 3739 (1991).

CHAPTER 7 HIGH-TEMPERATURE AND LOW-DENSITY PLASMAS IN LASER-INDUCED BREAKDOWN SPECTROSCOPY

7.1 Introduction

Laser-induced breakdown spectroscopy (LIBS) has been applied in different applications, such as soil and aerosol detection, aerospace exploration, artwork diagnostics and discrimination, remote elemental analysis, waste water diagnostics, real-time monitoring of radioactive materials, and etc. [1-4]. A number of techniques, such as introduction of purge gas [5] and dual-pulse excitation [6-18], have been used to improve the sensitivity of LIBS. A higher temperature of plasmas is beneficial to the sensitivity of LIBS. However, plasmas in typical LIBS also have high densities correlated to their high temperatures. High plasma density gives rise to the widened line widths and increased self-absorption of atomic lines, therefore, results in lower spectral resolutions. Spectral resolution of LIBS is very important for element analysis. Higher spectral resolution improves the accuracy of element determination. To improve the LIBS resolution, low density and high temperature in plasmas need to be achieved simultaneously. The profile of a line is the result of many effects, but under typical LIBS conditions the main contribution to the line width comes from the Stark effect (see Gornoshkin *et al.* [19], for a discussion of the different broadening effects influencing the spectral line shape in LIBS). In fact, the electric field generated by electrons in plasma perturbs the energy levels of ions, thereby broadening the emission lines from these upper (or excited) levels. Thus the Stark broadening has a well-established relation with plasma density (or plasma electron density). On the other hand, the self-absorption effect [20], in which some of the radiation emitted by a plasma is absorbed by the plasma itself, also takes place in the radiation from laser-induced plasmas.

Dual-pulse LIBS (DP-LIBS) originated in research performed more than 20 years ago, in which spatially overlapping laser-induced plasmas formed in bulk aqueous solution could improve the detection limits by orders of magnitude over those seen in nanosecond single-pulse LIBS [6]. Collinear and orthogonal reheating multipulse LIBS of solids were examined in air [7,8]. Orthogonal pre-ablative spark dual-pulse configuration was also characterized [9-14]. The fundamental physics of laser ablation and the recent explosion of applications of single- and dual-pulse LIBS have been discussed in the literature [15-18].

In conventional reheating DP-LIBS, optical emission drops drastically with interpulse delays (the delay between the two pulses in DP-LIBS) of more than 100 μs due to the limited plasma lifetime [21]. However, when the laser fluence is sufficiently large, there is an appreciable amount of laser-induced particles. With delays up to milliseconds, a second pulse can reablate the laser-induced particles to generate plasmas with high temperature but low density properties for improved spectral resolutions in LIBS.

With the aim to improve the spectral resolution of LIBS through the generation of high-temperature and low-density plasmas, we studied the reablation of laser-induced particles by introducing the second pulses with delays up to milliseconds. Fast imaging of optical scattering from particles generated by the first pulse was investigated to study the evolution of the first-pulse plasmas and the formation of the laser-induced particles. Time-integrated LIBS spectra of plasmas produced by reablation were studied. Plasma temperatures and densities, estimated using the emission intensities and line widths of atomic spectral line, were plotted to show the high-temperature and low-density properties of the plasmas generated.

7.2 Experimental methods

7.2.1 Experimental setup

The schematic diagram of the experimental setup used in this study is shown in Fig. 7.1. A KrF excimer laser (Lambda Physik, Compex 205, 248 nm, pulse duration 23 ns) that can deliver a pulse energy of 100-600 mJ was used in the experiments. The laser beam was reflected by a dichroic mirror, which is reflective to the laser light but transparent to the other wavelengths studied. The laser beam was focused normally onto an Al alloy target by an ultraviolet (UV) grade quartz lens (Lens 1 with *f*/15 cm focal length). The laser beam was slightly defocused to a spot size of about 2.5×0.5 mm^2. The laser fluence was 16 J/cm^2. A Q-switched Nd:YAG laser operating at 532 nm (Continuum, Powerlite Precision II 8010, pulse duration of 6 ns) with a 5.5 mJ/pulse energy for optical scattering of laser-induced particles or with a 200 mJ/pulse energy was introduced in parallel to sample surfaces for reablation of particles. Both lasers were synchronized by a digital delay generator (Stanford Research System DG535, 5 ps delay resolution). The pulse repetition rate was set to 6 Hz to minimize possible heating of the target. The Nd:YAG laser was focused by a convex lens (Lens 3 with *f*/10 cm focal length). The Nd:YAG laser can be focused to a spot with a diameter of about 50 μm. The distance between the Nd:YAG laser and sample surfaces was optimized to about 1 mm. The Nd:YAG laser was focused at about 2 mm beyond (overshoot) the excimer laser focal point (see Fig. 7.3). The experiments were performed in open air. To avoid over ablation, the Al alloy target was mounted on a motorized one-dimensional translation stage. The plume size was around several millimeters.

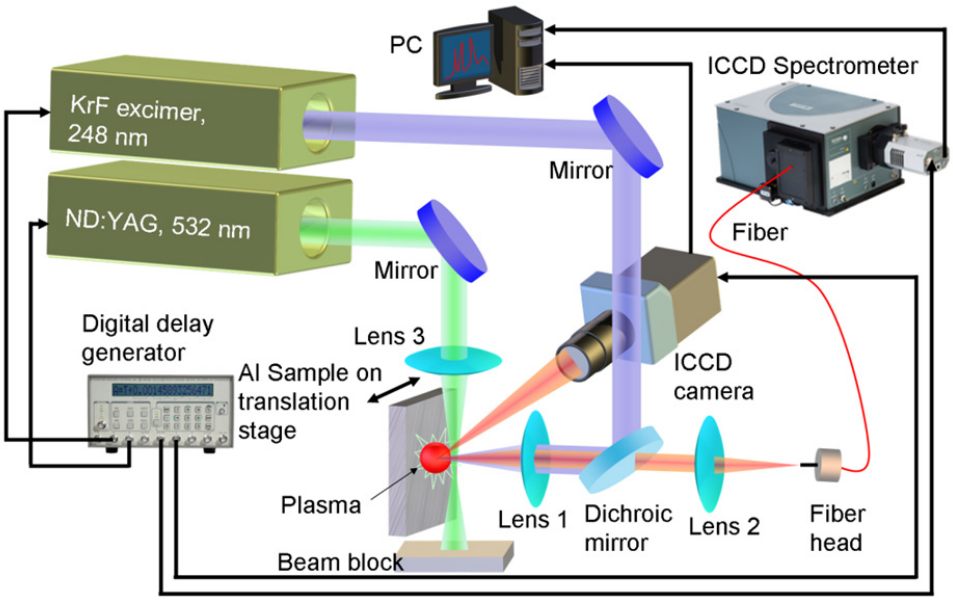

Figure 7.1 Schematic diagram of the experimental setup for LIBS with improved spectral resolutions.

7.2.2 Spectral measurements

The optical emission from plasmas was coupled to an optical fiber by Lens 1 and another UV-grade quartz lens (Lens 2 with *f*/5 cm focal length). The optical fiber with a core diameter of 100 μm was coupled to a spectrometer (Andor Tech., Shamrock 303i). The spectrometer has three gratings of 150, 600, and 2400 lines/mm, respectively. The spectral resolution for the 2400-line grating is 0.04 nm at 435 nm and the spectral region is 190–800 nm. A 512 × 512 pixel intensified charge-coupled device (ICCD) (Andor Tech., iStar, DH-712) was attached to the exit focal plane of the spectrograph. The gate delay and gate width can be adjusted so that the spectra at different time delays after the laser pulse can be obtained. In fast imaging, a Nikon micro lens (105 mm, *f*/2.8 D) was attached to an ICCD (Andor Tech., iStar, DH-734). During laser scattering experiments, a 532 nm band-pass filter was placed before the ICCD camera.

Optical scattering from laser-induced particles used delays of 1, 2, 5, 10, 20, 30, 40, 50, 60, 80, 100, 200, 300, 500, 1000, 2000, 5000, and 12000 μs between the two laser pulses to monitor the temporal evolution of the particles formation process. The ICCD camera was synchronized to the pulse used for optical scattering. Particle reablation process used interpulse delays of 15, 40, 60, 80, and 12000 μs. The spectrometer started to acquire spectra from 3 μs after the first-pulse plasma. For all delay experiments, the normal excimer laser was fired first to produce a plasma, and the 532-nm Nd:YAG laser was fired second for either optical scattering or particle reablation.

7.3 Results and discussion

7.3.1 Fast imaging of optical scattering from laser-induced particles

Particle formation was observed through optical scattering using pulses from the 532 nm Nd:YAG laser. The excimer laser with a pulse energy of 200 mJ/pulse was focused normally onto the Al sample to generate first-pulse plasmas. A laser pulse of 5.5 mJ from the Nd:YAG laser was introduced in parallel with the target surface for optical scattering of the particles. The gate width for scattering was set to 200 ns, considering the fact that the duration of the scattering from particles usually lasts for ~60 ns.

In Fig. 7.2, optical scattering images with a relative intensity scale were acquired with laser pulses produced by the Nd:YAG laser at different delays. The ICCD was synchronized with the Nd:YAG laser. The first image was taken at a delay of 1 μs and the following images were taken with increasing time delays. At a delay of 1 μs, the first-pulse plasma still has strong emission, which can be observed through the 532 nm band-pass filter in front of the ICCD camera. The plasma emission disappeared at a delay of 5

μs. At a delay of 20 μs, particles were observed with low concentration. The concentration of particles increased gradually after 20 μs and reached a maximum at a delay of 200 μs. The particle concentration remained high from 200 to 500 μs, after which the particle concentration gradually decreased. As shown in Fig. 7.2, particles stayed in the plasma-plume region for up to milliseconds before eventually drifting away. The optical scattering from dusts in air was too small to be detected, because we cannot see any Al lines only with Nd:YAG laser (not shown). The particle formation process includes two steps. The first step is the cool down process of the plasma, during which, material is condensed to form particles. The second step is the drifting movement of particles, which causes the concentration of particles to decrease. This phenomenon provides an opportunity to obtain high-temperature and low-density plasmas by reablation of the particles to improve spectral resolutions in LIBS. The reablation of particles was investigated using temporal and spectral analysis, followed by temperature and density calculations.

The spatial distribution of the particles changed with different interpulse delays. With delays under 80 μs, particles distributed in two areas, above and below plasma-plume region. The focused laser beam was used for optical scattering, only scattering from particles in the beam path were captured. The actually distribution of the particles should be surrounding the plasma-plume region. This was primarily due to the low pressure produced by the evacuated shock-wave volume [22]. With longer delays, the plasma disappeared with the volume returning to atmospheric pressure. As shown in Fig. 7.2, after 80 μs, the pressure in the plasma-plume region recovered to atmospheric pressure. Therefore, particles appeared in the plasma-plume region.

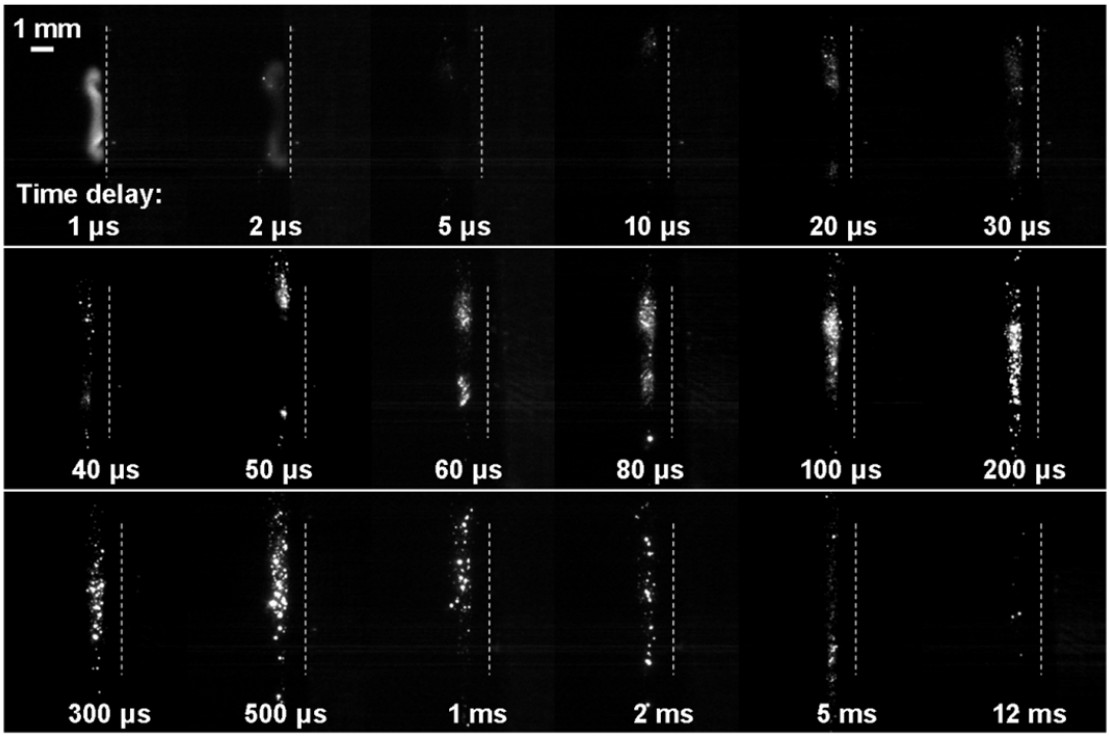

Figure 7.2 Optical scattering from first-pulse plasma using the 532-nm Nd:YAG laser at different interpulse delays. Dashed lines show the location of the substrate surface.

7.3.2 Temporal analysis

After the generation of first-pulse plasmas, the particles formed during and after the plasmas were reablated by a second pulse with an energy of 200 mJ/pulse from the Nd:YAG laser operating at 532 nm in parallel with the target surface when the concentration of the particles was sufficiently high. With the Nd:YAG laser pulse, an air spark (or air plasma) can be formed, the LIBS spectra of which disappear within 2 µs. The center of air plasma was ~2 mm below the center of the first-pulse plasma. On the pathway of this pulse, particles were reablated. By adjusting the delay and gate width of the ICCD, the LIBS spectra at different delays were acquired.

In Fig. 7.3(a), temporal evolutions of emission peak intensity at 394.4 nm with different focal point locations were plotted. The first data point was acquired with a delay

of 3 μs and a gate width of 2 μs. The following data points were acquired with increasing delays by a step of 2 μs and a gate width of 2 μs. Square symbols represent temporal evolution under first-pulse-only condition, that is, first-pulse plasma without reablation process. Circle symbols show temporal evolution when the focal points of the two lasers were overlapped (see Fig. 7.3(b)), while the triangle symbols show temporal evolution when the focal point of the Nd:YAG reablation pulse were ~2 mm beyond (overshoot) the focal point of the excimer laser (see Fig. 7.3(c)). When the focal points of the Nd:YAG laser and the excimer laser overlapped, the enhancement of emission was much less than that with ~2 mm overshooting. This was mainly due to the low pressure generated in the evacuated shock-wave volume (as mentioned in part 7.3.1). When the interpulse delay became larger (>80 μs), the pressure of the shock-wave volume recovered to atmospheric pressure. The Nd:YAG laser was also focused 2 mm before the focal point of the excimer laser. Although there were enhancements, they were not as good as overshooting condition. Thus we just consider overshooting condition. We fixed the focal point of the Nd:YAG laser at ~2 mm overshooting position during the experiments.

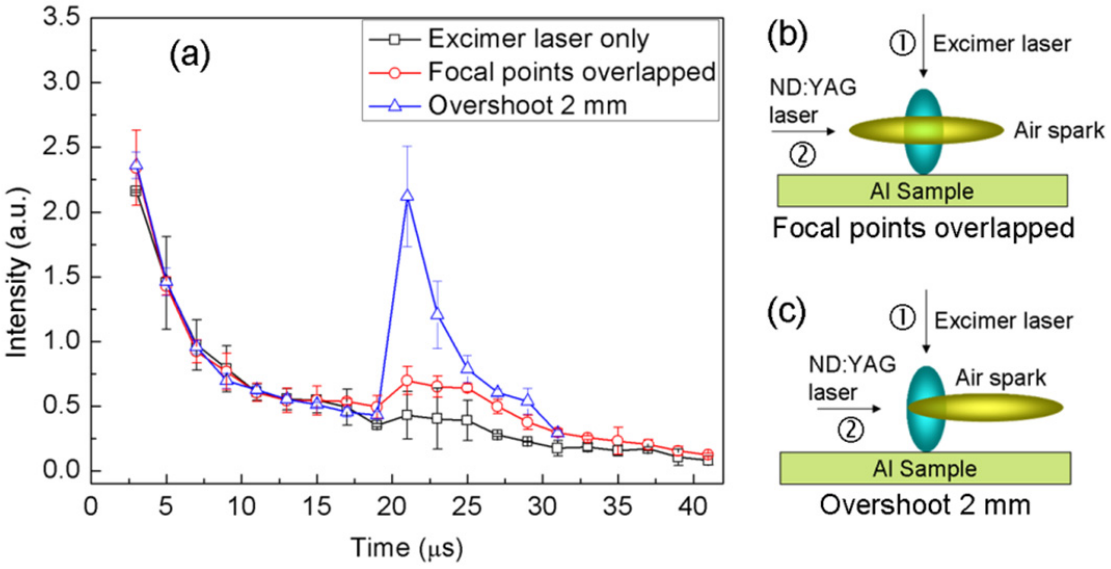

Figure 7.3 (a) Temporal evolutions of emission intensity at 394.4 nm with first-pulse plasma only (square symbols), with focal points of the Nd:YAG laser and the KrF excimer laser overlapped (circle symbols), and with focal points of the Nd:YAG laser overshoot 2 mm (triangle symbols); (b) Schematic diagram of overlapped focal points of the Nd:YAG laser and the excimer laser; (c) Schematic diagram of ~2 mm overshoot of the Nd:YAG laser (the focal point of the Nd:YAG laser was ~2 mm beyond the focal point of the excimer laser).

As shown in Fig. 7.4, temporal evolutions of emission peak intensity at 394.4 nm with different interpulse delays of 15, 40, 60, and 80 μs for reablation of laser-induced particles were plotted. The first data point was acquired with a delay of 3 μs and a gate width of 2 μs. The following data points were acquired with increasing delays by a step of 2 μs and a gate width of 2 μs. The inset graph shows temporal evolution of the intensity with an interpulse delay of 12 ms. The lifetime of the first-pulse plasma is around 50-60 μs, after which the emission from the plasmas drops to zero (not shown). There was enhancement of emissions before particle formation. The enhancement occurred with interpulse delays less than 20 μs, mainly due to the reheating process [21]. However, the enhancement of emission with interpulse delays longer than 20 μs was a combination of reheating effects and reablation of particles. With interpulse delays longer

than 60 μs, the Al atomic emission was mainly comprised of reablation effects, which can be observed with interpulse delays up to milliseconds.

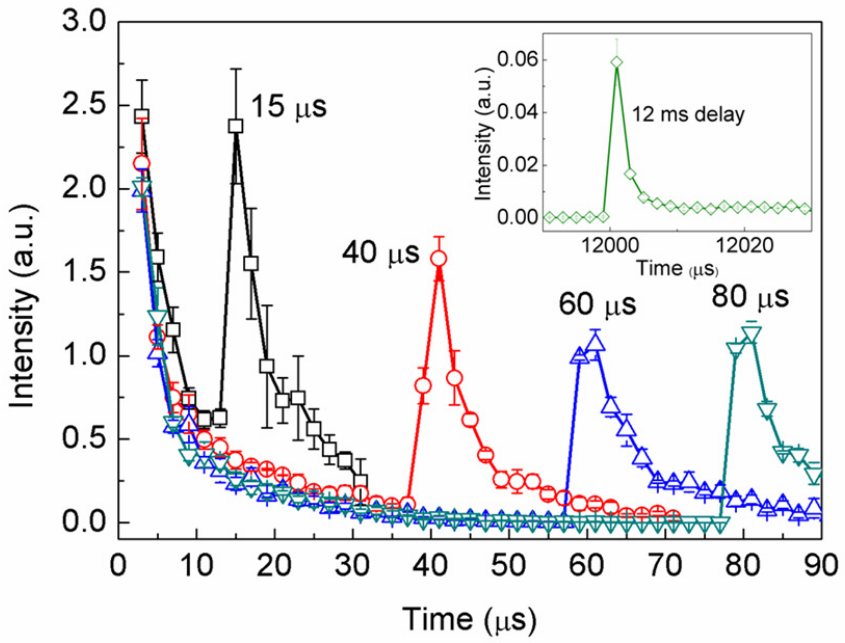

Figure 7.4 Temporal evolutions of emission intensity at 394.4 nm with different interpulse delays: 15, 40, 60, and 80 μs. Inset: intensity temporal evolution with 12 ms interpulse delay.

7.3.3 Spectral analysis

Figure 7.5(a) shows the temporal evolution of LIBS spectra from the reablation with an interpulse delay of 50 μs acquired using the 2400 line/mm grating. The first spectrum was acquired with a delay of 3 μs and a gate width of 2 μs. The following spectra were acquired with a step of 4 μs. In Fig. 7.5(b), time-integrated LIBS spectra of Al lines from reablation were compared to first-pulse LIBS spectra to show reduced atomic line widths.

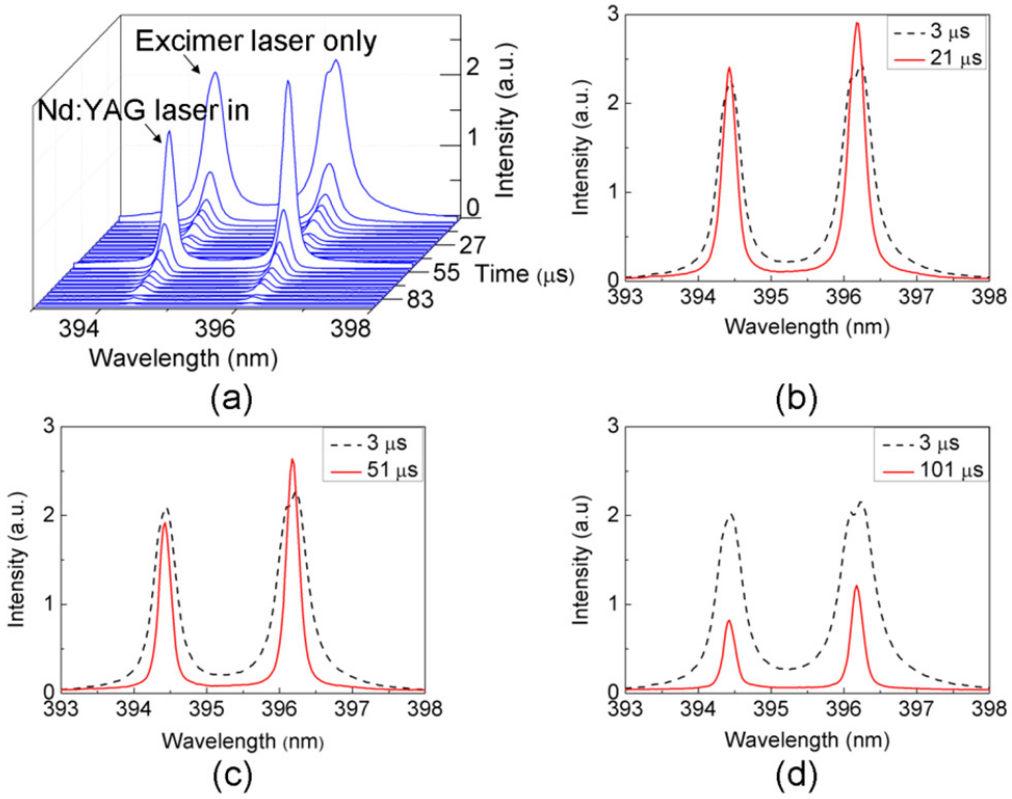

Figure 7.5 (a) Temporal evolution of LIBS spectra with 50 μs interpulse delay; time-integrated LIBS spectra of plasmas from an Al target under first-pulse only condition [3 μs after plasma generation (dashed lines)] and with reablation [1 μs after second pulse (solid lines)] at different interpulse delays of (b) 20, (c) 50, and (d) 100 μs.

All of the spectra were accumulated for 30 pulses to reduce the standard deviation. As indicated in the diagrams, after reablation of particles, the line widths of Al lines decreased significantly compared with first-pulse LIBS spectra. Time-integrated LIBS spectra from the plasmas of the Al target were acquired under conditions of first-pulse only condition (first-pulse LIBS) [3 μs after plasma generation (dashed lines)] and with reablation [1 μs after second pulse (solid lines)] at different interpulse delays: Figs. 7.5(b) 20, (c) 50, and (d) 100 μs. The line widths gradually reduced from ~0.32 nm (dashed curve) to ~0.09 nm (100 μs). The Al atomic lines show some self-absorption in first-pulse LIBS spectra. The self-absorption effect usually occurs when the plasmas are optically

thick (high plasma density). Comparing the spectra, self-absorption was reduced significantly in the high-temperature and low-density plasmas produced by the second pulse.

7.3.4 Plasma temperature and density

According to the local thermodynamic equilibrium (LTE) assumption, plasma temperatures can be deduced from the ratio of relative intensities of the spectral lines from the same element and ionization stage, which is expressed as [23]

$$\frac{I_1}{I_2} = \left(\frac{g_1 A_1}{g_2 A_2}\right)\left(\frac{\lambda_2}{\lambda_1}\right)\exp\left[\frac{-(E_1 - E_2)}{kT_e}\right], \tag{7.1}$$

where indices 1 and 2 refer to the first and second spectral lines of interests, respectively. I_i, λ_i, g_i, A_i, and E_i (i=1, 2) refer to the line intensity, the wavelength, the statistical weight factor for the upper states, the Einstein transition probability, and the energy of the upper states of the two spectral lines, respectively. k is Boltzmann constant, and T_e is the electron temperature of the plasma. The 150 line/mm grating was used to acquire a pair of spectral lines: 309.25 nm (from Al I 308.22, 309.27, and 309.28 nm) and 396.13 nm (from Al I 394.40 and 396.15 nm) (see Table 7.1) [24]. Within each spectral line (309.25 or 396.13 nm), atomic lines will not be distinguished from each other due to the low spectral resolution of the 150 line/mm grating. Therefore, the multiplications of A_i and g_i of each atomic line were added together for 309.25 and 396.13, respectively. An efficiency curve was measured and used for correction of spectrometer efficiency.

Under typical LIBS conditions, the main contribution to the line width comes from the Stark effect [19]. The Stark broadening of a well-isolated line is thus a useful

tool for estimating the electron density. The Stark broadening of a line, expressed as the FWHM in nanometers, is given with an accuracy of 20-30% [11] by [25]

$$\Delta\lambda_{Stark} = 2w\left(\frac{n_e}{10^{16}}\right) + 3.5A\left(\frac{n_e}{10^{16}}\right)^{1/4}\left[1 - BN_D^{-1/3}\right]w\left(\frac{n_e}{10^{16}}\right), \tag{7.2}$$

in which, value of w, the electron impact half-width, can be found in the extensive tables given by Griem [26]. n_e is plasma electron density with a unit of cm^{-3} and N_D is the Debye shielding parameter. B is a coefficient equal to 1.2 or 0.75 for ionic or neutral lines, respectively. The first term on the right side comes from the electron interaction, while the second one is resulted from the ion interaction. For typical LIBS conditions, the contribution from ion broadening is negligible, and thus equation (7.2) becomes

$$\Delta\lambda_{Stark} = 2w\cdot\left(\frac{n_e}{10^{16}}\right), \tag{7.3}$$

from which, assuming that other sources of broadening (natural, Doppler, etc.) are negligible (i.e. $\Delta\lambda_{line} \approx \Delta\lambda_{Stark}$).

Table 7.1 Parameters of the atomic lines used in the calculation of plasma temperatures.

Wavelength λ_i (nm)	Upper level energy E_i (cm^{-1})	Degeneracy g_i	Transition probability A_i (s^{-1})	Configurations
308.22	32435.453	4	6.3e+07	$3s^23p$ - $3s^23d$
309.27	32436.796	6	7.4e+07	$3s^23p$ - $3s^23d$
309.28	32435.453	4	1.2e+07	$3s^23p$ - $3s^23d$
394.40	25347.756	2	4.93e+07	$3s^23p$ - $3s^24s$
396.15	25347.756	2	9.8e+07	$3s^23p$ - $3s^24s$

As shown in Fig. 7.6, the temperature temporal evolution of first-pulse plasma was plotted. Plasma temperatures and densities at delays of 3, 10, 20, 30, 40, 50 μs were estimated from LIBS spectra using equation (7.1). The atom lines were too weak for temperature and density estimation with delays longer than 50 μs. The temperature at 3 μs delay was around 6400 K, and decreased drastically to 3200 K at 50 μs delay. At the

same time, plasma density decreased almost the same trend as temperature, from ~1.2×10^{18} (at 3 μs) to ~3.4×10^{17} cm^{-3} (at 50 μs). Lower density means improved spectral resolution, however, with first-pulse LIBS we can get low density only when the temperature of plasmas was sufficiently low. Therefore, we tried to use a second pulse to reablate the laser-induced particles for generation of high-temperature and low-density plasmas.

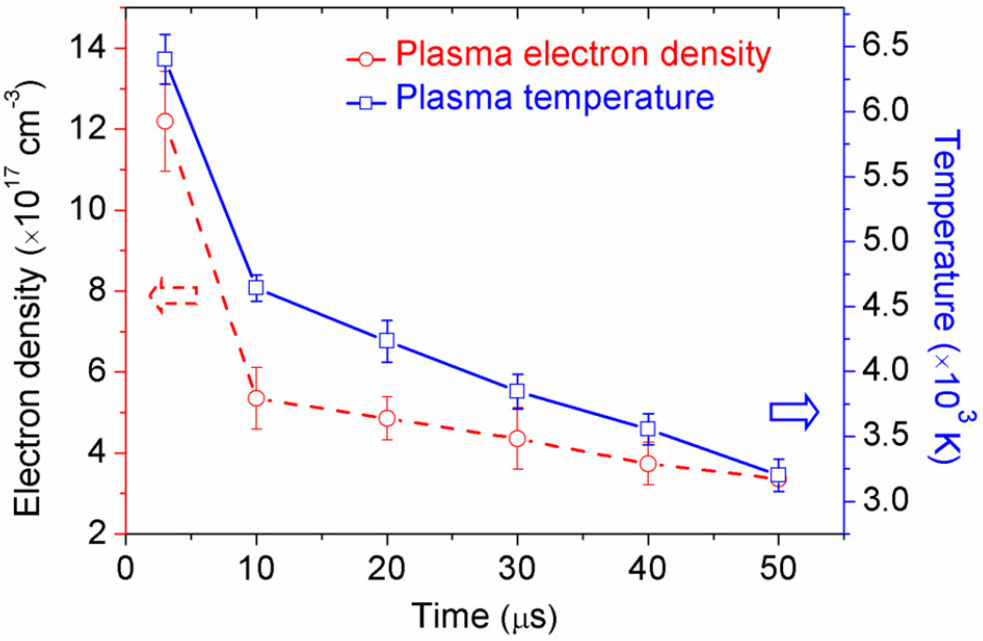

Figure 7.6 Temporal evolutions of the temperature (hollow square symbols) and density (hollow circle symbols) of first-pulse plasma.

In Fig. 7.7, hollow square symbols represent temperatures of Al plasma from reablation, obtained 1 μs after the second pulse, with different interpulse delays. Hollow circle symbols are electron densities calculated from spectra, acquired 1 μs after a second pulse, with different interpulse delays. The solid symbols (indicated by the dotted line) show data points obtained at 3 μs after first-pulse plasma without reablation. The temperature of the plasma produced by the second pulse increased several hundred

Kelvins from the first-pulse plasma (~6400 K) because of the reheating process. The temperature decreased to ~6300 K with an interpulse delay of 70 μs due to the lifetime of Al plasmas that were reheated. The temperatures with interpulse delays longer than 70 μs decreased slightly.

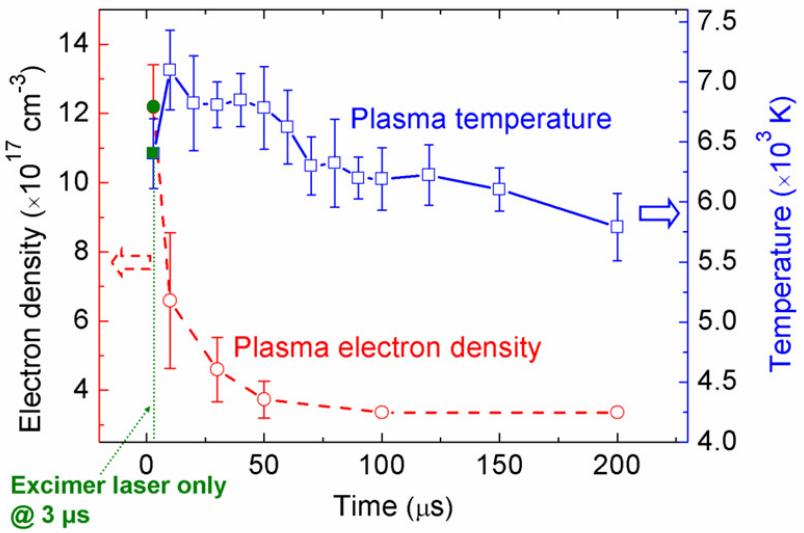

Figure 7.7 Temporal evolutions of the temperature and density of the reablation plasma. Hollow square symbols in the solid curve: temperatures of Al plasma acquired 1 μs after second pulse with different interpulse delays. Hollow circle symbols in the dashed curve: Al plasma electron densities 1 μs after second pulse with different interpulse delays. The solid symbols indicated by the dotted line shows data point 3 μs after the generation of first-pulse plasma without reablation.

The plasma density, however, decreased drastically from ~1.2×10^{18} (first-pulse plasma) to ~3.3×10^{17} cm^{-3} (plasma by reablation with an interpulse delay of 100 μs). The temperature with an interpulse delay of 100 μs was ~6200 K, which was almost the same temperature as the first-pulse plasma (~6300 K). Low plasma density was obtained while the plasma temperature was still high. Therefore, high-temperature and low-density plasma was achieved for improved spectral resolution for LIBS.

7.4 Conclusions

High spectral resolutions in LIBS were achieved by generation of high-temperature and low-density plasmas through reablation of laser-induced particles. Particles were formed using a KrF excimer laser to irradiate on an Al target. The particles were then reablated by a 200 mJ pulse from a 532 nm Nd:YAG laser. The line widths of plasmas decreased from ~0.32 nm (first-pulse plasmas) to ~0.09 nm (plasmas by reablation with an interpulse delay of 100 μs). The temperatures of plasmas in DP-LIBS increased due to the reheating process and then decreased gradually with longer interpulse delays. The plasma electron density, however, was significantly reduced from $\sim 1.2\times10^{18}$ to $\sim 3.3\times10^{17}$ cm^{-3}. The temperature of reablation plasma was as high as the temperature of first-pulse plasma. The temperature of first-pulse plasma was ~6400 K with a plasma density of $\sim 1.2\times10^{18}$ cm^{-3}. The temperature of the reablation plasma, for instance, with an interpulse delay of 100 μs, was ~6200 K. However, the plasma density was $\sim 3.3\times10^{17}$ cm^{-3}, much lower than the density of first-pulse plasma. Therefore, high-temperature and low-density properties in plasmas were simultaneously achieved for improved spectral resolutions in LIBS.

Table 7.2 Summary of LIBS techniques.

Laser-Induced Breakdown Spectroscopy (LIBS)	
Realization approaches	UV or visible light emitted from a laser-induced plasma, from solids, liquids, or gases, detected by an ICCD spectrometer.
Principle	Electronic transitions of atoms or ions in laser-induced plasmas
Combination possibility	The principle of LIBS is similar to OES, which is electronic transition of species in a combustion flame with different precursors, such as C_2H_2, C_2H_4, and O_2. LIBS can be used in a laser-assisted mass spectrometer for combined optical and ion current studies.
Spectral resolution	The spectral resolution of the LIBS spectra is mainly determined by the delay from generation of plasma, the grating used and the slit width. At the same delay time, our approach by generating high-temperature and low-density plasmas can decrease the linewidth by up to 50%. (Up to <0.1 nm)
Spatial resolution	50-100 μm (focused laser spot size of an Nd:YAG laser)
Application	Determining trace elements in a sample
Limit of detection (LOD)	part per million (ppm)

7.5 References

[1] D. W. Hahn and M. M. Lunden, "Detection and analysis of aerosol particles by laser-induced breakdown spectroscopy," Aerosol Sci. Technol. **33**, 30 (2000).

[2] D. Anglos, S. Couris, C. Fotakis, "Laser diagnostics of painted artworks: laser induced breakdown spectroscopy of pigments," Appl. Spectrosc. **51**, 1025 (1997).

[3] D. A. Cremers, J. E. Barefield, A. C. Koskelo, "Remote elemental analysis by laser-induced breakdown spectroscopy using a fiber-optic cable," Appl. Spectrosc. **49**, 857 (1995).

[4] J. P. Singh, F. Y. Yueh, H. Zhang, K. P. Karney, "A preliminary study of the determination of uranium, plutonium and neptunium by laser-induced breakdown spectroscopy," Rec. Res. Dev. Appl. Spectrosc. **2**, 59 (1999).

[5] S. Nakamura, Y. Ito, K. Sone, "Determination of an iron suspension in water by laser-induced breakdown spectroscopy with two sequential laser pulses," Anal. Chem. **68**, 2981 (1996).

[6] D. A. Cremers, L. J. Radziemski, R. R. Loree, "Spectrochemical analysis of liquids using the laser spark," Appl. Spectrosc. **38**, 721 (1984).

[7] R. Sattmann, V. Sturm, R. Noll, "Laser-induced breakdown spectroscopy of steel samples using multiple Q-switch Nd:YAG laser pulses," J. Phys., D. Appl. Phys. **28**, 2181 (1995).

[8] J. Uebbing, J. Brust, W. Sdorra, F. Leis, K. Niemax, "Reheating of a laser-produced plasma by a second pulse laser," Appl. Spectrosc. **45**, 1419 (1991).

[9] F. Colao, S. Pershin, V. Lazic, R. Fantoni, "Investigation of the mechanisms involved in formation and decay of laser-produced plasmas," Appl. Surf. Sci. **197**, 207 (2002).

[10] L. St-Onge, V. Detalle, M. Sabsabi, "Enhanced laser-induced breakdown spectroscopy using the combination of fourth-harmonic and fundamental Nd:YAG laser pulses," Spectrochim. Acta, Part B **57**, 121 (2002).

[11] F. Colao, V. Lazic, R. Fantoni, S. Pershin, "A comparison of single and double pulse laser-induced breakdown spectroscopy of aluminum samples," Spectrochim. Acta, Part B **57**, 1167 (2002).

[12] V. Sturm, L. Peter, R. Noll, "Steel analysis with laser-induced breakdown spectrometry in the vacuum ultraviolet," Appl. Spectrosc. **54**, 1275 (2000).

[13] D. N. Stratis, K. L. Eland, S. M. Angel, "Dual-pulse LIBS using a preablation spark for enhanced ablation and emission," Appl. Spectrosc. **54**, 1270 (2000).

[14] S. M. Angel, D. N. Stratis, K. L. Eland, T. Lai, M. A. Berg, D. M. Gold, "LIBS Using Dual- and Ultra-Short Laser Pulses," Fresenius J. Anal. Chem. **369**, 320 (2001).

[15] L. J. Radziemski and D. A. Cremers, Eds. *Laser-Induced Plasmas and Applications* (Marcel Dekker: New York 1989).

[16] R. E. Russo, X. Mao, S. S. Mao, "The physics of laser ablation in microchemical analysis," Anal. Chem. **74**, 70A (2002).

[17] W. B. Lee, J. Y. Wu, Y. I. Lee, J. Sneddon, "Recent applications of laser-induced breakdown spectrometry: a review of material approaches," Appl. Spectrosc. Rev. **39**, 27 (2004).

[18] K. Song, Y. I. Lee, J. Sneddon, "Recent developments in instrumentation for laser induced breakdown spectroscopy," Appl. Spectrosc. Rev. **37**, 89 (2002).

[19] I. B. Gornushkin, L. A. King, B. W. Smith, N. Omenetto, J. D. Winefordner, "Line broadening mechanisms in the low pressure laser-induced plasma," Spectrochim. Acta, Part B **54**, 1207 (1999).

[20] A. Essoltani, P. Proulx, M. I. Boulos, A. Gleizes, "Radiation and self-absorption in argon-iron plasmas at atmospheric pressure," J. Anal. At. Spectrom. **5**, 543 (1990).

[21] J. Scaffidi, S. M. Angel, D.A. Cremers, "Emission enhancement mechanisms in dual-pulse laser-induced breakdown spectroscopy," Anal. Chem. **78**, 24 (2006).

[22] H. Sobral, M. Villagrán-Muniz, R. Navarro-González, A. C. Raga, "Temporal evolution of the shock wave and hot core air in laser induced plasma," Appl. Phys. Lett. **77**, 3158 (2000).

[23] J. Sneddon, T. L. Thiem, Y. I. Lee, *Lasers in Analytical Atomic Spectroscopy* (VCH, New York, 1997).

[24] Y. Ralchenko, A. E. Kramida, J. Reader, NIST ASD Team (2010). NIST Atomic Spectra Database (version 4.0), [Online]. Available: http://physics.nist.gov/asd [Monday, 04-Apr-2011 23:19:27 EDT]. National Institute of Standards and Technology, Gaithersburg, MD.

[25] W. M. Andrzej, P. Vincenzo, S. Israel, *Laser-induced Breakdown Spectroscopy: Fundamentals and Applications* (Cambridge University Press, 2006)

[26] H. R. Griem, *Spectral Line Broadening by Plasma* (New York: Academic Press, 1974).

CHAPTER 8 LASER-ASSISTED MASS SPECTROMETRY

8.1 Introduction

Immediate acquisition of chemical information of solids without special pretreatment provides many advantages, especially when samples are difficult, hazardous or tedious to prepare. Little or no pretreatment, little sample consumption and fast analysis are some of the motivations for developing such techniques. One of these techniques, laser ablation/ionization, has been used extensively in solid sampling for chemical analyses, including laser-induced breakdown spectroscopy [1-3], laser ablation inductively coupled plasma mass spectrometry (LA-ICP-MS) [4], and laser ionization mass spectrometry (LIMS) [5-11]. Lasers can ablate/ionize solid materials, as long as the laser energy can be absorbed. Interferences can be minimized with laser-induced ionization compared with ionization by particle beams such as glow discharge mass spectrometry [12]. Lasers have already been used in the fields of solid analyses, including analysis of long-lived radio nuclides in solid samples [13], depth profiling of multilayer samples [14], elemental imaging of biological tissues [15], as well as geological and environmental analysis [16].

As a new ion source, direct analysis in real time (DART) was developed for rapid, noncontact analysis of materials at ambient pressure and at ground potential. It is based on the reactions of electronic or vibronic excited-state species with reagent molecules and polar or nonpolar analytes. DART has been applied to the analysis of gases, liquids, and solids. The direct detection of chemicals on surfaces without the need for sample preparation is a unique application. Because of the sampling versatility of DART, it became apparent that this device is an extremely powerful atmospheric pressure ion

source that can be combined with mass spectrometry [17]. In this study, DART was installed on a time-of-flight mass spectrometer.

The ions from laser ionization have kinetic energies of up to several hundred electron volts (eV), while time-of-flight mass spectrometry (TOFMS) can only handle ions with kinetic energies of less than 20 eV, even in reflectron mode [18]. If the pressure is too low, ions have deficient collisional cooling and cannot be sampled, whereas excessively high pressure may enhance the resistance and ion neutralization, resulting in signal reduction. According to previous studies [19], most ions can be sufficiently cooled and sampled in a relative low vacuum chamber.

Without the inductively coupled plasma (ICP) generator, ablation cell, and the consumption of buffer gas, the capital and operation costs of LIMS are much less compared with LA-ICP-MS. However, almost all LIMS systems employ vacuum chambers to hold samples, making the system unsuitable for specific applications in open air. The next major development in advancing MS technology is based on the availability of instruments that operate in ambient air. The ability to record mass spectra of samples in the laboratory or field, while they are simultaneously subject to chosen chemical and physical operations and environments, should make MS qualitatively more valuable and open many new areas of applications. Therefore, with LIMS in open air, the equipment can be further simplified for the chemical analysis of solids without a vacuum. In addition, air can play an important role as a buffer gas in reducing the kinetic energy of ions generated through laser ionization. In an open ambient environment, the LI-TOFMS process renders less signal intensity of trace elements or nonmetallic solids compared with that from a low pressure vacuum chamber. The combination of laser ionization with

another ambient chemical ionization source is a promising solution to the problem of improved ionization for chemical analysis of solids in open air.

In this study, a series of NIST copper rod samples and a pure carbon target were used in the experiment for laser ionization only and for laser ionization combined with DART. The goal of our research was to investigate the combined laser and metastable ionizations in TOFMS for element analysis of metallic or nonmetallic solids in open air. The results were compared to that from LIBS simultaneously acquired from the laser-induced plasmas. Trace elements can be detected with this system in open air with or without DART, whereas singly ionized carbon atoms can be detected from a pure carbon target only when DART was combined with laser ionization. The RSC was calculated and plotted as a function of concentration and laser pulse energy for a multielemental analysis. LODs were also calculated for different elements in both LI-TOFMS and LIBS.

8.2 Experimental methods

8.2.1. Laser system

The schematic diagram of the experimental setup used in this study is shown in Fig. 8.1. A Q-switched Nd:YAG laser (Continuum, Powerlite Precision II 8010, pulse duration of 6 ns) operating at the second harmonic (532 nm) was used in the experiments. The Nd:YAG laser beam was focused by a convex lens (with *f*/20 cm focal length). The laser beam was slightly defocused to a spot size with a diameter of about 100 μm. The laser pulse energies used in this study were between 10 - 200 mJ. The pulse repetition rate was set to 10 Hz during experiments. The distance between the Nd:YAG laser beam axis and orifice ion inlet was optimized to about 5 mm. The experiments were performed

in open air. The plume size was estimated to be around 3 mm. Samples used were certified NIST 494, 495, 498, 499, and 500 as well as a pure carbon target (Carbon Target, C, 99.999%, Kurt J. Lesker Company).

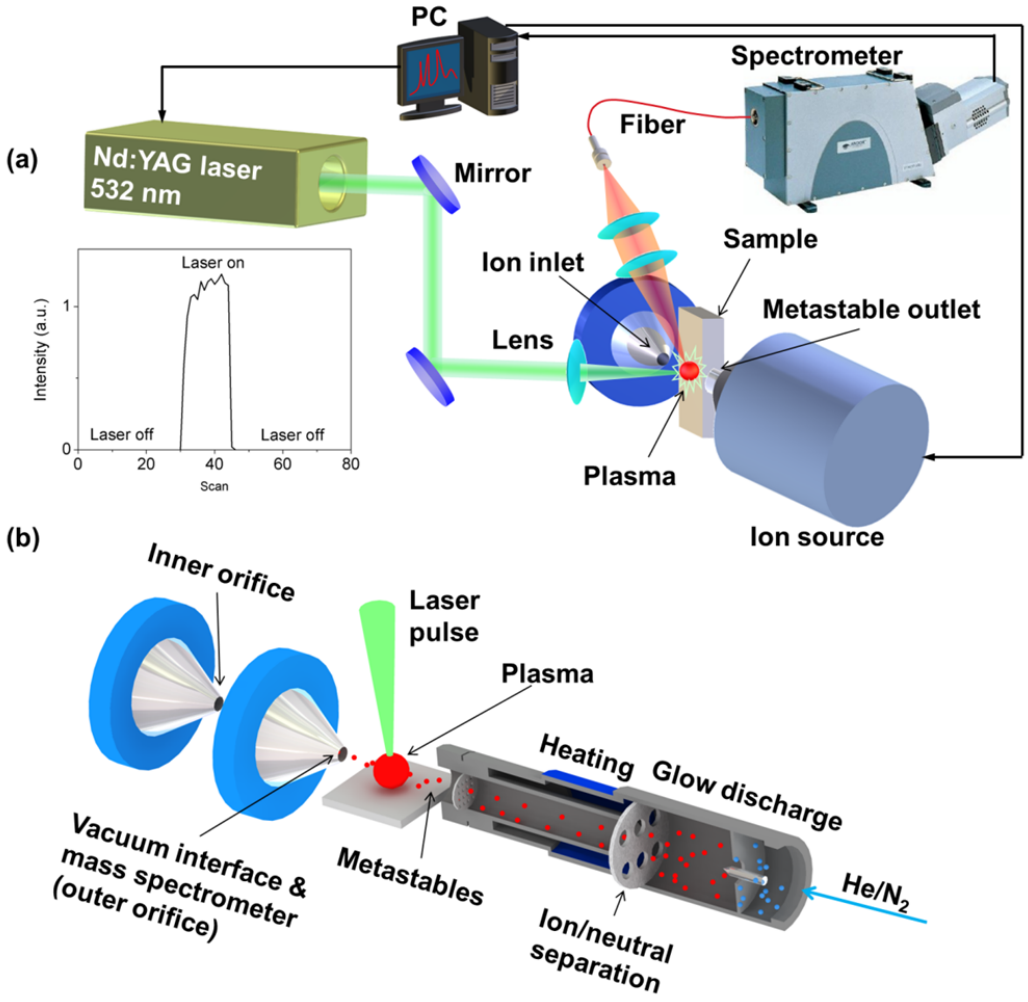

Figure 8.1 Schematic experimental setup of the LI-TOFMS system. (a) DART-combined LI-TOFMS and LIBS system. Inset: the total MS spectra signal intensity under "laser off"/"laser on" conditions; (b) illustration of the DART structure and working process.

8.2.2 LI-TOFMS

A TOF mass spectrometer (AccuTOF^{TM}, JEOL USA, Inc.) combined with a DART (DART^{TM}, JEOL USA, Inc.) ion source was used for LIMS of solids in open air. A simplified schematic of the DART ion source is shown above in Fig. 8.1(b). Helium

gas was passed into a chamber around a needle electrode held at a high potential. A glow discharge was produced between the needle and a grounded electrode. The glow discharge created both charged particles and excited-state species (metastable gaseous atoms or molecules). Afterwards, the gas flowed into a heater region that was used to control the overall temperature of the gas stream. The temperature was adjusted to facilitate thermal desorption and/or pyrolysis of the samples placed in the sample gap. Once the metastables left the heater region, they then passed through an exit grid electrode. This electrode was biased to a positive potential for positive-ion analysis (used in this study). Finally, the gas exited the ion source through a ceramic insulator cap that protects the operator from exposure to the exit grid. The resulting gas stream then ionized the samples that were placed in the sample gap. The sample ions formed in this region were then carried into the AccuTOF™ mass spectrometer inlet by both the DART gas flow and the slight vacuum at the spectrometer inlet.

The voltage of the outer orifice was set to 30 V, while the inner orifice was set to 5 V for extracting the ions using an electric field. The acquisition range was set to 8-250 m/z. The AccuTOF^{TM} mass spectrometer employs two off-axis skimmers and a bent radio frequency (RF) ion guide to efficiently transport ions from atmospheric pressure to high vacuum, while simultaneously keeping neutral contamination out of the system. The analyzer is an orthogonal, two-stage acceleration, TOFMS incorporating a single-stage reflectron. The detector is comprised of dual microchannel plates with a continuous digital averager as the data acquisition system. This system features high sensitivity, fast detection, and high dynamic range. The resolving power is R≥6000 (full width at half maximum (FWHM)). The mass range is 4-10000. The acquisition speed for the spectrum is up to 16000

spectra/sec. The spectrum recording speed is up to 10 spectra/second. Mass accuracy is a larger value of 5 parts per million (ppm) or 2 millimass units (mmu). Usually the MS spectra were acquired (counted by scans) during certain time periods and averaged over 30 seconds for each MS spectrum. The spectrometer can detect real-time change of the total spectral intensity. However, the temporal resolution was not high and cannot be controlled (or triggered) for temporal evolution measurement of the plasma. Therefore, we cannot analyze the evolution of plasmas, which have lifetimes of several tens of microseconds.

8.2.3 LIBS

The optical emission from the plasmas was coupled to an optical fiber by two convex lenses [with *f*/6 cm (closer to plasma) and *f*/10 cm focal length, respectively]. The optical fiber, with a core diameter of 50 μm, was coupled to the echelle spectrometer (Andor Tech., Mechelle 5000). We only studied the optical emissions at the center of the plasmas where the continuum background emission is the strongest. The spectrally resolved lines were detected by an intensified charge coupled device (ICCD) (Andor Tech., iStar, DH734). The ICCD camera was operated in the gated mode. The ICCD has a wide spectral range of 200-975 nm, with a wavelength accuracy better than ±0.05 nm. The spectral resolution ($\lambda/\Delta\lambda$) (FWHM) is up to 6000. The gate delay and gate width can be adjusted so that the spectra can be obtained at different time delays after the laser pulse. The laser and spectrometer were synchronized by a digital delay generator (Stanford Research System DG535, 5 ps delay resolution). The surface profile of the laser-ablated sample was characterized by a stylus profiler (XP-2, AMbios Technology).

8.3 Results and discussion

8.3.1 Investigation of the laser ablation ionization process

In the LI-TOFMS experiment, a plume-ion inlet orthogonal geometry in the source was used as an extraction process in which ions were cooled close to the thermal equilibrium state and then diffused into the orifice ion inlet [19]. The kinetic energies of the sampled ions were so small that they could be ignored in comparison with the electric potential energy that was determined by the voltage applied on the orifice ion inlet (outer orifice 30 V and inner orifice 5 V, net 25 V for extraction). Hence, all of the sampled ions had approximately the same energy.

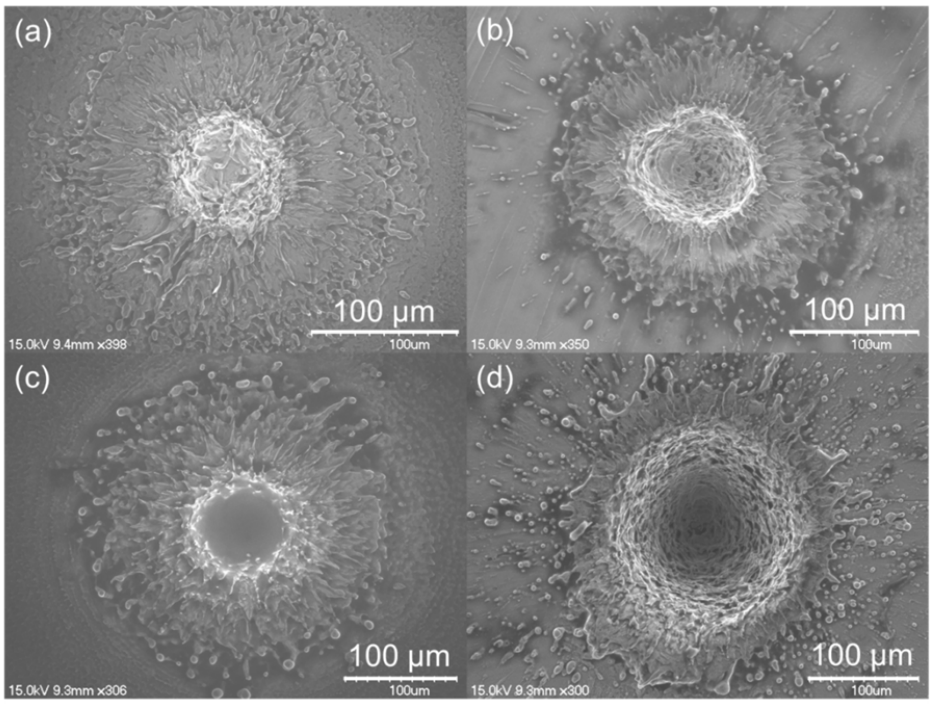

Figure 8.2 (a) and (b) are the SEM images of laser ionization pits produced by single pulses with an energy of 50 and 200 mJ, respectively; (c) and (d) are the SEM images of laser ionization pits produced by 50 pulses with an energy of 50 and 200 mJ, respectively.

Higher laser pulse energy can facilitate the ablation of more materials from the target. Therefore, when the laser pulses have sufficient energy, more matrix element (Cu) and trace elements at ppm levels in the target can be ablated and ionized for mass spectrometer collection. Figure 8.2 shows the scanning electron microscopy (SEM) images of the NIST 499 copper rod surfaces after laser ablation. The ablated material was spread outside the laser ablation pit. As shown in Fig. 8.2(a), only slight ablation can be found when a single low pulse energy (50 mJ/pulse) was used. However, when the pulse energy increased to around 200 mJ, the size of the laser ablation pit became larger (Fig. 8.2(b)). After 50 pulses, the one with 200 mJ (Fig. 8.2(d)) ablated much more material than the one with a pulse energy of 50 mJ (Fig. 8.2(c)).

The surface profiles of the laser-ablated areas were characterized by a stylus profiler. Figure 8.3 shows the surface profiles of the ablation pits. The volume of the 50 pulses with a pulse energy of 200 mJ was around 8.45×10^{-6} cm^{-3} (1.69×10^{-7} cm^{-3}/pulse), while the ablation volume of the pit with 50 pulses of 50 mJ was around 1.88×10^{-6} cm^{-3} (3.76×10^{-8} cm^{-3}/pulse). The weights of the ablated copper (8.94 g/cm^{-3}) according to the volumes were 7.55×10^{-5} g (1.51×10^{-6} g/pulse) and 1.68×10^{-5} g (3.36×10^{-7} g/pulse) for 200 and 50 mJ pulses, respectively. This can roughly be used as a reference of the amount of material ablated, including certified trace elements, which can be calculated from their concentrations. The profile diagrams showed a similar shape as that in the SEM images. When the pulse energy increased, the ablated pit became much larger than the one with lower pulse energy. Laser pulses with energies higher than 200 mJ can easily ablate large metal particles, which results in blockage of the entrance of the orifice

ion inlet. Therefore, laser pulses with a pulse energy lower than 200 mJ are recommended.

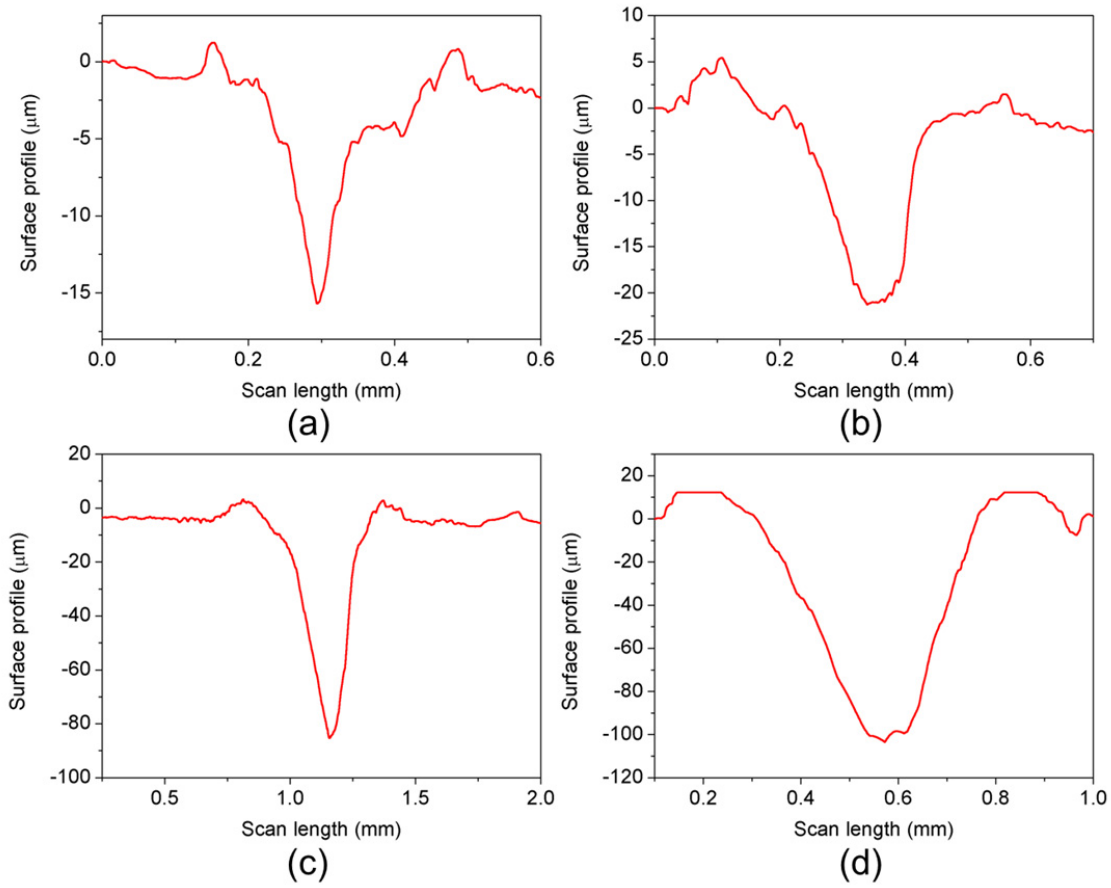

Figure 8.3 (a) and (b) are the surface profiles of the laser ionization pits produced by single pulses with an energy of 50 and 200 mJ, respectively; (c) and (d) are the surface profiles of the laser ionization pits produced by 50 pulses with an energy of 50 and 200 mJ, respectively.

8.3.2 LI-TOFMS determination of trace elements in NIST samples in open air

Trace elements from the NIST 499 sample were ionized and detected by LI-TOFMS. Several elements can be detected with a sufficiently high laser pulse energy. As shown in Fig. 8.4, the MS spectra were acquired with laser ablation only (without DART) with laser pulses with a pulse energy of 200 mJ. Several trace elements were observed in

the spectra as singly charged atoms, including Fe, Cr, Mn, Ni, Ca, Al, and Ag. Na element was also detected in the laser ionization process, which may be due to slight surface contamination.

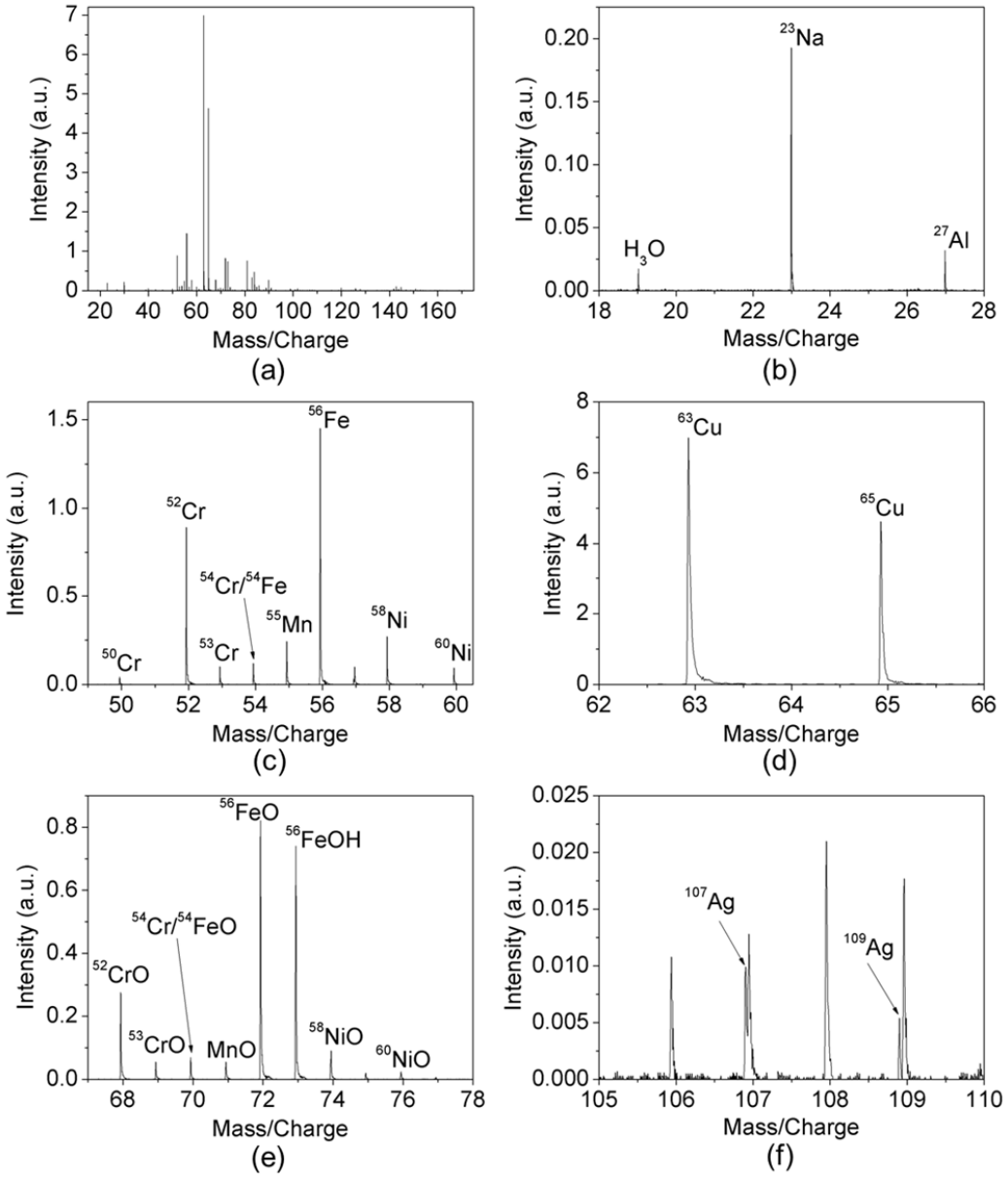

Figure 8.4 (a) The whole MS spectrum of the NIST 499 sample with laser ionization only; (b)-(f) different isotopes and their compounds detected at different m/z ratios, including $^{23}Na^+$, $^{52}Cr^+$, $^{56}Fe^+$, $^{58}Ni^+$, $^{63}Cu^+$, $^{65}Cu^+$, CrO^+, FeO^+, $FeOH^+$, MnO^+, NiO^+, and $^{107}Ag^+$.

Ionized metal oxides and hydroxides were also detected in the MS spectra. No doubly charged elements were observed in the spectra, since the ambient air provides enough collision cooling of the multicharged ions with high energies. The repetition frequency of the laser pulses was set to 10 Hz, whereas the laser-induced plasmas existed for less than hundreds of microseconds. Therefore, the effective detection duration was very limited. The amount of trace elements was very small compared with the copper matrix. Moreover, some elements are easily combined with air (such as oxygen and nitrogen) to form compounds with no charge on them, thus many other trace elements in the sample were not observed in the spectra. Another possibility is three-body recombination since the electron density can be very high at open-air condition [26, 29].

The laser ionization of solids in open air was a complex process which needs a systematic analysis. For this purpose, we selected several parameters of different elements to study the trend of this process. From Tables 8.1, 8.2, and 8.3, we listed the parameters of the elements contained in the sample and found that there are three major factors affecting the detectability of the elements. First, from Table 8.1, the first ionization potential of the element can affect the detection of the element. Elements with low ionization potential can easily be detected even though they have very low concentrations, such as Al, Ca, Cr, Mn, Ag, Ni, and Fe. For elements with high ionization potentials (e.g., Si, Sb, Cd, etc.), however, LI-TOFMS can hardly detect them even with very high pulse energy (200 mJ/pulse or higher). Second, elements with increasing atomic weight lower the detection sensitivity. Heavy atoms (such as Sn, Sb, Pb, etc.) can hardly be detected, since their heavy masses reduce the possibility of their flying into the orifice ion inlet. Third, there is a phase explosion [20] in the laser ionization process,

which leads to ablation and ionization. Therefore, the melting or boiling point partly influences this process. The interaction between the nanosecond laser pulses and solid surfaces is prone to preferentially atomize elements with low melting and boiling points, leading to high RSC values [21,22].

Table 8.1 Parameters of the elements in the NIST Cu sample with increasing ionization potential.

Elements	Boiling Point (°C)	First Ionization Potential (eV)	Concentration (μg/g)	Detected Atomic Mass
Al	2519	5.9858	<2	26.9846
Ca	1484	6.1132	<0.3	39.9632
Cr	2671	6.7665	0.5	51.9396, 49.9453, 52.9404, 53.9383
Mn	2061	7.4340	0.3	54.9379
Ag	2162	7.5762	114	106.9029, 108.9009
Ni	2913	7.6398	504	57.9359, 59.9300, 60.9292, 61.9286
Cu	2562	7.7264	99.79%	62.9304, 64.9290
Fe	2861	7.9024	21	55.9346
Si	3265	8.1517	<2	—(not detected)
Sb	1587	8.6084	30	—
Cd	767	8.9938	<1	—
Te	988	9.0096	50	—
Au	2856	9.2255	4	—
Zn	907	9.3942	41	—
Se	685	9.7524	95	—
As	603	9.7886	47	—
S	444.6	10.3600	10	—

As can be seen in Table 8.3, increasing the boiling point can reduce the detectability of the elements. Ti cannot be detected due to its high boiling point, although it has very low first ionization potential (6.8281 eV).

Table 8.2 Parameters of the elements in the NIST Cu sample with increasing atomic weight.

Elements	Boiling Point (°C)	First Ionization Potential (eV)	Concentration (µg/g)	Detected Atomic Mass
Al	2519	5.9858	<2	26.9846
Ca	1484	6.1132	<0.3	39.9632
Cr	2671	6.7665	0.5	51.9396, 49.9453, 52.9404, 53.9383
Mn	2061	7.4340	0.3	54.9379
Fe	2861	7.9024	21	55.9346
Ni	2913	7.6398	504	57.9359, 59.9300, 60.9292, 61.9286
Cu	2562	7.7264	99.79%	62.9304, 64.9290
Ag	2162	7.5762	114	106.9029, 108.9009
Cd	767	8.9938	<1	—
Sn	2602	7.3439	90	—
Sb	1587	8.6084	30	—
Te	988	9.0096	50	—
Au	2856	9.2255	4	—
Pb	1749	7.4167	114	—
Bi	1564	7.2855	10.5	—

Table 8.3 Parameters of the elements in the NIST Cu sample with increasing boiling point.

Elements	Boiling Point (°C)	First Ionization Potential (eV)	Concentration (µg/g)	Detected Atomic Mass
Ca	1484	6.1132	<0.3	39.9632
Mn	2061	7.434	0.3	54.9379
Ag	2162	7.5762	114	106.9029, 108.9009
Al	2519	5.9858	<2	26.9846
Cu	2562	7.7264	99.79%	62.9304, 64.9290
Cr	2671	6.7665	0.5	51.9396, 49.9453, 52.9404, 53.9383
Fe	2861	7.9024	21	55.9346
Ni	2913	7.6398	504	57.9359, 59.9300, 60.9292, 61.9286
Co	2927	7.881	0.5	—
Si	3265	8.1517	<2	—
Ti	3287	6.8281	<1	—

The orthogonal geometry between the plume and the orifice ion inlet can facilitate the laser beam introduction and avoid energetic ions from being injected into the ion inlet. However, the orthogonal extraction has less sampling efficiency compared to the

on-axis geometry routinely used. To enhance sensitivity, more intensive laser pulses were applied in this study. Though the generation of multicharge ions increases with increasing laser pulse energy [23-26], most of the highly charged ions were charge-reduced by frequent recombinations. During laser ionization, the amount of ions generated is strongly dependent on both the laser intensity and the surrounding conditions. After absorption of a high-energy laser pulse, the target is evaporated and ionized, creating a dense plasma plume above the material surface. Even in a high vacuum, most particles produced by laser ablation undergo extensive collisions and recombination in the freely expanding plumes. Electrons are preferentially attracted to multiply charged ions that have higher positive valences than singly charged ions. With the presence of the ambient gas, recombinations take place through frequent collisional processes (mainly three-body, possibly radiative two-body or charge exchange collisions), which result in preferential charge reduction of highly charged ions [26-29]. The ratio of highly charged ions in our experiment is significantly less than that found in other investigations in high vacuum. For example, it was observed that the Zn^{2+} to Zn^{+} and Y^{2+} to Y^{+} ratios were about 50% [30] and 30% [31], respectively, in LI-TOFMS at relatively high laser energies.

The time profiles of singly and doubly charged ions are evidently different. Singly charged ions exist for approximately 1 ms, while doubly charged ions last only tens of microseconds [19]. After the free expansion, the active ions and electrons undergo collisions with the abundant ambient air molecules. Most electrons are recombined or escape, whereas ions are slowed and cooled down after collisions, then diffuse into the ion inlet. In the experiment, the Nd:YAG laser was operated at the maximum repetition rate of 10 Hz, leaving 100 ms for ion detection per laser pulse.

With higher laser pulse energy, MS spectral signal intensity of some trace elements increase accordingly. As seen in Fig. 8.5(a), the intensities of elements increase according to the increasing laser pulse energy. The trace elements can hardly be observed with a pulse energy of less than 60 mJ. When the pulse energy increases to more than 100 mJ, many trace elements can be detected. With higher pulse energy (more than 150 mJ), the intensities reach their maximum. Further increase in the pulse energy would cause the larger polyatomic cluster to block the orifice ion inlet (0.4 mm diameter). The blocking will cause ion current saturation for the orifice, since the ion signals do not increase obviously after 150 mJ. From Fig. 8.5(b), ^{56}Fe intensity dependence on the pulse energy was compared to the ^{63}Cu peak intensity. The intensity of the ^{63}Cu increased slightly and then remained the same with increasing pulse energy, which may have reached its detection saturation. Figure 8.5(c) shows the whole spectrum with the species detected from the laser-induced plasmas produced by laser pulses with an energy of 200 mJ. Figure 8.5(d) shows the peak intensities of ^{63}Cu, ^{56}Fe, ^{52}Cr, ^{55}Mn, ^{58}Ni, ^{40}Ca, ^{27}Al, and ^{107}Ag with the pulse energy of 200 mJ. All the NIST copper rod samples (499, 494, 495, 498, and 500) were measured using the same process. The calculation of the LOD will require the spectral data from a series of NIST samples.

Ions generated in the laser-induced plasmas have initial kinetic energies of several hundred electron volts [32] and are subsequently cooled down by the collision with the buffer gas. The average collision number between ions and ambient air molecules, which decides the initial kinetic energies of ions entering the ion inlet, is determined by both the pressure and the distance. When the supersonic expansion is considered, however, the collision number drops drastically. The actual collision number is not yet well known.

Nevertheless, after these collisions, the kinetic energy has been reduced to a small range, within which ions can be successfully sampled into the ion inlet.

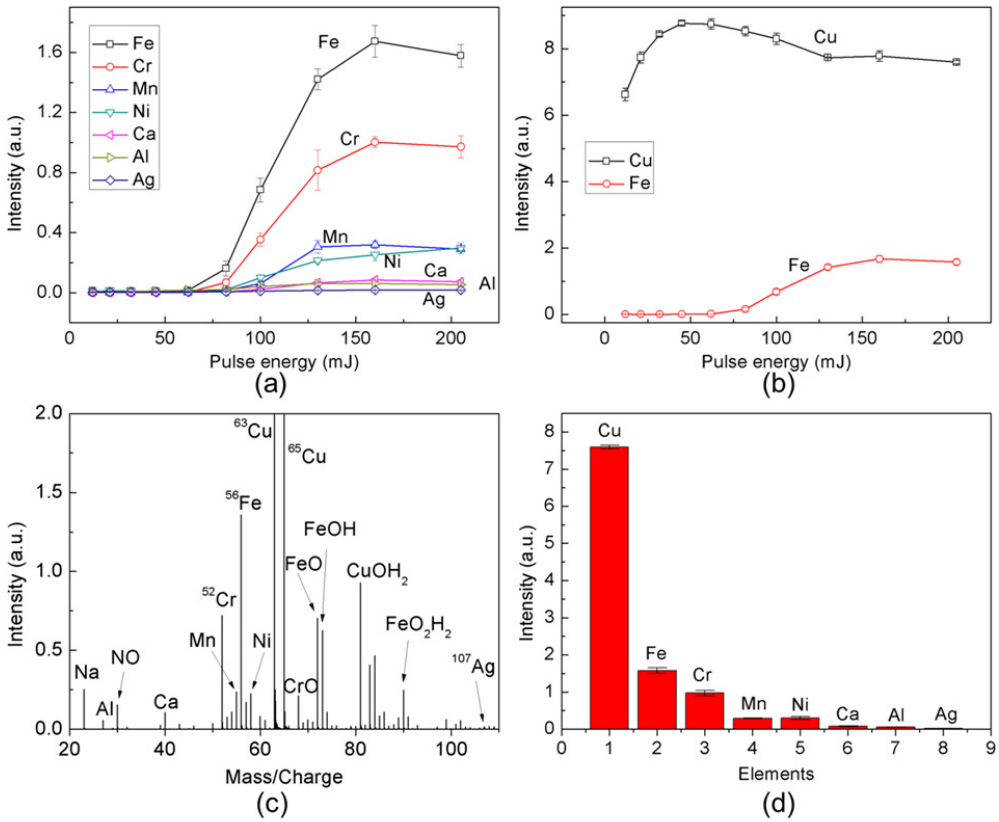

Figure 8.5 (a) MS isotope peak intensity as a function of pulse energy; (b) the matrix Cu peak intensity was compared to that of Fe; (c) MS spectrum showing the detected species from the laser-induced plasmas; (d) at 200 mJ, the peak intensity of different elements in the NIST 499.

8.3.3 Relative sensitivity coefficient and limit of detection

The relative sensitivity coefficient (RSC) is a function of the physical and chemical properties of the sample and the analyte (ionization potential, melting point, and boiling point of the trace element, dissociation energy of analyzed compounds, sample composition, etc.) and of laser ion source parameters (laser pulse energy, ion focusing

conditions, initial ion energy, etc.). By determining the RSC, all these effects can be considered indirectly and the detection accuracy can be improved [5].

The quantitative mass spectrometric analysis was carried out by measuring the ion current extracted from the laser plasmas. The ion current is proportional to the element concentration, c_x, of a trace element, x. A quantitative determination of element concentration, c_x, was carried out in comparison with an internal standard element with well-known concentration, c_v. The following analysis equation was applied to evaluate the concentration of the chemical elements [5]:

$$c_x = c_v\left(\frac{I_x}{I_v}\frac{E_v}{E_x}\frac{H_v}{H_x}\right), \tag{8.1}$$

where I_v and I_x are the ion currents (or the numbers of ions) measured for the internal standard v and for the trace element x (MS spectral intensities were used here); H_v and H_x are the respective isotopic abundances, and E_v and E_x are the respective relative element sensitivities. Thus the RSC is E_x/E_v, which can be derived from Equation (8.1):

$$RSC = \frac{E_x}{E_v} = \frac{I_x / C_x H_x}{I_v / C_v H_v}. \tag{8.2}$$

To calculate RSC in this research, multiple charged ions must be counted in since a large fraction of those peaks are typically present in spectra [9]. With ambient air as the buffer gas in our experiments, however, there were more frequent three-body combinations comparing with the situation in the vacuum. The multiple charged ions were recombined into singly charged ions or neutrals [7], such that their intensities were so low that they could be ignored in the RSC calculation. As expected, doubly charged ion peaks of $^{27}Al^{+}$, $^{40}Ca^{+}$, $^{56}Fe^{2+}$, $^{52}Cr^{2+}$, $^{55}Mn^{2+}$, $^{58}Ni^{+}$ and $^{63}Cu^{2+}$ were not observed.

LODs have been evaluated using the 3σ-International Union of Pure and Applied Chemistry (IUPAC) criteria. According to the 3σ-IUPAC definition, the LOD for a given element is the concentration that produces a net line intensity proportional to three times the standard deviation of the background, σ_B:

$$LOD = 3\frac{\sigma_B}{S}, \tag{8.3}$$

where S is the slope of the calibration curve for the specific m/z lines [33]. Linear fit was done with ORIGIN 7.5 using signal intensities and concentrations for all elements for five NIST copper samples with only one isotope representing each element.

As seen in Table 8.4, the RSCs are not uniform for most elements. The high RSCs of Ca, Cr and Mn are due partly to their relatively low ionization potentials and boiling points. The low RSC of Ag is due partly to its high atomic weight.

Table 8.4 Parameters of the elements in Cu sample with increasing boiling point.

Boiling Point (°C)	Elements (Isotope Used)	Ionization Potential (eV)	Concentration (μg/g)	Detected Atomic Mass	RSC	LOD (μg/g)
2519	^{27}Al	5.9858	<2	26.9846	0.41	—
1484	^{40}Ca	6.1132	<0.3	39.9632	5.27	—
2671	^{52}Cr	6.7665	0.5	51.9396	25.35	1.24
2061	^{55}Mn	7.4340	0.3	54.9379	12.13	3.02
2162	^{107}Ag	7.5762	114	106.9029	0.02	15.38
2913	^{58}Ni	7.6398	504	57.9359	0.54	12.69
2861	^{56}Fe	7.9024	21	55.9346	1	6.24

RSCs of elements were plotted as functions of their concentrations. As shown in Fig. 8.6(a), the RSCs depend on element concentrations, especially for Cr and Mn. It can be concluded that RSCs of most metal elements depend on their concentrations in samples.

The dependence of RSCs on the laser pulse energy in a range of 10 - 200 mJ/pulse was studied on the NIST 499 copper sample. As shown in Fig. 8.6(b), it can be observed that RSCs of ^{52}Cr and ^{55}Mn relative to ^{56}Fe increase with increasing laser pulse energy. However, the RSCs of ^{40}Ca and ^{27}Al decrease compared to ^{56}Fe. The reason is presumably due to the increase in the sensitivity of ^{56}Fe for the increasing laser pulse energy, while ^{55}Mn and ^{52}Cr increase even faster with respect to the increasing laser pulse energy because of their lower ionization potentials. The RSCs of ^{40}Ca and ^{27}Al are relatively high when the laser pulse energy is low, since their ionization potentials are very low (6.1132 and 5.9858 eV, respectively). The RSCs of ^{40}Ca and ^{27}Al decrease with increasing laser pulse energy, because the laser pulse energy is sufficiently high to ionize the reference element - ^{56}Fe. The increase in the RSC of ^{56}Fe results in the decrease in the RSCs of ^{40}Ca and ^{27}Al.

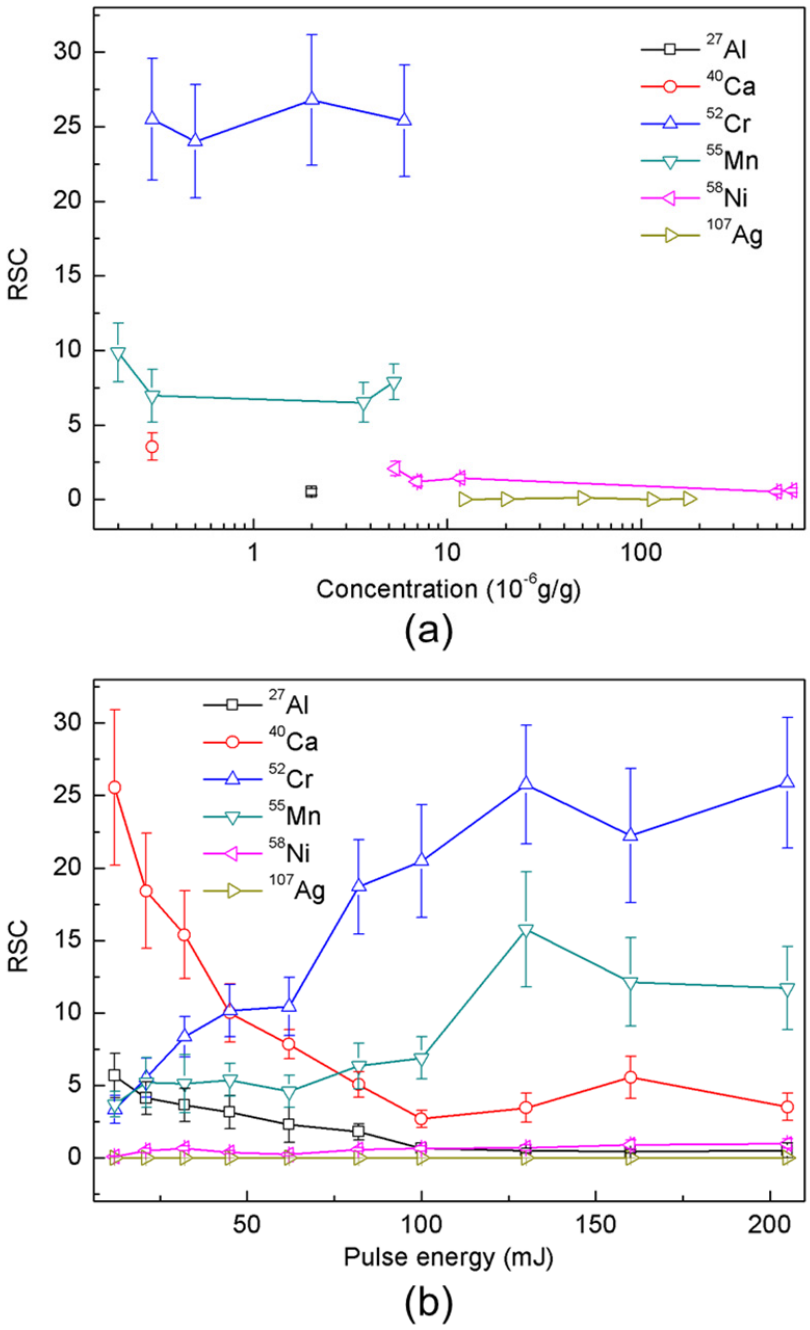

Figure 8.6 RSCs of different trace elements with ^{56}Fe as a reference element. (a) RSCs of elements at different concentrations; (b) RSCs of elements with different laser pulse energies.

8.3.4 DART-combined LI-TOFMS for metallic NIST samples and pure carbon target

Usually the MS signals obtained using DART as a single ionization source for metallic and nonmetallic samples are very low due to the ionization potentials. However, DART can be used for ionization of species produced by the laser ablation process. Therefore, DART was combined with LI-TOFMS to analyze both metallic and nonmetallic samples in this study. Metallic samples include NIST 494, 495, 498, 499, and 500, whereas the nonmetallic sample is a pure carbon target.

To improve the detectability of trace elements, especially those with higher first ionization potentials, ambient metastable (from DART) induced chemical ionization was used as an extra ionization process beside laser ionization. From Fig. 8.7, MS spectra were acquired when laser ionization was combined with DART. Figure 8.7(a) shows the whole spectrum from an m/z range of 15-175. The highest peak is the H_3O^+ metastable water molecule, which was mainly used for positive ionization purpose in DART. However, during our experiments on DART-combined LI-TOFMS, the enhancement of ion signals generated from laser-induced plasmas was not stable for metallic samples. This result is due to laser-induced breakdown of the H_3O^+ stream, which causes the reduction of laser pulse energy for ablation of the solid surface. Sometimes, the DART molecules can even reduce the ion signals of the metals due to the absorption of laser power by the DART molecules.

The DART-combined laser ionization can be used for metallic samples only when the laser pulse energy is sufficiently low. When the pulse energy reaches the ablation limit of the DART molecules, the laser energy is absorbed by DART molecules. Usually

laser pulses with an energy below 100 mJ were used in DART-combined LI-TOFMS. The laser pulse energy for the results shown in Fig. 8.7 was ~75 mJ.

The ionization process for nonmetallic elements stops quickly after the laser pulse because of the rapid drop in the plasma temperature and the high ionization potentials of nonmetallic atoms. On the other hand, due to the presence of ambient air, frequent recombination takes place through collisional processes in the plasmas. Recombination rates of nonmetallic ions are higher than those of metallic ions [26]. As a consequence, the duration of nonmetallic ions is less than that of metallic ions.

Signal of singly charged carbon atoms can be detected only when the LI-TOFMS was combined with DART. Although the signal was very low, singly charged carbon atoms can be detected only when the LI-TOFMS was combined with DART, due to the high ionization potential of carbon atoms. The DART stream assists the ionization process of materials with high ionization potential. The population of singly charged carbon atoms increased, since the laser ablation process itself cannot ionize a sufficient number of carbon atoms (as shown in Fig. 8.8).

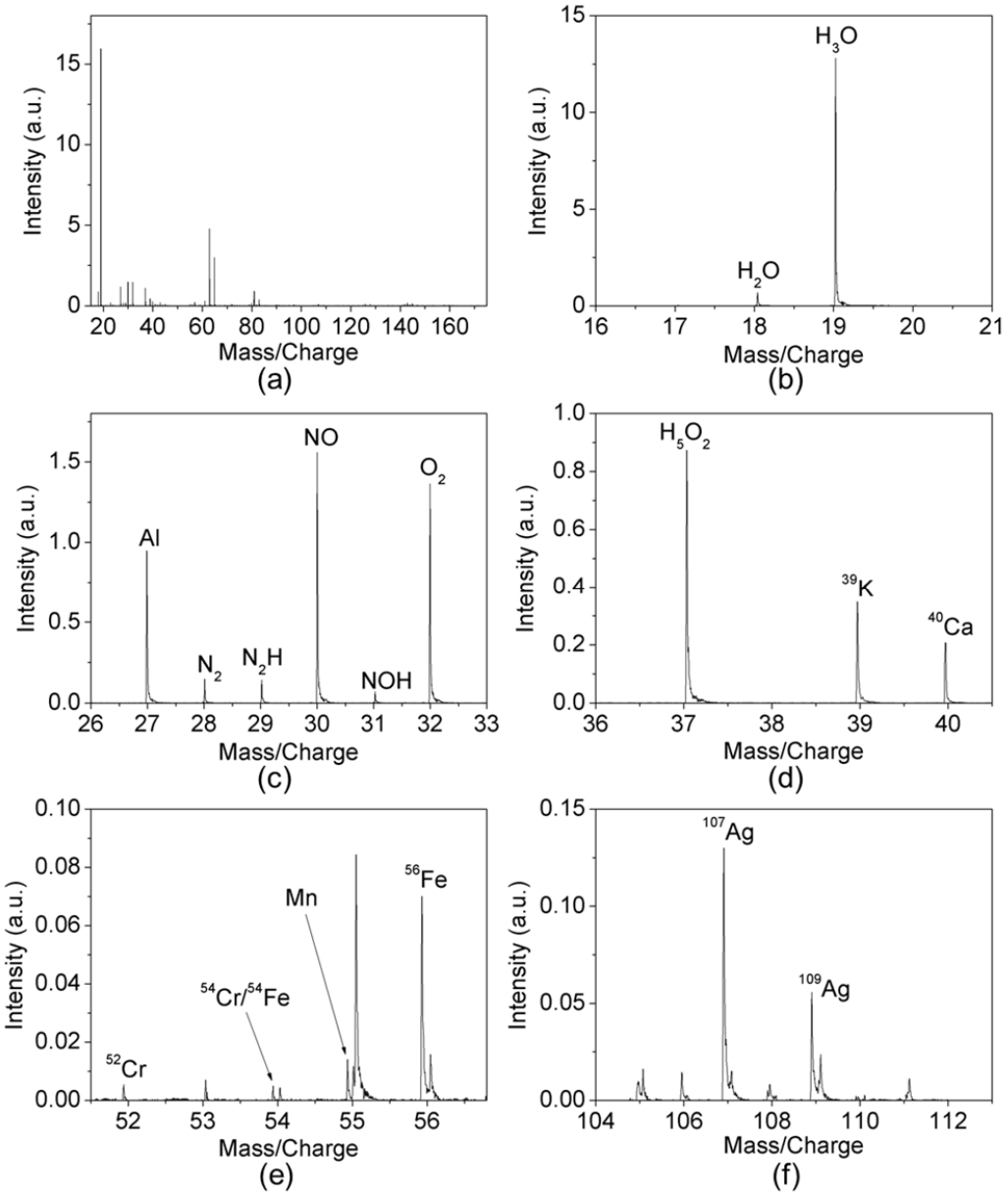

Figure 8.7 (a) The whole MS spectrum of the NIST 499 sample under LI-TOFMS + DART condition; (b)-(f) different isotopes and its compounds detected at different m/z, including H_2O^+, H_3O^+, $^{27}Al^+$, N_2^+, NO^+, O_2^+, $H_5O_2^+$, $^{39}K^+$, $^{40}Ca^+$, $^{52}Cr^+$, $^{55}Mn^+$, $^{56}Fe^+$, $^{107}Ag^+$, etc.

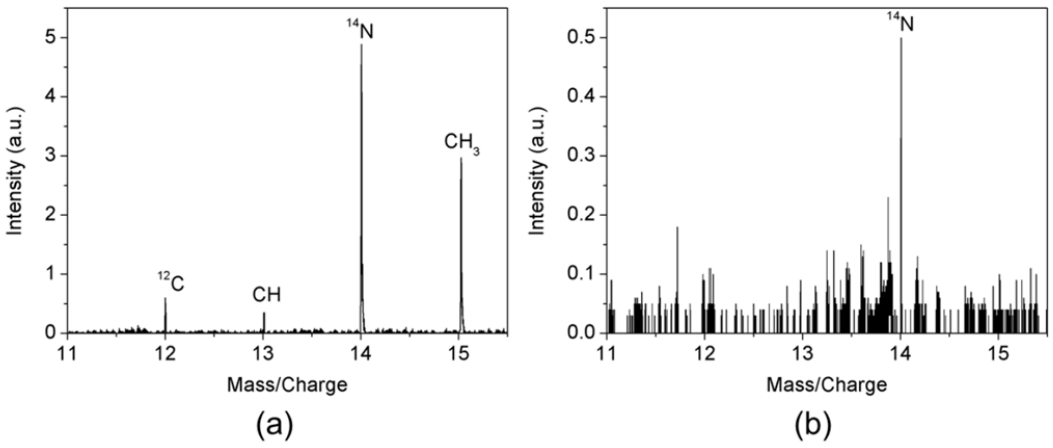

Figure 8.8 (a) MS spectrum acquired with laser ionization combined with DART. (b) MS spectrum with only laser ionization.

8.3.5 LIBS spectra of the NIST 499 sample

The LIBS spectra setup was shown in Fig. 8.1(a). They were acquired simultaneously with the TOFMS spectra for comparison. As shown in Fig. 8.9 and Table 8.5, the LIBS spectra consist largely of Cu and O atomic lines. In addition, some trace elements can also be detected through the spectrometer, including singly and doubly charged ions due to their atomic properties (such as ionization potential). The spectra were acquired with a delay of 5 μs. Within tens of microseconds, the plasmas remained at sufficiently high temperature. Therefore, doubly charged ions can be seen in the LIBS spectra. Nevertheless, the lifetimes of doubly charged ions are much shorter than those of the singly charged ions [19], and the doubly charged ions disappear faster than singly charged ions.

The LODs calculated through Equation (8.3) are shown in Table 8.5. The LODs were higher than those obtained from LI-TOFMS (Table 8.4). Therefore, LIBS has relatively poor LOD compared to LI-TOFMS, although it can provide temporal evolution of atomic lines for the determination of laser-induced plasma process.

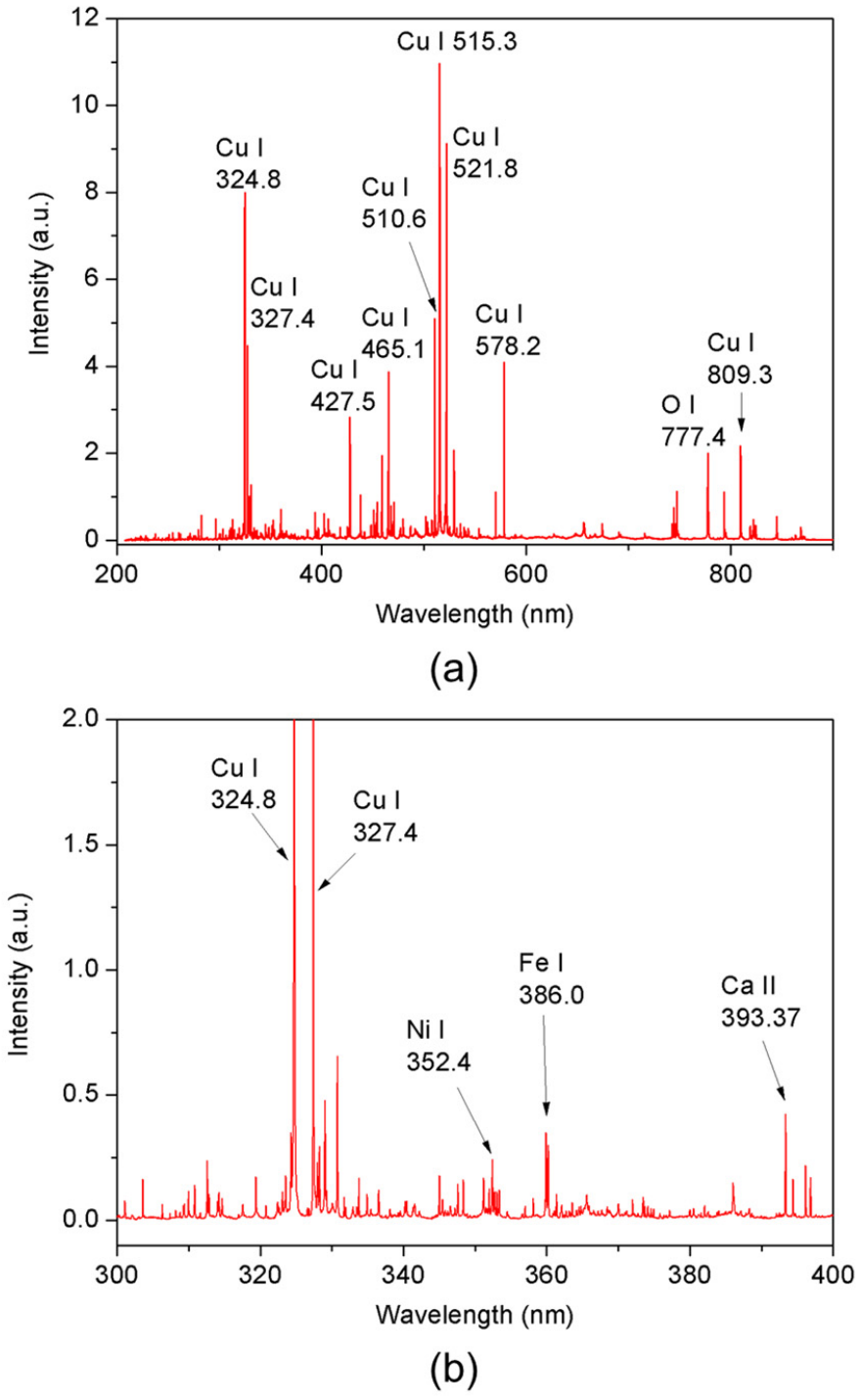

Figure 8.9 (a) LIBS spectrum of a NIST 499 sample with a laser pulse energy of 200 mJ; (b) magnified spectrum for showing atomic lines other than Cu, including Ni I, Fe I, and Ca II.

Table 8.5 Detected LIBS spectral lines (beside Cu lines).

Elements	Detected Atomic Lines (nm)	LOD (μg/g)
Al	308.22 (I), 309.3 (I), 396.16 (I), 394.42 (I)	—
Ca	393.37 (II), 396.85 (II), 373.72 (II), 422.67 (I)	—
Mn	403.076 (I), 403.33 (II)	~13.8
Ni	352.454 (I), 226.61 (II)	~253.5
Fe	386.02 (I), 371.99 (I), 259.95 II, 239.53 II	~89.5
Mg	285.21 (I), 518.36 (I), 383.81 (I)	—

8.4 Conclusions

In summary, combined laser ionization and metastable ionization TOFMS (LI-MI-TOFMS) in open air has been investigated for qualitative and semiquantitative multielemental analyses of solid samples. The LI-MI-TOFMS of solids in open air was carried out by analyzing MS spectra and semiquantitative numerical calculations. Trace elements in the NIST samples were detected, such as Fe, Cr, Mn, Ni, Ca, Al, and Ag. MS signal intensities from these trace elements were found to increase with increasing laser pulse energy. The RSCs of the elements with relatively high ionization potentials increase with increasing laser pulse energy (e.g., Fe, Cr, Mn, and Ni). The effects of the DART and LI-TOFMS combination were not significant for those trace elements due to the absorption of laser energy by the DART H_3O^+ stream. Although the signal intensity was very low, the pure carbon target could be detected only when DART was combined with LI-TOFMS due to the high ionization potential of carbon atoms and the ambient air environment. Semiquantitative measurements were performed according to the correlation between signal intensity and element composition. RSCs were calculated and analyzed and found to depend on element concentrations and laser pulse energy. Higher laser pulse energy leads to an increase in the RSCs of some trace elements (e.g., Mn, Cr, and Ni). The data from LIBS spectra was analyzed and compared with the MS spectra.

The LI-MI-TOFMS approach is a promising alternative for qualitative and semiquantitative elemental analysis of solid samples in open air.

Table 8.6 Summary of the LAMS technique.

Laser-Assisted Mass Spectrometry (LAMS)	
Realization approaches	Laser ionization combined with metastable ambient ion source – direct analysis in real-time (DART).
Principle	Ion current due to the ionization from both a laser irradiation and metastable stream.
Combination possibility	LAMS can be combined with LIBS, which is electronic transition of atoms in a laser-induced plasma.
Spectral resolution	λ/Δλ (FWHM) is up to 6000
Spatial resolution	50-100 μm (focused laser spot size of an Nd:YAG laser)
Application	Determining trace elements in a target. Samples can be nuclear isotopes, trace elements from soil, and biological samples.

8.5 References

[1] L. J. Radziemski, “From LASER to LIBS, the path of technology development,” Spectrochim. Acta Part B **57,** 1109 (2002).

[2] X. N. He, W. Hu, C. M. Li, L. B. Guo, Y. F. Lu, “Generation of high-temperature and low-density plasmas for improved spectral resolutions in laser-induced breakdown spectroscopy,” Opt. Express **19**, 10997 (2011).

[3] L. B. Guo, C. M. Li, W. Hu, Y. S. Zhou, B. Y. Zhang, Z. X. Cai, X. Y. Zeng, Y. F. Lu, “Plasma confinement by hemispherical cavity in laser-induced breakdown spectroscopy,” Appl. Phys. Lett. **98**, 131501 (2011).

[4] R. E. Russo, X. L. Mao, H. C. Liu, J. Gonzalez, S. S. Mao, “Laser ablation in analytical chemistry-a review,” Talanta **57**, 425 (2002).

[5] A. Vertes, R. Gijbels, F. Adams, *Laser Ionization Mass Analys*is, Wiley Interscience: New York, 1993.

[6] J. He, W. Zhong, C. Mahan, W. Hang, “Laser ablation and ionization time-of-flight mass spectrometer with orthogonal sample introduction and axial field rf-only quadrupole cooling,” Spectrochim. Acta Part B **61**, 220 (2006).

[7] W. Hang, “Laser ionization time-of-flight mass spectrometer with an ion guide collision cell for elemental analysis of solids,” J. Anal. At. Spectrom. **20**, 301 (2005).

[8] D. Peng, J. He, Q. Yu, L. Chen, W. Hang, B. Huang, “Parametric evaluation of laser ablation and ionization time-of-flight mass spectrometry with ion guide cooling cell,” Spectrochim. Acta Part B **63**, 868 (2008).

[9] A. A. Sysoev, A. A. Sysoev, "Can laser-ionisation time-of-flight mass spectrometry be a promising alternative to laser ablation/inductively-coupled plasma mass spectrometry and glow discharge mass spectrometry for the elemental analysis of solids?" Eur. J. Mass Spectrom. **8**, 213 (2002).

[10] J. S. Becker, H. J. Dietze, "Laser ionization mass spectrometry in inorganic trace analysis," Fres. J. Anal. Chem. **344**, 69 (1992).

[11] J. He, R. Huang, Q. Yu, Y. Lin, W. Hang, B. Huang, "A small high-irradiance laser ionization time-of-flight mass spectrometer," J. Mass. Spectrom. **44**, 780 (2009).

[12] N. Omenetto, "Role of lasers in analytical atomic spectroscopy: where, when and why – Plenary lecture," J. Anal. At. Spectrom. **13**, 385 (1998).

[13] J. S. Becker, C. Pickhardt, H. J. Dietze, "Laser ablation inductively coupled plasma mass spectrometry for the trace, ultratrace and isotope analysis of long-lived radionuclides in solid samples," Int. J. Mass Spectrom. **202**, 283 (2000).

[14] V. Margetic, M. Bolshov, A. Stockhaus, K. Niemax, R. Hergenroder, "Depth profiling of multi-layer samples using femtosecond laser ablation," J. Anal. At. Spectrom. **16**, 616 (2001).

[15] J. S. Becker, M. Zoriy, J. S. Becker, J. Dobrowolska, A. Matusch, "Laser ablation inductively coupled plasma mass spectrometry (LA-ICPMS) in elemental imaging of biological tissues and in proteomicsw," J. Anal. At. Spectrom. **22**, 736 (2007).

[16] L. Matus, H. M. Seufert, K. P. Jochum, "Microanalysis of geological samples by laser plasma ionization mass spectrometry (LIMS)," Fres. J. Anal. Chem. **350**, 330 (1994).

[17] R. G. Cooks, Z. Ouyang, Z. Takats, J. M. Wiseman, “Ambient mass spectrometry,” Science **311**, 1566 (2006).

[18] TOF Fundamentals. TOF Tutorial by R.M. Jordan Co. http://www.rmjordan.com/index.html.

[19] Q. Yu, R. Huang, L. Li, L. Lin, W. Hang, J. He, B. Huang, “Applicability of standardless semiquantitative analysis of solids by high-irradiance laser ionization orthogonal time-of-fight mass spectrometry,” Anal. Chem. **81**, 4343 (2009).

[20] P. Lorazo, L. J. Lewis, M. Meunier, “Short-pulse laser ablation of solids: from phase explosion to fragmentation,” Phys. Rev. Lett. **91**, 225502 (2003).

[21] P. M. Outridge, W. Doherty, D. C. Gregoire, “Ablative and transport fractionation of trace elements during laser sampling of glass and copper,” Spectrochim. Acta Part B **52**, 2093 (1997).

[22] M. E. Taylor, D. L. Blaney, G. Cardell, “Elemental fractionation in ultraviolet laser ablation sampling of igneous silicate minerals relevant to Mars,” Appl. Surf. Sci. **165**, 166 (2000).

[23] J. I. Apinaìniz, B. Sierra, R. Martiìnez, A. Longarte, C. Redondo, F. Castaño, “Ion kinetic energy distributions and mechanisms of pulsed laser ablation on Al,” J. Phys. Chem. C **112**, 16556 (2008).

[24] S. Kondrashev, T. Kanesue, M. Okamura, K. Sakakibara, “Features of ion generation using Nd-glass laser,” J. Appl. Phys. **100**, 103301 (2006).

[25] I. B. Gornushkin, A. Y. Kazakov, N. Omenetto, B. W. Smith, J. D. Winefordner, “Experimental verification of a radiative model of laser-induced plasma expanding into vacuum,” Spectrochim. Acta, Part B **60**, 215 (2005).

[26] S. Namba, R. Nozu, K. Takiyama, T. Oda, "Spectroscopic study of ablation and recombination processes in a laser-produced ZnO plasma," J. Appl. Phys. **99**, 073302 (2006).

[27] V. E. Levashov, K. N. Mednikov, A. S. Pirozhkov, E. N. Ragozin, "Aperiodic x-ray multilayer mirrors and their application in plasma spectroscopy," Radiat. Phys. Chem. **75**, 1819 (2006).

[28] I. L. Beigman, V. E. Levashov, K. N. Mednikov, A. S. Pirozhkov, E. N. Ragozin, I. Y. Tolstikhina, "Charge exchange of multiply charged laser plasma ions with rare-gas jet atoms," Quantum Electron. **37**, 1060 (2007).

[29] G. P. Gupta, B. K. Sinha, "Effect of ionization and recombination coefficients on the charge-state distribution of ions in laser-produced aluminum plasmas," Phys. Rev. E **56**, 2104 (1997).

[30] C. C. Garcia, J. M. Vadillo, S. Palanco, J. Ruiz, J. J. Laserna, "Comparative analysis of layered materials using laser-induced plasma spectrometry and laser-ionization time-of-flight mass spectrometry," Spectrochim. Acta, Part B **56**, 923 (2001).

[31] X. Wang, S. Amoruso, M. Armenante, A. Boselli, R. Bruzzese, N. Spinelli, R. Velotta, "Pulsed laser ablation of borocarbide targets probed by time-of-flight mass spectrometry," Opt. Lasers Eng. **39**, 179 (2003).

[32] A. A. Sysoev, S. S. Poteshin, G. B. Kuznetsov, I. A. Kovalev, E. S. Yushkov, "Analysis of bulk and powdered samples using a LAMAS-10M laser ionization tme-of-flight mass spectrometer," J. Anal. Chem. **57**, 811 (2002).

[33] X. K. Shen, H. Wang, Z. Q. Xie, Y. Gao, H. Ling, Y. F. Lu, "Detection of trace phosphorus in steel using laser-induced breakdown spectroscopy combined with laser-induced fluorescence," Appl. Opt. **48**, 2551 (2009).

CHAPTER 9 SUMMARY AND OUTLOOK

9.1 Summary

Micro-Raman and tip-enhanced Raman spectroscopy (TERS) systems were developed for measurement of different micro-/nanostructures and micro-/nanomaterials. Two micro-Raman systems are developed. One is based on a microscope, while the other one is based on a single crystal fiber probe. Better sensitivity of sapphire fiber probe compared to normal glass fiber probe was demonstrated. Near-field optical effect was employed by using apertureless metallic gold tips mounted on a scanning tunneling microscope system. TERS spectra of silicon, nanosphere lithography nanostructures, and carbon nanotubes were demonstrated. Using side-illumination optics, the TERS instrument can accommodate both opaque and transparent samples. Au tips were fabricated and used in this study. The single-walled carbon nanotube (SWCNT) samples on the Si substrates. The Raman peaks of different bands, including the RBM, D, G, and G′ bands, were obtained and analyzed. The Raman mapping of the SWCNTs at microscales and nanoscales was performed. The successful mapping of the individual SWCNTs using the tip-enhanced Raman spectrometer demonstrates that this apparatus has a spatial resolution of 30 nm. The correlated characterization capability of the system provides a new approach to understanding the relationship among the morphology, electronic, thermal, chemical, mechanical, and optical properties of nanoscale materials and devices, while eliminating sample contaminations during transportation among different instruments.

Surface-enhanced Raman spectroscopy using gold-coated horizontal carbon nanotube (Au-VA-CNT) substrate was studied. Rhodamine 6G (R6G) was measured using the new SERS substrate, from which significant SERS enhancement was observed. Enhancement factor (EF) was calculated to be ~10^7 for this SERS substrate. The substrate features simple, easy to prepare, and large SERS active area. At the same time, biological samples, such as fatty acids and algae cells, were also measured using the substrate. Limit of detection (LOD) was calculated. EF varies with the relative direction of the CNTs to the polarization direction of the incident laser beam. When the direction of the CNTs is parallel to the polarization of the incident beam, the EF reaches its maximum. The EF reduced to its minimum when the alignment direction of the CNTs is perpendicular to the E-field of the incident beam. Simulations using the 2D FDTD method were carried out to explain the experimental results. The simulation results closely agree with the experimental results. Biological samples, including ^{13}C- and deuterium (D)-labeled fatty acids and Coccomyxa sp. c-169 microalgae cells, were also measured using this SERS substrate. The limit of detection (LODs) of D- and ^{13}C-labeled fatty acids on the SERS substrate were measured to be around 10 nM and 20 nM, respectively. Significantly enhanced Raman signals from the microalgae cells were acquired using the SERS substrate.

A broadband CARS system was built for CARS spectroscopy and imaging based on a lens pair setup. While a more advanced microscope based B-CARS was used to measure algae cells. The CARS spectroscopy and imaging is compared to Raman spectroscopy and imaging. CARS spectra are taken from microalgae cells with or without nitrogen depletion, diamond thin film, ethanol, and methanol. The Raman spectra, using a

commercial Raman spectrometer, were taken from microalgae cells with or without N-depletion for comparison with the CARS spectra. The spectral resolution of the Raman spectroscopy system is much better than the B-CARS system, however, the imaging ability is not as good as CARS system from speed and.

The optical emission from the excited species in a $C_2H_4/C_2H_2/O_2$ combustion-flame was enhanced by introducing a CO_2 laser excitation and the CH rotational temperatures have a raising trend according to increasing laser powers. The increase in the emission intensity from the flames was found to be proportional to the laser power used. The laser excitation of the flame resulted in the deposition of diamond films with larger grains on the substrate. The CH rotational temperatures calculations showed that the 10.591-μm laser excitation had relatively smaller effects on the CH rotational temperature. Great temperature change appeared when the flame was excited by the 10.532-μm laser beam. From the increasing OES intensities and temperatures, it is concluded that the CO_2 laser can excite the C_2H_4 molecules by infrared absorption corresponding to the CH_2-wagging vibrational mode of the C_2H_4 molecules centered at 949 cm^{-1}, and this excitation is beneficial for diamond film depositions.

High spectral resolutions in LIBS were achieved by generation of high-temperature and low-density plasmas through reablation of laser-induced particles. Particles were formed using a KrF excimer laser to irradiate on an Al target. The particles were then reablated by a 200 mJ pulse from a 532 nm Nd:YAG laser. The line widths of plasmas decreased from ~0.32 nm (first-pulse plasmas) to ~0.09 nm (plasmas by reablation with an interpulse delay of 100 μs). The temperatures of plasmas in DP-LIBS increased due to the reheating process and then decreased gradually with longer

interpulse delays. The plasma electron density, however, was significantly reduced from ~1.2×10^{18} to ~3.3×10^{17} cm^{-3}. The temperature of reablation plasma was as high as the temperature of first-pulse plasma. The temperature of first-pulse plasma was ~6400 K with a plasma density of ~1.2×10^{18} cm^{-3}. The temperature of the reablation plasma, for instance, with an interpulse delay of 100 μs, was ~6200 K. However, the plasma density was ~3.3×10^{17} cm^{-3}, much lower than the density of first-pulse plasma. Therefore, high-temperature and low-density properties in plasmas were simultaneously achieved for improved spectral resolutions in LIBS.

Combined laser ionization and metastable ionization TOFMS (LI-MI-TOFMS) in open air has been investigated for qualitative and semiquantitative multielemental analyses of solid samples. The LI-MI-TOFMS of solids in open air was carried out by analyzing MS spectra and semiquantitative numerical calculations. Trace elements in the NIST samples were detected, such as Fe, Cr, Mn, Ni, Ca, Al, and Ag. MS signal intensities from these trace elements were found to increase with increasing laser pulse energy. The RSCs of the elements with relatively high ionization potentials increase with increasing laser pulse energy (e.g., Fe, Cr, Mn, and Ni). The effects of the DART and LI-TOFMS combination were not significant for those trace elements due to the absorption of laser energy by the DART H_3O^+ stream. Although the signal intensity was very low, the pure carbon target could be detected only when DART was combined with LI-TOFMS due to the high ionization potential of carbon atoms and the ambient air environment. Semiquantitative measurements were performed according to the correlation between signal intensity and element composition. RSCs were calculated and analyzed and found to depend on element concentrations and laser pulse energy. Higher

laser pulse energy leads to an increase in the RSCs of some trace elements (e.g., Mn, Cr, and Ni). The data from LIBS spectra was analyzed and compared with the MS spectra. The LI-MI-TOFMS approach is a promising alternative for qualitative and semiquantitative elemental analysis of solid samples in open air.

Table 9.1 Summary of laser-based spectroscopy and spectrometry techniques.

	SERS	TERS	CARS	OES	LIBS	LAMS
Principle	Molecular or crystal lattice vibration	Molecular or crystal lattice vibration	Molecular or crystal lattice vibration	Transitions involving electronic, vibrational, and rotational transitions of species in flame	Electronic transition of atoms or ions in laser-induced plasmas	laser ionization combined with metastable ionization
Combination possibility	TERS, CARS	SERS, CARS	SERS, TERS	LIBS	OES	LIBS
Resolution	Nanoscale (based on structure size)	<30 nm (spatial)	~500 nm(spatial)	<0.1 nm (spectral resolution)	<0.1 nm (spectral resolution)	$\lambda/\Delta\lambda$ (FWHM) is up to 6000
Application	Molecules, biological imaging, nanomaterial imaging	Biology, physics, and nanoscience	Fast-real time imaging, 3D-imaging (self-confocal)	Combustion flames, plasmas, or other excited emissions	Solids, liquids, or gases. (Isotopes)	Solids, liquids, or gases. (Isotopes)
Enhancement factor	10^7 (Best reported is 10^{14})	~200% (peak intensity enhancement)	-	-	-	-
Limit of detection	nM-μM	nM-μM	nM-μM	-	ppm (part per million)	ppb (part per billion)

9.2 Future directions

The laser-based spectroscopy and mass spectrometry techniques developed in the research in this dissertation are far from maturity. Further studies need to be conducted to improve these techniques to achieve better sensitivity, resolution, selectivity, and etc. A few possible future research directions are listed below:

(1) By combine an SPM system with a CARS system, a tip-enhanced CARS (TE-CARS) system can be developed for improved sensitivity and spatial resolution. Atomic force microscopy (AFM)-based transmission TE-CARS system can be a future direction. This system will have the ability to simultaneously observe and characterize morphological, structural, and functional properties of materials and organisms at micro- and nano-scales, in materials science, cellular biology, and other fields in the near future. For example, many great technological advancements in biotechnology and medicine will depend upon the ability to visualize, characterize, and externally manipulate cellular organelles and molecules. A major obstacle to making progress in micro/nanoscale characterization is the lack of powerful diagnostic techniques to characterize *individual* micro/nanostructures to explore their properties in a correlated manner. The absence of a system that can provide such characterization prevents correlated investigation of physical and chemical properties of individual micro/nanostructures in a single experiment. The *goal of this direction* is to develop a versatile, multifunctional TE-CARS imaging system that will be capable of nondestructive and noninvasive measurement of correlated geometrical, chemical, and biomedical properties such as shape, dimension, and chemical bonding with 3D confocality and nanoscale resolutions. The *objective of this direction* is to design, install, test, and complete a CARS system as shown in Fig. 9.1,

consisting of: 1) pump and Stokes beam generation, 2) a tip-enhancement module, and 3) a detection module. The setup will enable flexible and nondestructive broadband CARS imaging either in free-space or tip-enhanced modes (TE-CARS). There is no comparable system available, commercially or otherwise, that incorporates such a uniquely-combined set of functions into a single instrument.

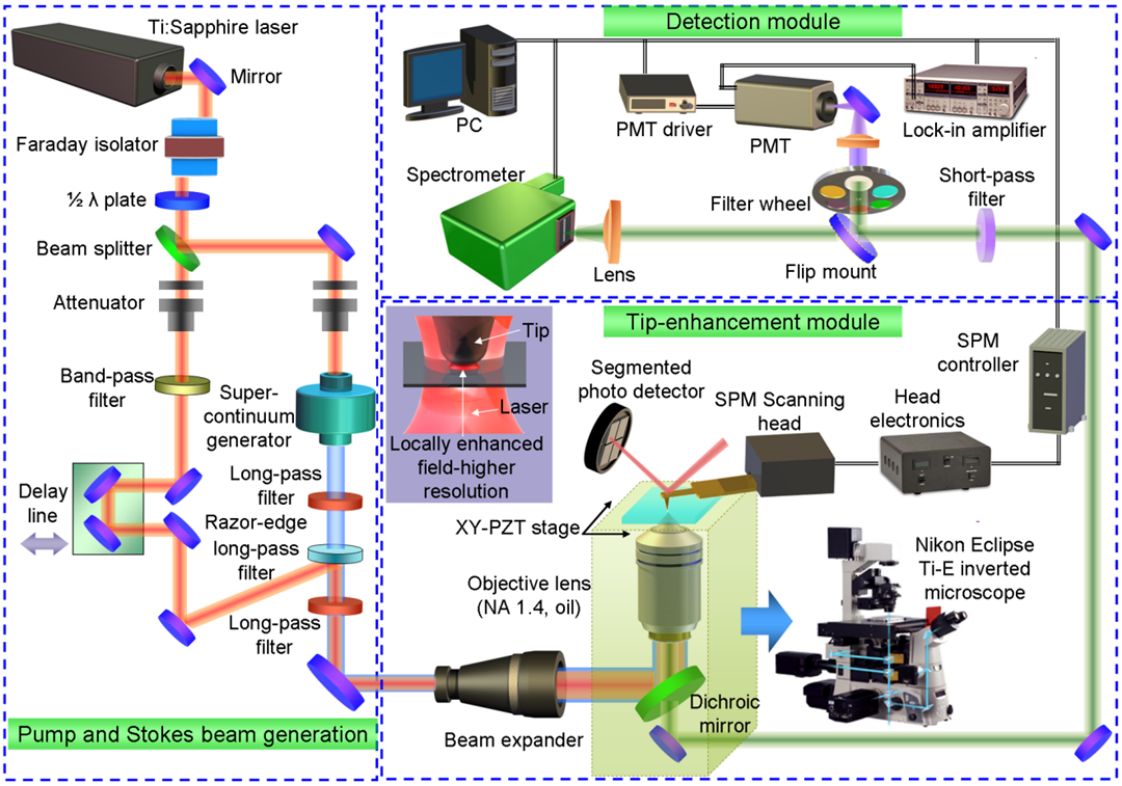

Figure 9.1 The proposed multifunctional TE-CARS system setup.

The instrument will feature three configurations and five characterization functions (Fig. 9.2). In configuration (A), it will operate as a conventional atomic force microscope (AFM) (function 1) for characterization of morphology and small bio-molecules. In configuration (B), CARS microscopy (function 2) will be combined with second-harmonic generation (SHG) microscopy, two-photon fluorescence (TPF) microscopy (function 3) to realize multimodal imaging of complex biological samples. In

configuration (C), addition of the SPM probe will enable local nanoscale intensity and spectral imaging (functions 4 and 5). Each function offers complementary capabilities. The unique capabilities of this instrument will allow researchers to obtain detailed local information on materials, cellular constituents, and biomolecules. Figure 9.3 shows a possible experimental setup diagram.

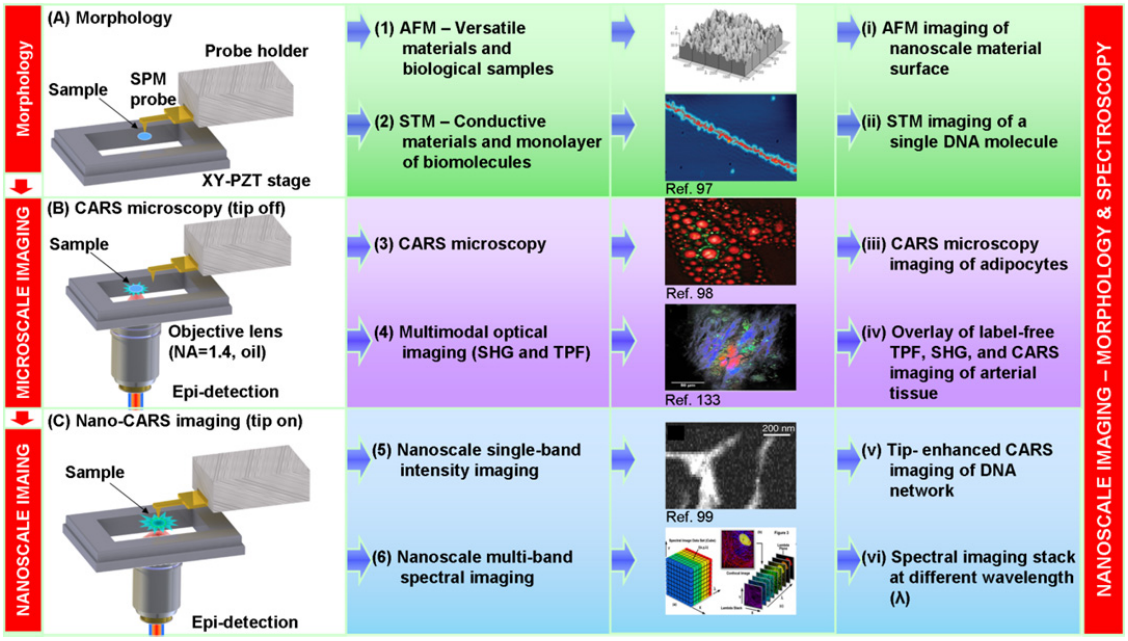

Figure 9.2 The functionality of the TE-CARS system.

(2) The Au-VA-CNT substrate will need to be further studied and improved. Based on our current experiment, the SERS effect can achieve 10^7 for this kind of substrate. However, the enhancement effect is not very stable, especially when the coating is too thin or too thick. Further study can be carried out to investigate enhancement factor change versus the thickness of sputtering coating. Optimal thickness need to be confirmed to make sure a stable SERS substrate.

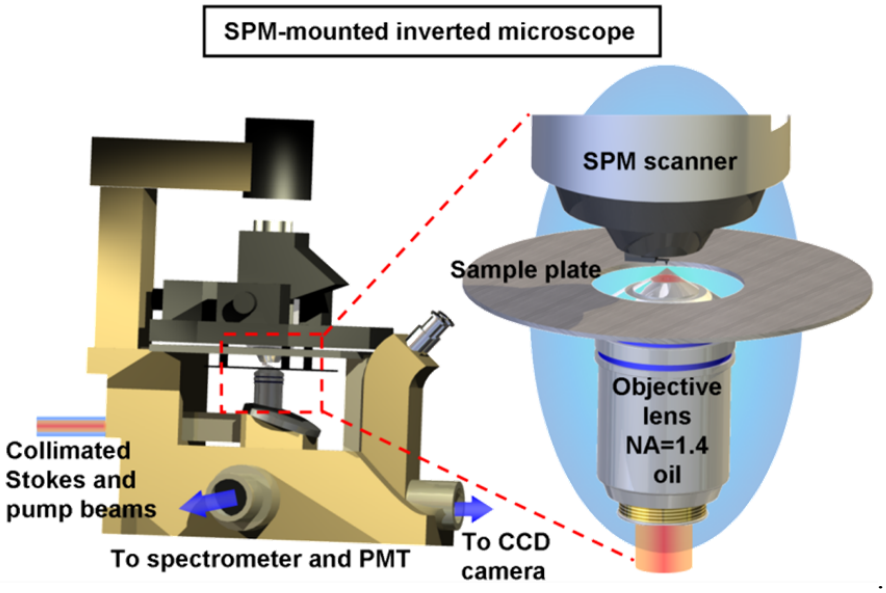

Figure 9.3 A schematic drawing of the experimental setup proposed.

(3) Optical emission spectroscopy study of diamond synthesis combustion flames was carried out for investigation of transitions of different states of various atoms, molecules, and radicals. Further improvement is needed to study the spatial distribution of atoms, molecules, and radicals, since there is only a very small location in the flame can achieve diamond thin film growth. Laser-induced fluorescence of the elements in the flame using a broadening optics can illuminate the whole flame area can be imaged using a CCD camera to have a spatial distribution of the elements in the flame.

(4) Current laser-based manufacturing industries do not have feedback mechanisms for their laser processing, thus the process is a blind process. The device discussed here (already filed to invention disclosure) is a low price simplified laser-induced breakdown spectroscopy (LIBS) detection system. It avoids high cost of a LIBS system. It features ultraportablility and high stability, and it is a very easy to use unit.

The purpose of the proposed LIBS device is to monitor laser-based manufacturing in industries, such as electronics, flat panel displays, photovoltaics, and automotives.

Figure 9.4 shows the schematic of the proposed device, including a focusing lens, optical filters, photodiodes, an operational amplifiers (Op-amp), an analog-to-digital convertor (ADC), an digital signal processor (DSP), a universal serial bus, and a frame tube for integration and packaging.

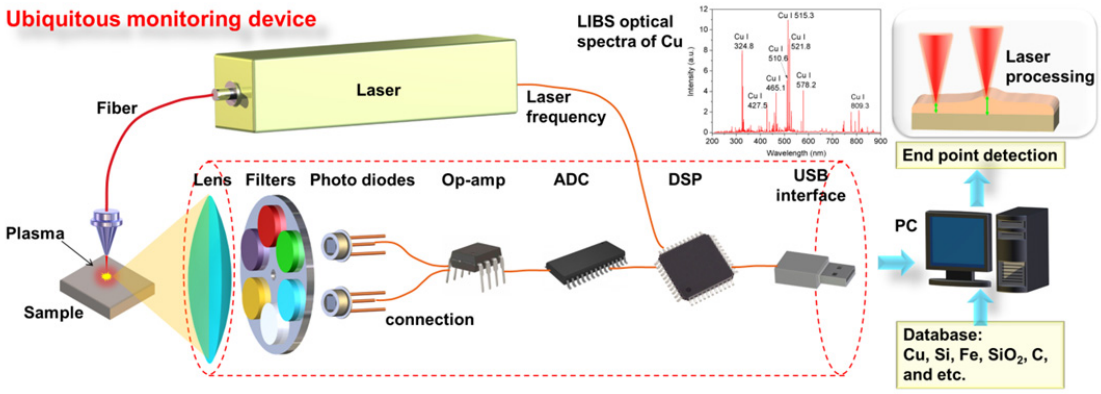

Figure 9.4 A schematic diagram of the LIBS monitoring device.

The software in this device will include a sector-specific database for processing materials (LIBS spectral data), signal acquisition, and interface with laser manufacturing equipment. Optical emission from the laser-induced plasmas will be collected through the lens (see Fig. 9.5), filtered by the optical filters, and detected by the photodiodes. The electric signals from the photodiodes will be processed by the Op-amp, ADC, and DSP. The DSP will also temporally filter out the strong plasma continuum in initial 1~2 μs after plasma formation. The devices will be ubiquitous in hardware and be customized for specific manufacturing sectors by software. One of the advantages of this device is shown in Fig. 9.6

(5) Laser-assisted mass spectrometry combined with DART ambient ion source can be improved if we can use an extra beam from an OPO laser to resonantly excite specific elements in the plasma plume to excite more ion in the plasma, so that the mass spectrometry signal will be higher, that is the sensitivity and selectivity of the LAMS will be significantly improved.

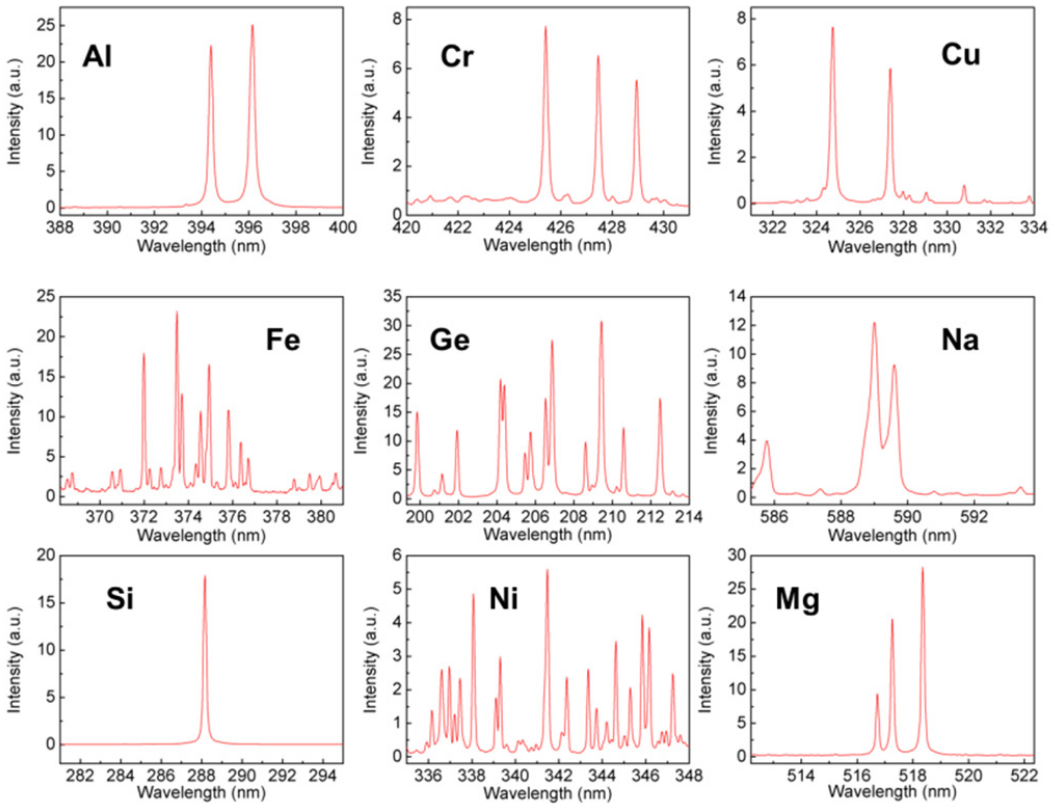

Figure 9.5 LIBS spectra of different elements.

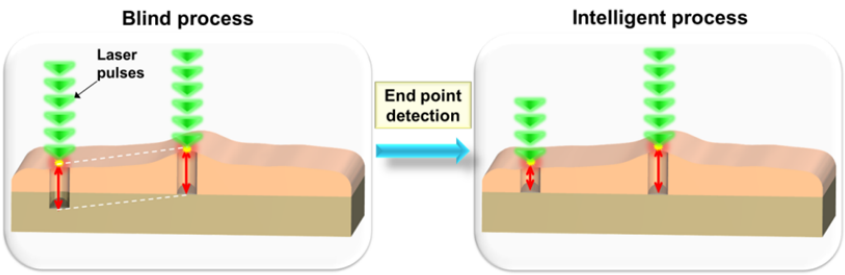

Figure 9.6 The diagram showing of the advantages when using the proposed device.

A new approach to detecting low concentration materials in open air using laser ablation for atomization of solid samples followed by resonant ionization to selectively ionize analyte atoms and time-of-flight (TOF) mass spectrometry combined with an ion source. The objectives of this direction are to develop an ion-source-assisted laser ablation resonant ionization mass spectrometry (LA-RIMS) system with the capability of detecting low concentration isotopes in ambient air. This will be achieved by successfully accomplishing the following research tasks: 1) develop a laser ablation mass spectrometer (LAMS), 2) combine the LAMS with an optical parametric oscillator (OPO) laser to realize LA-RIMS for selectively detecting ultra-low concentrations of isotopes, 3) combine an ambient ion source with the LA-RIMS system to further improve signal-to-noise (S/N) ratios, and 4) detect trace-level isotopes from calibrated NIST samples.

As shown in Fig. 9.7, an Nd:YAG laser, an optical parametric oscillator (OPO) laser, and a DART (direct analysis in real time) ion source will be used to atomize a trace amount of analytes, resonantly ionize selected analyte elements, and increase the ion populations, for fast and direct detection of elements in open air based on time-of-flight mass spectrometry (TOFMS).

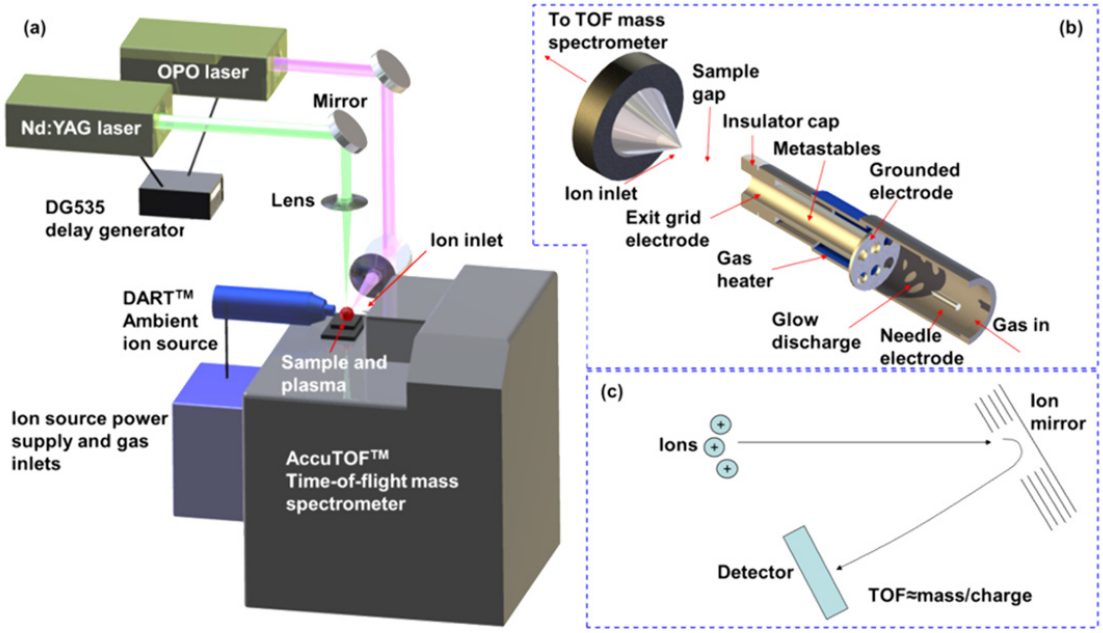

Figure 9.7 (a) Schematic of the LA-RIMS system. (b) Schematic of the DART ion source. (c) Schematic of TOFMS

In addition to the laser ablation process, the population of the ions will be selectively enhanced by the resonant ionization process (through excitation by the OPO wavelength-tunable laser) to produce sufficient amount of singly charged ions from the analyte element, which will be followed by an excitation from the DART ion source, enabling ultra-sensitive detection of elements of interest. The proposed approach has many advantages over existing state-of-the-art commercial equipment for trace-level element detections, including high selectivity, little sample preparation, and fast and real-time analysis. This method will allow researchers to obtain detailed and qualitative/semiquantitative information on trace elements in gas, liquid, or solids, allowing better understanding of sources and history of the samples.

Figure 9.8 shows the steps in the LA-RIMS system: 1) Laser ablation of a solid sample using a Nd:YAG laser will result in laser-induced breakdown of the specimen. 2)

The laser-induced breakdown process will form relatively stable plasmas (on microsecond scale) for MS analysis. Assuming the specimen has ultra-low level analyte, the plasma will only contain a few analyte ions. However, there will also be higher-concentration neutral analyte atoms in the plasma during this laser-induced breakdown process (suppose plasma temperature is sufficiently low). 3) Using a wavelength-matched OPO laser pulse, the neutral analyte atoms can be resonantly ionized, leaving the background neutral atoms unaffected, which will greatly improve the S/N ratio. 4) Using an ambient ion source, all the ions, atoms, and molecules of the analyte in the plasma plume region can be further ionized to provide higher signal intensity. 5) The ions will then be collected through TOF mass spectrometer inlet for detection. The whole setup of LA-RIMS can be seen in step 6.

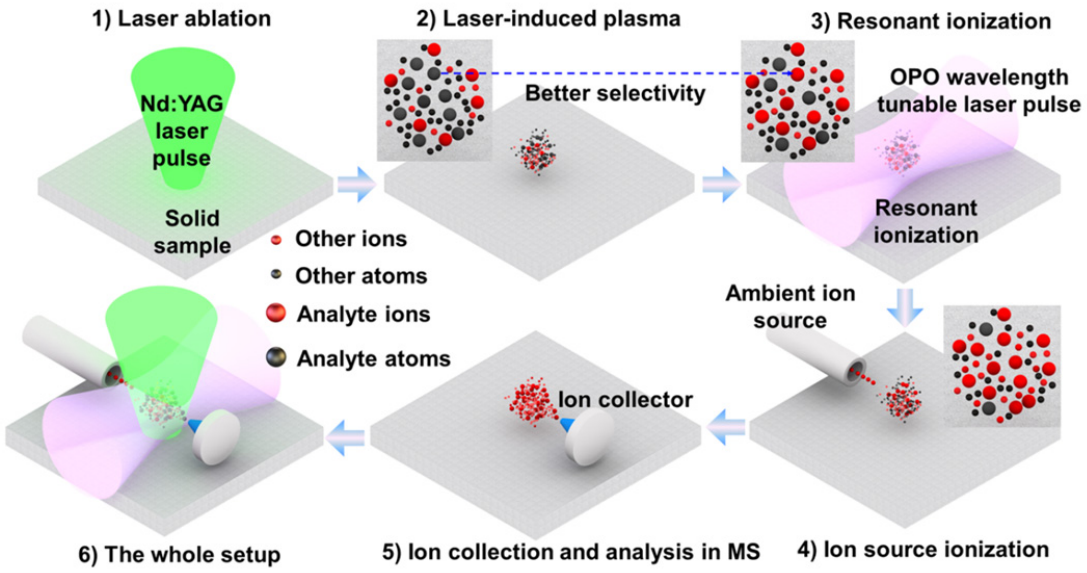

Figure 9.8 Experimental steps in the LA-RIMS system.

APPENDIX

Nanosphere lithography (NSL) process

In this dissertation study, we fabricated metallic nanostructures with different metals such as silver, gold, and molybdenum through nanosphere lithography (NSL) technique. NSL technique is an inexpensive, simple to implement, inherently parallel, high-throughput and materials general nanofabrication technique capable of making large-area nanostructures and well-distributed particle arrays (periodic particle arrays-PPAs) with sharp edges. A variety of PPA surfaces have been prepared using single layer (SL) and double layer (DL) NSL masks which were made by self-assembly of silica nanoparticles. We found that particle diameter, metal type and life-off process are three major factors governing the properties of the nanostructures.

Self-assembly of silica nanospheres

A variety of PPA surfaces have been prepared using identical single-layer and double-layer nanolithography masks made by self-assembly of Silica nanospheres. First, silica particles were dispersed into deionized water with a ratio of 1:10, and the mixed suspension was dropped on a well-prepared silicon substrate with a certain tilt angle ($\theta \approx 15°$) (Fig. A1). Hexagonally arranged, close-packed arrays of silica nanospheres were self-assembled on substrate surfaces. The cleaned substrates were wetted by surfactant. Large areas of the self-assembled 0.8, 0.51, and 0.33 μm particles were achieved (Fig. A2). The as-prepared substrates were examined with a field emission scanning electron microscope (Hitachi S-4700) and the AFM (Agilent 5500). Analysis on the SEM images

of the sample surfaces indicates that the particles can be very well used as a mask to fabricate NSL.

Sputtering process

Two sputtering systems were used to prepare metallic nanostructures. The gold layer with a thickness of ~50 nm was deposited on the particle-covered substrates with the small sputtering system (Emscope SC500), while silver and molybdenum were deposited using the home-made sputtering system. The silver and molybdenum layers were fabricated by the home-made sputtering system with much higher vacuum (1×10^{-7} ~ 1×10^{-8}) Torr.

Lift-off and characterization process

The particles were removed from the sputtered self-assembly substrates using ultrasonic agitation, and single layer or double layer PPA were left on the substrates. The period of ultrasonic agitation varied from 30 seconds to 2 minutes with an interval of 30 seconds, while the time of chemical etching in hydrofluoric (HF) acid was approximately 10 seconds. Figure A3 presents the full procedure of the process.

AFM images and SEM images of the nanostructure fabricated are shown in Figs A4-A9. These nanostructures can be obtained in well-ordered and large-area manners.

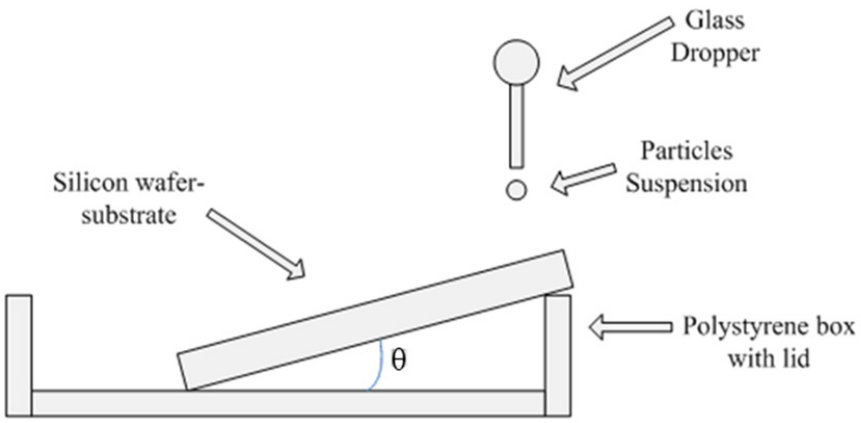

Figure A1 Experimental setup for self-assembly.

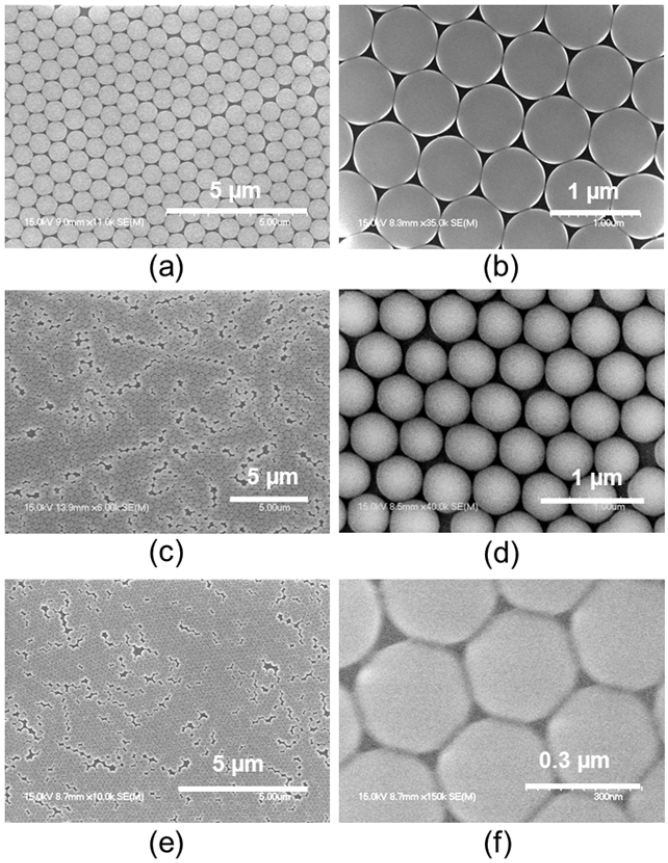

Figure A2 Self-assembly samples of different size particles. (a) and (b) are self-assembly of 0.8-µm (diameter) nanospheres; (c) and (d) are self-assembly of 0.51-µm nanospheres. The two pictures in each couple are at different magnifications; (e) and (f) are self-assembly of 0.33-µm nanospheres.

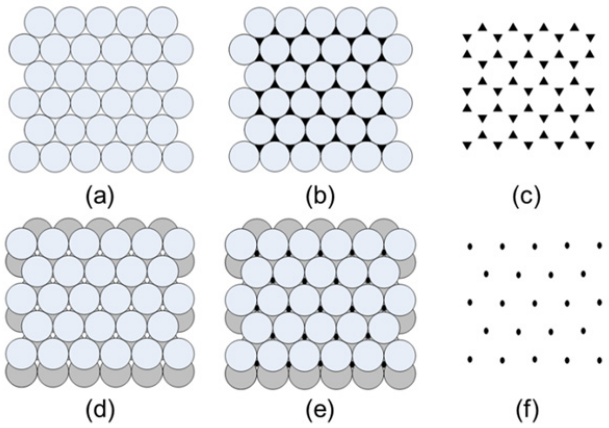

Figure A3 Schematic diagrams of single-layer (SL) and double-layer (DL) nanosphere masks and the corresponding periodic particle array (PPA) surface. (a) SL mask; (b) SL mask (after sputtering); (c) SL PPA (after lift-off); (d) DL mask; (e) DL mask (after sputtering); (f) DL PPA (after lift-off).

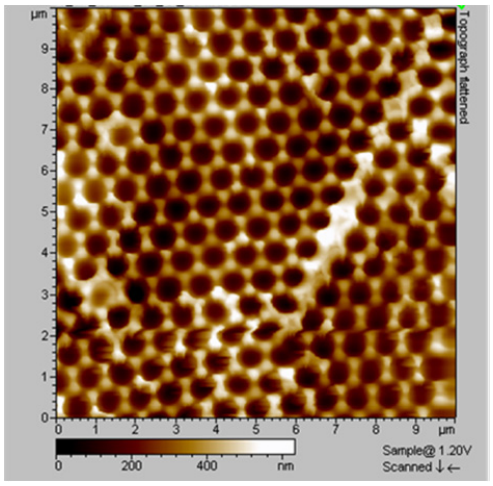

Figure A4 AFM image of NSL using 0.8 µm single layer silica nanospheres as a mask with 50-nm gold deposition.

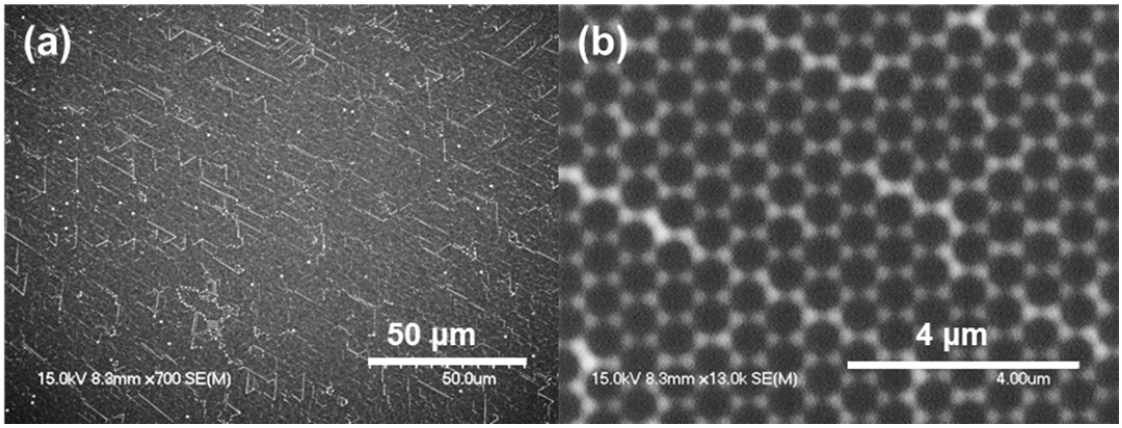

Figure A5 SEM images of NSL formed by sputtering on self-assembly samples of 0.8-µm silica nanospheres on Si substrate at different magnifications using molybdenum (Mo) target, the particle was then lifted off by ultrasonic in deionized water for 1 minute. (a) larger area (low magnification). (b) Smaller area (higher magnification).

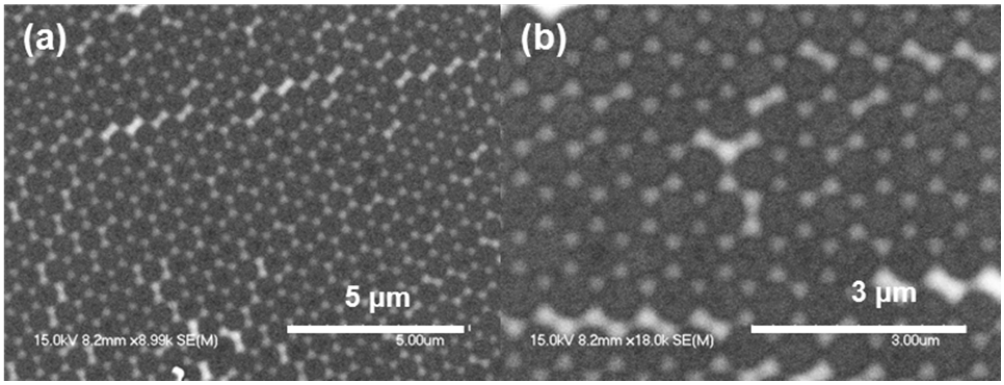

Figure A6 NSL formed by sputtering on self-assembly mask of 0.8-µm silica nanospheres on Si substrate at different magnifications using molybdenum (Mo) target, the particle was then lifted off by hydrofluoric acid (HF) acid in 15 seconds.

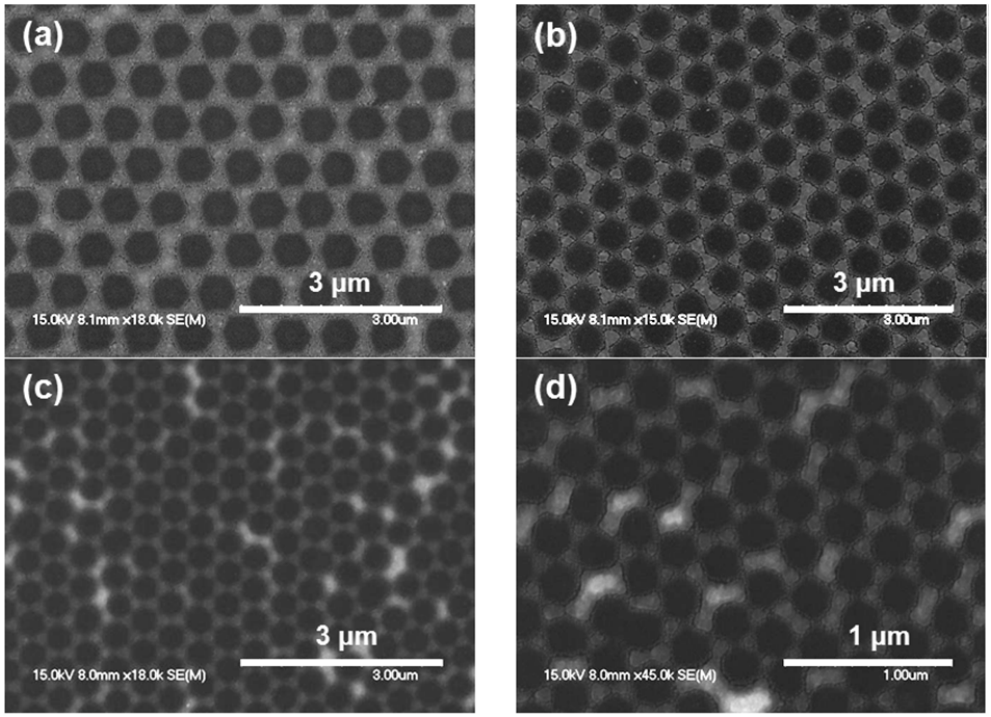

Figure A7 SEM micrograph of the NSL nanostructures fabricated using self-assembly of different size particles with 50-nm Ag deposition. (a) and (b) are NSL structures using self-assembly of 800-nm particles, but (a) shows the area that the triangle structures are connected, while in (b), the triangles are well isolated; (c) is NSL structure using self-assembly of 510-nm particles; and (d) is NSL using self-assembly of 330-nm particles.

Besides the typical SL PPAs, we also found several ring-like structures (Fig. A9). The thickness of these ring-like nanostructures is generally less than half of the total deposition depth. This structure was frequently found when we use ultrasonic agitation as a lift-off method. These nanostructures can be obtained in well-ordered and large-area manners.

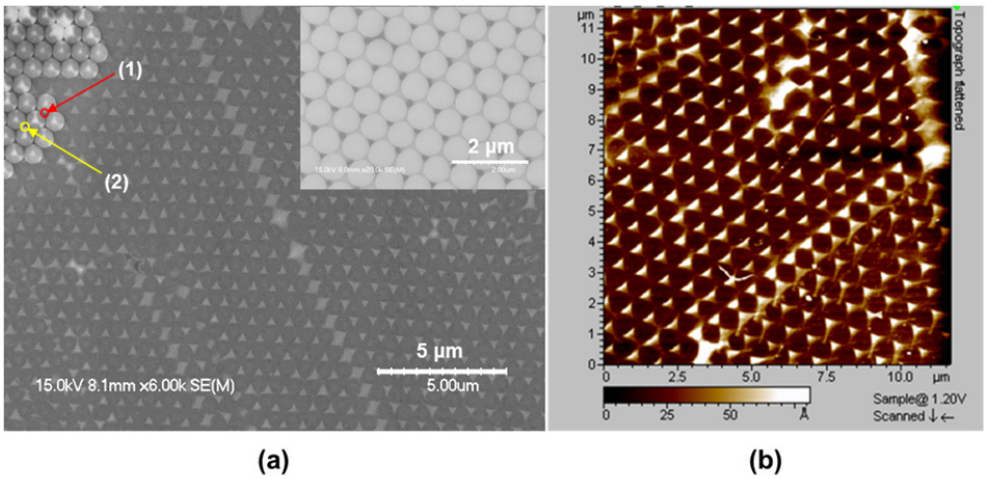

Figure A8 (a) Double-layer (DL) PPA formed by sputtering on self-assembly samples of 0.8-µm silica nanospheres on Si substrates with 100-nm silver deposition, and the particle removal was ultrasonic agitation in acetone for 2 minutes. (1) Interspaces like these will cause the gap escape from being deposited. (2) Interspaces like these will accept the deposition and make the triangle array on Si substrate. (Inset): DL mask of 0.8µm particles before sputtering. (b) AFM micrograph of the DL PPA formed by sputtering on self-assembly samples of 0.8 µm silica nanospheres on Si substrates with silver deposition, and the particles were removed in ultrasonic agitation in acetone for 2 minutes.

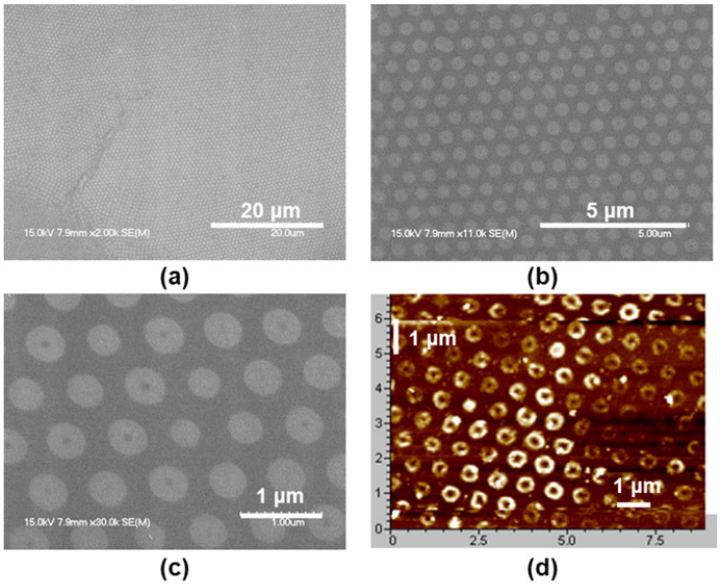

Figure A9 Ring structures formed by sputtering on self-assembly samples of 0.8 µm silica nanospheres with 40 nm Mo deposition and lift-off method of ultrasonic agitation. SEM images (a), (b), and (c) are the same sample at different magnifications. Picture (d) is an AFM image of the same sample.

Summary

In this section, the processes to prepare nanostructures using NSL technique were discussed. A sophisticated sputtering system for NSL nanofabrication was employed to obtain the desired nanostructures. Three different shapes of nanostructures including triangle shape, ring shape, and double-layer PPA shape were obtained. AFM and SEM characterization were carried out to measure the nanostructure fabricated.

LIST OF PUBLICATIONS

1. Journal papers

X. N. He, Y. Gao, M. Mahjouri-Samani, P. N. Black, J. Allen, M. Mitchell, W. Xiong, Y. S. Zhou, L. Jiang, and Y. F. Lu, "Surface-enhanced Raman spectroscopy using gold-coated horizontally aligned carbon nanotubes for enhanced sensitivity", Nanotechnology 23, 205702 (2012).

X. N. He, Z. Q. Xie, Y. Gao, W. Hu, L. B. Guo, L. Jiang, and Y. F. Lu, "Mass spectrometry of solid samples in open air using combined laser ionization and ambient metastable ionization", Spectrochimica. Acta Part B: Atomic Spectroscopy 67, 64-73 (2012).

X. N. He, W. Hu, C. M. Li, L. B. Guo, Y. F. Lu, "Generation of high-temperature and low-density plasmas for improved spectral resolutions in laser-induced breakdown spectroscopy", Opt. Express 19, 10997-11006 (2011).

X. N. He, X. K. Shen, T. Gebre, Z. Q. Xie, L. Jiang, and Y. F. Lu, "Spectroscopic Determination of Rotational Temperature in $C_2H_4/C_2H_2/O_2$ Flames for Diamond Growth with and without Tunable CO_2 Laser Excitation", App. Opt., 49(9), 1555-1562 (2010).

W. Xiong, Y. S. Zhou, **X. N. He**, Y. Gao, M. Mahjouri-Samani, L. Jiang, T. Baldacchini, and Y. F. Lu, "Simultaneous additive and subtractive three-dimensional

nanofabrication using integrated two-photon polymerization and multi-photon ablation", Light: Science & Applications 1, e6 (2012).

Z. Q. Xie**,** Y. S. Zhou, **X. N. He**, Y. Gao, T. Guillemet, J. B. Park, M. M. Wang, L. Jiang, and Y. F. Lu "Mode-selective reactions in chemical vapor deposition of diamond through laser vibrational excitations". (In preparation)

L. B. Guo, B. Y. Zhang, **X. N. He**, C. M. Li, Y. S. Zhou, T. Wu, J. B. Park, X. Y. Zeng, and Y. F. Lu, "Optimally enhanced optical emission in laser-induced breakdown spectroscopy by combining spatial confinement and dual-pulse irradiation", Opt. Express 20, 1436-1443 (2012).

C. Raml, **X. N. He**, M. Han, D. R. Alexander, and Y. F. Lu, "Raman spectroscopy based on a single-crystal sapphire fiber", Opt. Lett. 36, 1287-1289 (2011), which has been selected by the Editors, A. Dunn and A. Durkin, for publication in the most recent issue of the Virtual Journal for Biomedical Optics (VJBO).

L. B. Guo, W. Hu, B. Y. Zhang, **X. N. He**, C. M. Li, Y. S. Zhou, Z. X. Cai, X. Y. Zeng, and Y. F. Lu, "Enhancement of optical emission from laser-induced plasmas by combined spatial and magnetic confinement", Opt. Express 19, 14067–14075 (2011).

Y. Gao, Y. S. Zhou, J. B. Park, H. Wang, **X. N. He**, H. F. Luo, L. Jiang, and Y. F. Lu, "Resonant excitation of precursor molecules in improving the particle crystallinity, growth rate and optical limiting performance of carbon nano-onions", Nanotech. 22, 165604 (2011).

Z. Q. Xie, **X. N. He**, W. Hu, T. Guillemet, J. B. Park, Y. S. Zhou, J. Bai, Y. Gao, X. C. Zeng, L. Jiang, and Y. F. Lu, "Excitations of Precursor Molecules by Different Laser Powers in Laser-Assisted Growth of Diamond Films", Cryst. Growth Des., 10(11), 4928-4933 (2010).

Z. Q. Xie, Y. S. Zhou, **X. N. He**, Y. Gao, J. B. Park, H. Ling, and Y. F. Lu, "Fast Growth of Diamond Crystals in Open Air by Combustion Synthesis with Resonant Laser Energy Coupling", Cryst. Growth Des., 10, 1762-1766 (2010).

W. Xiong, Y. S. Zhou, M. Mahjouri-Samani, W. Q. Yang, K. J. Yi, **X. N. He**, S. H. Liou, and Y. F. Lu, "Self-Aligned Growth of Single-Walled Carbon Nanotubes Using Optical Near-Field Effects", Nanotechnology, 20(2), 025601 (2009).

K. J. Yi, **X. N. He**, Y. S. Zhou, W. Xiong, and Y. F. Lu , "Tip-Enhanced Near-Field Raman Spectroscopy with a Scanning Tunneling Microscope and Side-Illumination Optics", Rev. Sci. Instrum. 79, 051807 (2008).

2. Conference papers and presentations

X. N. He, Z. Q. Xie, Y. Gao, X. Huang, Y. S. Zhou, and Y. F. Lu, "Combined laser ionization and ambient metastable ionization in mass spectrometry of solid samples in open air", submitted to the 13th International Symposium on Laser Precision Microfabrication (LPM 2012).

X. N. He, L. B. Guo, Z. Q. Xie, X. Huang, W. Hu, X. Y. Zeng and Y. F. Lu, "Laser-induced breakdown spectroscopy with improved spectral resolutions through the generation of high-temperature and low-density plasmas", Proc. SPIE 8244, 82440H (2012).

X. N. He, Z. Q. Xie, Y. S. Zhou, L. B. Guo, W. Hu, and Y. F. Lu, "Spectral resolution improvement in laser-induced breakdown spectroscopy through the generation of high-temperature and low-density plasmas", the 30th International Congress on Applications of Lasers & Electro–Optics (ICALEO) (2011).

X. N. He, X. K. Shen, Z. Q. Xie, T. Gebre, and Y. F. Lu, "Spectroscopic determination of rotational temperature in C2H4/C2H2/O2 flames for diamond growth with and without tunable CO_2 laser excitation", presentation at the 47th Annual Technical Meeting of Society of Engineering Science (2010).

X. N. He, T. Gebre, X. K. Shen, Z. Q. Xie, Y. S. Zhou, and Y. F. Lu, "Optical Emission Spectroscopy Study of Premixed C_2H_4/O_2 and $C_2H_4/C_2H_2/O_2$ Flames for

Diamond Growth with and without CO_2 Laser Excitation", Proc. SPIE, Vol. 7585, 75850A (2010).

X. N. He, K. J. Yi, and Y. F. Lu, "Mapping of Individual Single-Walled Carbon Nanotubes Using Nano-Raman Spectroscopy", Proc. SPIE, Vol. 7202, 72020E (2009).

L. B. Guo, **X. N. He**, B. Y. Zhang, C. M. Li, W. Hu, Y. S. Zhou, W. Xiong, X. Y. Zeng, and Y. F. Lu, "Enhancement of laser-induced breakdown spectroscopy signals using both a hemispherical cavity and a magnetic field", Proc. SPIE 8244, 82440I (2012).

Z. Q. Xie**, X. N. He**, W. Hu, Y. Gao, T. Guillemet, J. B. Park, Y. S. Zhou, and Y. F. Lu, "Laser-Power-Resolved Excitations of Ethylene Molecules in Laser-Assisted Synthesis of Diamond Films", the 30th International Congress on Applications of Lasers & Electro–Optics (ICALEO) (2011).

L. S. Fan, Z. Q. Xie**,** J. B. Park, **X. N. He**, Y. S. Zhou, and Y. F. Lu, "Synthesis of nitrogen-doped diamond films by vibrational excitation of precursor molecules using CO_2 laser in a combustion flame process", the 30th International Congress on Applications of Lasers & Electro–Optics (ICALEO) (2011).

Z. Q. Xie**,** Y. S. Zhou, **X. N. He**, Y. Gao, J. B. Park, T. Guillemet, and Y. F. Lu. "Laser-assisted synthesis of diamond crystals in open air through vibrational excitation of precursor molecules". Proc. SPIE 7921, 79210E (2011).

X. K. Shen, **X. N. He**, H. Huang, and Y. F. Lu, "Spatial confinement effects in laser-induced breakdown spectroscopy", in Laser Applications to Chemical, Security and Environmental Analysis, OSA Technical Digest Series (CD) (Optical Society of America, 2010), paper LWD4.

Z. Q. Xie**, X. N. He**, Y. Gao, Y. S. Zhou, J. B. Park, T. Guillemet, and Y. F. Lu, "Laser-induced resonant vibrational excitation of precursor molecules in multi-energy processing for diamond synthesis", the 29th International Congress on Applications of Lasers & Electro–Optics (ICALEO) (2010).

Z. Q. Xie**,** J. B. Park, **X. N. He**, Y. Gao, Y. S. Zhou, and Y. F. Lu, "Resonant excitation of ethylene molecules in the combustion flame CVD of diamond using a wavelength tunable CO_2 laser", Proc. SPIE 7585, 758509 (2010).

Z. Q. Xie**,** J. B. Park, **X. N. He**, Y. Gao, T. Guillemet, Y. S. Zhou, and Y. F. Lu. "Laser Resonant Vibrational Excitations of Precursor Molecules in Multi-Energy Processing for Diamond Synthesis". 47th Annual Technical Meeting of Society of Engineering Science (2010).

K. J. Yi, **X. N. He**, Y. F. Lu, "Surface- and Tip-Enhanced Raman Spectroscopy of Silicon", ICALEO 2008 (27^{th} International Congress on Applications of Lasers and Electro-Optics).

K. J. Yi, **X. N. He**, and Y. F. Lu , “Tip-enhanced Near-field Raman Spectroscopy Using an Scanning Tunneling Microscope with Side Illumination Optics”, Proc. SPIE, 6880, 688006 (2008).